INFORMATION TO USERS

This manuscript has been reproduced from the microfilm master. UMI films the text directly from the original or copy submitted. Thus, some thesis and dissertation copies are in typewriter face, while others may be from any type of computer printer.

The quality of this reproduction is dependent upon the quality of the copy submitted. Broken or indistinct print, colored or poor quality illustrations and photographs, print bleedthrough, substandard margins, and improper alignment can adversely affect reproduction.

In the unlikely event that the author did not send UMI a complete manuscript and there are missing pages, these will be noted. Also, if unauthorized copyright material had to be removed, a note will indicate the deletion.

Oversize materials (e.g., maps, drawings, charts) are reproduced by sectioning the original, beginning at the upper left-hand corner and continuing from left to right in equal sections with small overlaps. Each original is also photographed in one exposure and is included in reduced form at the back of the book.

Photographs included in the original manuscript have been reproduced xerographically in this copy. Higher quality 6" x 9" black and white photographic prints are available for any photographs or illustrations appearing in this copy for an additional charge. Contact UMI directly to order.

UMI

A Bell & Howell Information Company
300 North Zeeb Road, Ann Arbor MI 48106-1346 USA
313/761-4700 800/521-0600

Effects of Secondary Air Injection on the Hydrodynamics of Circulating Fluidized Beds

by

Levent Erdogan Ersoy

A Thesis Submitted to the
Faculty of Engineering
in Partial Fulfillment of the Requirements
for the Degree of

DOCTOR OF PHILOSOPHY

Major Subject: Mechanical Engineering

APPROVED:

[redacted]

Dr. Feridun Hamdullahpur, Supervisor

[redacted]

Dr. Julio Militzer

[redacted]

Dr. Prabir Basu

[redacted]

Dr. Adel M. Al Taweel

[redacted]

Dr. Khalil Shahkarzadeh, External Examiner, Université de Compiègne

DALHOUSIE UNIVERSITY DALTECH

Halifax, Nova Scotia **1998**

DALHOUSIE UNIVERSITY, DALTECH LIBRARY

"AUTHORITY TO DISTRIBUTE MANUSCRIPT THESIS"

TITLE:

Effects of Secondary Air Injection on the Hydrodynamics of Circulating Fluidized Beds

The above library may make available or authorize another library to make available individual photo/microfilm copies of this thesis without restrictions.

Full Name of Author: Levent Erdogan ERSOY

Signature of Author: 

Date: 06/24/1998

TABLE OF CONTENTS

LIST OF TABLES

LIST OF FIGURES

Nomenclature

a : Exponential decay constant (-) in type I modeling

a1, a2, a3, a4 : Constants used in core radius formulation

Ar : Riser cross sectional area (m^2)

c, d, n : Constants defining the particle velocity profile

C_1, C_2, C_μ, : Constants of k-ε closure model

C_d : Drag coefficient(-)

C_{xx} : Autocorrelation of a signal Xn

C_{xy} : Cross correlation of two continuous functions

dL : Axial distance between the two consecutive pressure probes (m)

d_o : Diameter of SA jets (m)

d_p : Diameter of a single particle (m)

D_t : Hydraulic diameter of the riser (m)

E_{max} : Maximum acceptable error in velocity probe calibrations

f : Sampling frequency (Hz)

Fr : Froud Number (-)

Fr_t : Froud number based on the terminal velocity of a single particle (-)

G : External solids circulation rate (kg/m^2s), Local solids flux (in Eq 5.43)

g : Gravitational acceleration (9.81 m/s^2)

G_k : Generation of turbulent kinetic energy

Gr : Local solids flux at radial position r (kg/m^2s)

Gs : Solids flux (kg/m^2s)

h : Axial distance (m)

H_{SA} : Height of SA injection plane (relative to the distributor plate)

H_{SAE} : The distance between the SA effective region and the distributor plate

H_t : Height of the riser (m)

K : Constant used in various empirical equations

k : Turbulent kinetic energy

L_{acc} : Height of the acceleration region (m)

L_{SA} : Height of SA effective region (-)

m : Constant of parabola (-) defining solid flux profile

$\dot{m}_s$: Mass flow rate of solids (kg/s)

M_s : Lateral momentum imposed by the SA jets

M_t : Total momentum of the flow

PA : Primary air

r : Jet propagation depth (radial coordinate, m); radius of SA jets in calculations of height of SA effective region; Time lag (sec), radial coordinate (m)

R : Riser radius (m)

r_c : Radius of the core region (m)

Re_p, Re : Particle Reynolds number (V_t*d_p/v)

Re_t : Reynolds number of flow (gas phase; Uo*Dr/v)

SA : Secondary air

SAR : Secondary air ration (SA/PA, Volume flow rate ratio)

St : Stokes number

t : Time (sec)

Torr : Pressure Unit (133.32 Pa)

U_0 : Superficial gas velocity (m/s)

U_{center} : Gas velocity in the centerline of the pipe (m/s)

$U_{g,core}$: Average gas velocity in the core (m/s)

$U_{g,max}$: Maximum gas velocity (m/s)

U_{mean} : Average gas velocity (m/s)

$V_{j,r}$: The cross sectional area occupied by radial the SA jets (m^2)

$V_{j,t}$: The cross sectional area occupied by the tangential SA jets (m^2)

v_p : Particle velocity (cross sectional average, m/s)

$V_{p,a}$: Average particle velocity in the annulus (m/s)

$V_{p,max}$: Particle velocity at the centerline of the riser (m/s)

$v_{p,r}$: Particle velocity at local radial position r at a given axial position (m/s)

V_{sl} : Slip velocity (Ug-Vp; m/s)

V_t : Terminal velocity of a single particle (m/s)

W : Tangential velocity component

x : Axial distance downstream the swirling SA injection; radial distance from the center of the disk (m) in velocity probe validation

z : Axial coordinate (m)

z_i : Axial coordinate of inflection point (Kwauk's model)

ΔP : Difference in the static pressure between the two sections of the riser

Δt : Time step used in the calculations (s)

Greek Letters

Γ_{xy} : Normalized cross correlation function

α : Angle of dispersion of SA jets(degrees)

δ_{ij} : Kronecker delta function

ε : Gas volume fraction (-), dissipation rate of turbulent kinetic energy

ε^* : Limiting voidage at the riser top (-)

ε_a : Average void fraction in the annulus (-)

ε_{ave} : Cross sectional average voidage (-)

ε_b : Voidage at the base of the riser (-)

ε_c : Average void fraction in the core (-)

ε_s : Solids volume fraction (-)

$\varepsilon_{s,cutoff}$: Solids fraction due to the cutoff effects of SA jets

φ : Slip factor (-)

σ_k, σ_ε : Constants of k-ε closure model

μ_l : Laminar dynamic viscosity (Ns/m^2)

μ_t : Turbulent dynamic viscosity (Ns/m^2)

τ_a : Aerodynamic response time of a particle (s)

$\tau_{ij,l}$: Laminar stress tensor

$\tau_{ij,t}$: Turbulent stress tensor

ρ : Density (kg/m^3)

ν : Kinematic viscosity (m^2/s)

λ : Momentum ratio of the cross flow (-)

ϕ : Ratio of the core cross sectional area to riser cross sectional area (-); variable of interest in conservation equations (*CFD Modeling); and angle of deflection of SA jets (degrees) in calculation of jet penetration depth.

Ω : Swirl intensity (-)

δ : Thickness of the annulus region (m)

Subscripts

j : Refers to the properties of SA jets in calculations of L_{SAE}; refers to the vertical coordinate in conservation equations

c : Core

a: : Annulus

p : Particle

g : Gas

Superscript

' : Denotes the properties for the acceleration region in the hydrodynamic model

ACKNOWLEDGMENTS

I would like to express my sincere gratitude to my supervisor, Dr. Feridun Hamdullahpur, who has been a major source of support in scientific, financial, and social problems encountered throughout the course of this study. He always provided the most logical solutions to the problems brought to him. I very much enjoyed, and feel honored working under his guidance. Also, I am thankful to Dr. Julio Militzer, who has been very helpful not only by opening up his resources for this study, but also by responding quickly to the problems brought to him.

I am grateful to Mr. Murat Koksal, a graduate student in Mechanical Engineering Department. His assistance during the experimental work, help in CFD modeling, the valuable discussions and support during the preparation of the thesis are gratefully acknowledged. Special thanks to fellow graduate students; Mr. Bulent Belibagli, for his continuous backing in solutions of computer related problems, to Mrs. Merih Aydinalp for her help in preparation of the manuscripts, and to Mr. Antonio Bemfica for his helps in utilization of the optical probe.

I would like to thank to Mr. Angus MacPherson, to Mr. Felix Roma and to Mr. Steward Carr, mechanical technicians in the department, for their excellent performance in production of the SA port and the cyclone. Technical assistance for the design and construction of the data acquisition system provided by Mr. Gregory Jollimore, electronics technician, is highly appreciated.

Finally, I am very grateful to my wife, Arban Citak, for her valuable suggestions backed up with constant motivation, and to my parents for their continuous support, encouragement, motivation and understanding throughout my education. Only this time, it has been somewhat more difficult since it was a little further away from home.

ABSTRACT

Circulating fluidized bed combustion of fossil fuels has many advantages over the conventional combustion systems, such as effective NO_x control, high sulfur capture efficiency, and high combustion efficiency. These advantages are much more pronounced with the application of staged combustion by secondary air injection. The concept of secondary air arises from splitting the fluidization air into a primary air stream, which is injected axially from the bottom of the riser, and a secondary air stream injected laterally to the riser.

Although the benefits of staging are well appreciated, due to complexity of the fluidization process, optimization of staging is yet to be completed. For example, Basu(1991) notes that the amount of staged air varies between 30-70 % of the total combustion air from one manufacturer to the other. This example shows the requirement for detailed studies for better utilization of secondary air in CFB systems.

In this work the most effective parameters of staging are considered as the *mode*, the *height* and the *amount* of secondary air, and the individual effects of these parameters on the overall hydrodynamics of a CFB riser is sought. Experimentally, the particle velocity profiles in the lower sections, and pressure profiles throughout a cold type CFB riser are measured under varying secondary air parameters. Computationally, jet emerging patterns and the effect of mode and intensity of SA jets on the gas flow patterns in the riser are studied using 3-D computational fluid dynamics (CFD) approach. The knowledge obtained from experimental and computational work is used in constructing a two dimensional core-annular hydrodynamic model for CFB risers. The hydrodynamic model accounts for the effects of individual parameters of secondary air injection.

Chapter 1

Overview of Fluidized Bed Systems

1 Introduction

This work investigates the hydrodynamics of circulating fluidized bed (CFB) risers under various combinations of secondary air (SA) injection parameters. The considered parameters of SA injection are: the amount of secondary air injection (SAR), the height of SA injection, and the orientation of SA jets.

The problem is analyzed experimentally by measuring the local particle velocity at various sections of the riser, and monitoring the pressure drop and pressure fluctuations inside the riser under varying parameters of SA injection. The results of the experiments revealed indications that the jet emerging patterns may be important in terms of hydrodynamic blockage. Therefore, a computational fluid dynamics (CFD) study is performed to see the changes in the gas flow patterns in the riser under varying jet emerging patterns and in the absence of particles. Finally, the knowledge gained is implemented in a two-dimensional core-annular model, which accounts for the SA injection parameters and predicts the riser hydrodynamics.

The problem studied is a two phase (gas-solid) flow problem and usually analyzed under the topic: *Fluidization*. Therefore this chapter is composed of a brief description of behavior of particles under fluidized conditions, problem definition, objectives, and scope of the study.

1.1. Fluidization

"*Fluidization is the operation by which fine solids are transformed into a fluidlike state through contact with a gas or liquid. This method of contacting has a number of unusual characteristics, and fluidization engineering is concerned with efforts to take advantage of this behavior and put it to good use.*" (Kunii and

Levenspiel, 1977).

Fluidized bed processes are widely encountered in industrial processes such as fluid catalytic cracking, combustion of fossil fuels, waste incineration, drying and sizing of powdery materials, gasification and in other numerous chemical processes. The attractive features of fluidized beds are consequences of rapid mixing of gas and solids, which lead to nearly isothermal conditions throughout the reactor and high heat and mass transfer rates within the bed interiors; the gas, the particles and the heat transfer surfaces.

A gas-solid fluidized bed can hydrodynamically be in bubbling, turbulent, fast or in transport regime depending on the operating conditions; fluidization velocity and the properties of the bed material. When the superficial gas velocity exceeds the minimum fluidization velocity (the minimum gas velocity in which solid particles are suspended), the bed passes from the fixed state to fluidized state. Depending on the type of the particles, further increase in the superficial gas velocity results in gas bubbles whose size increase with particle diameter, gas velocity and elevation. At this stage, the bed is said to be in *bubbling regime*. A typical characteristic of bubbling beds is that the solids volume fraction is very high at the bottom portion of the chamber while the fluidizing gas passes through this region in form of bubbles. Bed expansion is not very high, solid particles are in motion and there is a sharp but oscillating boundary between the dense bed and above (the freeboard). Most of the particles stay in the bed while some low density and/or small diameter particles are entrained with the up-flowing gas. Those entrained particles either fall back to the bed or become elutriated and captured by the particle collection systems such as cyclone(s) or dust collectors.

A continued increase in the superficial gas velocity may result in a change in the fluidization pattern. At this stage, bubbles loose its identity inside the bed due to rapid coalescence and breakup, resulting in a violently active and highly expanded bed in which particles are thrown into the freeboard above the bed. Beds with such characteristics are called *turbulent beds* (Basu, 1991). A

turbulent fluidized bed is also characterized by having two different coexisting regions: a lower region where the solids are the continuous phase, and an upper region where the gas is the continuous phase while the solids are dispersed.

Further increase in the superficial gas velocity may cause the fluidization process to operate in the *fast fluidized bed* regime where high velocity of gas-solid suspension, particle elutriation by the fluidizing gas above the terminal velocity of single particles are main characteristics. In the fast fluidization regime, the bed does not have a distinguishable upper surface and the particles that are transported out at the top must be replaced by adding solids near the bottom (Grace, 1997). The bed hydrodynamics does not only depend on the superficial gas velocity but also the solid feed rate. Kwauk et al. (1986)'s definition of fast fluidization stresses that the vague boundary that appears in high velocity fluidization is a boundary typical of fast fluidized beds and a much sharper boundary is of bubbling fluidized beds.

Increasing the superficial gas velocity at a fixed solid feed rate results in *dilute-phase pneumatic transport regime* in which there is no axial variation of solids concentration except in the bottom acceleration section. The particles follow the gas with a slip velocity approximately equal to the single particle terminal velocity.

The response of the bed material to the increase in the superficial gas velocity is shown in Figure 1.1.

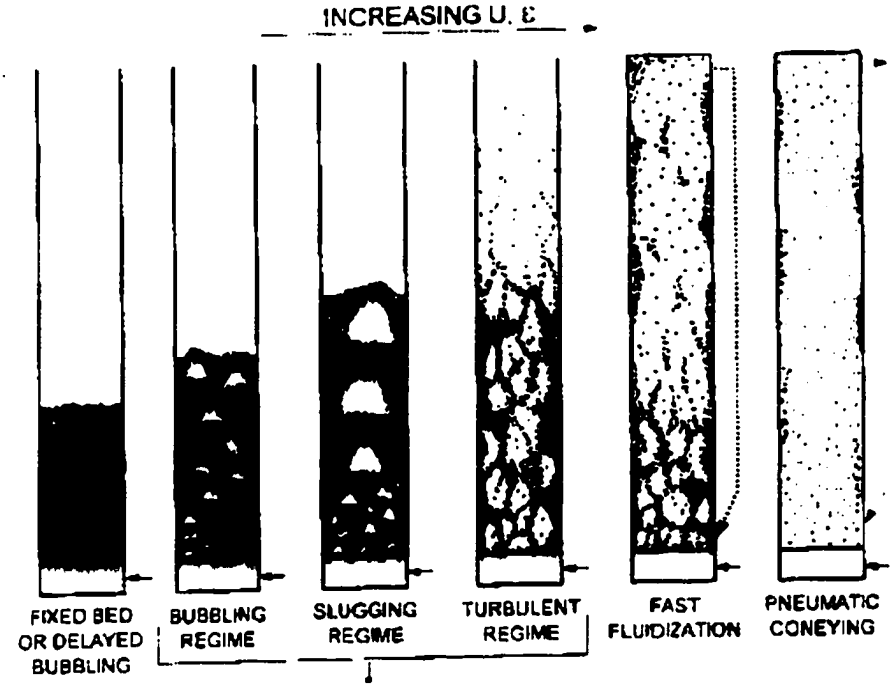

Figure 1.1 Flow patterns in gas-solid fluidized beds (Grace, 1997)

The behavior of particulate solids in fluidized beds depends largely on a combination of their mean particle size and density (Geldart, 1986). The most common classification of particles is the Geldart's classification, which is based on the mean diameter of the particle and the density difference between the particle and the fluidizing medium. In this classification, the particles, according to their own fluidization characteristics are grouped into 4 classes. These groups are;

Group A : Particles that have a small mean size (<45 μm) and/or a low density (less than 1.4 g/cm^3) expand considerably before bubbling commences. If the gas supply is abruptly shut off, the bed will slowly collapse. Gross circulation of the powder occurs even when only a few bubbles are present, producing a very well mixing. All bubbles within the bed rise more rapidly than the interstitial gas velocity.

Group B : Group B contains most particles in the mean size range of 40 μm < d_{sv} < 500 μm, and a density range of; 4 g/cm^3 > ρ_s > 1.4 g/cm^3. Sand is the

most typical powder in this group. Naturally occurring bubbles start to form in this group at or slightly above the minimum fluidization velocity. Bed expansion is small and the bed collapses very quickly when the fluidizing gas supply is cut off. There is a very little or no circulation of the particles in the absence of bubbles. These bubbles burst at the surface as discrete entities. Most bubbles rise faster than the interstitial gas velocity, and the bubble size increases linearly with both excess gas velocity and bed height.

Group C: Powders that are in anyway cohesive belong to this group (e.g. cement, flour). The normal fluidization of these particles is extremely difficult. These particles lift as a slug in small diameter beds or channel profusely; that is, the gas passes through voids that extend from the distributor plate to the bed surface. This problem is a result of the inter-particle forces, which are greater than those, which the fluid can exert on the particle. These are usually the result of extremely small particle sizes, strong electrostatic charges or the presence of very sticky material in the bed. This results in poor particle mixing and poor heat and mass transfer within the bed.

Group D : Particles which fall into this group are relatively large, and/or very dense. There is less information on the behavior of these particles compared to the published literature of the previous three groups. All but the largest bubble flows more slowly than the interstitial gas velocity so that gas flows into the base of the bubble and out the top. This provides a mode of gas exchange and by-passing different form that observed with group A or B particles. The flow regime around these particles can be very turbulent, which may cause some particle attrition with quick elutriation of fines Geldart(1986).

1.2. Circulating Fluidized Beds

Bubbling fluidized beds has been expansively utilized in a wide spectrum of industrial applications due to its benefits such as high process efficiency, higher heat transfer rates and low emissions, system flexibility etc. In bubbling bed combustion of fossil fuels, the combustion and heat transfer process

mostly take place in a restricted area, in the lower dense part of the bubbling bed. The temperature of the flue gas decreases quickly as it travels along the freeboard due to the heat transferred to superheater and due to lack of combustion. This gradient in temperature, indeed, reduces the rate of combustion reaction of entrained char, resulting in an increase in the amount of unburned carbon in the flue gas. Lower freeboard temperatures may decrease NO_x formation reactions but it also suppresses N_2O reduction reactions.

As explained in the previous section, an increase in the superficial gas velocity in a bubbling bed results in the entrainment of the particles at the top of the bed depending upon the height of the freeboard. These particles may then, be collected with a particle collecting mechanism (usually a cyclone) and return back to the bottom of the bed from a separate line forming a circulation loop. Such beds designed for high solids circulation rates are called circulating fluidized beds (Lim et al. 1995).

Circulating fluidized beds, due to the higher slip velocities between the phases, higher circulation rate of bed solids and good mixing characteristics, provide more homogenous riser flow then the bubbling beds. Another feature of circulating fluidized beds, is the staged combustion with application of secondary air which is seen as an effective way of controlling the riser temperature (Wu and Alliston, 1993; Boemer et al. 1993; Hippinan 1993). Controlling the amount of oxygen and temperature in the combustion chamber is a very effective way of reducing hazardous product emissions, such as N_2O, NO_x and SO_2 (Basu, 1991).

1.3. Secondary Air Injection in CFB's

The effects of supplying split combustion air to the CFB are numerous. On the combustion side; the utilization of sub-stochiometric primary air is an effective solution for NO_x formation during the volatile combustion, Talukdar (1996). On the hydrodynamics side; the application point of secondary air is a conclusive

parameter on the fluidization regime. The location of secondary air injection is referred as the transition point from turbulent to fast bed regime, Basu (1991), Arena (1993), Talukdar (1996). The region below the secondary air injection port shows a dense and highly turbulent behavior, whereas the fast bed is comparably dilute. The flow structure above the secondary air injection is usually core-annular, Aguillon (1996), and the flow can either be in fast bed or pneumatic transport regime. On the mixing patterns of the bed material; the secondary air jet may prevent solids back-mixing in the bottom portions of the fast bed while enhancing the gas-solid and solid-solid mixing in the turbulent bed. Arena (1993) explained that the air jet most likely causes a cut off in the motion of solids along the walls.

The orientation of the secondary air injection ports may also be effective in determining the type of the riser flow. In majority of systems operating with staged combustion, the secondary air stream is injected radially into the riser. The radial type of injection, at a first glance, promotes a very quick mixing and seems to be the easiest method to manufacture. Secondary air can also be injected tangentially into the riser. In this type of injection, secondary air streams create a swirling circulating flow pattern in which higher solids residence time, higher solids holdup and higher slip velocities can be achieved due to the helical motion of the solid particles, Illias et al. (1988).

1.4. Previous Studies

1.4.1. Cold Bed Studies

Wang and Gibbs (1991) observed an increased solids holdup in the bottom part of the riser with application of secondary air. Arena (1993) showed that the axial location of secondary air injection directly influences the voidage profile in the riser by creating a local maximum around the SA injection region. Results of his experiments in a 0.12-m ID riser showed that due to the cutting off effect of secondary air streams, the suspension appears to be more dilute in the secondary air injection region whereas it become denser in the lower region.

Aguillon et al. (1996) observed flattened particle axial velocity profile below the secondary air injection ports. They also noted that jet formation at the secondary air injection level must be avoided since it seemed to obstruct the solid transfer between the dense and the lean bed in their 0.28 X 0.17-m cross section riser operating with FCC. Arena and his co-workers (1993) had similar observations, also. Their pressure fluctuation data showed that the amplitude of pressure fluctuations along the riser is higher with secondary air injection, indicating a plug type of flow around the SA injection region.

The height of injection and the intensity of the air jets (SAR) seem to be two of the major design parameters of secondary air injection. Kim et al. (1994) have shown that with increasing height of secondary air injection port, the solids holdup in the lower dense phase increases and the position of transition moves upwards. Keeping a constant total air, as the secondary air ratio increased, all of the above investigators observed a denser solids suspension in the primary region. Kim et al. (1994)'s reasoning for such a behavior was decreasing amount of primary air, whereas Aguillon et al. (1996) and Arena et al. (1993), mentioned the barrier effects of the secondary air jets.

Contrary to the remarkable effect on the solids holdup pattern in the turbulent region, neither of Arena et al. (1993), Aguillon et al. (1996), Wang and Gibbs, noticed a noteworthy influence of SA injection on the solids holdup profile in the upper bed. Whereas, Kim et al. (1994), with radial secondary air injection, noticed a slightly reduced suspension density and Illias et al. (1988) observed an increase in the solids holdup in the same region with tangential secondary air injection.

Wu and Alliston (1993) tested a cold model spouted SA bed, and mentioned that the solids holdup in the upper portions of the riser is higher in case of spouted secondary air injection. They observed that the solids flow pattern in the upper bed shows a core annular behavior, giving a parabolic solids flux distribution over the cross section, dispersed solids particles moving upwards

with a high velocity in the core region, and a denser down-fluxing wall region, with a velocity around 1 m/s. The down-flow of solids along the walls happens in form of quickly forming and disappearing clusters, or in a continuous form depending on the loading and properties of the particles. The suspension density decreases exponentially along the fast bed Kunii and Levenspiel (1977).

In the case of a swirling secondary air injection, Illias et al. (1988) have shown that the solids holdup increases in all sections of the riser with increasing SAR and/or increasing height of secondary air injection. Contrary to the radial injection case, solids move upward in helical paths, keeping a higher solids suspension density and a more homogenous bed within the effective region of swirl intensity. Illias et al. (1988) also measured the solids residence time distributions (RTD), and found that both gas and particle residence time increases with increased swirl intensity and/or increased secondary air injection height. Therefore for a fixed design RTD, a swirling type bed would require a shorter riser height and thus economically justifiable.

1.4.2. Hot bed Studies

Numerous authors study the effect of staging combustion air on the emission characteristics of fluidized bed combustion. Hippinen et al. (1993) performed experiments in a pressurized bubbling bed reactor to study the emission characteristics. Their results showed nitrogen oxides emissions can be lowered by reducing the amount of primary air. However, an increase in the SO_2 emissions is also reported in cases where the bubbling bed is operated with sub-stochiometric air. Nitrous oxides emissions, on the other hand, are found to be dependent on the bed temperature.

SO_2 emissions in CFB combustion can be decreased by limestone injection to the reactor. Shimizu et al. (1993) studied the effect of SO_2 removal with limestone on the effect of NO_x and N_2O emissions. They concluded that limestone feed to a CFBC increased NO_x emissions while it decreased N_2O and SO_2 emissions. The rate of N_2O decomposition reported as to be as high as SO_2

removal.

Xu et al. (1993) studied the effect of staged combustion air in a laboratory type swirling fluidized bed reactor. Their results showed that secondary air injection have strong effect on combustion efficiency, which can be increased by 5-10 percent with the optimized secondary air fraction between 0 to 30 percent. They used two sets of secondary air nozzles mounted along the height of the freeboard, each set had four nozzles arranged at four corners of the rectangular section to form a tangential circle flow. The lower set was spaced at 1.8m above the distributor plate and the distance between the two sets was 0.5-m. Sampling the particles for carbon content, they found that the position of maximum carbon content migrates from the wall to the center with the injection of swirling secondary air. Also, they found that with increasing injection velocity, the mean carbon content of fly ash collected by cyclone reduced sharply, while the mean carbon content of the fly ash that escaped from the cyclone reduced slightly, suggesting an increase in the combustion efficiency. The height of secondary air injection also effected the combustion efficiency. The combustion efficiency obtained with injecting the secondary air from lower positions was found to be higher than that of higher position injections. They also reported that increasing the superficial gas velocity increased the NOx and NO emissions due to shorter gas residence times. More experiments were carried out to study the effect of fuel properties on the emissions. Results show that NOx and N_2O emission is highly dependent on the nitrogen content of the fuel since higher temperatures are required to burn the air bound nitrogen.

1.4.3. Present Studies of Commercial Design

Boemer et al. (1993) conducted experiments and summarized the emission characteristics of four different large-scale circulating fluidized bed combustors located in Germany. The characteristic features of the plants are given Table 1.1

They concluded that beside the coal rank, excess air and bed temperature are the most important parameters influencing N_2O and NO_x emissions. Higher levels of excess air supports the oxidation of fuel bound nitrogen and elevates both N_2O and NO_x formation. Higher combustion temperatures supports NO_x formation but hinders N_2O formation. Measurements in the riser indicated that the net change of N_2O and NO_x concentration in the combustion chamber depend on its design and resulting temperature and oxygen profiles. They found that the influence of air staging depends on the design of SA parameters in the plant. In some cases they observed that it was possible to diminish N_2O without elevating other emissions by optimizing these parameters. They also reported that the addition of limestone did not influence the N_2O emission. Effect of Ca/S ratio on NO_x emission was studied experimentally by Illias et al. (1988) which showed an increase in the NOx emissions with increased Ca/S ratio.

1.5 Current research

The previous works on hot beds reveal that an increase in combustion temperature increases the NO_x emission and decreases the N_2O emission. Unburned carbon (CO) decreases at high bed temperatures, whereas SO_2 emission shows a minimum at a bed temperature of 835 ^oC. As oxygen is needed for the oxidation of fuel nitrogen, a higher oxygen level increases both N_2O and NO_x. Higher oxygen level (excess air) also means a reduction in gas residence time. Therefore, parameters such as local temperature and oxygen distribution in the circulation fluidized bed combustors have key roles on the amount of environmentally hazardous emissions and combustion efficiency of the process.

Table 1.1 Characteristic features of 4 CFB boilers operating in Germany. (from Boemer et al., 1993)

Manufacturer	EVT (Alshtrom)	D. Babccock	Steinmuller	Lurgi
Thermal Power	72 MW	120 MW	229 MW	105 MW
Fuel	Hard Coal	Hard Coal	Brown Coal	Hard Coal with 20% Brown C.
Cross Section	4.1m X 5.7m	6.0m X 6.3m	7.4m X 11.3m	5.3m Diameter
Height (Comb.)	25 m	30 m	31 m	31 m
Fluid Velocity	3.9 m/s	4.5 m/s	5.5 m/s	6.3 m/s
Primary Air Fraction	40 - 60%	50 %	40 – 50 %	40 %
Secondary air Port I, Height	2.8 m	3.7 m	5.5 m	2.3 m
Secondary air Port II, Height	4.7 m	6.7 m	9.0 m	6.9 m
Flue Gas Recirculation	Yes	Yes	Yes	No
Superheater in the Riser	Yes	Yes	Yes	No
Control of Bed Temp	By recirculation of flue gas	By siphon fluidization	Not controlled	By lance
$\frac{\text{Height(SA)}}{\text{Height(Riser)}}$	0.112- 0.188	0.123 – 0.223	0.177 – 0.29	0.074 – 0.223

Results of previous cold bed studies, on the other hand, show that the above mentioned parameters are a part of the hydrodynamics of the process, and that they may be controlled to some extend by introducing staged combustion with secondary air injection. Both Kunii and Levenspiel (1977), and Basu (1991) pointed the importance of the staging, however no guidelines for the optimized use of staging are revealed due to the lack of quantitative information in the open literature. The information given by Basu (1991) show that the secondary air ratio (SA/PA) used in commercial boilers may show a wide variation from 0.5 to 1.3. Also, same scatter can be seen in the amount of secondary air ratio (SAR = SA/PA) used in previous cold model experiments, which varies between 0 and 4.5, Aguillon (1996), Wang (1991). From Basu (1991) one finds that the height of secondary air injection point may vary from 3 to 6-m from one manufacturer to the other. Also, with a quick look at Table 1, one can easily see the inconsistency in location of the secondary air jets in similar plants. The secondary air injection height varies from 7 to 17% of the total riser height, and the tertiary air injection height varies from 19 to 29% of the total riser height in plants that operate under similar conditions while burning similar coals. This example clearly indicates the necessity for extensive studies on the utilization of staged combustion air in CFB combustion process.

1.6 Objectives of the Study

The primary objective of this thesis is to study the two phase flow behavior in a CFB riser, and gather quantitative information on the flow behavior in the riser under varying parameters of secondary air injection.

1.7 Scope and Goals

The scope of the thesis includes:

Experimental:

- Design and construction of a cold type CFB equipped with a non-intrusive secondary air injection system, which suits for varying individual parameters of secondary air injection.
- Seeking quantitative information which represent the effects of individual parameters of SA injection on the solids holdup profiles and particle velocity profiles in a CFB riser.

Mathematical:

Analysis of experimental data in search for possible trends related with SA injection parameters.

1.8 Methodology

In this study the secondary air to primary air ratio (SAR), the distance between the distributor plate and the secondary air injection port (the *height of injection*), and the *mode* or the *orientation* of the secondary air injection are considered to be the most significant design parameters of secondary air injection. The solids holdup distribution and the particle velocity field have been referred as indicators of riser flow. Therefore the variations in the above flow variables (riser pressure and velocity field) under varying SA injection parameters will be sought.

1.9 Expected outcome

This work investigates the individual contribution of each design parameter of secondary air to the hydrodynamics of a cold CFB. The expected outcome of the thesis is to gather experimental data in order for fully comprehending the effect of secondary air parameters on the riser flow. The gathered information may be used in the development of a mathematical model, which accounts for the staging parameters.

Chapter 2

Experimental

2.1 Introduction

The experimental set-up used in this study was designed to study the effect of a number of important parameters. The distance between the distributor plate and the SA injection plane determines the volume of the sub-stochiometric region and, this may be a conclusive parameter in determining the residence time of the particles in dense bottom region (Wang et al., 1991). The injection geometry, on the other hand, includes other parameters such as the number of injection ports on the same plane, horizontal alignment of SA jets, vertical orientation of the SA jets, the number of vertically distributed injection ports, SA injection velocity, etc. These parameters are also seen as conclusive parameters in the design of mixing patterns between the primary and secondary air streams. In addition to these, more dependent and independent parameters arise from the complex nature of fluidization, such as the regime of fluidization, which may be effected by the size of the riser, solids circulation rate, velocity of primary air, particle characteristics etc.

An experimental study is undertaken the investigate effects of each individual parameters of secondary air on the hydrodynamics of CFB riser. Some researchers (Wang et al., 1991; Arena et al., 1990, 1993, Aguillion et al., 1996; Kim et al., 1994; Illias et al., 1988) studied the effect of some of these parameters on the riser hydrodynamics. However, the scope of investigation in these studies was limited. Thus, it is very difficult to relate the published data even in its own scope, and further to integrate the interpretations from individual studies, mainly because of different geometrical and/or operational parameters used in the experiments. It is necessary to carry out a complete experimental work for the understanding of the flow behavior, and to gather

quantitative data under varying staged air parameters. It is, therefore, essential to use an experimental set-up, which provides enough flexibility to investigate the effects of each parameter, represent the hydrodynamic behavior inside commercial boilers, and yet permit comparable results from different experiments.

The variables defining the hydrodynamics of a CFB riser include the velocity field of gas and solid phases, local void fraction map and external solids circulation rate. Although the first three parameters are considered as pure system responses to the input parameters, depending on the operating conditions, the solids circulation rate can be considered also as a dependent parameter. Therefore, a complete experimental study must include measurements towards capturing the individual responses of the above variables to the changes in the secondary air parameters.

The local gas velocity in a single-phase flow can precisely be measured with many techniques such as pitot tubes, laser Doppler velocimetry, hot wire anemometer, etc. However, in case of a dense two-phase flow, the presence of small particles makes it is very difficult to measure the dynamic head of the flow with pitot tubes due to plugging. The hot-wire anemometer technique is also not applicable due to the inertial effects of the particles. The non-intrusive techniques, such as LDV systems, are not considered as effective for dense suspension flows. On the other hand, with the use of fiber-optical probes, it is possible to conduct particle velocity measurements at a local point (Militzer et al., 1992).

The differential pressure measurement has been a reliable tool for the estimation of axial voidage profiles. Easy to use, comparably affordable, and is a reliable data source for statistical analysis if acquired through adequate transducers. In addition, the fluctuations in the pressure field can be used as a tool to obtain information about the regime of fluidization. On the other hand, gathering information on the local voidage profile is not as straight forward as

that of the axial voidage profile, and has been the center of attention due to its use in the optimization of fluidized bed processes. Various techniques including radioactive particle tracing, fiber optical bundles, high-speed video systems with image processing, and isokinetic sampling probes have been tested. Although the techniques reported as promising, non-of them are found superior over the others. In this study, the axial pressure drop profile is measured to estimate the axial solids holdup profile.

The three parameters, namely *mode*, *amount* and *height* of secondary air injection, are considered as the parameters of primary importance in studying the hydrodynamics of CFB risers with SA injection. Thus, the related experiments are designed to monitor the effect of individual parameters of SA on the particle velocity field and solids holdup profile. The following section covers the reasoning behind the selection of SA parameters of primary importance.

2.2 Parameters of Secondary Air Injection

2.2.1 Amount of Secondary Air:

The theoretical air requirement for a combusting system is fixed by the composition of the fuel and the design capacity of the plant. Additional air, i.e. excess air, is necessary in order to achieve a complete utilization of the combustibles in the fuel. This excess amount of air is usually selected around 20 - 30 % depending on the fuel properties. It is also a known fact that excessive amount of excess air increases the amount of NO_x emissions. Therefore, the total amount of air supplied to the riser is fixed by the fuel properties and design capacity of the plant. The problem here is what percentage of the total air must be supplied as staged air. Referring to previous works, the answer requires knowledge on both fuel composition and flow hydrodynamics, which involves SA injection parameters.

In this work, the amount of secondary air is presented in non-dimensional form, as the ratio of amount of secondary air to primary air, and it is represented as SAR or SA/PA.

2.2.2 Height of Secondary Air Injection:

Previous works on emission characteristics showed that it is possible to achieve lower NO_x emissions under sub-stoichiometric air conditions during the combustion of volatile gases. Volatile combustion occurs in the lower part of the bed where the temperature is measured as the highest in the riser. Extending the sub-stoichiometric combustion region by increasing the height of secondary air injection also seen as a useful method to help reduce the emissions by controlling the temperature and oxygen profile in the primary bed, and to attain a homogenous temperature distribution along the riser.

Hydrodynamically, CFB's may operate under two distinct regimes along the riser axis and a transition regime between them at an instant. In such a case, turbulent fluidization forms at the bottom portion, and a fast bed regime from over the transition bed up to the exit of the riser. Injection point of secondary air streams is, therefore, a crucial parameter, since the region of SA injection is referred as the transition region between the two operating regimes along the riser (Basu, 1991).

The vertical distance between the distributor plate and the secondary air injection plane is referred as the *injection height* and it will be denoted by H_{SA} throughout this work.

2.2.3 Angle of Secondary Air Injection:

Secondary air can be injected radially into the riser, or it can be injected inside the riser within an envelope forming an angle with the radial line on horizontal plane. This creates a tangential velocity component in the upcoming suspension, resulting in a swirling motion in the riser. Depending on the swirl

intensity imposed, one may expect changes in the radial profile of gas-particle suspension, also. Particles with higher inertia may move towards the walls and fall down due to the centrifugal forces, whereas smaller particles are likely to move with the core region upward, following helical paths.

The angle of secondary air injection may give rise to different gas-mixing patterns. For tangential injection case, for example, the secondary air is likely to diffuse into the main stream gradually from the walls inward as the flow advance through the riser. Whereas, in radial injection case, one may expect a very quick mixing between the upcoming flow and the SA jets in the center region of the riser. Therefore, the *angle of SA injection*, sometimes referred as the *mode of injection*, is considered as an important parameter of staging with secondary air injection.

In this work, in addition to both radial and tangential SA injection cases, 45° injection of secondary air is also studied experimentally, to see the transient effect of changing the injection angle from one extreme to the other.

In addition to the above parameters, one may suggest that some other parameters may also effect the hydrodynamics of riser flow while staging, such as the number of injection ports at one level, the ratio of area of injection to the total encircling area of the riser, number of levels of secondary air injection and angle of injection with horizontal plane, etc. But the effect of these parameters may be considered as minor when compared to the effects of the above three major parameters. These minor parameters may be studied at later stages, after gaining a sound knowledge about the effects of selected parameters of primary importance.

2.3 Experimental Setup

Figure 2.1 shows the schematics of the experimental circulating fluidized bed assembly. High velocity fluidization up to 5.5 m/s could be maintained in a 0.23 m ID, 7.62-m high transparent column. Fluidization air is supplied from a roots type blower with a rate of 0.23 m^3/s at 3 psi (20.7 kPa) and at 2440 rpm.

Superficial gas velocities from 0 to 5.50 m/s can be maintained in the riser. A bypass valve is used to control the amount of air into the riser before it enters to the CFB system. At the bottom of the column, a 10-position butterfly valve controls the flow of air to the riser. The solids are fed into the vertical column from a rectangular 1.73-m high plexiglass return box, which is used as a solids reservoir. An L-valve feeding system is used to replenish the solids into the riser. The flow of solids into the riser is controlled with pressurized air injected into the opposite side of the box. The two butterfly valves at the bottom of the return box need partial opening when large solids flow rates are required.

Secondary air is injected into the riser from two identical lines located symmetrically at a horizontal plane. The details of the SA injection will be explained later in this chapter. The secondary air supplied by diverting the fluidization air with two slide valves from the main line. Both secondary and primary airflow rates are instantly monitored and controlled using pitot tubes

The solids leaving the riser are collected by a cyclone and a bag filter. The cyclone is 0.32 m in diameter and 1.33 m high. A flexible hose and a metal adapter is used to achieve a smooth transition between the circular riser exit and rectangular cyclone inlet. The bag filter assembly was housed in a box with a cross section of 0.5m X 0.5 m and 1 m high. The hopper at the bottom of the bag filter was connected to the return leg and maintained partly open during all runs. Such a configuration would allow the bed material including the very fines, assuring a constant solids inventory during all runs. The solids collected by the capturing devices are returned to the solids reservoir via 0.152 m ID plexiglass return leg.

Two different particle groups are used in the experiments. A medium fine sand, Nova Scotia type 00 silica sand, mean diameter 300 μm, density 2600 kg/m^3 (bulk density 1500 kg/m3) is used to achieve better similarity with the hydrodynamics of commercial CFB boilers. Some experiments are repeated using FCC catalyst particles, mean diameter 60 μm, and density 1600 kg/m^3 to simulate FCC processes. External solids circulation rate is measured by

manually closing a flapper valve located in the return leg and timing the returning solids to fill a known volume. The mass flow rate is determined at the beginning and at the end of each run in order to assure that the mass flow measurements do not effect the steadiness of the riser flow. Kan (1991), reported that although the technique was very simple, it gave reproducible results within 10% accuracy.

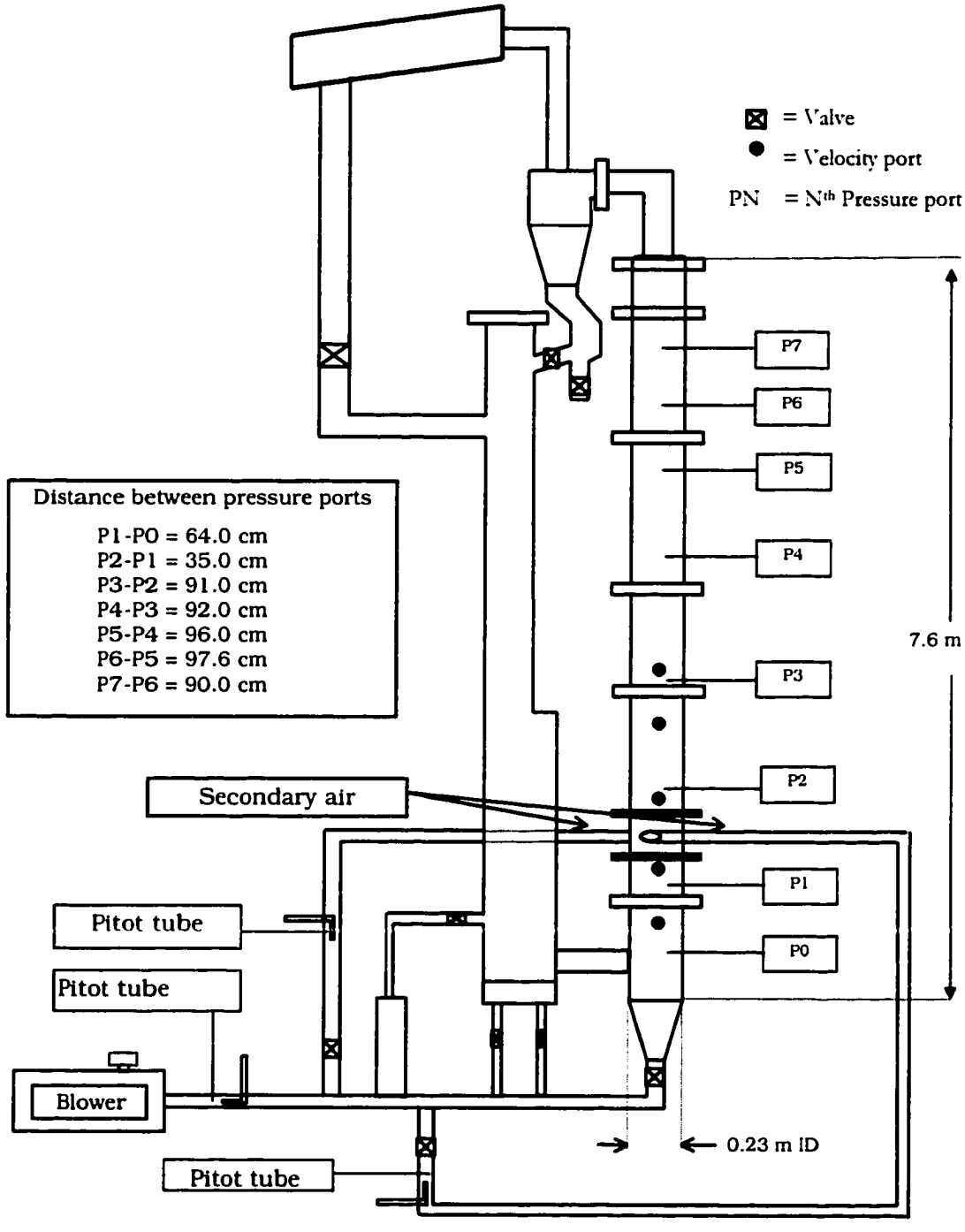

Figure 2.1. Experimental setup

Table 2.1. Relative positions of velocity probe with varying height of SA injection port. Numbers in parenthesis shows the height of the probe relative to the distributor plate.

		Axial Location of Velocity Measurement Plane			
		V_Level 1 (cm)	V_Level 2 (cm	V_Level 3 (cm	V_Level 4 (cm)
Axial Position of SA port	1st level h_1=70 cm	52 (- 18)	102 (+ 38)	126 (+ 56)	182 (+112)
	2nd level h_2=120 cm	52 (- 68)	93 (-17)	126 (+ 6)	182 (+62)
	3rd level h_3=214cm	52 (-162)	93 (-121)	111 (-103)	167 (-47)

2.3.1 Swirl Generator Design and Operation:

Figure 2.2 shows the secondary air injection port, which is composed of a body and two identical injector heads. The body is made of steel, 0.14 m high and 0.23-m ID with steel flanges identical to that of the riser column. The port is designed to permit independent control of the secondary air parameters. The secondary air can be injected to the riser from two identical but symmetrically located openings over the periphery. These opening are equipped for easy mounting of secondary air injectors. The injectors are made of 3.97 cm ID, 40 cm long steel tube to ensure fully developed flow before the riser inlet. The mounting mechanism of the injector heads is designed to permit injection only from the horizontal plane. Each secondary air stream are to pass through a PVC tubing, 3.97 cm ID and 50 cm long to ensure fully developed flow during flow measurement process. The steel injector heads are connected to the PVC pipes with flexible hoses of the same diameter.

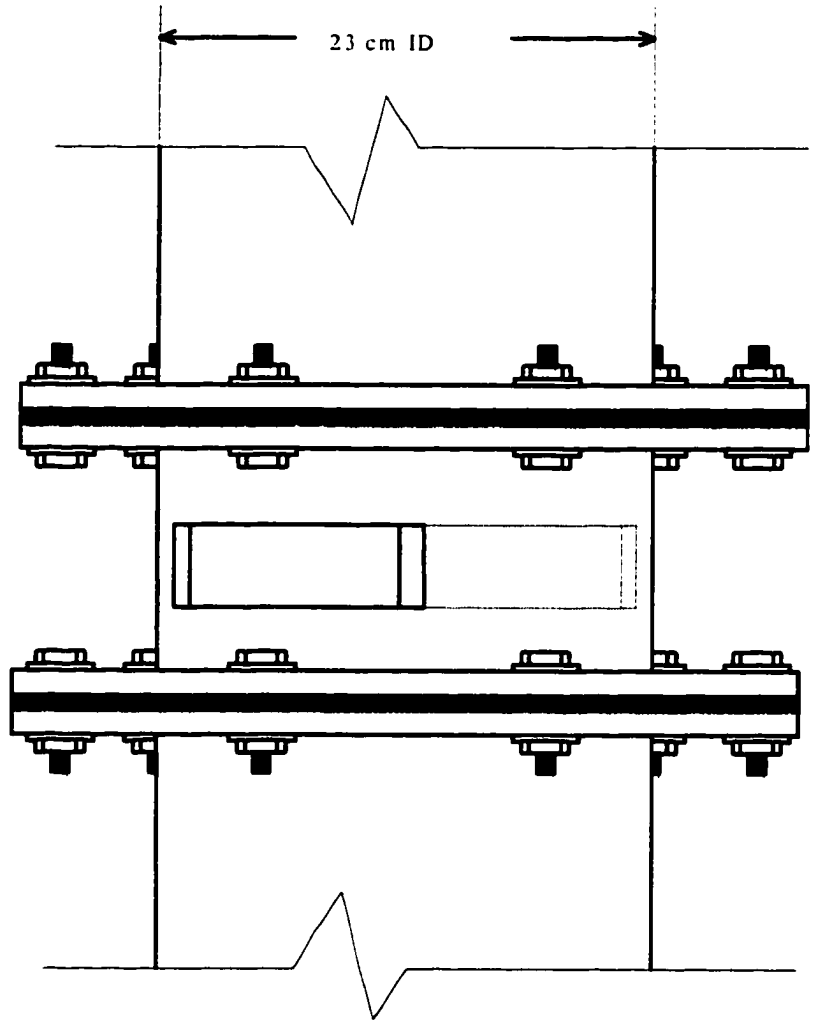

Figure 2.2. A schematics of SA injection port, without SA nozzles mounted.

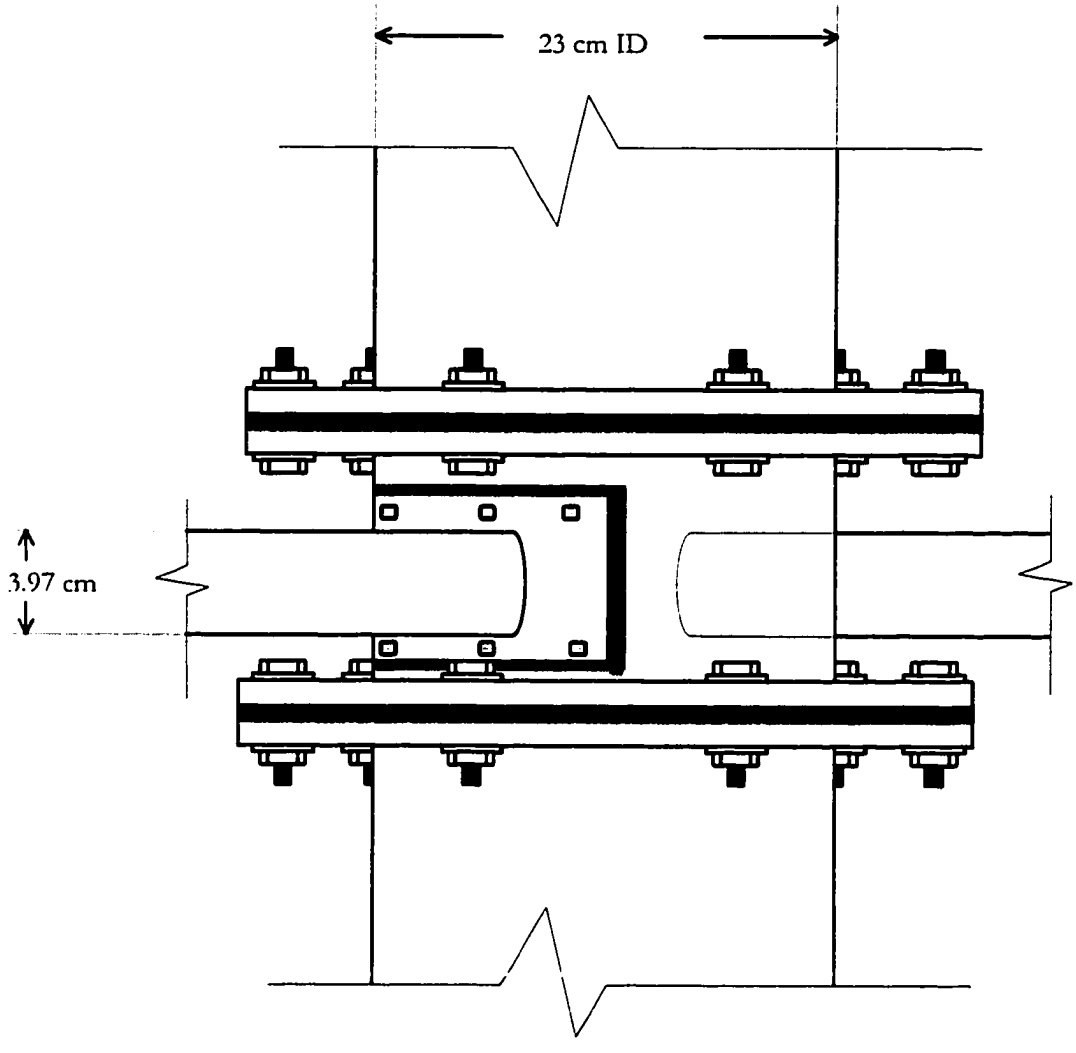

Figure 2.3. Schematics of SA port assembled on the riser with mounted injector nozzles.

2.3.2 The amount of SA injection:

A manually operated slider valve is used in controlling the amount of secondary air. The air velocity in the secondary air pipes is measured with pitot tubes that are connected to the data acquisition system for instant monitoring. Please refer to the appendix for validation procedure of airflow rates. Preliminary tests to calibrate the pitot tube showed that, a mean velocity of 0.9 times the centerline velocity successfully represents the flow within the ranges examined.

$$U_{mean} = 0.9\ U_{center} \qquad 2.1$$

Thus, Equation 2.1 is used for instantly monitoring the air velocity in the system. With the present set-up, it is possible to maintain the amount of secondary air ratio (SA/PA) in a range from 0 to 1.

2.3.3 Swirl Angle

Three different pairs of injection heads are produced in order to study the effects of injection angle. Figure 2.4 shows the schematics of these injectors. All the three pairs have the same mounting surfaces, but different approach angles. One of the pairs is oriented to inject a pure radial air, and a second pair is to inject the SA stream tangentially. The third one, referred as 45 degree injector, align the secondary air jets to be tangent to an imaginary circle which is concentric with the riser but having a radius half of the risers.

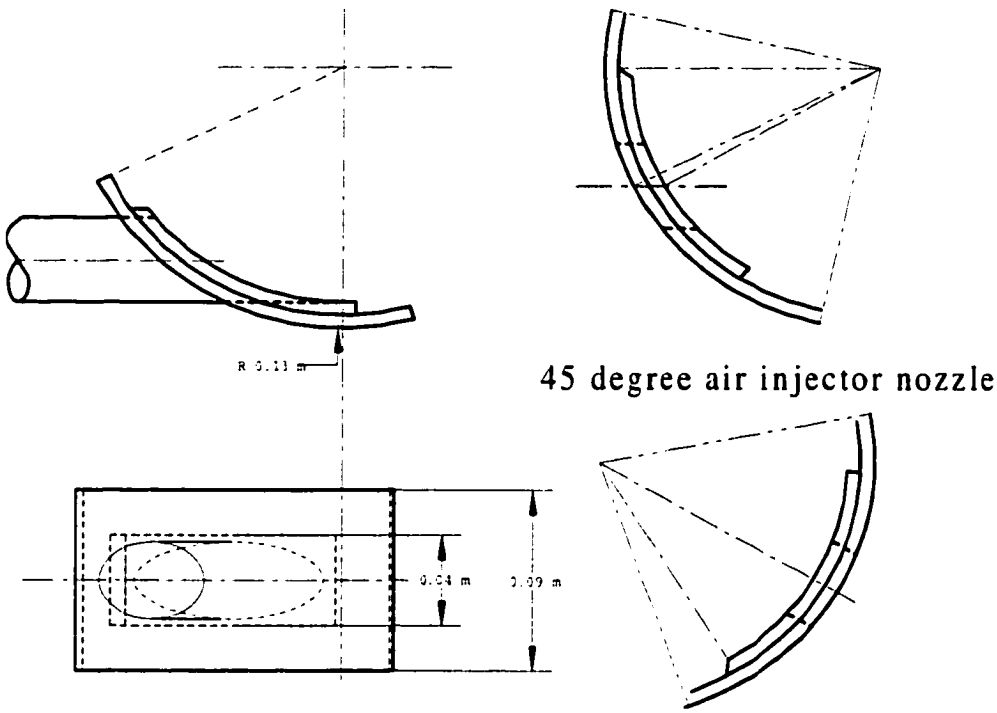

Figure 2.4. Schematics of SA injection nozzles; radial, tangential and 45 degree orientations.

2.3.4 Height of Injection:

The SA port is designed to be as compact as possible and it would take less than an hour for two people to change its elevation. The pre-selected injection heights for this study are 0.7 m, 1.2 m and 2.14 m above the distributor plate. By moving the port to the desired height and re-assembling, one can easily change the axial location of SA injection port.

2.4 Instrumentation

2.4.1 Velocity Measurements

In order to determine the hydrodynamic behavior of circulating fluidized beds it is essential to know radial and axial distributions of its main flow parameters, namely velocity, pressure and voidage profiles.

The local particle velocity data can provide valuable information for gas-solid and solid-solid mixing in the riser column. Recently, Nieuwland et al. (1996), summarized various techniques used in measurement of particle velocities. Among them the laser Doppler velocimetry (LDV), fiber optical probes and particle tracing techniques are found to be the most widely used techniques in the previous works. Hamdullahpur and MacKay (1986) and Tsuji et al. (1984) used LDV to measure the particle velocity field in bubbling and circulating fluidized beds. Although this technique is non-intrusive and provides an accurate way of measuring particle velocity field, it is limited to relatively lean flows. Direct methods such as rapid photography (Rhodes et al., 1988) and stroboscopic multicolor photography (Zheng et al., 1992) are also used in particle velocity measurements. Particle tracer methods have also been used successfully, but it requires complex injection mechanisms, which is believed to effect the nature of the flow (Nieuwland et al., 1996).

Recent works in optical fiber probe methods show that although it is an intrusive technique, it can successfully be used for particle velocity measurements and direct measurements of particle concentrations, (Aguillion et al., 1996; Militzer et al., 1992; Nieuwland et al., 1996). Particle velocity measurements in this work are performed by using an optical probe whose operating principles and parameters are given in the next section.

2.4.1.1 Optical Probe (Vector VSI-2000)

The particle velocity measurement system (Vector VSI- 2000) is composed of a probe head, optical fibers, Vector box, and a PC equipped with necessary hardware and software for data acquisition purposes.

The probe head was comprised a hallow cylinder, made of stainless steel, 8 mm OD, 30-cm long. The two 1-mm OD bundles made up of approximately 300 very thin optical fibers are inserted inside probe head. Each fiber bundle is approximately two meters long and at the extremity each is split randomly into two bundles of about 150 fibers. One of the split bundles is connected to a light emitting diode (LED) in the vector enclosure and the other to a photocell. The other 1-mm bundle is similarly connected to another pair of LED/photocell.

The working principle of the system is as follows: once the probe is inserted into a flow of particles, a portion of the light emitted by the LED is reflected back by the particles in the close vicinity of probe tip. The fiber transmits the reflected light to a photocell, which converts its intensity into a voltage scale. The intensity of the light reflected by the solids passing in front of the fibers depends on the particle's composition, on its shape, on its size distribution and on its concentration. However the intensity of the voltage versus time curve is essentially a function of the velocity and concentration of the particles. This value was amplified to a value between 0 and 10 V in the vector enclosure. Since the two pairs of receiving/emitting fibers are at a known distance apart (4 mm and 2.6 mm probes were tested in this study), the signals that sent to the photocells have a characteristic time delay directly related to the flow velocity.

The voltage signals are then digitized by an A/D data acquisition board and transferred to a file for processing. 256 to 4096 samples can be taken from each channel with a frequency between 1 to 50000 Hz per channel. For a 1024 point sampling this gives a sampling time between approximately 1000 to 20 ms. An online software was available to calculate the correlation between the two samples. Position of the maximum correlation on the correlation versus time-

shifts curve gives the characteristic time delay as well as whether the signal from channel 1 leads or lags the signal from channel two. The velocity of the solids particles is calculated from the time delay and the distance between the fibers.

2.4.1.2 Signal Processing

The cross correlation between two signals give a degree of similarity between a time signal x(t) and a displaced version of the time signal y(t).The cross correlation function is calculated with the following equation.

$$C_{xy}(t) = \int_{-\infty}^{\infty} x(t)\, y(t + r)\, dt \qquad 2.2$$

Where C_{xy} is the correlation of two continuous functions for a time lag r. Since the sampling is done discretely, the following procedure is followed for the cross correlation of the two sets of signal from two channels of the optical probe.

Considering N data values for each signal, x_n and y_n ,with n=1,2,3,....,N sampled at equally spaced time intervals Δt., the auto correlation for x_n, for example, is given by the following relation (Vector- User Guide):

$$C_{xx} = \frac{1}{N-r} \sum_{n=1}^{N-r} x_n x_{n+r} \qquad r = -m,..0,1,2,..m \qquad 2.3$$

Where r is called the lag number and m is the maximum lag number (m<N). The cross correlation of the samples x_n and y_n is given by:

$$C_{xy} = \frac{1}{N-r} \sum_{n=1}^{N-r} x_n y_{n+r} \qquad r = -m,...,0,1,2,...,m \qquad 2.4$$

$$C_{yx} = \frac{1}{N-r} \sum_{n=1}^{N-r} y_n x_{n+r} \qquad r = -m,...,0,1,2,...,m \qquad 2.5$$

The cross-correlation function is normalized as:

$$\Gamma_{xy} = \frac{C_{xy}}{\sqrt{C_{xx}}\sqrt{C_{yy}}} \qquad 2.6$$

The above normalized correlation equation (Eq. 2.6) is solved for all the lag numbers (r) in search of the time lag, which gives the maximum correlation. Then, once the maximum correlation and the corresponding time lag are determined, with the assumption of this time lag being the time difference between the signals from the two channels obtained by the disturbance of the same particle or particle group, the particle velocity can be found by dividing the distance between the fiber optic beams by the time lag. Here, calculation of normalized correlation equation requires very high CPU times for discrete sampling functions, but the problem is solved by zero padding at the end of each series of sampling. By this way, the discrete series could be converted into periodic functions and correlation coefficients for periodic functions can be evaluated very efficiently using Fast Fourier Transform technique (Vector User Guide).

An adequate knowledge on the flow phenomena, on signal processing procedure, on hardware set up and acquisition parameters is necessary in order for efficient and precise usage of the probe. Once the beam distance is selected, one must set the followings acquisition parameters prior to the experiment.

Clock Frequency or *the Sampling Frequency*: The frequency used for sampling. User can select a sampling rate within the choices of a range 5.859 kHz to 50 kHz. It is a function of the flow speed and the beam distance of the selected probe. To determine recommended frequency for a pre-selected accuracy the clock frequency can be expressed in terms of the acceptable error (E_{max}), the beam distance and the velocity to be measured.

$$f = \frac{V_p}{d}\left(\frac{V_p}{E_{max}} - 1\right) \qquad 2.7$$

Where, f is the sampling frequency and d is the beam distance. Derivation of the above formula is given in the User Manual for Vector Hardware Set-Up.

Number of Series: This is the amount of velocity data to gather per measurement. In other words, number of series defines the number of times the specified sampling should be performed. Higher number of series is required to

acquire enough data for statistical analysis depending on the irregularity of the flow.

Number of Samples: Represents the amount of data points, or in other words, the size of the data vector (n- in the above correlation formulation) per series of measurement. This value could be chosen as either of 512, 1024, 2048, or 4096. Longer samples carry more information but take longer to process. Longer samples are advised for irregular flows in order to gain better representative average. Shorter samples can best describe the instantaneous velocities.

2.5 Preliminary Experiments and Validation of Velocity Measurement System

The validation of output from the velocity measurement system was necessary in order to verify that the system output represents the considered flow within an acceptable tolerance. The first stage involved probe calibration, optimization of acquisition parameters and then setting an acceptance criteria for the probe readings. The optimized acquisition parameters are selected by performing preliminary tests. The following section explains the calibration and data processing processes.

2.5.1 Probe Calibration

Measurement parameters for the Vector velocity measurement system are composed of a physical parameter, which is the fiber distance, and the acquisition parameters, which are explained above. All of these parameters are user defined, and must be selected prior to the experiments. The distance between the fibers however is fixed for each individual probe but the value supplied by the manufacturer is recommended to be validated by testing against a known velocity.

Saberi (1996) recently studied the effect of fiber spacing on the performance of Vector acquisition systems. He tested 3 different probes, fiber spacing being 3, 5, and 13 mm, with a similar instrument - sand watch (hour glass) set-up, and found that all the probes measured similar velocities, but shorter fiber spacing probes gave higher correlation coefficients then 13 mm probe. Same trend was reported for all the sampling frequency values except the lowest one. For lowest sampling frequency applicable, 13-mm fiber spaced probe measured slightly higher velocities than that of others, suggesting that increased distance between the two fibers decreases the probability of a particle's path, aligning with that of the probe. Very close fiber spacing on the other hand, may require very high sampling frequency, which, in turn, may mislead the researcher about the direction of the flow. Therefore, especially for an irregular flow, the combination of small fiber spacing and high sampling frequency seems a better solution. In the experiments an available Vector system with 4-mm fiber spacing is used.

The best method to test the reliability and the error margin of the measurements is to compare the output with a known input. Therefore, the available system needed to be tested against a range of known velocities. Using two different methods to calibrate and test the Vector system completed this task. First, a calibration test was performed in order to find the exact optical distance between the fibers as advised by the manufacturer. The probe had 4-mm spacing between the centers of the two fiber optical bundles. The experiment to validate the fiber spacing is designed to create a known velocity to be measured with the probe. A black disc (24-cm diameter), subjected to a constant angular velocity of 300 rpm is covered with a thin slice of light reflecting (white) material along the diameter. Then the tangential velocities at pre-defined points of 5, 8 and 11 cm along the disc radius are measured. Since the angular velocity of the disc is fixed the tangential component of the velocity at a distance x from the center must read as:

$$V = \omega\, 2\, \pi\, x/60 \quad (m/s) \tag{2.8}$$

The results, as shown in Table 2.2, represents the velocity at the specified points on the disc very well. The consistency being around 3 %. Therefore, the fiber spacing is accepted as 4-mm throughout the experiments. Similar tests are performed with different combinations of the acquisition parameters and, the results are found as insensitive to the acquisition parameters for the regular input.

Table 2.2. Results from the preliminary experiments to validate the fiber spacing.

Radial Distance, (cm)	Velocity (from equation Eq (2.8), m/s)	Velocity readings (experimental, m/s)	Difference (%)
5 cm	1.57	1.62	3
8 cm	2.51	2.58	3
11 cm	3.43	3.53	2.9

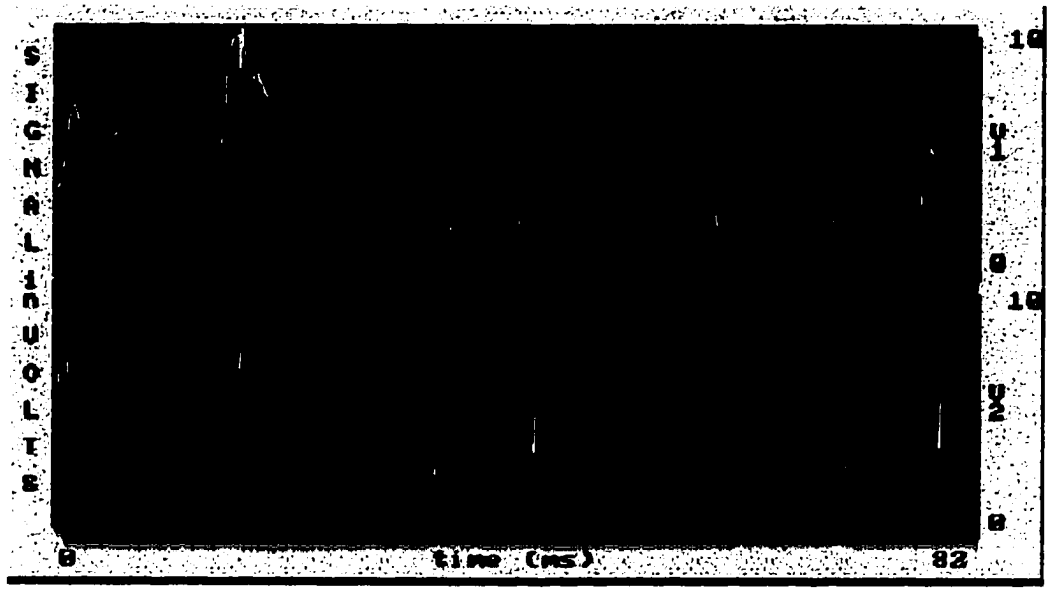

Figure 2.5. Sample signal output from Vector optical velocity measurement system.

Velocity values are calculated by using the time lag between the two signals obtained from each fiber bundle of the probe. The similarity between the two signals is reflected on a scale, which is called the correlation scale. The correlation coefficient for each pair of signals can be seen from the upper right corner of the screen (Figure 2.6).

The second test is designed to see the effect of acquisition parameters on the instrument output to determine the optimum parameters for a sand flow. A plexiglass cylinder container, having an orifice at the bottom, filled with silica sand (300-μm) is operated, and the velocity measurements are performed at different downstream locations. Ignoring the air resistance, the velocity at a distance (h) downstream of the opening must read $\sqrt{2gh}$ according to the rules of physics. The measurements are repeated for different combinations of acquisition parameters to see the effect of each parameter on the efficiency of the system.

Table 2.3 and 2.4 summarize effects of the acquisition parameters *number of samples per series* and the *acquisition frequency* on the probe readings for known velocity inputs. The probe output seems insensitive to *number of samples per series* while reduction in the *acquisition frequency* increased the error considerably for the ranges considered in the case of a regular sand-watch flow. Table 2.5, on the other hand, show that the Vector optical velocity measurement system with the selected acquisition parameters is capable of capturing the sand velocity within a consistency margin of 0-5 % within the ranges considered.

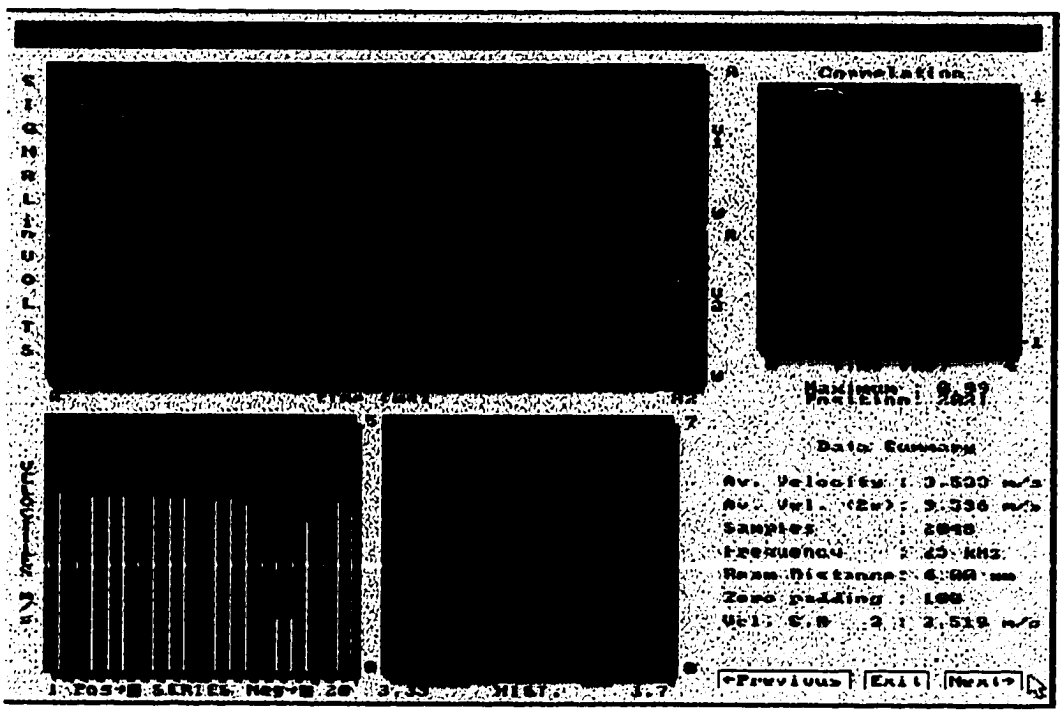

Figure 2.6. A full screen from the Vector optical velocity measurement software.

Figure 2.6 shows the time series of a pair of signals, the correlation graph between the selected signals, and information about statistical analysis of the data acquired from a single experiment. The screen captured shows the tangential velocity of the disc, measured at 11-cm radial location.

Table 2.3. Effect of the measurement parameter "#of samples per series" on the probe output against a known input.

Distance mm	Sampling Frequency	# Samples per series	Measured velocity (m/s)	Standard deviation	Calculated velocity (m/s)	Difference %
100	25 kHz	2048	1.382	0.059	1.400	1.2
		1024	1.388	0.095		0.9
		512	1.385	0.115		1.1

Table 2.4. Effect of sampling frequency on the probe output against a known input.

Distance mm	# Samples per series	Sampling Frequency	Measured velocity (m/s)	Standard deviation	Calculated velocity (m/s)	Difference %
80	2048	25 kHz	1.208	0.062	1.250	3.3
		12.5 kHz	1.190	0.097		4.8
		6.25 kHz	1.185	0.155		5.2

Table 2.5. Probe validation against known velocities

Sampling Frequency	# Samples per series	Distance (mm)	Measured velocity (m/s)	Standard deviation	Calculated velocity (m/s)	Error %
25 kHz	2048	80	1.208	0.062	1.250	3.3
		100	1.382	0.059	1.400	1.2
		240	2.109	0.046	2.169	2.7

Optimization tests for sampling parameters were also performed by measuring the irregular flow in the cold type circulating fluidized bed. This time, since the actual value of the particle velocity is unknown, tests are based on searching the combination of parameters that result in higher correlation coefficients. The best combination for the probe with 4-mm beam distance is seen as:

Sampling frequency = 25 kHz,

Number of Series = 100 series per run

Number of samples = 2048 samples per series

The experiments are performed by using the above sampling parameters as defaults.

2.5.2 Data Processing

The results from the preliminary test runs concerning the nature of the riser flow are in agreement with literature and it showed that the gas-solid flow pattern in CFB risers is highly irregular. This highly turbulent particle flow pattern might be considered as the main reason behind the homogenous temperature distribution in CFB combustion. One can easily observe through a

transparent riser that in the wall region, particles form clusters which move up or down for a short period, then disperse into the riser. The path of particles in the flow is not streamlined like it is in a regular sand-watch flow, and the probability of a particle cluster velocity vector having a comparable second and/or third dimension component is very high. Therefore, meaningful data gathering from a fiber optical probe, which is adequate for one-dimensional uniform flows, requires further analysis or post processing of acquired data.

In order to extract meaningful series of data, 3 distinct criteria are considered in the first stage of data processing. The first criterion involves setting a high lower limit to the correlation coefficients. Reliable data from such a flow should have a correlation coefficient of at least 0.70, which is also used by some other investigators. Second criteria based on the existence of both positive and negative (up and down) particle velocities inside the riser whose average values could show different patterns. Therefore, these data must be processed separately in order not to average out the useful trend. The third criterion is based on the necessity of a human check. Early experiments have shown that there may remain some irrelevant data even after application of the first two criteria. Therefore, the data set must be carefully examined before drawing any results.

A spreadsheet program is written to apply the first two criteria to the raw data. First, the measurements with a correlation coefficient of 0.70 and lower are filtered out. Then the remaining data are sorted to separate negative and positive velocities. These groups then, subjected to further statistical analysis. After the visual checking and calculations of standard deviation, data that stand outside an acceptable standard deviation are subjected to further filtering. The remaining data set, then, is accepted as *meaningful* and used in further analysis.

Particle axial velocity measurements are performed at 4 sections along the riser axis to see the flow development, and at 8 points along the radius per section in order to see the radial distribution of particle velocity. These experiments are

repeated for various operating parameters such as SAR, height of SA injection, and mode of SA injection, under varying solids circulation rates and for two different particle groups. Attempts are also made to measure the tangential component of particle velocity vector for swirling secondary air injection case. The probe was rotated for 5 different angles along a horizontal axis (for vertical, 80°, 60°, 30° and horizontal alignments of the two fiber channels) in order to see the amount of particles passing from such an alignment. Results are presented in the next chapters, and the method is seen as useful since it gave a good representation of development of swirl flow along the riser radius.

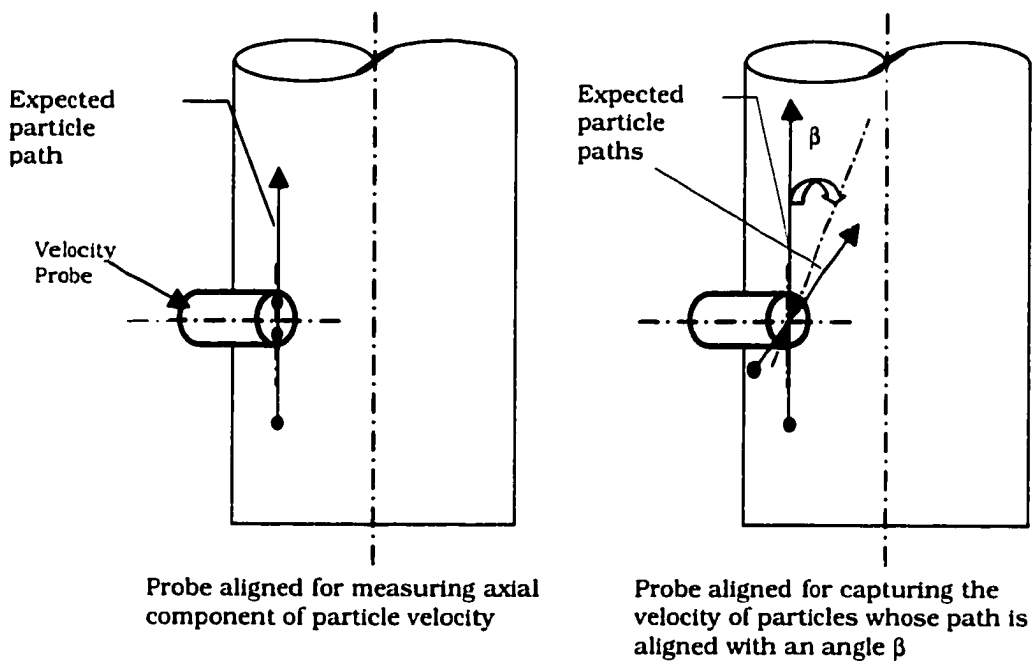

Figure 2.7. Orientation of velocity probe for vertical and helical flows. The favored solids flow angle in swirling SA injection case is scanned by rotating the probe for various β angles.

2.6 Differential Pressure Measurements

Li and Kwauk (1980) after measuring axial solids concentration in a CFB with pressure profile data mentioned the existence of a dense bottom region and lean upper region, which can be depicted by an S-shaped concentration curve. Others (Hartge et al., 1988; Sinitzlein and Weinstein, 1988) have since observed this profile. In recent years, however, other profiles have also been observed (Arena et al., 1988; Hartge et al., 1988; Bai et al., 1992; Brereton and Grace, 1994; Harris et al., 1994). Bottom dens region may not always be present and a denser region may exist at the top for constricted exist. Operating variables such as solids circulation rate, total solids inventory, particle characteristics, solids inlet configuration, riser exit structure, secondary air injection and the level of solids re-introduction into the riser effect the axial voidage profile (Lim et al. 1995).

Based on the assumption that pressure losses due to particle-wall friction and particle acceleration are negligible, differential pressure measurements have often been used to estimate suspension densities. Lim et al. (1995) mentioned that the effect of acceleration on pressure drop might not be negligible for risers with a very dense phase region at the bottom. Therefore, the acceleration effects must be considered in solids holdup predictions upon observation of a very dense bottom bed.

When the above assumption is applied, the difference in the pressure readings between two consecutive pressure taps results from the weight of the material suspended in the region considered. Since the density of air is very small compared to that of the solid particles, the weight of the gas phase may also be ignored. Therefore the pressure drop can be modeled as equal to the weight of the solids.

$$\Delta P = m_s / A_r \qquad (2.9)$$

$$m_s = \rho \ \varepsilon_s \ A_r \ \Delta L. \qquad (2.10)$$

Therefore substituting equation 2.10 in equation 2.9 one can obtain the relation between the pressure drop and solids holdup (ε_s) as:

$$\varepsilon_s = \Delta P/(\rho * \Delta L) \qquad (2.11)$$

Figure 2.1 shows the location of 8 pairs of static pressure taps distributed along the riser wall. These pressure taps are connected to a computer controlled servo valve-switching network via equal length plastic tubes. A Labveiw computer program generates digital signals through a National Instruments AT-MIO-64E-3 board. These signals are used to control 32 pneumatic servo valves. This arrangement allows for automatic sampling of static pressures along the wall of the riser, along the radius of the riser, and also for the sampling of the velocity heads from the pitot tubes.

Both differential and gauge pressure readings are widely used in the previous works to study the pressure profiles and its fluctuations. Schnitzlein and Weinstein (1988), for example, studied differential pressure readings between two pressure taps and Satija et al. (1985) used gauge pressure readings for the same purpose. In the present study, differential pressure readings are used for monitoring the static pressure profile and it is fluctuations along the riser.

2.6.1 Signal Processing for Pressure Fluctuation Analysis:

Spectral analysis of pressure fluctuations may give valuable information about the quality of fluidization. Fan et al. (1981) defined an index for the quality of fluidization by using the spectral analysis of pressure fluctuation data. Drahos et al. (1988) found that, for their cold type CFB setup, the frequency of fluctuations were around 15 Hz in the absence of solids and it was approximately 1 Hz. with a low solids circulation rate of approximately 2 kg/m^{2}s. Yerushalmi et al. (1979) used the amplitude of pressure fluctuations as an indication of flow regime transition, whereas Mori et al. (1988) used standard deviation of pressure fluctuations to identify the regime of fluidization. They also measured the standard deviation of pressure fluctuations with varying

superficial gas velocity and particle properties to help predicting the choking velocity. Bai et al. (1996) also searched for a relation between the standard deviation of pressure fluctuation the regime of fluidization. They reported that the standard deviation of pressure fluctuations stayed indifferent to the changes in superficial gas velocity and solids circulation rate if the average cross sectional solids holdup is kept constant. This result, in fact, supports his previous findings (Bai et al., 1995) on the dependence of core radius to the cross sectional average voidage only.

Differential pressure fluctuation measurements in circulating fluidized beds can be performed with three different methods of referencing. The pressure signal from a point in the riser can be measured with reference to the constant atmospheric pressure, and subtraction of mean value from the acquired signal gives a continuous signal representing the pressure fluctuations. With this method the resulting fluctuation signal reflects the fluctuations in the pressure at the horizontal plane of measurement. However, before such a referencing one should consider that the difference between the constant atmospheric pressure and the local pressure inside the riser is much higher than the expected amplitude of pressure fluctuations. Since the pressure transducers are chosen by considering the highest-pressure difference expected, for this type of referencing, a wide span transducer would be required. Thus, the fluctuation data acquired from such referenced transducer will likely be outside the range of transducers reliability limits. This type of referencing, therefore, would require a very sophisticated transducer and considered as not feasible for our study.

The second method of referencing considers measurement of the pressure difference between two different axial locations along the riser, which reflects the instantaneous solids holdup profiles within the test volume. Since this type of referencing would require a pressure transducer with a smaller span, reliable fluctuation data can be acquired with a moderate transducer. It may be necessary to point out that, although this type of referencing is used in most of

the previous works, the pressure fluctuations gathered reflects the cumulative of fluctuations within the test volume. Thus, the data will less likely to represent the local turbulence structure in the riser as the height of the test section is increased.

A third type of referencing would be monitoring the pressure fluctuations at a single horizontal plane, by referencing the static pressure at the wall for example with the static pressure at the center of the same cross section. Kan (1991) also used this type of referencing. With this type of referencing, a sensitive and low span transducer may gather valuable information about the instantaneous turbulent structure of the riser flow. In this work, pressure fluctuation measurements with all three types of referencing are performed, but results from first two types of referencing are disregarded since the third type of referencing gave better representative data about the turbulent flow structure in the riser.

Signal Processing:

The pressure signals are received by 3 MKS BARATRON type 223 B capacitance pressure transducers with ranges of 0-1 mmHg, 0-10 mmHg and 0-100 mmHg. The transducers are very precise, having a resolution of 0.01 % and an accuracy of 0.3 %. The signal output from the pressure transducers is received and digitized by the Labview data acquisition board and monitored instantly.

Fast Fourier transforms (FFT) analysis during the preliminary tests showed that the relevant pressure fluctuations are below 10 Hz for the experimental conditions. Data acquisition board is capable of performing the sampling with much higher frequencies (up to 10KHz). The sampling rate is set to 1 kHz and the number of samples to 4096 for all the experiments in order to minimize the effects of sampling rate on the acquisition performance. In addition, the samplings at each point were performed 10 times, waiting 2 seconds between each sampling to assure better representation of the flow. Some of the experiments are repeated randomly later in the following days to check reproducibility and consistency of the measurements.

2.7 Experiment Design

The experiments are designed to reflect particle motion and holdup patterns in the bottom dense bed, within the transition region where SA jets are considered as effective, and in the upper part of the bed until the fully developed flow resumes. Therefore, the development of the flow must be monitored until a riser height where the flow seems to reach a uniform pattern.

Particle velocity measurements are scheduled for 4 different axial locations along the riser, and at 8 radial positions for each axial location. The radial positions of velocity probe are decided after performing preliminary tests. Measurements are performed at 8 positions along the radius whose relative position to the center being (r/R): 0, 0.2, 0.4, 0.6, 0.8, 0.85, 0.9 and 1. Here, 0 and 1 represents center and wall respectively.

The experiments designed for the measurements of axial component of particle velocity represented with '●' in Table 2.6. Attempts for measuring the tangential component of particle velocity are also planned and represented with '◒' in the same table. These experiments are scheduled for capturing the favored direction of particle helical path imposed by the swirling air, and its radial profile. The experiment is performed by rotating the probe to 5 predefined angles with vertical axis for each radial location, the rotation and angle β is illustrated in Figure 2.7.

Axial profile of static pressure and its fluctuations are scanned by using 8 pairs of pressure probes located along the riser wall.

Table 2.6. Experiment design table. ⧈ Symbolizes that 3 different tests for varying angle of SA injection positions are to be performed for the present configuration of SA/PA and height of SA injection. The legend for the above symbols is provided in Table 2.7.

Configuration		Amount of Injection (SA/PA)			Mode of SA injection (Degrees)		
		0	0.25	0.5	0(radial)	45	90(tang.)
SA Port Height (m)	0.7	⧈	⧈	⧈	●◆■	◒●◆■	◒●◆■
	1.2		⧈	⧈	●◆■	◒●◆■	◒●◆■
	2.14		⧈	⧈	●◆■	●◆■	●◆■

Table 2.7. Legend for Table 2.6

Legend	Represents
●	For the present configuration of SA parameters, velocity measurements to capture *radial* and *axial* variations of particle axial velocity are to be performed.
◒	20, 30, 60 and 90 degrees offset from vertical direction to capture the swirling component of particle velocity at each radial position.
◆	Measurements of pressure drop along the riser axis.
■	Measurements of pressure fluctuations.

2.8 Conclusion

A modular secondary air injection port is designed to vary the parameters of SA injection independently, is produced. With the present SA port it is possible to direct the secondary air jets radially, tangentially or with a forty-five degree angle into the riser. The port can be installed at various axial positions along the riser. The volumetric flow ratio of SA jets over the primary air (SAR = SA/PA) can also be varied.

The variables of interest in the gas solid flow field are selected as the axial component of particle velocity, and the pressure drop profile along the riser. A fiber optical probe (Vector) is tested, calibrated, and the optimum acquisition parameters are selected for gas-solid flows in CFB risers. The selected acquisition parameters require a continuous scanning of 8.192 seconds duration for each measurement.

The pressure drop profile along the riser can be scanned by using 8 pairs of static pressure probes distributed along the riser, concentrated in the SA injection region. The acquisition parameters are selected to give at least 4 seconds of continuous measurement at a single section in order to acquire representative average values in the pressure drop profiles.

Preliminary experiments are performed. The results show that both experimental set-up and measurement systems consistently give good representation of the flow field.

Chapter 3

Experimental Results and Discussions

3.1 Introduction

The results obtained from various experiments are presented in this chapter. Two major sets of measurements are conducted; pressure, and particle velocity. The pressure drop between certain sections of the riser is measured to obtain information on the axial profile of solids holdup with varying SA parameters. Local pressure fluctuation measurements are also conducted to obtain the auto-correlation and spectrum functions of pressure fluctuations in the flow field with varying SA injection parameters.

Particle velocity experiments are undertaken to measure the axial component of the particle velocity vector and its variations in the axial and radial directions. Measurements are also performed to capture the variations in tangential component of the particle velocity field in search for a favored particle path for swirling SA injection.

The results from measurements of pressure fluctuations shows that introduction of SA changes the pressure fluctuation pattern throughout the riser by reducing its amplitude. The axial pressure drop measurements, on the other hand, revealed that not only the amount of injection, but also the mode and height of SA injection may have remarkable effects on the axial distribution of solids in the riser.

Measurements of axial component of particle velocity revealed quantitative data on both flow development in the bottom portion of the riser, and on the effects of mode of SA injection to the particle flow patterns. The velocity measurements are repeated for Geldart's A and B class particles, and comparisons of the results showed that the regularity of fluidization, in the sense of steadiness, may change for different particle groups under similar experimental conditions.

The discussions related to the experimental results are provided together with the presentation of the results in the following sections.

3.2 Analysis of Pressure Fluctuations

The fluctuation data presented in this section are gathered measuring the difference between the static wall pressure and the static pressure in the center of the riser at the same elevation. Therefore, it reflects the radial difference in the pressure at a horizontal section of the riser. Figure 3.1 shows a representative sketch of the measurement system. A very sensitive pressure transducer (0-13 mmH_2O range) was used to capture the pressure fluctuations for various elevations along the riser axis. With the present measurement system, online analysis of acquired data is made possible with a program written with the Labview software. The details of the experimental and measurement systems are given in Chapter 2.

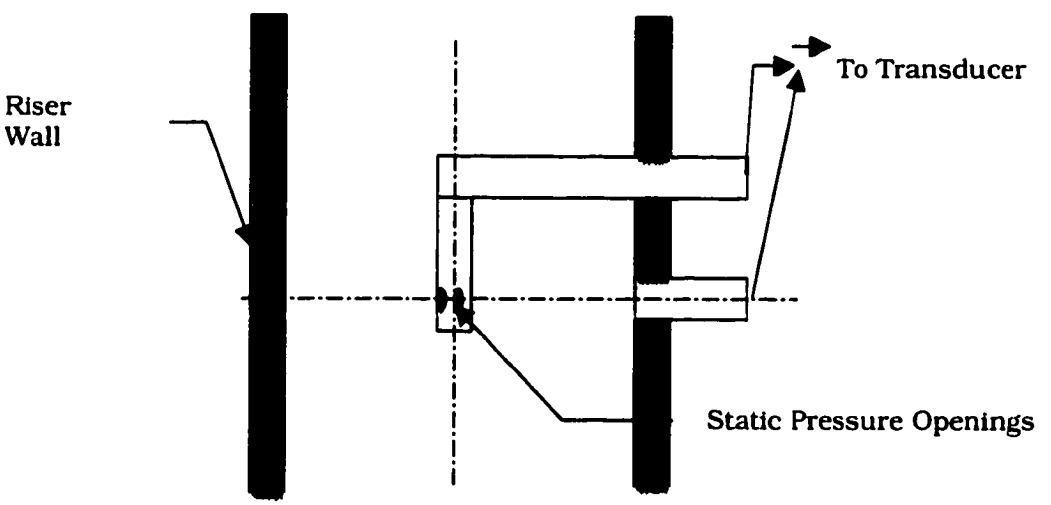

Figure 3.1. Orientation of pressure lines for radial profile of pressure fluctuations

The amplitude of pressure fluctuations can provide useful information on the motion patterns in the riser (Fan et al., 1981). The main source for the fluctuations in pressure at a local point of the riser is generally accepted as resulting from the instantaneous changes in the weight of the particles above the local measurement point. Regarding the above assumption, one may deduce

that higher amplitudes may represent the degree of unsteadiness in the suspension, suggesting local segregation in the flow. Whereas, the flow with lower amplitude pressure fluctuations indicates a comparably steady flow structure.

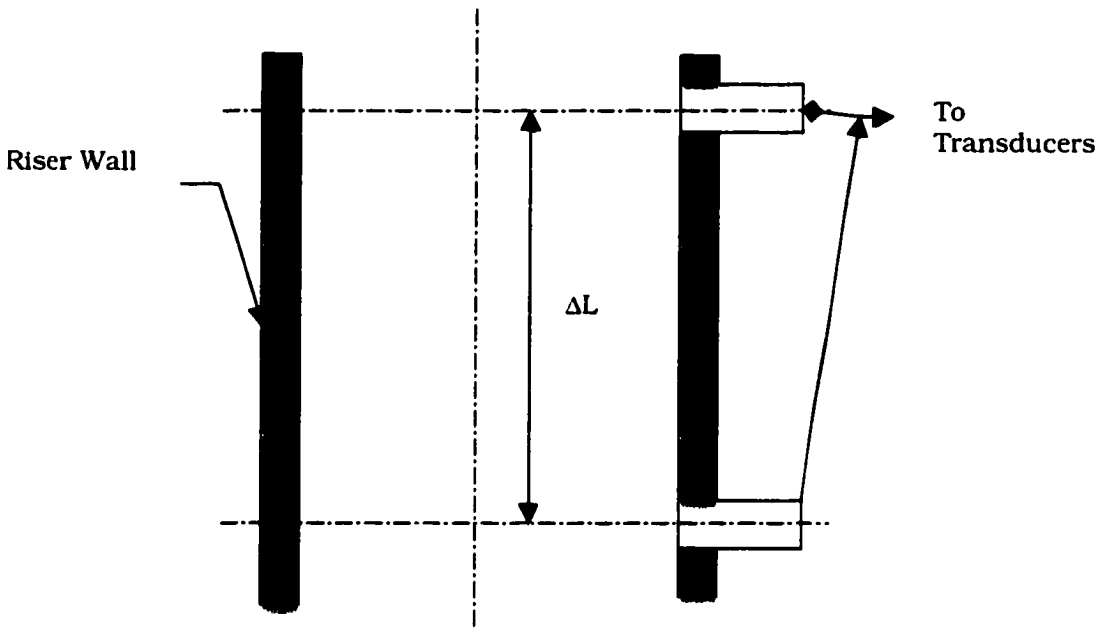

Figure 3.2. Schematic representation for axial referencing for pressure fluctuations.

The pressure drop data, which is gathered between two consecutive pressure taps along the riser height (Figure 3.2), represent the instantaneous amount of solids within the test volume. Therefore the fluctuations in the pressure drop, acquired upon such a referencing designate the instantaneous deviations from the time averaged solids holdup value within the test section. Whereas, the difference in pressure fluctuations at a horizontal cross section reflect the pressure gradient formed due to the instantaneous (cross sectional) location of solid particles above the test section. This type of referencing which is illustrated in Figure 3.1, may provide useful information about the radial distribution of cluster formation whereas consecutive tap type of referencing providing information on the axial unsteadiness of the riser flow. Experiments are performed using both type of referencing, and the results gained by radial

referencing gave better representations to show the effect of secondary air injection on the hydrodynamics of riser flow.

The power spectra data, which is presented in Figure 3.3, reveal that the highest amplitude fluctuations occur at the bottom of the bed if secondary air is employed. The dominant frequency and the amplitude of fluctuations seem similar along the height of the riser in the absence of secondary air as it can be seen from Figure 3.4.

Figure 3.5 very clearly shows the dampening effect of secondary air injection, and its mode on the amplitude of pressure fluctuations. For the same superficial gas velocity and external solids flux, although the dominant component of the frequency of fluctuations seems similar for all cases, the highest amplitude fluctuations are attained when the air is introduced only from the bottom, i.e. when SAR = 0. Contrary to Arena et al. (1993)'s findings, the figure reveals that staging with secondary air decreased the amplitude of fluctuations throughout the riser axis. This behavior may be attributed to the changes in the motion patterns of clusters with the introduction of secondary air[1].

Throughout the course of the experiments, a more disperse upper bed was consistently noticeable with the introduction of secondary air. Below this region, around the walls both below and above the SA injection plane, it was possible to observe dense regions of particle clouds, different from that of flow without SA injection. In this SA effective region, particle clouds were denser and their uniform movement seemed like the clouds were forced towards the wall. These clouds, appearing as axial strands along the wall while SAR=0, covered the whole periphery of SA effective portion of the riser wall with the injection of secondary air. This visual observation may suggest a radial pressure gradient driven flow, since the inner strands of particle down-flow were observed to be pushed towards the wall region, increasing the solids holdup fraction of wall

---

[1] This observation is also in very good agreement with Crowe (1982)s commends on particle-turbulence interactions. The turbulence intensity in a dilute-conveying type flow is smaller than it is in a dense flow due to the lack of particle agglomeration and particle-particle collisions.

region in the SA effective zone. This visually observed pattern was more visible in case of tangential SA injection, which may be due to the centrifugal force imposed on the particles. With tangential SA configuration, the core-annulus interface may be closer to the wall, giving rise to a dispersed and continuous gas-particle flow in the core region. Unfortunately, the solids holdup measurement technique reveals information on the volume averaged value and not on its radial distribution. Therefore it was not possible to support the above argument quantitatively by direct measurements.

It may be interesting to note that the changes in the pressure fluctuation pattern imposed by the injection of secondary air remains effective throughout the riser rather than diminishing just at the extent of secondary air injection zone.

Figures 3.5 and 3.6 show the power spectrum and auto-correlation of pressure fluctuations, respectively just above the SA injection port. The amplitude and the power of pressure fluctuation are smaller in the staged air cases, which indicate a comparably more steady and continuous local profiles of solids holdup are attained with staging. Also, the sinusoidal trend in the auto-correlation function indicates the existence of periodic phenomena (Fan et al., 1981). Thus, the comparably sinusoidal behavior obtained for SAR = 0 in Figure 3.6 reveals a shift in the flow structure, from cluster dominated motion to a dispersed particle flow with the application of secondary air.

The effect of mode of secondary air injection on the amplitude of pressure fluctuations can be seen via the probability distribution function of pressure fluctuations in Figure 3.7. The 90% fluctuating interval of a pressure fluctuation signal is calculated by determining the difference between the amplitude of pressure fluctuations corresponding to 0.95 and 0.05 at the vertical axis (Fan et al. 1981). After drawing two horizontal lines at PDF = 0.05 and PDF = 0.95, one can determine the intersection points with the signal and corresponding values in the amplitude axis. The difference between the two determined amplitudes gives the 90 % fluctuating interval, which shows the amplitude range in which the majority of fluctuations took place. The 90 %

fluctuating interval calculated for Figure 3.7 shows that 31 and 55 per cent reduction in the amplitude of pressure fluctuations are attained with the application of tangential and radial secondary air, respectively.

The effect of mode of SA injection on the auto-correlation of pressure fluctuation pattern is shown in Figure 3.8. Normally, the auto-correlation of pressure fluctuation signals for a fast bed is expected to show the characteristics of a wide band noise, which is not sinusoidal but show a sharp peak at t=0. Whereas in a bubbling bed, they are more likely to show sinusoidal characteristics due to the effective bubble frequency [Thomson, 1993].

In the forty-five degree SA injection case, with a strong secondary air (SAR =0.5), the jets formed an effective barrier over the upcoming gas solid flow. The region below the SA injection plane became very dense and the region above the SA injection port very dilute compared to that of other modes of SA injection. Therefore, the very distinct pattern in the auto-correlation and power spectrum of pressure fluctuation signals from the turbulent bed (0.5 m below SA injection) in Figures 3.8 and 3.9 may represent the cutting off effect of secondary air jets, supporting the observations of Arena et al. (1993). Figure 3.10 shows the fluctuation signals used to produce Figures 3.8 and 3.9. The distinct pattern obtained from forty-five degree SA injection case indicates the periodical nature of the pressure fluctuations in a dense turbulent bed.

The results from pressure fluctuation measurements gave clear indications that the staged air creates distinct zones along the riser axis. It is also made clear that the mode of injection also influence the fluctuation patterns in the riser. The above qualitative findings from pressure fluctuations can be taken in consideration in a future mathematical model to describe the riser flow with secondary air injection.

3.3 Solids Holdup Measurements

The methodology used in the calculation of axial solids holdup profile from pressure drop measurements was explained in chapter 2. Only a brief

description of the experimental procedure is included here, prior to the presentation of the results obtained from these measurements.

The solids holdup profile between the two consecutive pressure taps is calculated from the pressure difference within the test volume. This calculation is based on the common assumption that the pressure difference is caused only from the weight of the particles present in the test volume. This assumption ignores the acceleration effects, friction and the weight of the carrier phase.

The data used to calculate the solids holdup profiles are acquired through 8 pressure taps mounted along the riser wall. The taps were located at positions starting from 0.32-m above the distributor plate, and the top one was located 1.5-m below the riser exit. The relative positions of the pressure taps are given in Table 2.5, and it is provided in Table 3.1 for convenience.

It may be useful to note that the relative positions of some of the pressure taps with respect to the adjacent taps, change with the axial location of the modular secondary air injection port. The pressure drop experiments are performed for pure radial, forty-five degree and tangential orientation of secondary air jets for varying secondary air ratio (SAR) and height of injection for both silica sand and FCC particles.

A large number of authors including Li et al. (1988), Kunii and Levenspiel (1990), Kan et al. (1989), and Puggsley et al. (1996) investigated solids holdup profile along the riser for CFB's where only primary air is used. In the above works, the axial profile of solids holdup is reported as showing a denser region in the lower section of the riser, becoming leaner along the axial direction and eventually assuming a constant value at a certain height. Further up along the riser, an increase in the pressure drop profile around the exit region is also reported, pointing a slightly increased suspension density due to the exit configuration. Similar results for the axial pressure drop profile, in the absence of secondary air, are obtained in the present study. The pressure measurement in the exit region is not performed in our experiments, since the focus of the present study concentrates on the SA injection region.

3.3.1 Pure Radial SA Injection

In the case of pure radial secondary air injection, effects of the SA parameters on the bed hydrodynamics may be quite significant, especially in the close proximity of the injection section. An immediate response of the bed to the secondary air injection can be seen as an increased solids holdup in the region below the secondary air injection, which is referred in this work as the primary region. The suspension density in the upper region either remains the same or slightly decreases depending on the secondary air ratio as can be seen from Figure 3.11. There may be two reasons for the increase in the suspension density in the primary region. First, the amount of air introduced from the bottom of the riser or the primary superficial gas velocity decreases with the injection of secondary air since the total air is kept constant. Therefore, solids carrying capacity in the primary region decreases, and consequently, the amount of solids in the primary region increases. Second, as the SA jets emerge from the injection ports, a high kinetic energy zone is created in the plane at which level the interaction with the primary air occurs. At this point, the gas-gas mixing is not fully complete, and thus, the radial component of the SA jets can cause hydrodynamic blockage, reducing the net cross sectional area for the up-flowing suspension. This effect appears to be similar to that effect of SA observed and referred as "cut off effects of secondary air" by Arena et al. (1993).

A representative sketch of the riser cross section at the plane of radial SA injection can be seen in Figure 3.12. In this figure L represents a radial jet penetration length, which may be considered to be a function of a number of flow parameters including the SAR. As the SAR increases, the lateral jet becomes stronger and stretches towards the riser center, reducing the cross sectional flow area while increasing the hydrodynamic blockage for the upcoming flow. Under these circumstances, a local increase in the axial velocity of suspension is also expected due to the continuity. The estimation of the jet penetration length is explained in the section describing the mathematical modeling.

Increasing the secondary air ratio further increases the suspension density in the primary region for different modes of injection and for different particle groups, consistently supporting the arguments presented above. Figures 3.13 and 3.14 show the solids holdup profiles for tangential and forty-five degree injection cases, respectively, for various secondary air ratios and, Figure 3.15 shows the same profile for FCC particles. From the figures it can be seen that, total solids holdup in the riser increase with the application of secondary air, and the additional amount of solids are mostly absorbed by the primary region.

3.3.2 Effect of the Particle Group

Similar responses in the pressure drop profile are observed when the bed material is switched from sand to FCC particles. A comparison of pressure drop profiles obtained for silica sand and FCC particles for SAR=0 (Figures 3.13, 14, 15 and 16) shows that, a smaller axial gradient in the suspension density exists when FCC particles are fluidized. Due to their low Stokes number (S_{t_fcc} = 0.247, S_{t_sand}=4.71), FCC particles have a shorter response time thus, they behave faster in assuming the fluid flow. The difference in gradients may be considered as the result of the difference in terminal velocities of particles. The drag force required to keep the up-flow for FCC particles, for example, is much smaller than that of sand particles due to their smaller diameter and lower density.

Considering the radial gradient in the gas velocity profile due to the no slip condition, it is plausible to deduce that the amount of solids holdup in the upper portions of the riser would be higher for fluidized FCC particles than that of sand, under similar operating conditions. Unfortunately, from the pressure drop experiments, a quantitative representation of the above behavior is not possible due to considerable differences between the operating parameters such as superficial gas velocity and external solids circulation rates required in testing different particle groups. However, the above argument can be supported with the higher external solids circulation rates attained with FCC particles

than with sand particles for the same superficial gas velocity. (Uo= 5 m/s, G_{s_FCC} = 33 Kg/m²s, G_{s_sand} =10 Kg/m²s, Figures 3.14 and 3.20).

3.3.3 Tangential and forty-five degree Injections

The effect of SAR on the axial solids holdup profile is presented in Figures 3.13 and 3.14 for tangential and forty-five degree SA injections, respectively. The solids holdup profile either remained the same or slightly decreased in the region above the SA injection plane, while the amount of solids in the primary region increased considerably.

Both Figures show that as the secondary air ratio increases, the bed density increases considerably, and the axial gradient in the pressure drop profile becomes steeper in the primary region. However, the pressure drop profile in the upper bed assumes a comparably steady value regardless of the amount of secondary air injected. In the forty-five degree injection case however, although a considerably low external solids flux used (G_s = 5 kg/m²s), secondary air injection with SAR = 0.5 resulted in a leaner upper bed which may be attributed to the cutting off effects of SA jets due to the jet inlet configuration.

3.3.4 Mode of Injection

The effect of mode of injection on the axial pressure drop profile is presented in Figures 3.13-17 for both sand and FCC particles.

Tangential injection of SA results in higher-pressure drop values within the region considered when compared to that of radial injection case. This may be due to the helical ascending path of the particles assumed from the swirling fluid motion. Same behavior is clearer when FCC particles are fluidized as can be seen from Figures 3.15 and 3.16.

Figure 3.17 shows the effect of mode of injection on the pressure drop profile when secondary air is injected from the third level (2.14 m above the distributor plate) for a lean phase silica sand flow (G_s=5 kg/m²s). The tangential injection of secondary air created the highest-pressure drop profile whereas the radial injection gave the lowest and forty-five degree injection resulting in an

intermediate profile. In Figure 3.17, the only operational difference between the three different experiments is the mode of SA injection. Therefore, the difference in the axial pressure drop profile may be attributed to the changes in the fluid-fluid mixing patterns induced by the orientation of secondary air jets. It is quite likely that the tangential velocity component must have resulted in a helical particle motion, creating denser suspension within its effective region. This swirl effective region stretches further out as the relative strength of tangential velocity component (i.e. *the swirl intensity*) increases, which is more apparent when FCC particles are fluidized (Figure 3.15). With such a particle path one may also expect increase in both *particle residence time* and the *gas-particle slip velocity*.

3.3.5 The Height of SA injection

The effect of axial location (height above the distributor plate) of SA injection on axial pressure drop profile is presented in Figures 3.18 and 3.19 for various modes of injection and operating parameters. One can easily see that the extent of the dense *primary region* varies with the injection height of secondary air, and the axial gradient in suspension density in the primary region decreases with the elevation of secondary air injection plane.

However, during the third level SA injection experiments, an unusual solid accumulation in the primary bed, a *collapsing bed*, is observed for 45-degree injection of SA while SAR is increased from 0.25 to 0.5. Although a steady circulation of solids (G_s=10 kg/m^{2}s) is achieved for radial and tangential injections, increasing the SAR to 0.5 resulted in very quick solids accumulation in the primary region. In the meantime, the suspension density in the upper bed strikingly reduced while the external solids circulation rate decreased considerably. At this point, the primary region seemed operating under the envelope of a bubbling/turbulent regime, while the region above the SA jets was strikingly dilute, measuring an external solids circulation rate of Gs < 0.1 kg/m^{2}s. Therefore, planned experiments for the above configuration could not be performed since it was not possible to establish the desired circulation rate. This observation may stress the dependence of flow structure on the SA

injection parameters. Here, it is interesting to note that for the injection of SA from the third level, achieving steady flow for the above conditions for both radial and tangential injection cases was very difficult. It required fine tune adjustments in the L-valve aeration, implying again the effectiveness of axial location of secondary air jets on the flow structure. Therefore, one may suggest that the cut-off effects of secondary air may be augmented with increasing height of secondary air injection.

The empirical correlations proposed in the literature (Yang et al., 1983; Basu and Fraser, 1991) to calculate choking velocity consider the superficial gas velocity as the sole variable, while the results presented here suggest considerable role of staging parameters on the onset of choking. It may also be important to note that the effect of staging parameters must be taken into consideration in calculating the choking velocity if the SA is injected from higher elevations.

3.3.6 Solids Loading

The effect of solids circulation rate on the axial pressure drop profile can be seen from Figures 3.14, 3.17 (G_s=5 kg/m^{2}s), and Figures 3.13 and 3.18 (G_s=10 kg/m^{2}s) for sand flow, and Figure 3.15, 16 (G_s = 18 kg/m^{2}s, FCC), and Figures 20 and 21(G_s=33 kg/m^{2}s, FCC).

Comparisons of the related figures reveal that, for the solids circulation ranges considered ($5<G_s<18$ kg/m^{2}s), increasing solids loading increases pressure drop uniformly throughout the riser, suggesting a uniform increase in the solids holdup of the riser. A consistent change in the axial development of the pressure drop is not observed with varying solids loading. Figure 3.21 shows that for the high solids loading (G_s = 33 kg/m^{2}s), although the axial pressure drop profile shows similar pattern to that for smaller solids loading, a slight increase in the slope is noticeable in the fast bed region for higher external solids circulation rates.

3.4 Particle Velocity Measurement

Particle velocity measurements are performed at 8 different locations along the radius and at 4 different locations along the riser height, concentrated around the effective region of secondary air. The measurements are repeated not only for different mode, height and intensity of secondary air, but also for different external solid fluxes and particle groups. Experiments for randomly selected configurations are also repeated to verify the reproducibility of the results.

At each measurement location 100 velocity measurements were taken, and among those only the measurements with high correlation coefficients (CORR > 0.70) are considered as *reliable* and thus subjected to further statistical analysis. These measurements having a correlation coefficient of higher than 0.7 is referred as *meaningful data* throughout this chapter. The data having correlation coefficients lower than 0.7 were discarded. The procedure is described in more detail in Chapter 2.

The results obtained from the particle velocity measurements revealed both qualitative and quantitative information about the nature of the riser flow. A qualitative information on the regularity of the flow is obtained during statistical analysis of the acquired data. The *number of meaningful data* (out of 100 measurements) per measurement and the standard deviation of the meaningful data per location appear to be a very good indication of the regularity of the flow.

In the core region, between the riser centerline and core-annulus interface, usually 50 or more measurements out of 100 would have a correlation coefficient higher than 0.7, which mostly give upward velocities for FCC particles. In the wall region, however, this amount would drop to around 10-20 measurements out of 100, reading both upward and downward velocities. Again, this seems like a good indication of regularity of the core flow, and intermittent behavior in the wall region. This quantitative observation also supports the theories on the existence of core-annular flow structure in the riser. With such a data structure, it would be reasonable to estimate the

location of core-annulus interface, by considering the averaged velocities with negatives indicating the annulus.

3.4.1 Radial Variations of Particle Axial Velocity

Figure 3.22 shows variation axial component of particle velocity in the radial direction for SAR = 0.25, for FCC particles. It can be seen from the figure that, regardless of the mode of injection, the particle velocity is lower in the primary region when the fluidization air is staged. Keeping in mind that the measurement are taken the bottom region of the bed, the difference in the magnitudes is most likely to be the outcome of reduced primary air. This effect is clearer when the ratio of secondary air is increased. Comparing Figure 3.22 and Figure 3.23, one can see that the difference in the magnitude of particle velocities with and without the secondary air injection increases considerably when the intensity of the secondary air jets are increased.

The effect of air staging on the radial location of the core radius can also be seen from Figures 3.22 and 23. The non-dimensional core radius for the first level of measurements remains in the range 0.9 – 0.95 for all runs, but the annulus is thinner for the flow without secondary air injection. This effect is more clear when SAR = 0.5 (Figure 3.23), implying that the suspension density in the primary region increases with increasing secondary air ratio.

The velocity profiles obtained from different modes of injections are similar at the first level, suggesting that the effect of mode of injection does not have considerable influence at this level (68 cm below the SA injection). The effect of secondary air jets on the particle velocity field becomes more visible at locations closer to the SA injection port (level 2: 17 cm below, and level 3: 6 cm above the SA injection plane). Figures 3.24 and 3.25 show that at 17 cm below the secondary air injection maximum average particle velocity is obtained when SAR = 0. Same figures also reveal that at this axial position, radial injection of SA results in a flatter velocity profile with a lower magnitude in the core region. On the other hand, tangential injection of SA imposes higher velocity values in the core region with a smaller core radius.

It is very interesting to note that when SAR is increased to 0.5 (Figure 3.25), despite the lowered primary superficial gas velocity, particles just below the SA port gained considerable acceleration. Especially in the center region, they reached values very close to the velocity of flow without secondary air injection. This can be considered as a good indication of the gas flow pattern around the SA injection region since the FCC particles used in the experiments have smaller Stokes number, therefore assume closer values to that of the fluid motion.

The above behavior can be attributed to the size effects of secondary air jets and may be explained with an *area contraction* theory. Depending on the SAR, the jets occupy some portion of the riser cross section similar to a three dimensional solid body. This obstruction force the upcoming flow to proceed from a *contracted area* which is simply the riser cross sectional area minus the area occupied by the SA jets. The upcoming suspension, therefore, is first subjected to acceleration in the effective region of SA jets due to area contraction. Then, just above the SA injection port, there are the combined effects of further acceleration due to the increased superficial gas velocity, and deceleration due to increased flow area. For the tangential injection case, the area contraction seems analogous to flow in a converging diverging nozzle, whereas in the radial injection case, SA jets, extending over the diameter, may divide the circular cross section into two regions, depending on the intensity of secondary air jets. The area contraction applies to all modes of SA injection, and its amount may be approximated for modeling purposes if the diameter, intensity, and angle of SA jets are known.

Schlichting (1979) studied the problem of fluid motion near a stationary wall when the fluid at a large distance above the bottom wall surface rotates with a constant angular velocity. Referring to U.T. Boedewalt's findings, he noted that for the case when the fluid rotates over the wall, the fluid particles which rotate at a distance from the wall are in equilibrium under the influence of the centrifugal force, which is balanced by a radial pressure gradient. The peripheral velocity of the fluid particles near the disc wall is reduced, thus

decreasing materially the centrifugal force, whereas the radial pressure gradient directed towards the axis remains the same. This set of circumstances causes the particles near the wall (bottom surface) to flow radially inwards and for reasons of continuity that the motion must be compensated by an axial flow upwards. This phenomenon is generally referred to as *secondary flows* and illustrated in Figure 3.26. Considering that the swirling motion superimposed by the tangential secondary air jets decay with the axial distance from the injection plane, it would be quite reasonable to suggest that the increased particle axial velocity in the core region just below the swirling SA injection plane is due to both the *secondary flow* and the area contraction.

The effect of mode of SA injection on the radial profile of axial velocity can be seen from Figures 3.27 and 28 at the third level (6 cm above the SA injection plane). It is very interesting to see that, with the application of staged air, unlike the other test sections in the riser, the mean particle velocity even in the close vicinity of the wall, measured upwards regardless of the mode of injection. This behavior can be accepted as a proof that the presence of secondary air jets not only blocks some portion of the up coming suspension from the primary region, but also blocks the down-coming suspension from the annulus, acting like a second distributor plate. It was visually observed that the majority of the particles descending from the annulus region are captured either by the core flow or by the swirling secondary air jets and changed their direction of motion. The velocity patterns seem similar for all cases for small SAR in the core region, which shows that flow is in developing stage and the measurements are consistent. In the core to jet interface region however, tangentially injected secondary air jets resulted in higher velocities, suggesting gradual mixing of secondary air with the upcoming suspension from the wall region. This behavior however, is slightly different in Figure 3.28, when the secondary air ratio is increased to 0.5. With the effect of reduced primary superficial gas velocity, stronger tangential SA jets keep their momentum longer and stretch out longer through the close vicinity of the wall region in helical paths. This effect results in a higher upward particle velocity in the wall region due to the considerably higher momentum of the SA jets.

Although the particle velocity in the wall region is measured as mostly upwards just above the SA injection plane, fourth level velocity measurements reveal the re-formation of annulus region 62-cm above the SA injection plane. Figures 3.29 and 3.30 show that the annulus region in this section is thinner than it is for non-SA operation. It is visually observed that the clusters in this region are denser for the tangential injection case. The gross particle motion in the wall region is more helical than vertical, but it was not possible to measure a favored direction. Both figures reveal that in the core region the particle acceleration is completed at this level since similar velocity magnitudes and profiles are obtained for various modes and SAR in the core region. In the core annulus interface, radial SA injection resulted in wider core region, while the tangential injection resulted in a flatter velocity profile in the core region. Surprisingly, tangential injection resulted in a thicker annulus region than radial injection for both of the SAR tested, suggesting the effectiveness of swirl induced centrifugal force on the particles.

Figures 3.31 through 3.35 show the development of velocity profiles for different modes of injection and for various SAR for FCC particles. Figure 3.31 shows that the first two levels of velocity test section are within the acceleration region, and starting from the third level on, the particle velocity profile is fully developed for SAR=0. Suggesting that the acceleration of FCC particles is complete within 1.26 m above the distributor plate for a superficial gas velocity of 3 m/s.

Figures 3.34 and 3.35 show the flow development for tangential injection case with SAR 0.25 and 0.5, respectively. Similar trends with that of radial injection case is observed from the second and third level velocity measurement. The velocity profile at the second level measures higher when SAR is 0.25 than it is for SAR=0.5, which seems quite reasonable due to the higher primary superficial gas velocity in the former case. But, considering the values in the core region that reach to its fully developed value for tangential injection, one must suggest the presence of some other mechanism to further accelerate the upcoming suspension just below the SA injection plane. This mechanism may

also be explained with the reduced flow area, and the induced circulation regions with the application of SA jets, i.e. the horizontally introduced strong SA jets, extend tangentially around the inner wall region while loosing intensity and expanding within the distance traveled. The extent of the jets towards the center, i.e. the thickness of the jet, physically occupy some portion of the riser cross section, resulting in local high pressure regions and forming an obstruction over the upcoming flow. This obstruction of SA jets may even cause separation in the upcoming flow just below and above the physical boundary of the tangential SA jets, reducing the area of the core region.

Figure 3.36 through 3.39 are generated from the velocity measurements of FCC particles to show quantitative representations of the effects of SAR on the axial development of particle axial velocity. Figure 3.36 compares the velocity profiles at the first velocity test section (68 cm below SA injection plane). A clear indication of SA injection and SAR is obtained. The velocity magnitudes seem to be a function of the SAR, regardless of the mode of injection, suggestion that the gas jet propagation does not have a considerable influence on the axial velocity profile at this specific axial position. It can clearly be seen from the same figure that although the annulus region becomes thicker with increasing SAR, no influence of mode of injection is seen at this axial position. For the second test section (17 cm below SA port), however, a clear influence of mode of injection is observed (Figure 3.37), tangential SA injection resulting in more parabolic velocity profile with thinner core region.

At the first and second test sections for the radial injection case, the magnitudes of particle velocities are measured to be lower for more intensive SA jets (SAR = 0.5) due to the reduced primary superficial gas velocity. For smaller SAR (SAR = 0.25), the particle velocity in the center region, due to having gained some extra acceleration, reaches to its fully developed value, while the velocity in the region from r/R = 0.6 to 0.8 reads less than that of the fully developed value. On the other hand, such a trend does not exist for SAR = 0.5. This may be attributed to the presence, size and extent of the SA jets. The secondary air streams penetrating towards the center of the riser, loose their effectiveness in

the region from wall to r/R =0.4 for weak secondary air streams, leaving a gap of radius r/R = 0.4 in the center region. The jets seem to occupy the whole diameter for strong SA/weak PA flow (SAR = 0.5), which may cause a separation just below and above the SA jets.

At a plane 6 cm above the SA injection the annulus region seems to diminish for all runs with secondary air injection. At this axial position, particle axial velocity reads lower for SAR =0.5 although the superficial gas velocity for all cases is the same, suggesting that particle acceleration due to increased superficial gas velocity is not complete. Since these figures represent the axial component of particle velocity, one should keep in mind that for the tangential SA injection case, particle velocity vector may have a considerable tangential component. At the fourth velocity test section (Figure 3.39), the flow seem fully developed since velocity magnitudes in the core region read the same for all of the cases considered, the effect of SA injection is still present in the core-annulus interface. The thickness of the annulus is within 5 percent of the radius for all runs, while the experiments with SA injection show thinner annulus regions.. Since the pressure drop measurement showed that tangential injection of SA is resulted in higher suspension density in this region, the annulus region must be denser than that of non-SA operation, which explains the visually observed dense wall region formed with application of secondary air.

The development of core radius along the riser axis is presented in tabular and graphical form (Table 3.2 and Figures 3.40 and 3.41) for various modes and SAR for FCC and sand particles. It can clearly be seen from Figure 3.40 that the staged supply of air had an enormous distortion on the axial development of core radius in SA injection region. Flow with SAR = 0 resulted in the widest core radius underneath the SA injection plane, implying a leaner suspension in the region. Whereas same configuration gave the smallest core radius above the SA injection plane, suggesting that the vertical location of SA injection is the adjoining plane between the distinct secondary air induced dense and lean suspension regions in the CFB riser. Although the radial location of the core radius is similar for all cases further down in the riser (first test section), the

effect of SAR and the mode of injection becomes more apparent in the close vicinity of the SA jets. The deviation of core radius from that of the non-SA operation increases with the SAR, and tangential injection of SA results in the widest annulus region.

The annulus region seems to diminish with injection of SA in the third velocity test section, and re-develops at a higher axial location (test section 4) where thicker annulus is measured for tangential injection case which is attributed to the centrifugal forces exerted on the particles at higher elevations. It is interesting to see that increasing SAR augments the annulus below the SA injection plane while attenuating it above the SA injection plane.

Figure 3.41 shows axial development of the core radius for sand particles. Although the fluidization with sand particles was comparably irregular, similar trends with that of the FCC particles are obtained. Figure 3.42 shows the core radius profiles for various heights of SA injection for sand particles. The core radius seem to be the same at 52 cm above the SA injection plane, whereas the thickness of the annulus region reduces sharply just below the SA injection plane. Note that all of the test sections are below the SA injection port when SA is injected from the third level. A quasi-linear decrease in the core radius profile is seen from the third level SA injection experiments.

The effect of particle group on the core development can be seen by comparing Figures 3.40 and 3.41. Note that the superficial gas velocity of sand flow (5 m/s) was higher than that of the FCC flow (3m/s). A quantitative comparison shows that, despite the low solids circulation rate used in sand flow, the annulus region formed under the SA port is thicker than it is for FCC particles. This is also another indication of irregularity of the fluidization with dense particles. This irregular behavior, on the other hand, may enhance particle-particle and particle-gas mixing in CFB risers.

Figures 3.43 through 3.45 show the particle axial velocity profiles obtained with fluidized sand particles. Figure 3.43 shows the axial development of particle velocity for tangential injection with SAR = 0.5. Although a smooth profile is not obtained due to the irregular fluidization, the figure reveals a good rep

representation of the increased superficial gas velocity. The first two levels of velocity test section are located under the SA injection port, and the superficial gas velocity in this region is 3.37 m/s. Considering that the terminal velocity of the particles is 3 m/s, and the magnitudes of the particle axial velocity in the core region reads close to 2.5 m/s, one has to suggest presence of local non-uniformity in the flow structure since the local gas velocity in this region must be higher than 5.5 m/s. Therefore the particles are not completely dispersed in this region, and cluster motion dominates the flow. Same behavior is also present in the region above the secondary air injection. Although the thickness of the annulus region is greater than that of the FCC particles in the primary region, diminishing annulus region is observed for both of the test sections above the SA injection plane, suggesting that the effectiveness of the SA jets when SAR = 0.5.

Figure 3.44 shows the particle velocity profiles for the same solids loading but for radial injection of SA from the highest injection position (2.14 m above the distributor plate) with SAR =0.25. The velocity profile is more parabolic and the maximum velocity in the first test section reads 3 m/s while the primary superficial gas velocity in this region is 4.04 m/s, suggesting again the presence of clustering behavior even in the core region. The effects of secondary air ratio on the particle velocity profile for sand particles can be seen by comparing Figures 3.44 and 3.45. Intensive SA jets resulted in more scattered velocity profiles. It is interesting to see that for SAR = 0.5, although the thickness of the annulus region reads the same as that of SAR = 0.25, the profile is more parabolic and the particles seem to flow with a velocity very close to its fully developed velocity. This behavior is also attributed to the increased interstitial gas velocity due to cluster motions. More figures involving the velocity profiles of sand particles can be found in the literature (Ersoy et al., 1997)

3.4.2 Measurements of tangential Component of Particle Velocity

The particle velocity field in risers is known to be mostly vertical, with up-flow in the central core region and some down-flow in the annulus in cases of non-swirling SA injection. In the case of tangential injection, a helical particle flow

pattern becomes visible along the walls upon introduction of the secondary air. The helical particle motion, however, appears to decay as the suspension advance along the riser axis. The extent of this swirling region seems to be very much dependent on both suspension density and the relative strength of angular momentum induced by the tangentially injected secondary air jets. Although the flow pattern in the wall region is visible, the effects of swirling air on the radial variation of flow parameters are yet unclear due to the presence of dense particle groups around the walls.

Chang and Dhir (1994) experimentally studied the radial and axial variations in the swirl velocity in a similar geometry for single-phase (air) flow. Their data provide valuable information on the axial and radial decay of swirl velocity for single-phase flows, and thus can be useful in comprehending the decay patterns of swirling component of velocity as the flow develops. However, the preliminary experiments conducted in the present study, showed that the solids loading is an effective parameter in the decay of angular momentum for swirling gas-solid flows. Therefore, the flow field in the presence of particles must also be studied for full comprehension of the riser flow structure when swirling patterns are introduced.

The present experimental system for measuring particle velocity is capable of capturing the instantaneous velocity of particles at a single plane only. i.e., it can only measure the component of particle velocity vector in a plane-aligned perpendicular to the centerlines of optical fibers. Therefore in an attempt to measure the tangential component of particle velocity, the Vector probe is aligned relative to the riser axis with predefined angles, and measurements were performed accordingly at 8 different locations along the radius. The pre selected probe angles with riser axis are 0, 5, 10, 15, 20, 30, 60, and 90 degrees at each radial position. Later, preliminary experiments showed that the results obtained with 0-20 degrees do not differ considerably, therefore the related experiments are performed with only 0, 30, 60 and 90 degree orientations with riser axis.

The results obtained with such configurations are presented in Figures 3.46 through 3.53. Each of these figures shows the variations in the measured

particle velocities at a single radial location, but with different probe angles with riser axis. It can clearly be seen that in the central core region, majority of the measured velocities has the vertical direction (Figures 3.46, 3.47 and 3.48). As the probe moves towards the wall, it can be seen that particles move to each direction evenly, without favoring any of the tested directions, around the core-annulus interface (Figures 3.49-50). In the wall region, however, the particles gained considerable amount of tangential velocity, and that they are under the effect of swirling secondary air (Figures 3.51 to 3.53).

Considering the dense particle clouds around the wall region, and assuming that the gas surrounding the individual particle must follow a similar flow pattern, one may suggest that the majority of the upward gas flow occurs from the central core region in gas-solid flow. This type of flow would create 3 distinct flow patterns over the cross section: a high velocity core flow in the core region, an intermittent core-annulus interface, and a comparably stagnant down flow in the annulus.

The following qualitative results can be drawn from the related figures (Figure 3.46 through 3.53).

A distinct core region with vertically upward solids flow exists.

There is an intermittent core-annulus interface, which is not fixed and moves along the radius as a response to the instantaneous local solids holdup in the region. In this region, it was not possible to observe a steady and dominant particle flow direction. The unsteadiness of the suspension flow widens the core annulus interface and increases the intermittency in the region.

There is a comparably stagnant wall region in which the particles follow helical paths (upwards or downwards). The presence of solids dampened the local swirl intensity considerably, suggesting that the extent of the swirling motion is a function of not only the SAR but also the local solids holdup in the region.

Same types of experiments are carried out under various operating conditions 45-degree SA injection, also. Results obtained are similar, expressing the non-uniformity of the flow in the core-annulus interface and lack of a clear favored

particle velocity pattern. Therefore only one set of experiments are presented here to express the qualitative findings on the radial variations of particle tangential velocity.

Also, in order to quantify the effect of particle loading on the axial decay of swirl intensity, another set of measurements is taken during the course of experiments. Although the visible helical particle motion around the riser walls does not have a steady path, the extent of the swirling motion is noticeable. The particle groups, descending vertically along the riser walls divert their vertical motion and continue to descend in helical paths until the close vicinity of the SA injection plane. Although it is fluctuating, the upper extent of the swirling motion is considered as measurable for different solids loading and SAR. For each tangential SA injection experiment, the maximum and the minimum elevations of the extent of the swirling motion are recorded. Table 3.3 shows the results of this set of measurements. Chang and Dhir (1994) observed experimentally that the radial location of maximum swirl velocity moves towards the center of the tube as the flow proceeds through the tube. Therefore, these measurements, taken from the wall region only, can not be considered as the exact extent of swirling motion. But they can be used in comprehension of effect of particle loading and initial swirl intensity on the axial decay of swirling motion.

3.5 Conclusions

The effects of SA injection on the hydrodynamics of a CFB riser are studied, experimentally. Three different parameters of secondary air injection, namely the mode, the height and the intensity of secondary air jets are considered as the most important parameters of staging air supply to CFB risers, and related experiments are performed to understand the effects of individual parameters on the riser hydrodynamics.

The axial profile of cross sectional average solids holdup in the riser is determined with differential pressure measurements. 8 pairs of static pressure probes are used to obtain information on the radial and axial variations in the

pressure inside the riser. Although the application of secondary air considerably increase the solids holdup profile in the region below the SA injection, its effects in the upper regions is found to be minor. The solids holdup in the primary region increases with increasing secondary air ratio (SA/PA). The solids holdup in the primary region also varies with the mode of secondary air injection. The increase in the solids holdup below the SA jets is found to be joint effect of two different parameters; the reduced superficial gas velocity and the jet emerging patterns. Since the total air is constant, application of SA lowers the superficial gas velocity in the region below the SA injection. The low superficial gas velocity, in turn, requires an increase in the solids holdup since the external solids flux is kept constant. Due to the peculiarity of tangential jet emerging pattern, also due to the centrifugal forces exerted on the particles by the swirling air motion, the tangential injection of secondary air results in the highest solids accumulation in the primary region.

The experiments are repeated for various heights of SA injection and the results show that the extent of the dense region varies with the axial location of SA injection port. An axial gradient in the solids holdup profile is observed, which is more gradual in the primary region if SA is injected from lower axial positions.

The signals from the pressure transducers are subjected to further statistical analysis to obtain the variations in pressure fluctuation patterns, and the results showed that injection of secondary air slightly dampens the amplitude of pressure fluctuations in the riser.

Experiments to measure the axial component of particle velocity and its radial variations are performed in the lower sections of the riser, in order to understand the particle flow patterns in the turbulent bed of a CFB riser. The measurements are repeated for varying SA injection parameters to see the effects of secondary air injection jets on the particle flow patterns in the riser. Experiments are performed at 4 different axial locations, some repeated for two different particle groups, to see the axial development in the particle velocity profiles and its variations.

The magnitude of the particle axial velocity in the primary region reduces considerably, due to the low primary superficial gas velocity attained with staging, suggesting an increase in the overall particle residence time due to the slower particle motion in the primary region. Therefore in CFB combustors, this consequence of secondary air injection may well be utilized to optimize the particle residence time, during the combustion of volatile in fossil fuels.

Results of the particle velocity measurement experiments also revealed that, although a high level of intermittency exists, the particle flow pattern in the riser is core-annular. Part of the particles ascending from the core region may change direction and descend towards the riser base, mostly form the annulus region formed in the vicinity of the riser walls. This behavior is seen as an indication of particle re-circulation in the riser. The amount of particle re-circulation is considered as related with the thickness of the annulus region, which varies with the SA injection parameters. Experiments showed that addition of secondary air increased the thickness of the annulus region below the SA injection plane, while it decreased the annulus thickness above the SA injection plane. Therefore, for design purposes, parameters of the secondary air injection maybe utilized to obtain desired particle re-circulation rates in CFB risers.

Results from the velocity measurements also showed that the mode of secondary air injection is another important factor in determination of annulus thickness, tangential injection of SA jets resulting in thicker annulus regions both below and just above the SA injection plane, suggesting an enhanced gas-solid mixing in the regions considered.

Results obtained from velocity measurements also show the difference in fluidization characteristics peculiar to specific particle groups. Under similar operating conditions, much higher external solids flux with more uniform flow is attained if FCC particles are fluidized. On the other hand, under similar operating conditions, the fluidization of sand particles is comparably irregular, which is conceived through acquired non-uniform local particle velocity, and higher RMS of velocity fluctuations.

The tangential SA jets impose a considerable tangential component to the particle velocity vector in the wall region just above and below the SA injection plane. Above the injection plane, the particles in the wall region assume a helical (upward or downward) motion, which decays with the axial distance. The extent of the helical motion, in which suspension is denser, found to vary with SAR and external solids circulation rate. It is conceived that the radial position of maximum tangential velocity moves towards the center with axial distance, creating a region where the particles flow under the influence of centrifugal forces. In this region, particles with higher inertia are most likely to move towards the wall and descend from the annulus region, while the particles with smaller inertia are most likely be captured by the high velocity core flow and exit the riser. Therefore this peculiarity of swirling secondary air injection may be utilized in optimization of particle residence time distribution in CFB risers.

A special set of particle velocity measurement is performed in search for the radial and tangential velocity components in the particle for tangential SA injection case. Related results showed that the particle velocity path in the core-annulus interface (which is approximately 40 % of the riser radius) is very scattered which may be an indication of enhanced mixing in the region.

Finally, the Vector particle velocity measurement system is found as adequate to capture a good representation of the particle flow field. A consistent agreement between the results of differential pressure measurements and particle axial velocity measurements are obtained, in terms of thicker annulus regions representing denser suspension densities.

Table 3.1. Axial locations of velocity measurement sections relative to the distributor plate. Numbers in parenthesis show the distance to the secondary air port.

		Axial Location of Velocity Measurement Plane			
		V_Level 1 (cm)	V_Level 2 (cm	V_Level 3 (cm	V_Level 4 (cm)
Axial Position of SA port	1st level h_1=70 cm	52 (- 18)	102 (+ 38)	126 (+ 56)	182 (+112)
	2nd level h_2=120 cm	52 (- 68)	93 (-17)	126 (+ 6)	182 (+62)
	3rd level h_3=214cm	52 (-162)	93 (-121)	111 (-103)	167 (-47)

Table 3.2. Axial development of non-dimensional core radius along the riser axis

Probe Level	Distance to SA Port (m)	Non dimensional Core Radius (r_c/R)				
		SAR = 0	Tangential (SAR)		Radial (SAR)	
			0.25	0.5	0.25	0.5
1	-0.68	0.9247	0.9236	0.9163	0.9239	0.9210
2	-0.17	0.946	0.9326	0.9289	0.9421	0.9400
3	0.06	0.9470	1	1	1	1
4	0.62	0.9490	0.9620	0.9730	0.9789	0.993

Table 3.3. The extent of the swirling wall region. Maximum and minimum values show the axial location of adjoining plane between vertical downflow and particle helical motion along the walls of the riser. Figures are relative to the injection plane of SA.

SAR	SAND				FCC	
	Gs = 5 kg/m²s		Gs = 10 kg/m²s		Gs = 18 kg/m²s	
	Max	Min (m)	Max	Min (m)	Max	Min (m)
0.25	1.2	0.5	1	0.5	1.1	0.6
0.5	2.2	1.5	1.7	0.9	1.8	1.4

Table 3-1 The extent of the swirling wall region. Maximum and minimum values show the axial location of adjoining plane between vertical downflow and particle helical motion along the walls of the riser. Figures are relative to the injection plane of SA.

SAR	SAND				FCC	
	Gs = 5 kg/m²s		Gs = 10 kg/m²s		Gs = 18 kg/m²s	
	Max	Min (m)	Max	Min (m)	Max	Min (m)
0.25	1.2	0.5	1	0.5	1.1	0.6
0.5	2.2	1.5	1.7	0.9	1.8	1.4

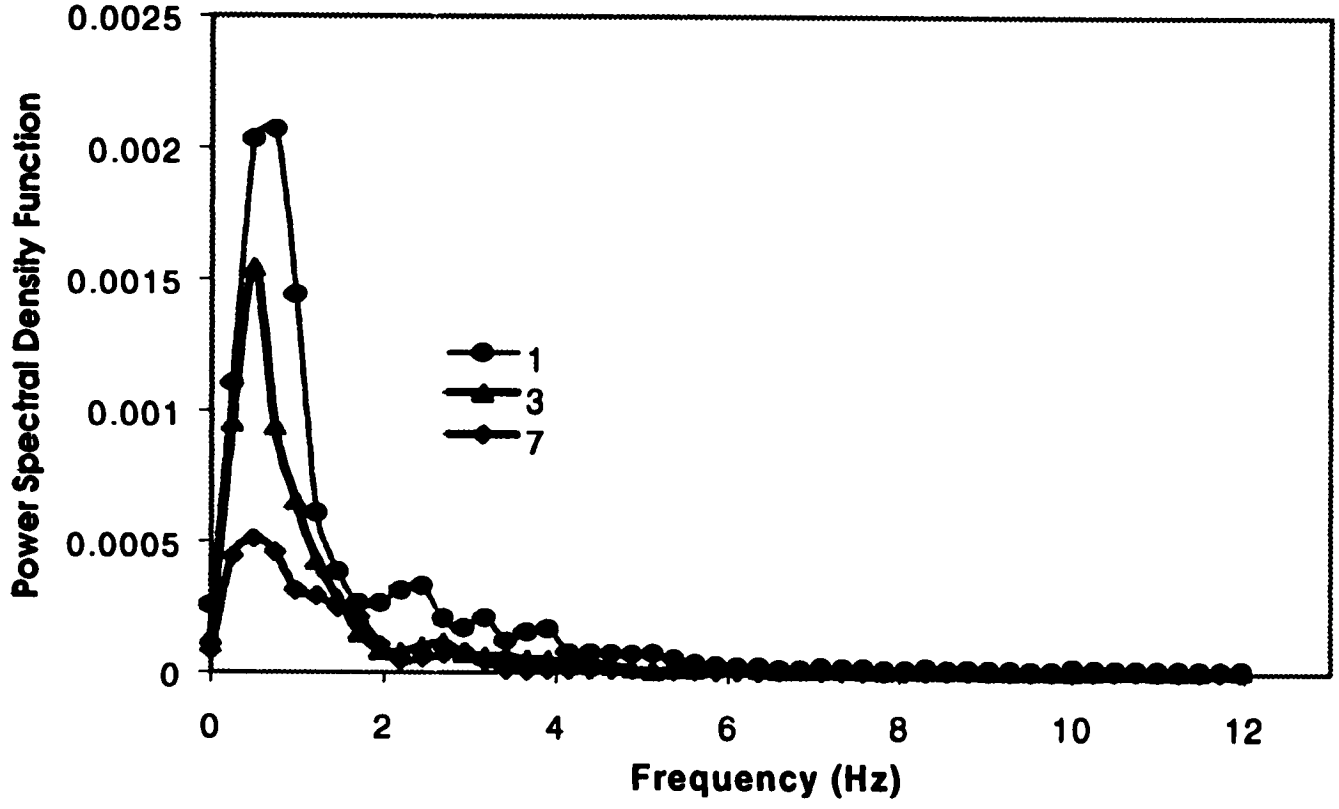

Figure 3.3. Power spectral density of pressure fluctuations. Tangential injection, SAR =0.25, sand particles (d_p = 300μm). Power of pressure fluctuations versus frequency at different elevations along the riser. PL7 represents the top of the riser, PL3 represents just above the SA injection, and PL1 is located at the bottom of the riser.

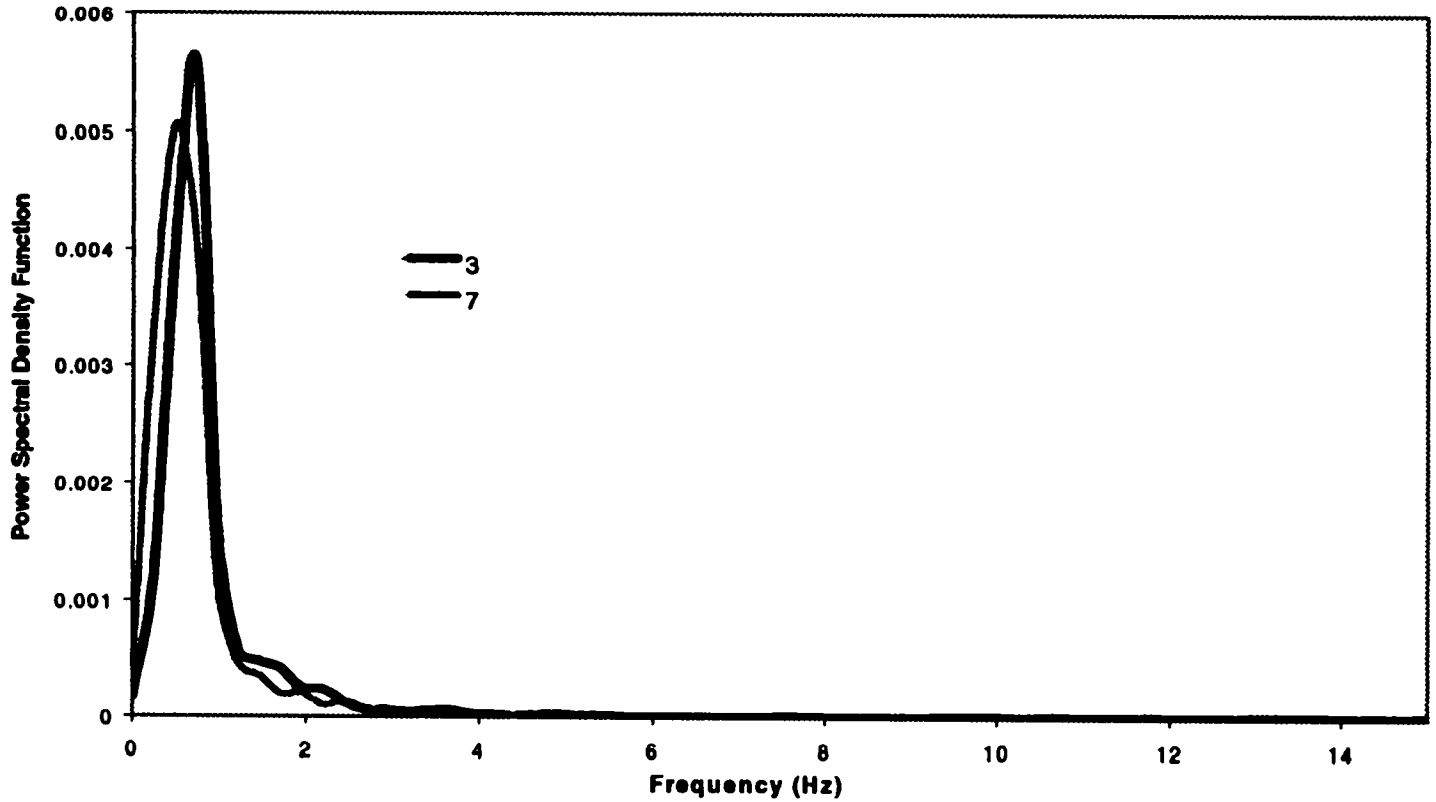

Figure 3.4. Power spectral density of pressure fluctuations versus frequency at different elevations along the riser. Sand particles, SAR = 0. The numbers in the legend correspond to the location of the pressure probe pairs; PL3 shows the location just abobe the SA injection port, and PL7 indicates the top of the riser.

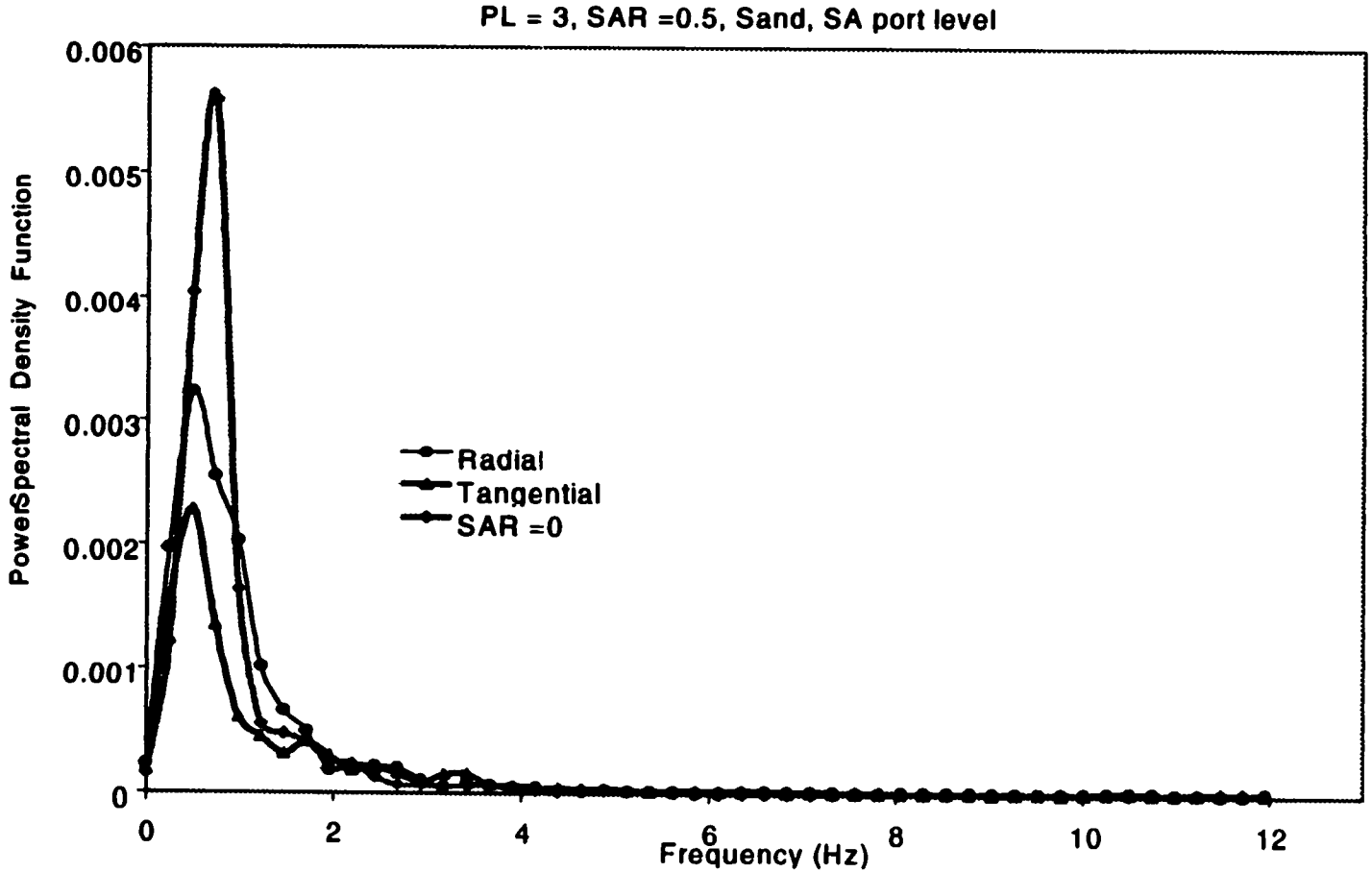

Figure 3.5. Effect of mode of SA injection on the Power Spectrum of pressure fluctuations just above SA injection port for sand particles. SA injection level; 2. Sand particles.

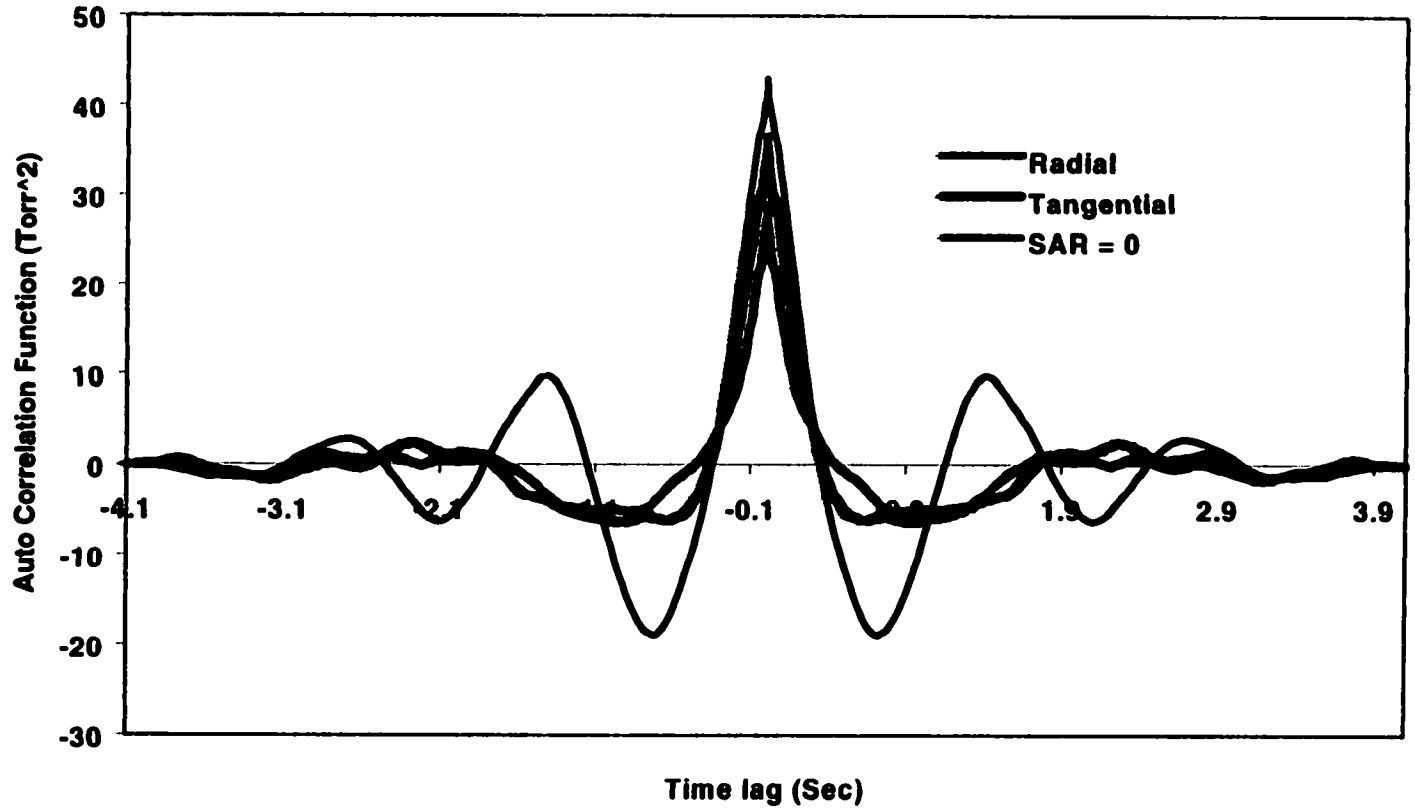

Figure 3.6. Auto-correlation of pressure fluctuation signals just above secondary air injection plane for various modes of SA injection. Sand particles, SAR = 0.5

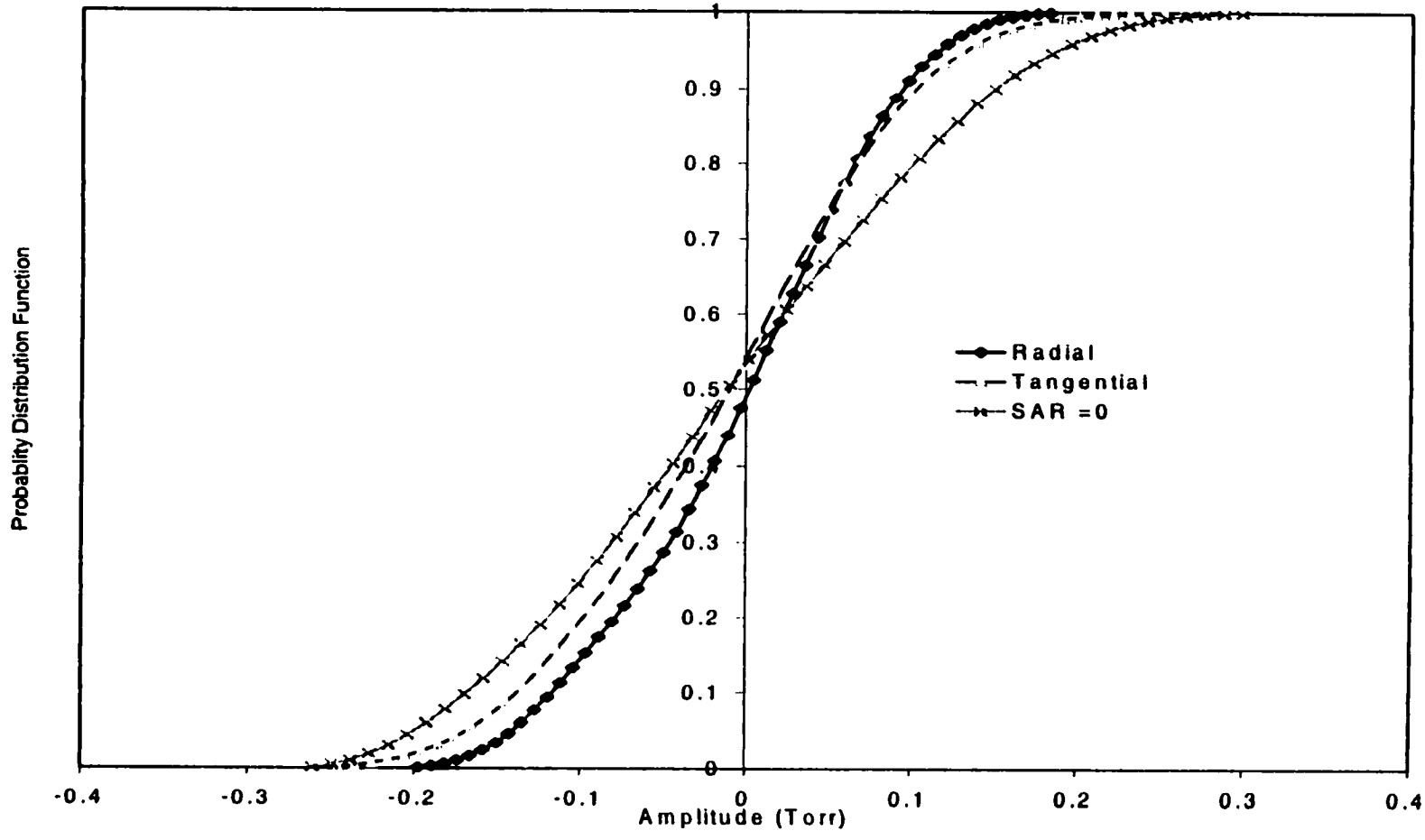

Figure 3.7. Effect of Mode of injection on the Probability distribution function of pressure fluctuations for Silica Sand particles just above the SA injection plane. Radial and Tangential injection with SAR = 0.5, Probe level 3.

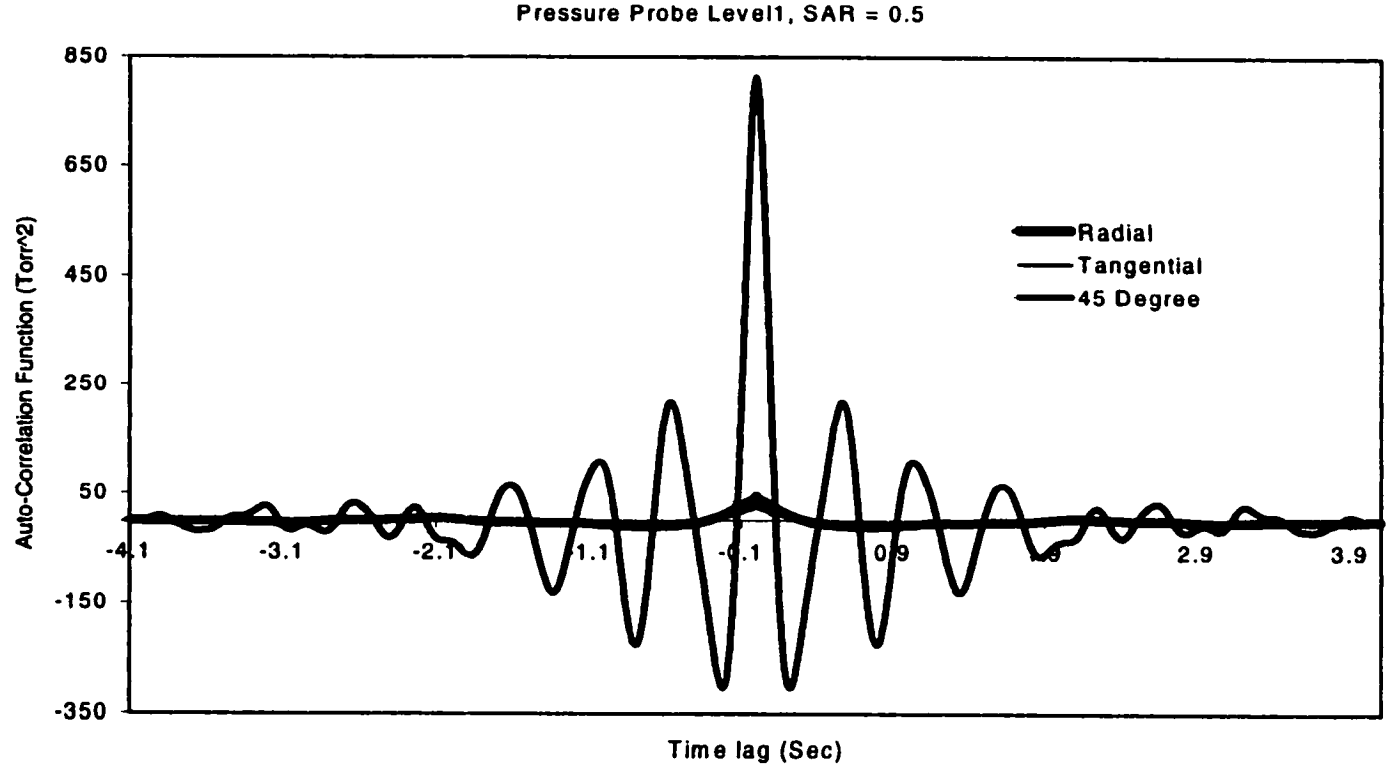

Figure 3.8. Effect of mode of SA injection on the auto-correlation of pressure fluctuations in the primary bed. SAR=0.5 for radial and tangential SA injections from second level. Silica sand particles with Gs = 10 kg/m²s.

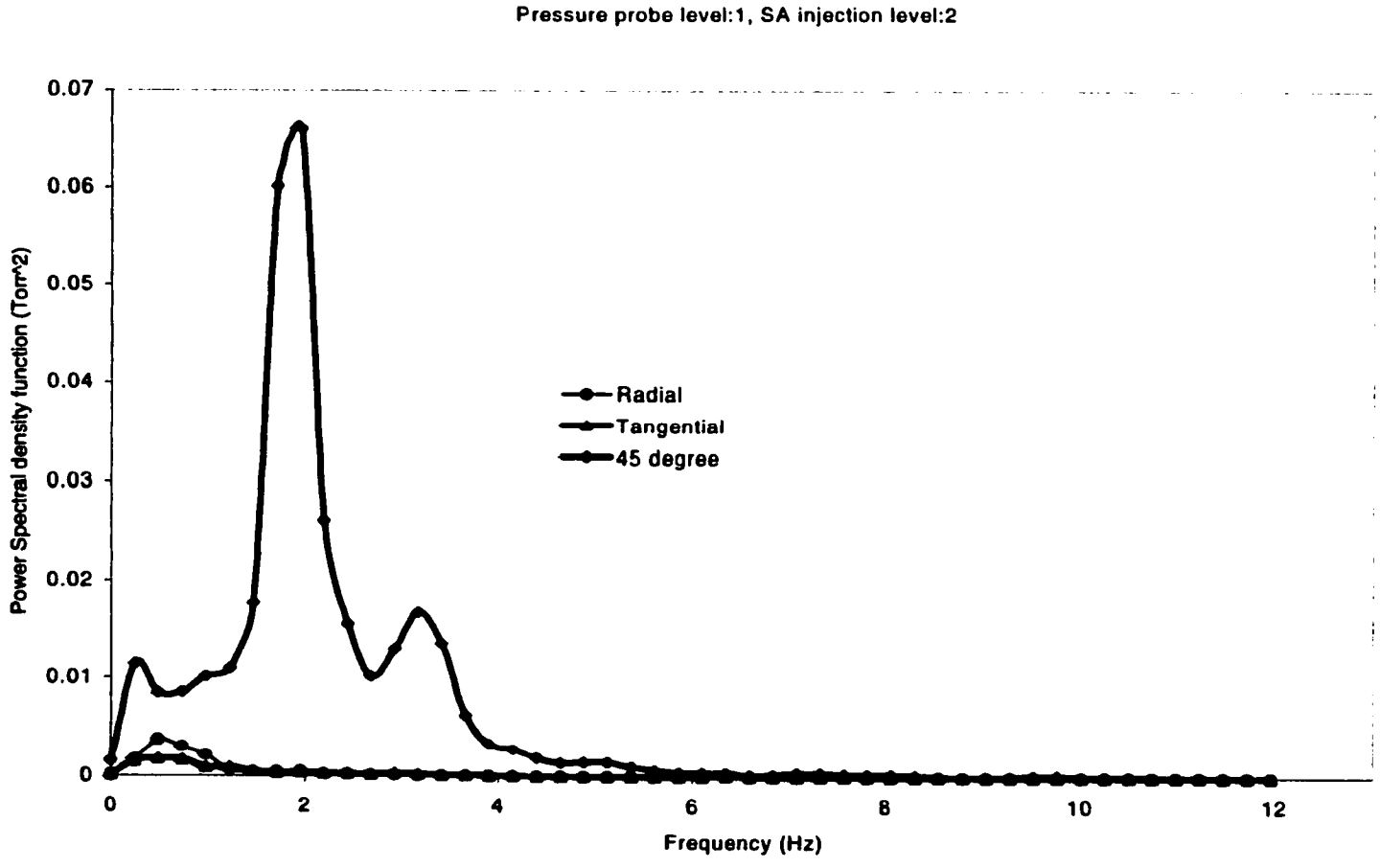

Figure 3.9. Power spectrum of pressure fluctuations in the primary bed for different modes of SA injection. SAR =0.5, Silica sand particles

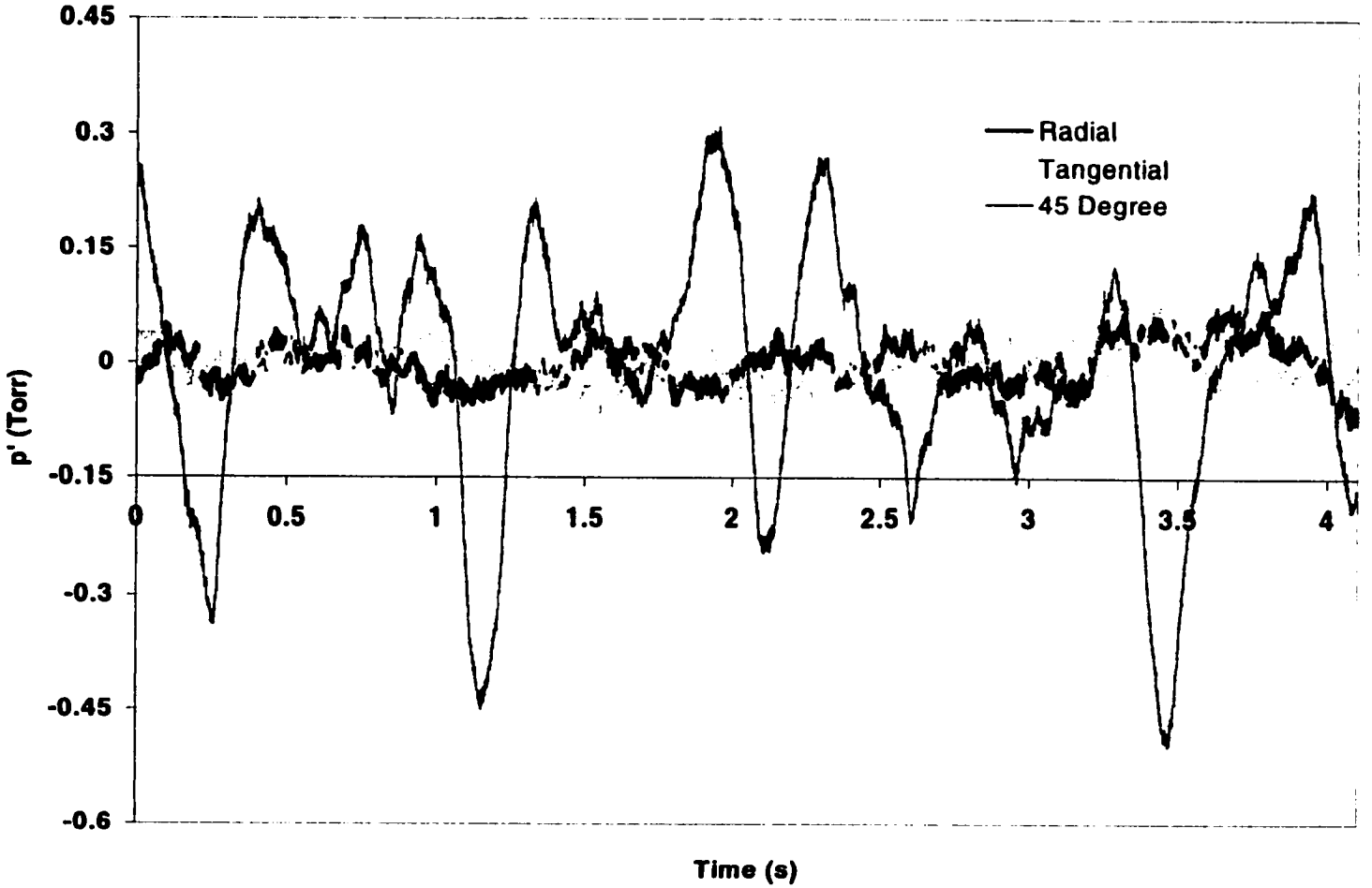

Figure 3.10. Typical pressure fluctuation signals acquired at the bottom of the bed. This specific set of data is used in generating Figures 3.8 and 3.9.

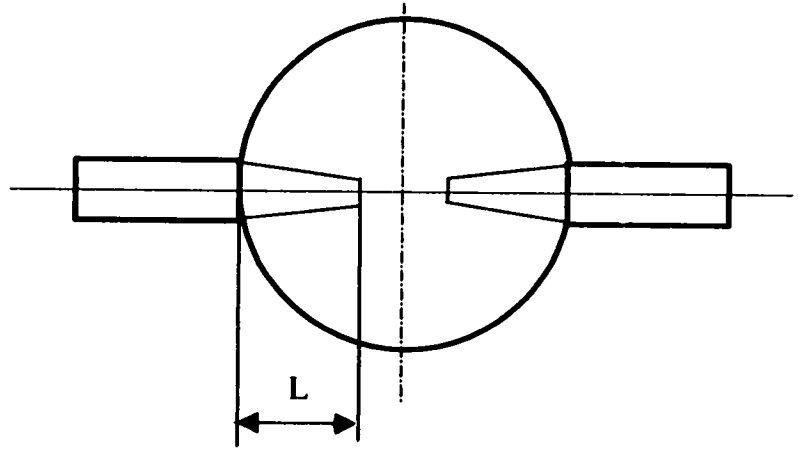

Figure 3.12. Illustrative figure for the penetration of SA jets at the plane of injection.

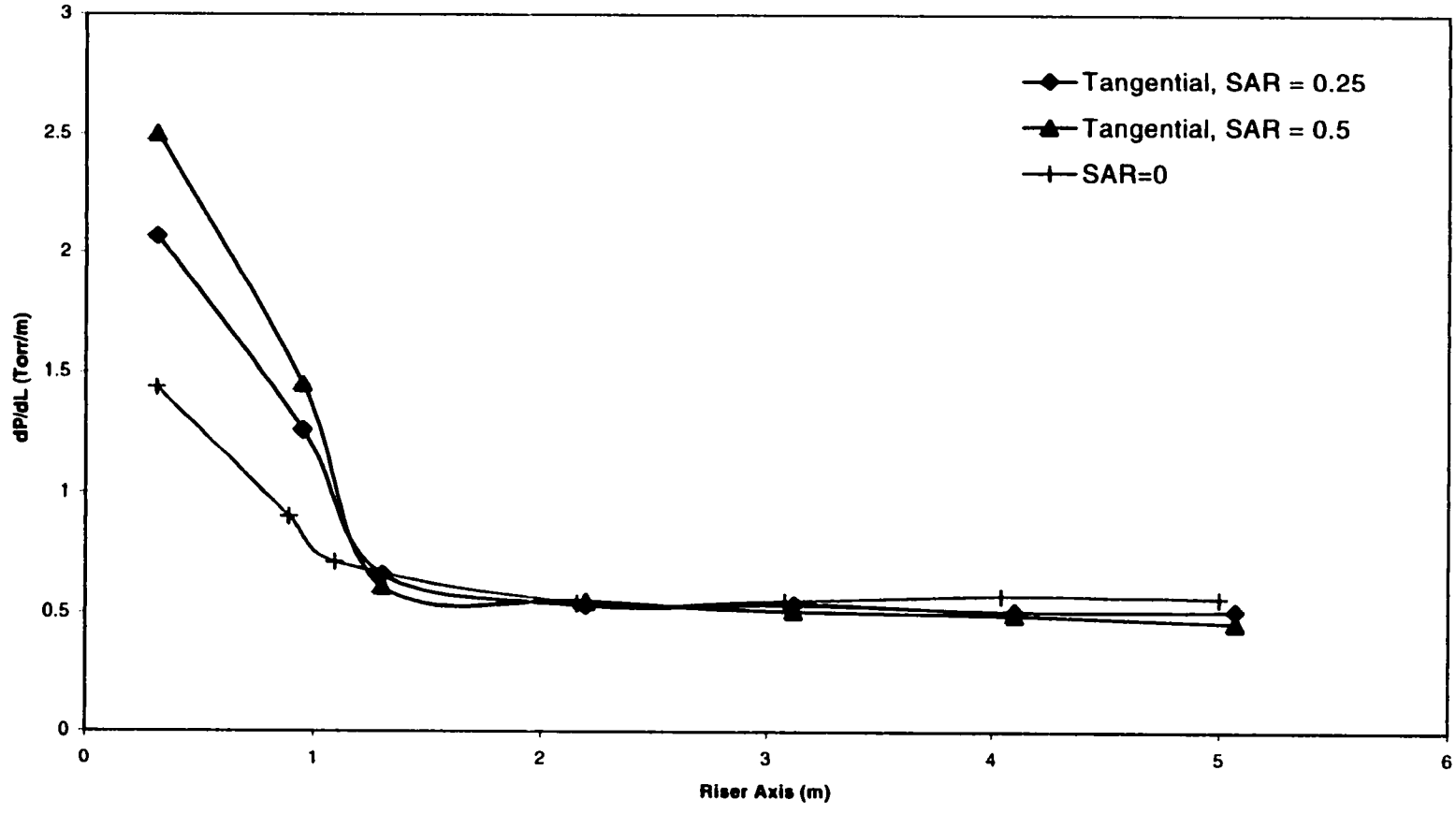

Figure 3.13. Effect of tangential secondary air injection on the solids holdup profile along the riser. Silica sand, Gs = 10 kg/m²s, tangential injection of secondary air from 1.2 m above the distributor plate.

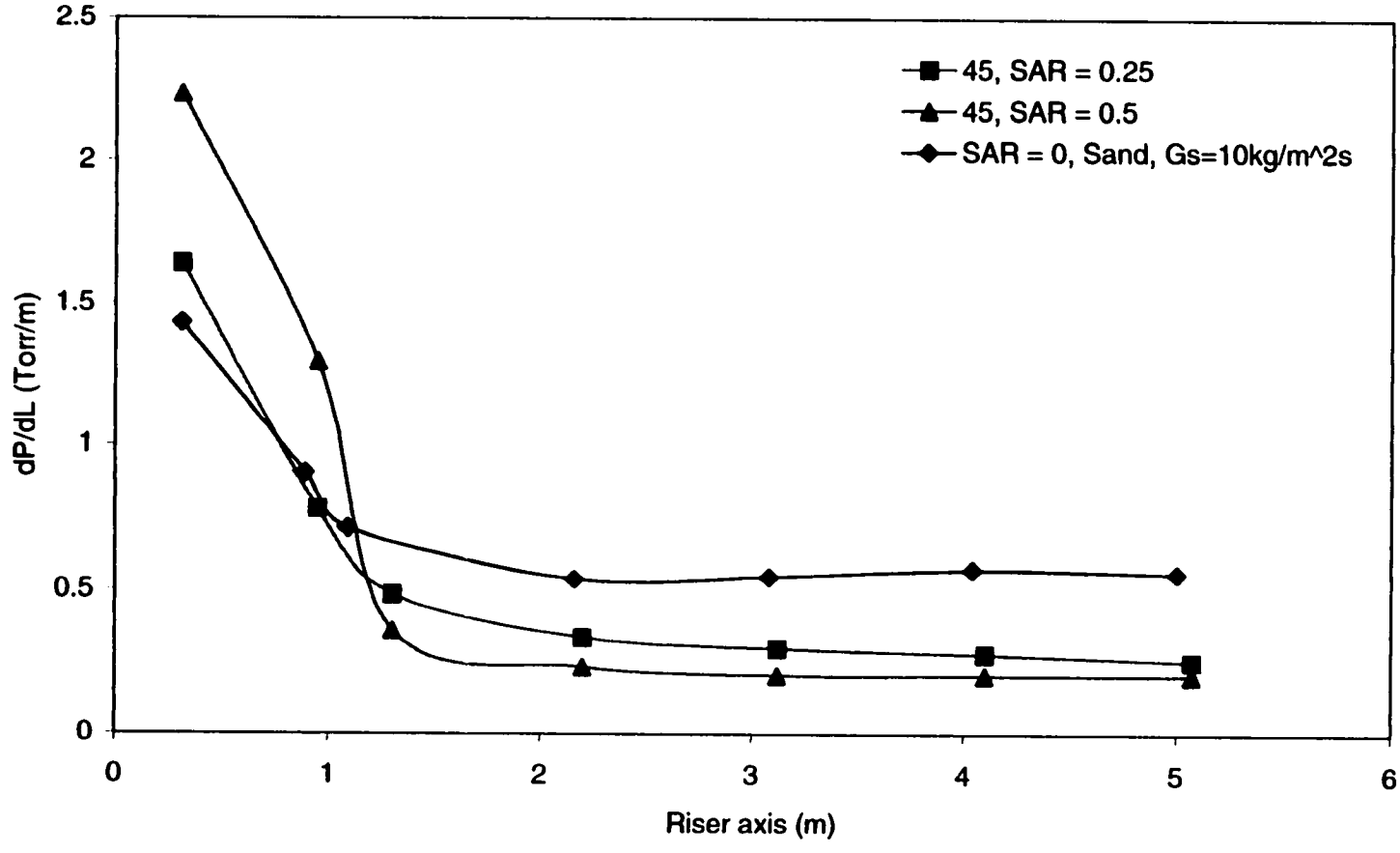

Figure 3.14. Effect of forty-five degree secondary air injection on the solids holdup profile along the riser. Silica sand, Gs = 10 kg/m²s, injection of secondary air from 1.2 m above the distributor plate.

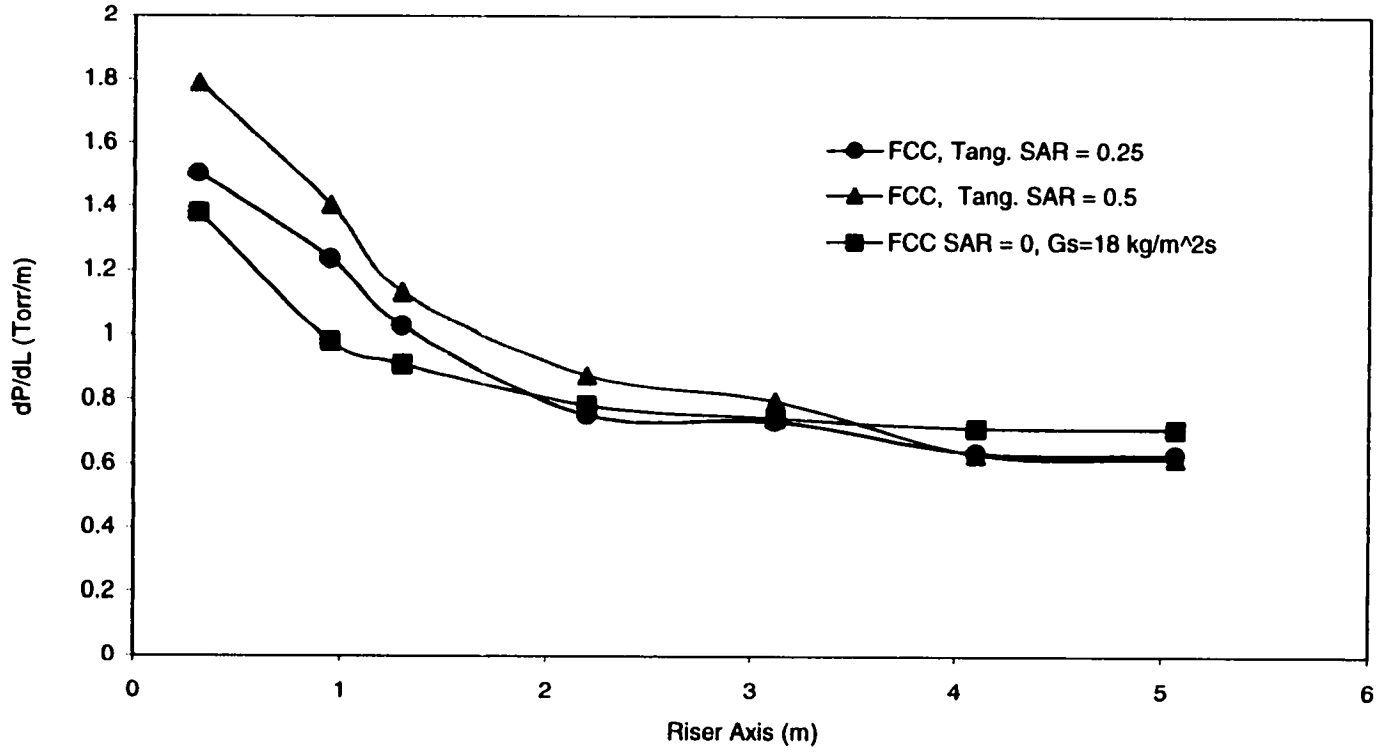

Figure 3.15. Effect of tangential secondary air injection on the solids holdup profile along the riser for FCC particles. Gs = 18 kg/m^{2}s, SA injection from 1.2 m above the distributor plate.

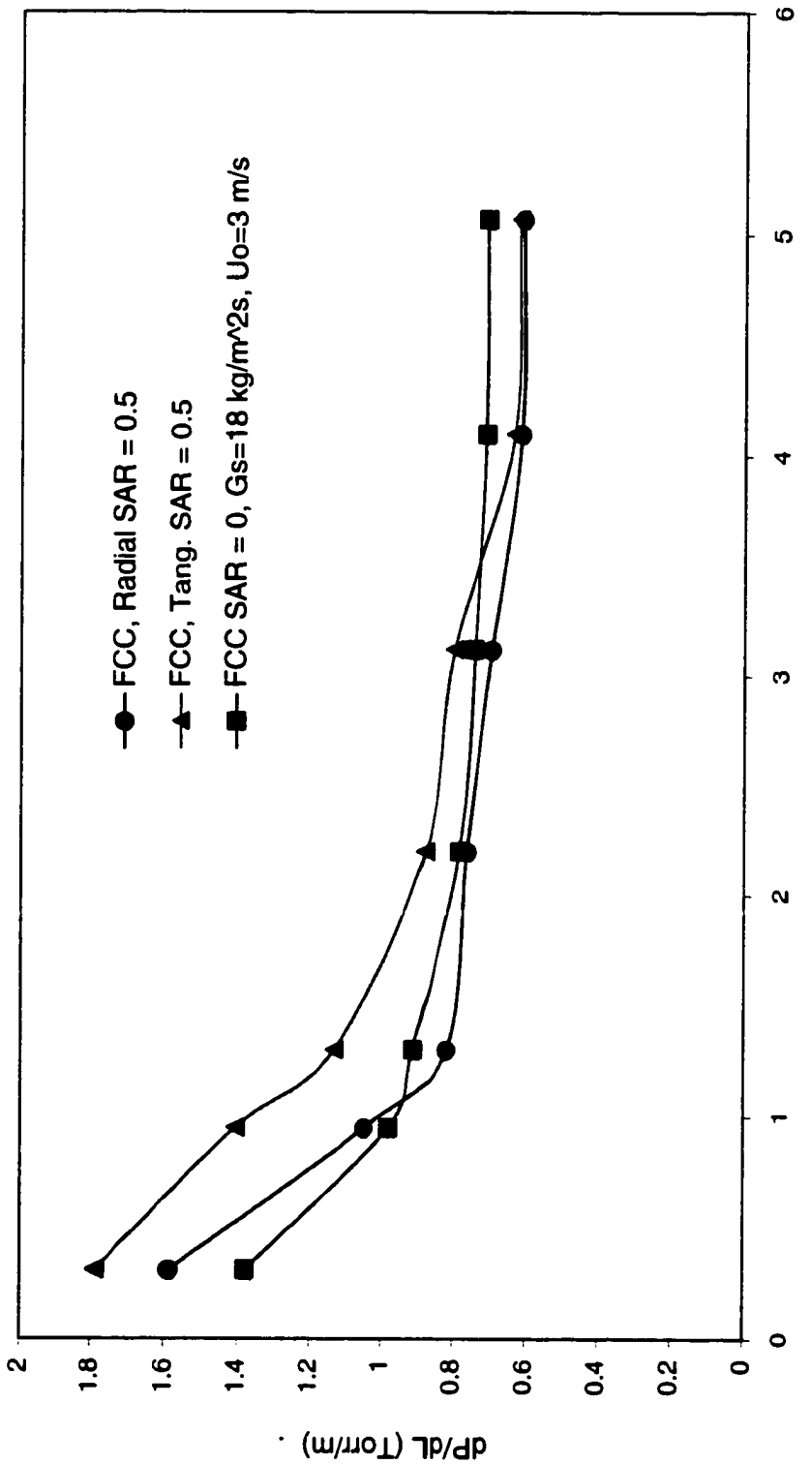

Figure 3.16. Effect of mode of secondary air injection on the solids holdup profile along the riser. FCC Particles, Gs = 18 kg/m²s, Injection of secondary air from 1.2 m above the distributor plate (Uo = 3 m/s)

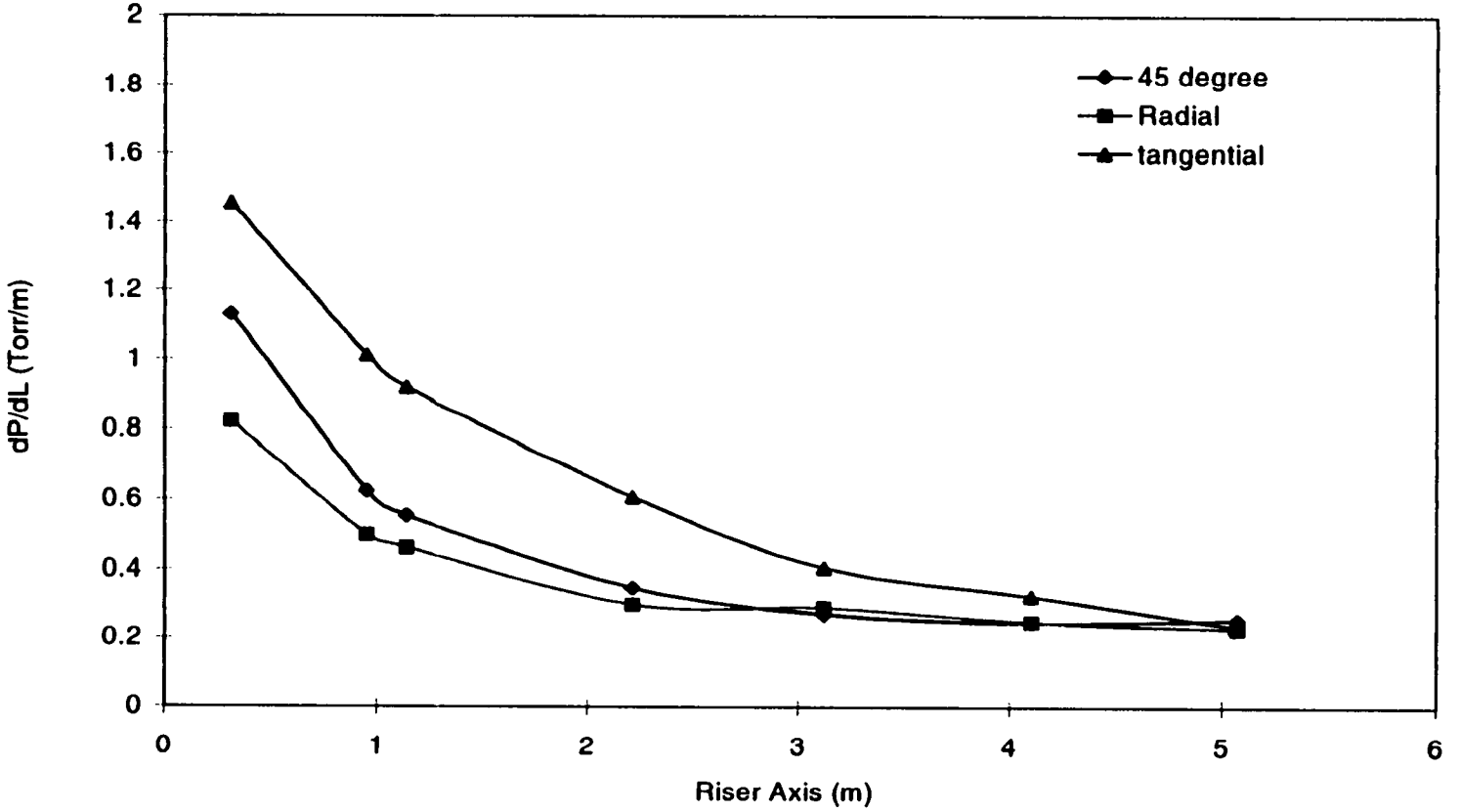

Figure 3.17. Effect of mode of injection on the pressure drop profile along the riser axis. Sand particles, secondary air injection from the third level (2.14 m above distributor plate), SAR =0.25, Gs = 5 kg/m²s

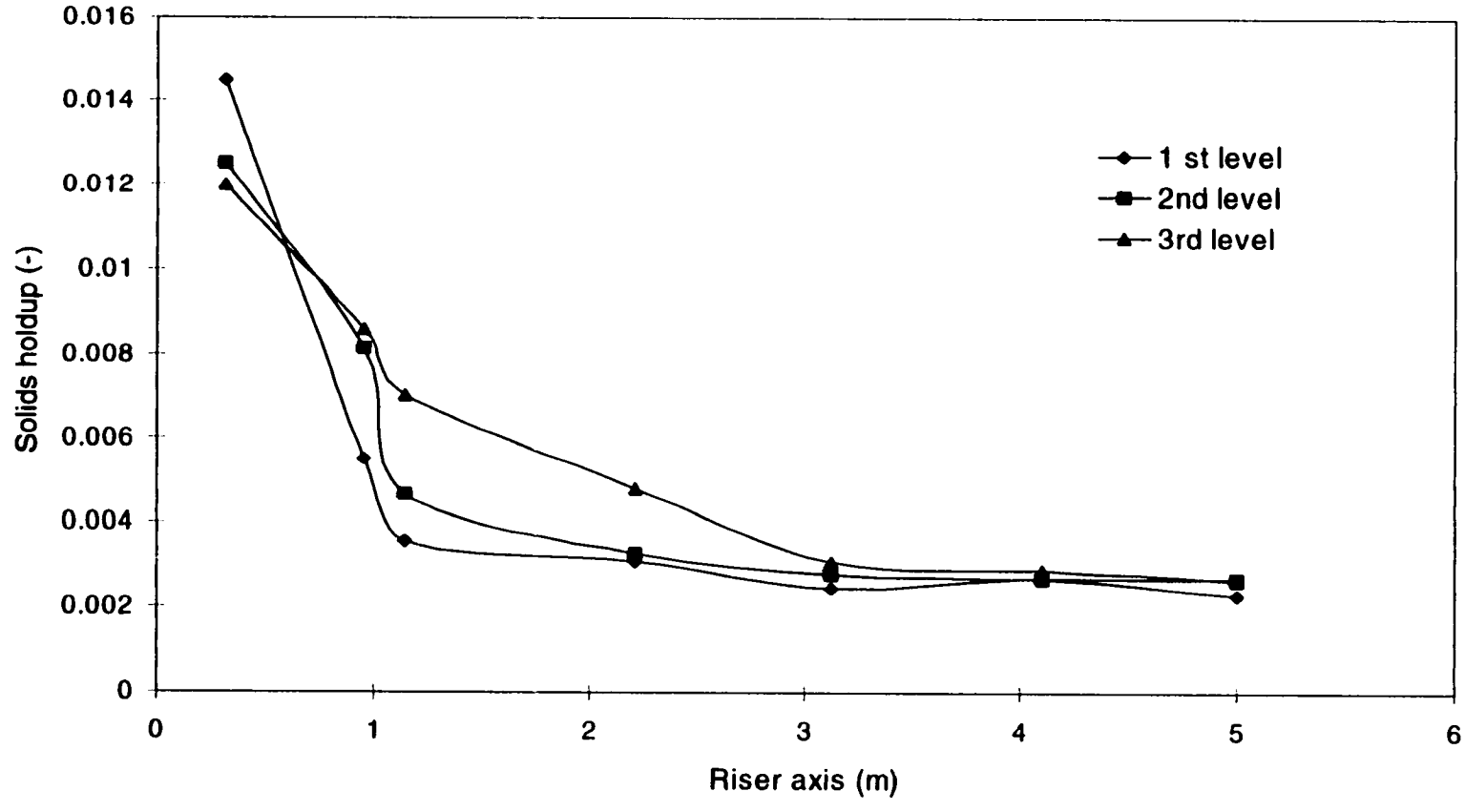

Figure 3.18. Effect of location of secondary air jets on the solids holdup profile along the riser. Silica sand particles, SAR = 0.25, Gs = 10 kg/m²s, 45-degree injection of secondary air from various elevations.

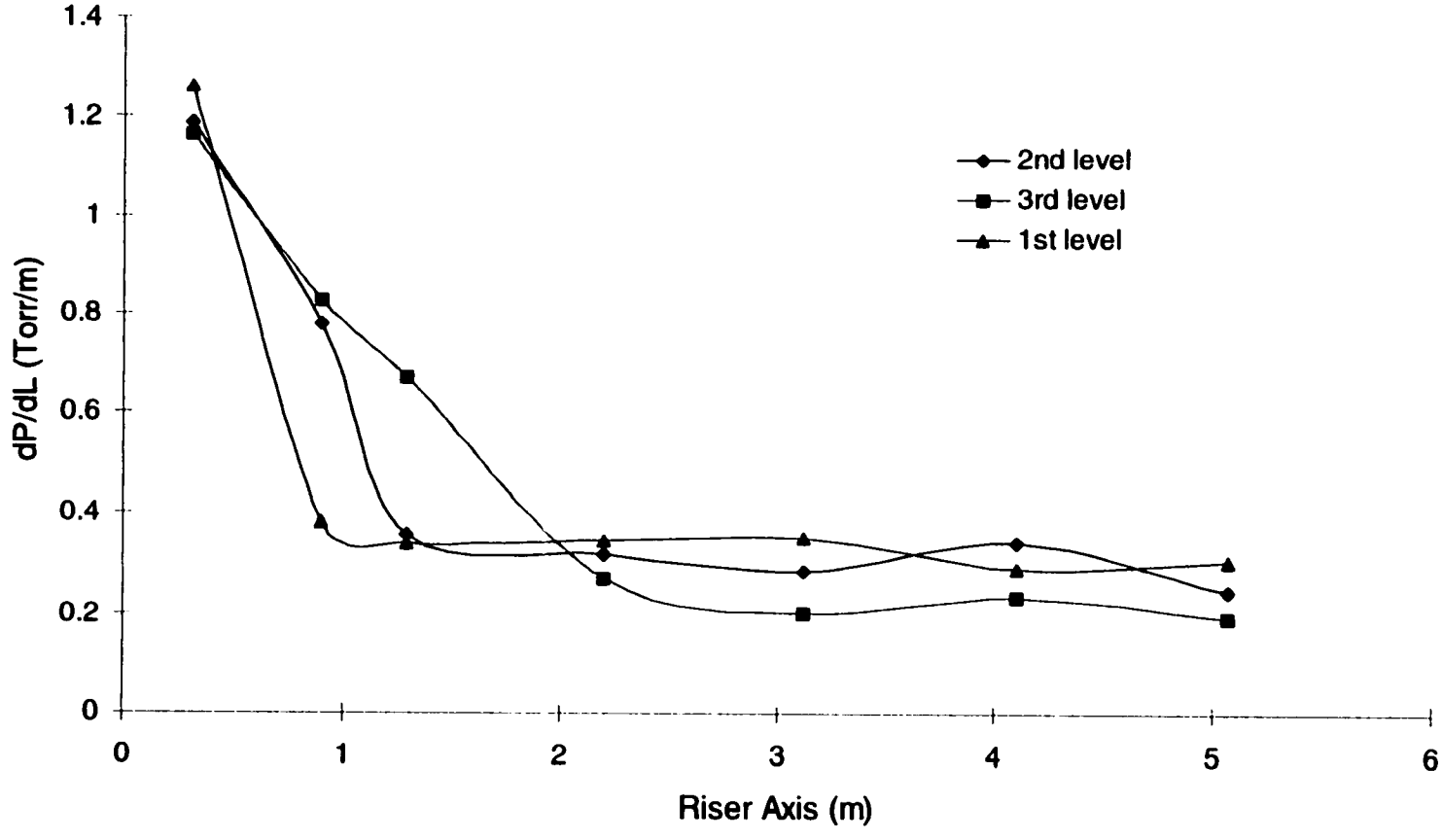

Figure 3.19. Effect of axial location of secondary air jets on the pressure drop profile along the riser. Silica sand particles, SAR = 0.5, Gs = 5 kg/m²s, Radial injection of secondary air from various elevations.

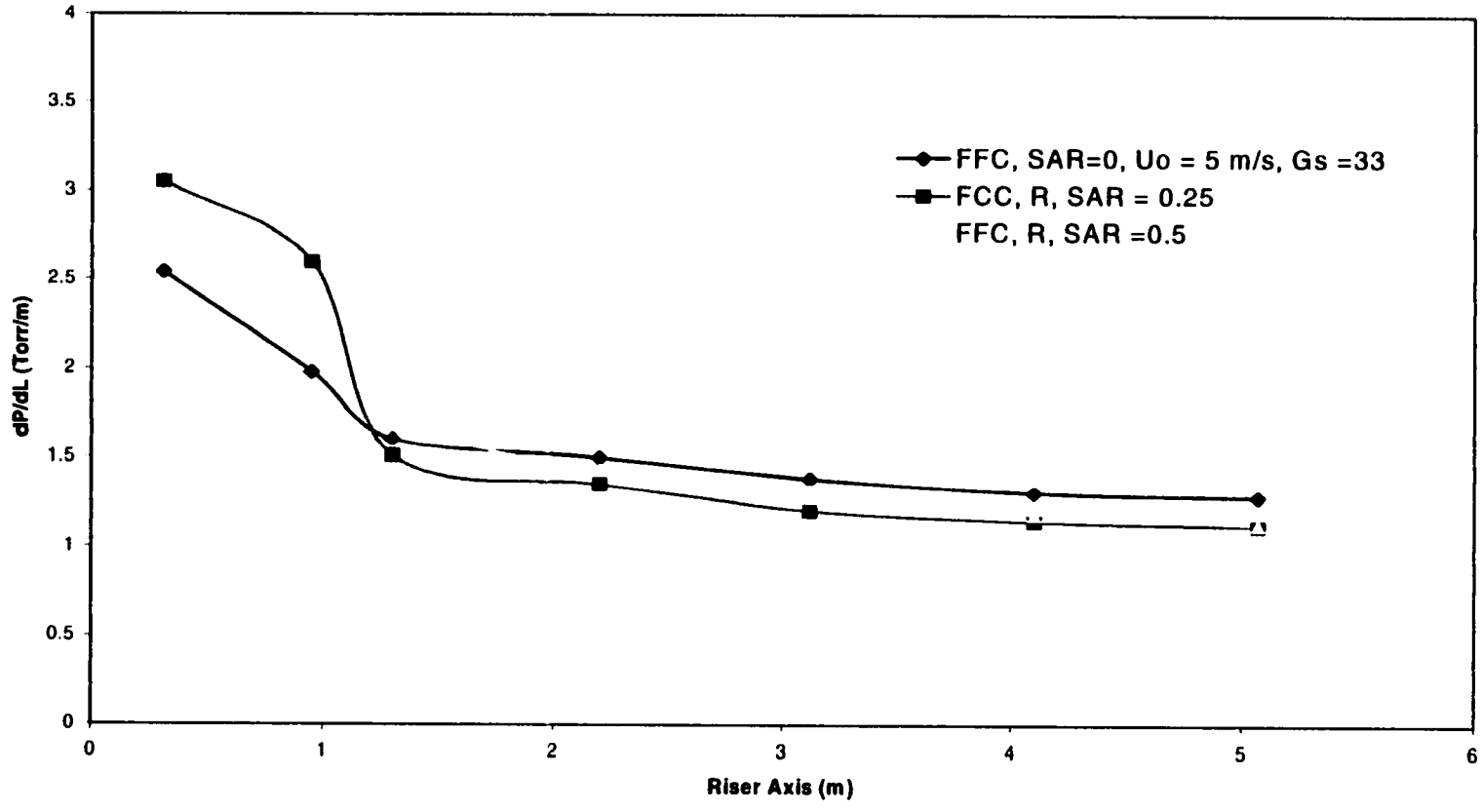

Figure 3.20. Pressure drop profile along the riser axis for radial SA injection with various secondary air ratios. FCC particles, Gs=33 kg/m²s Uo=5m/s.

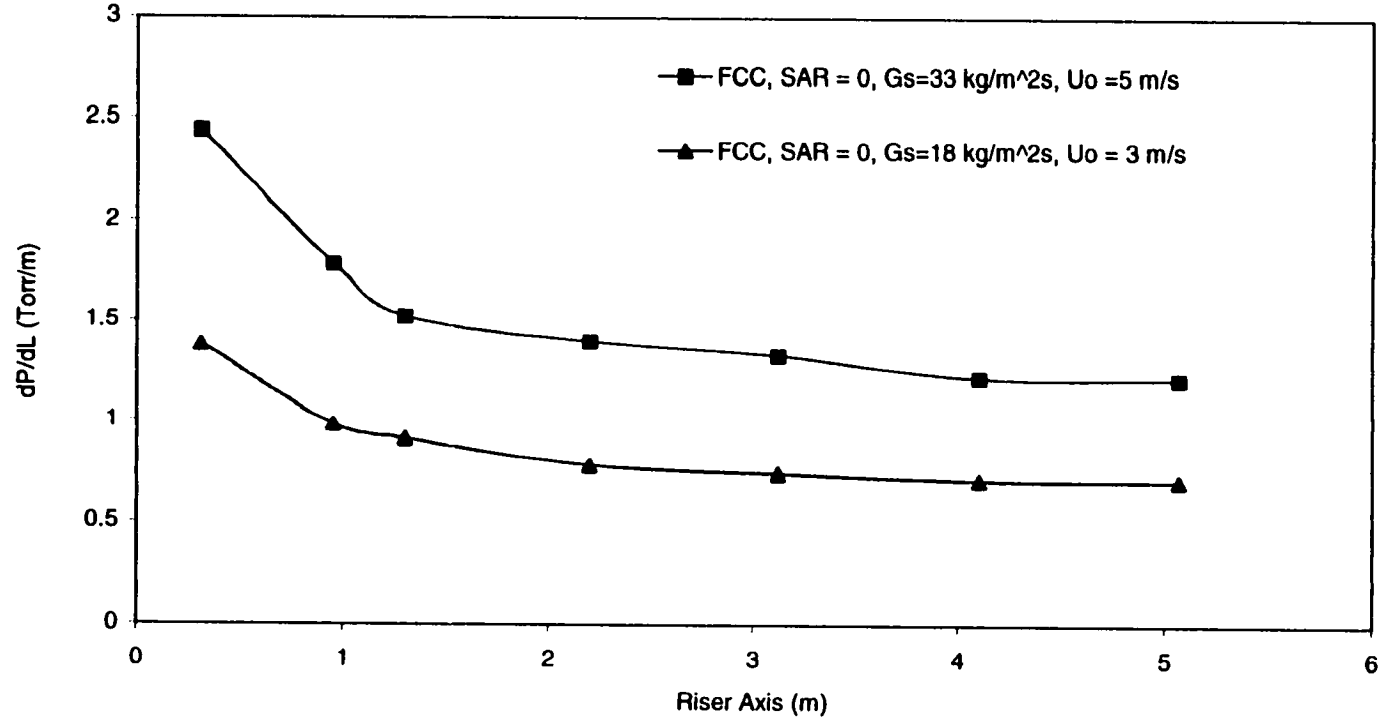

Figure 3.21. Pressure drop profile along the riser axis for SAR = 0 and for various external solids circulation rates. FCC particles.

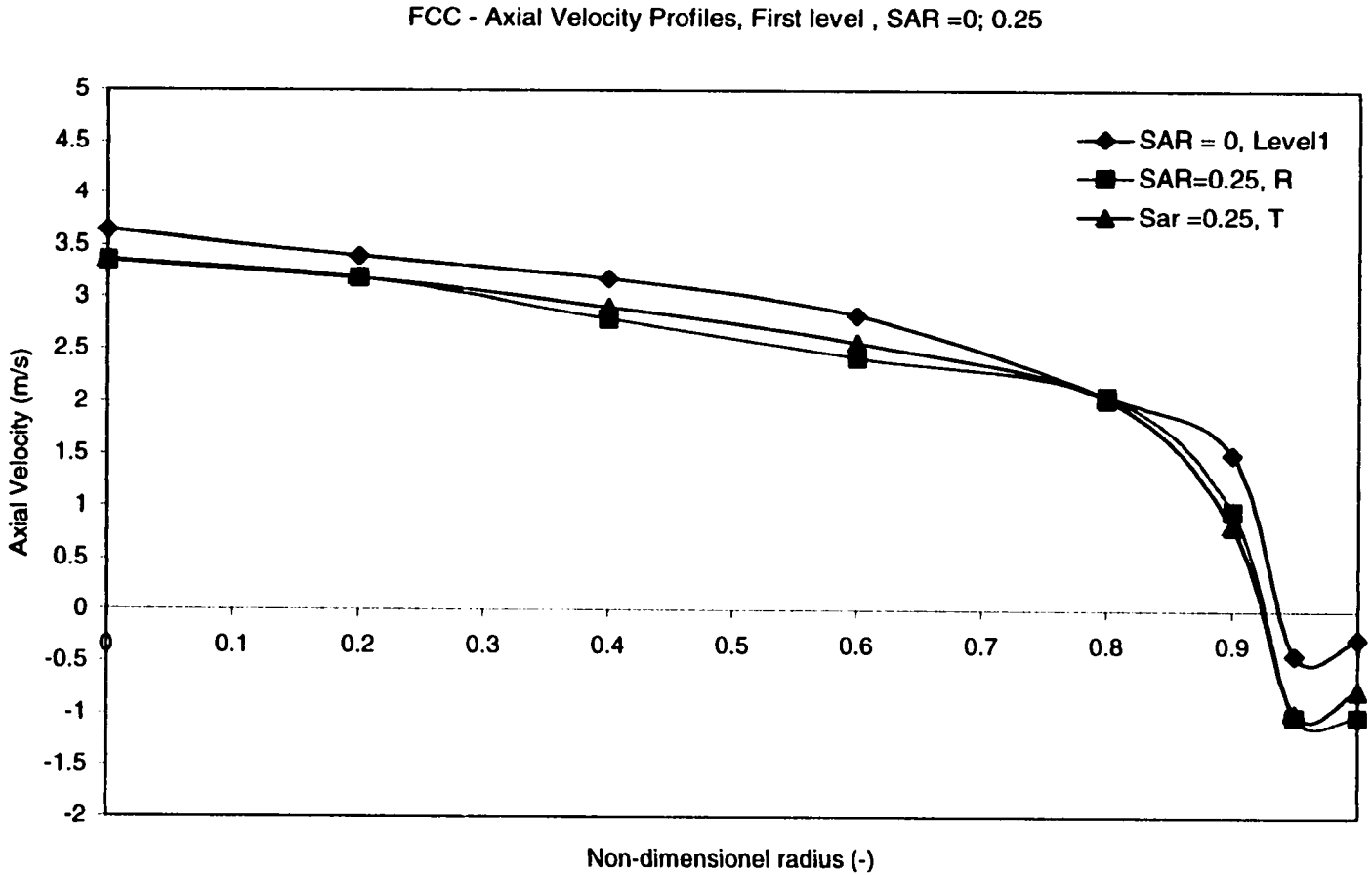

Figure 3.22. Effect of mode of SA injection on radial variation of particle axial velocity, SA injection level 2, velocity test section: 1, at 68 cm below SA injection port. Uo= 3 m/s. Gs = 18 kg/m²s.

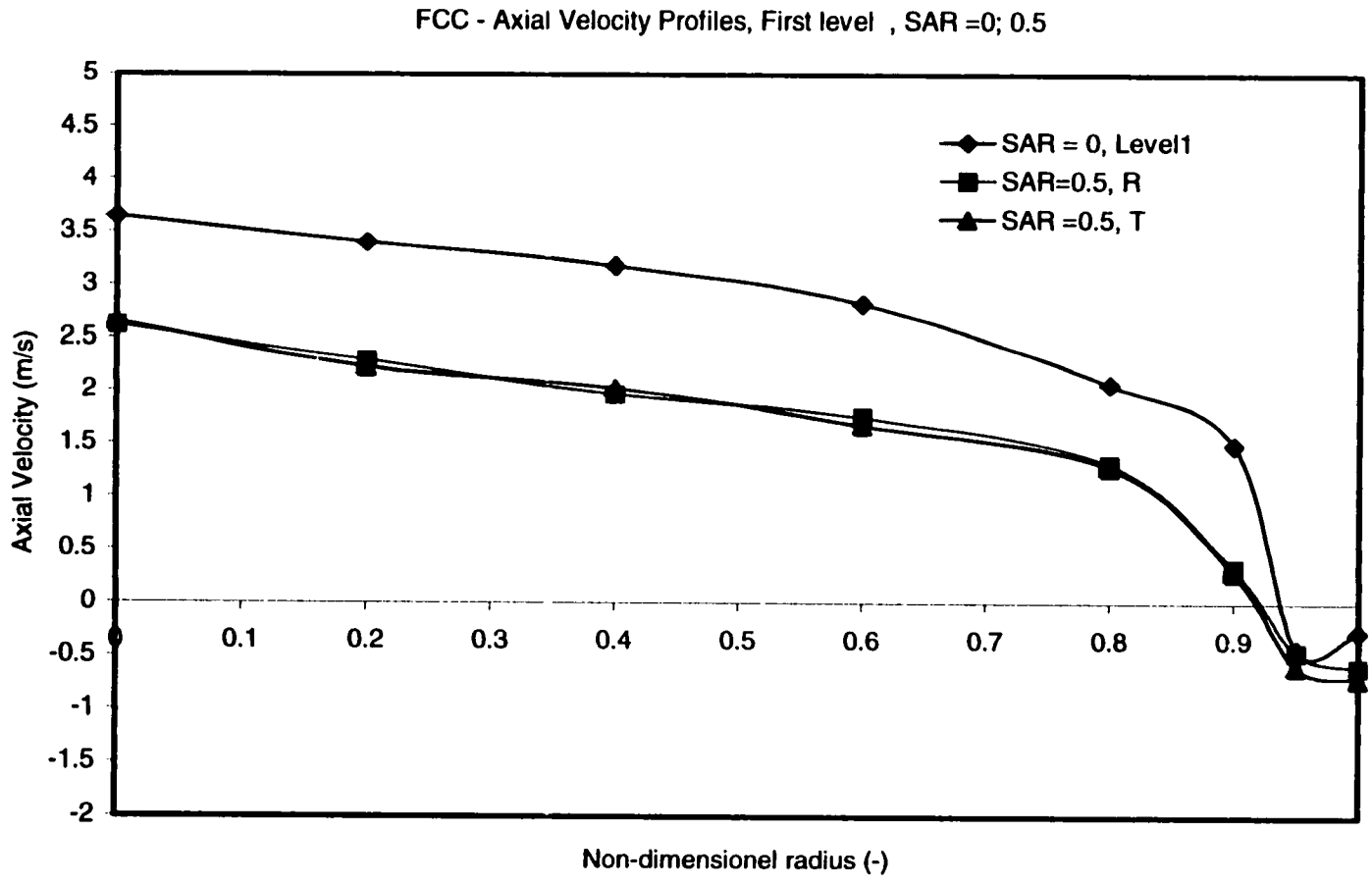

Figure 3.23. Effect of mode of SA injection on radial variation of particle axial velocity. FCC particles Uo= 3 m/s Velocity test section: 1, at 68 cm below SA injection port. Gs = 18 kg/m²s. SA injection level: 2.

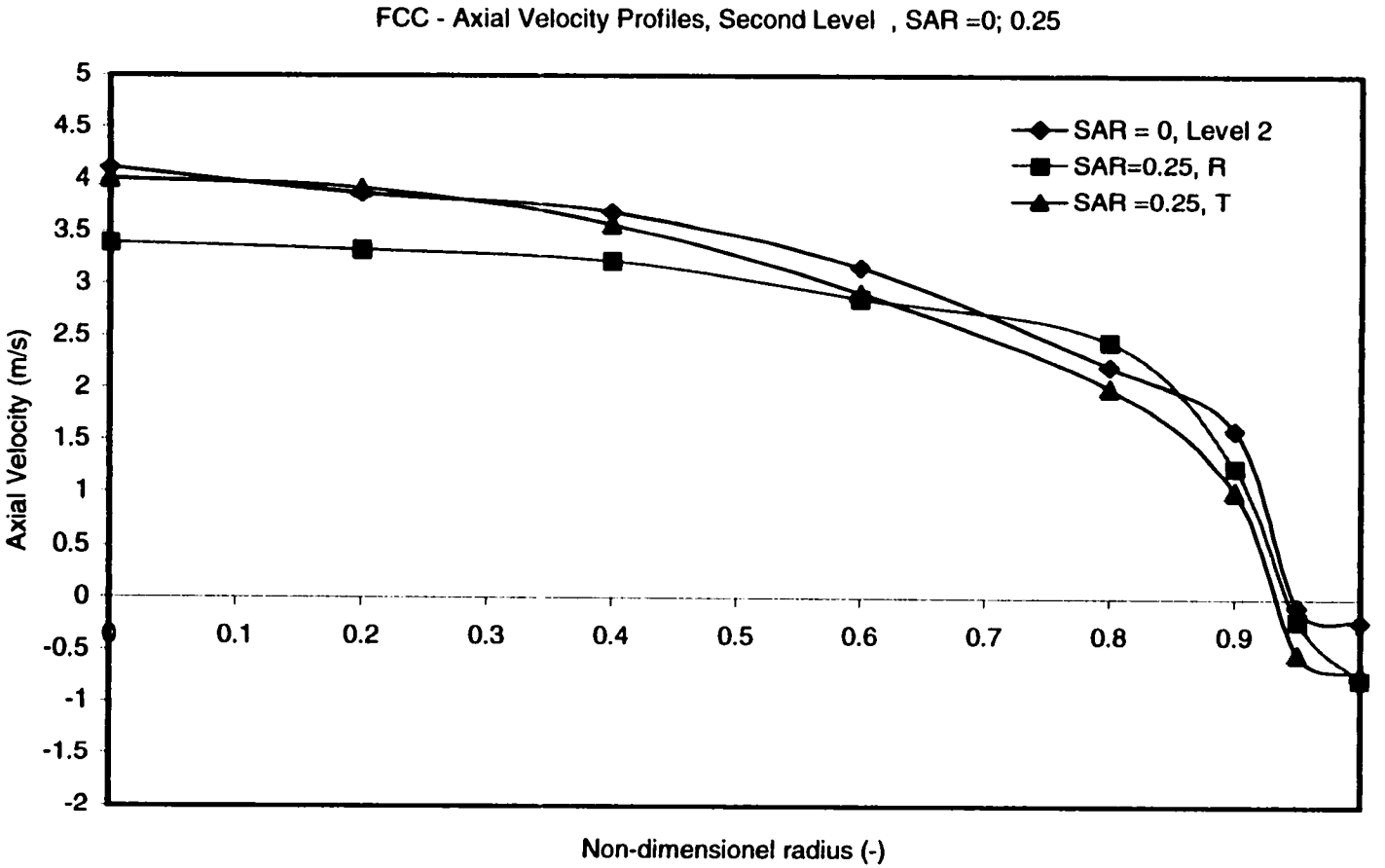

Figure 3.24. Effect of mode of SA injection on radial variation of particle axial velocity. FCC particles Uo= 3 m/s Velocity test section: 2, at 17 cm below SA injection port. Gs = 18 kg/m²s. SA injection level 2.

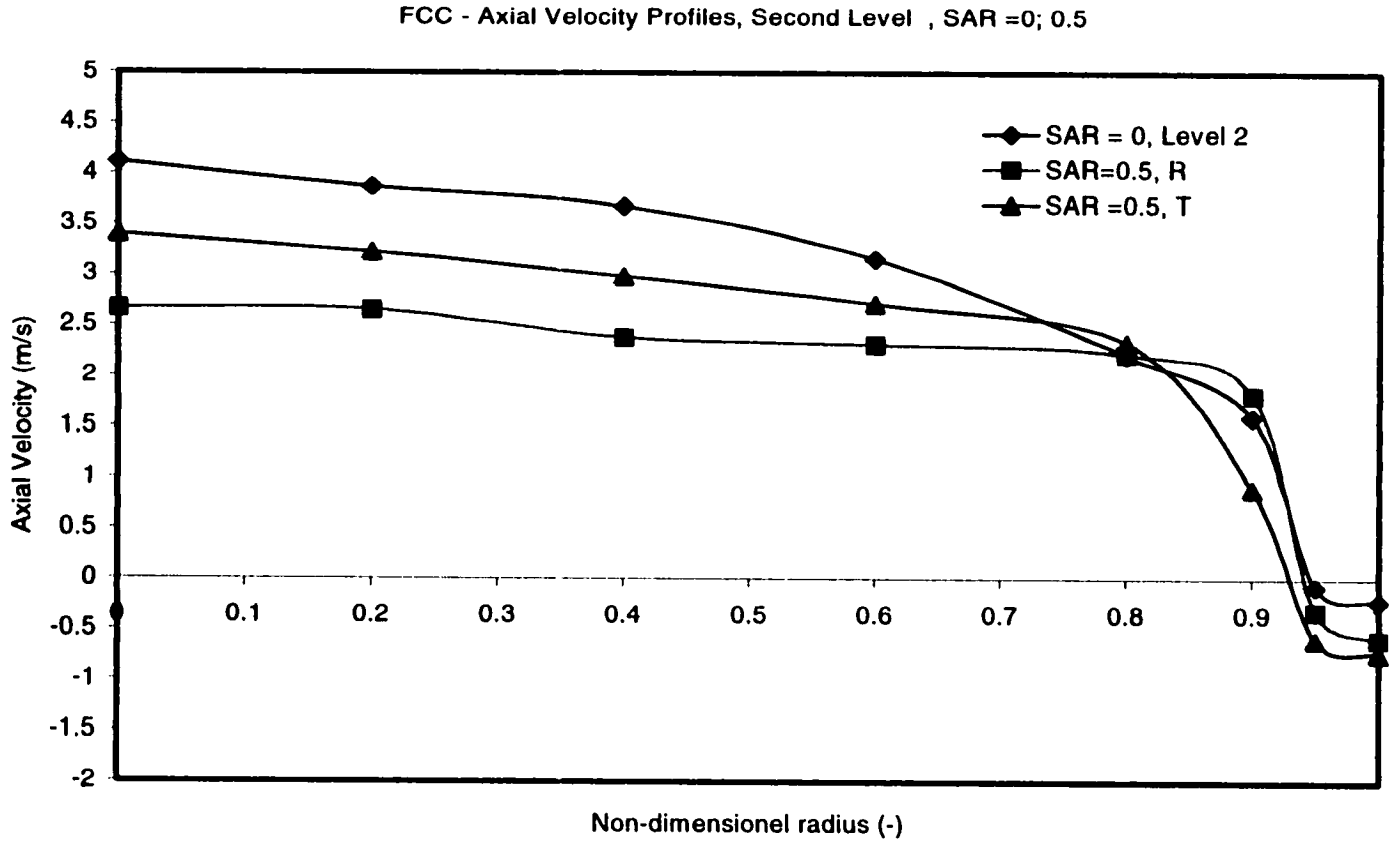

Figure 3.25. Effect of mode of SA injection on radial variation of particle axial velocity. FCC particles Uo= 3 m/s. Velocity test section: 2, at 17 cm below SA injection port. Gs = 18 kg/m²s. SA injection level 2.

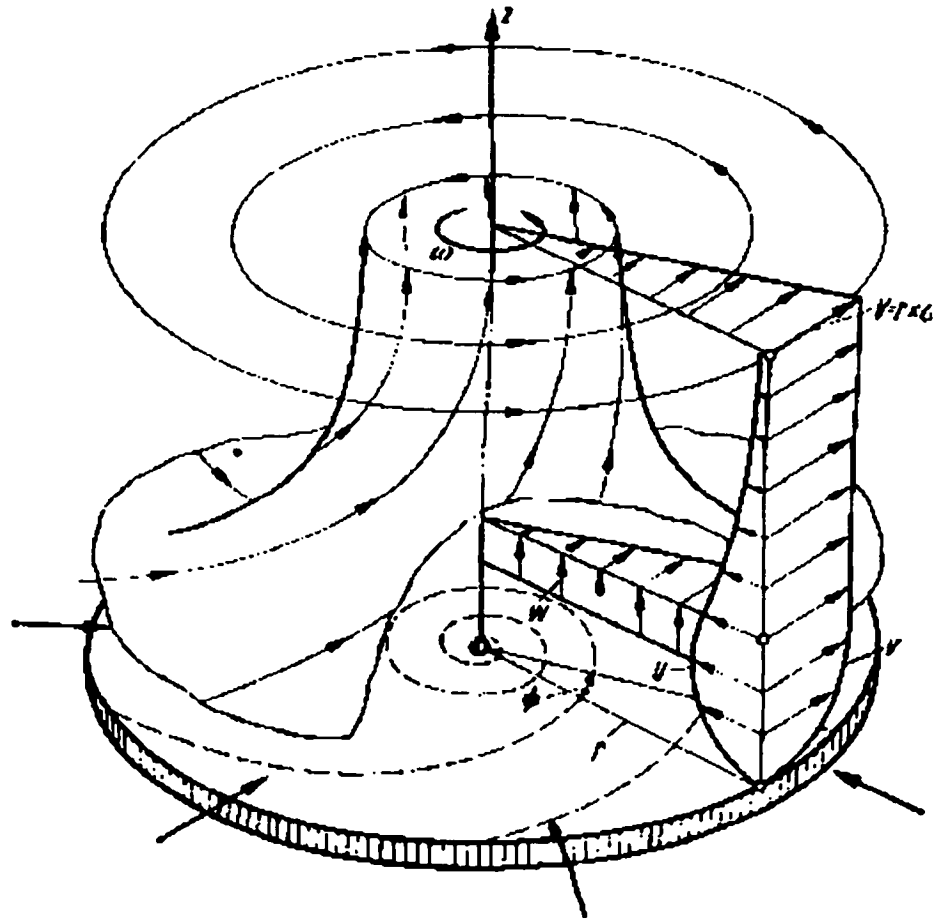

Figure 3.26. Illustration of secondary flows from Schlichting [1987]

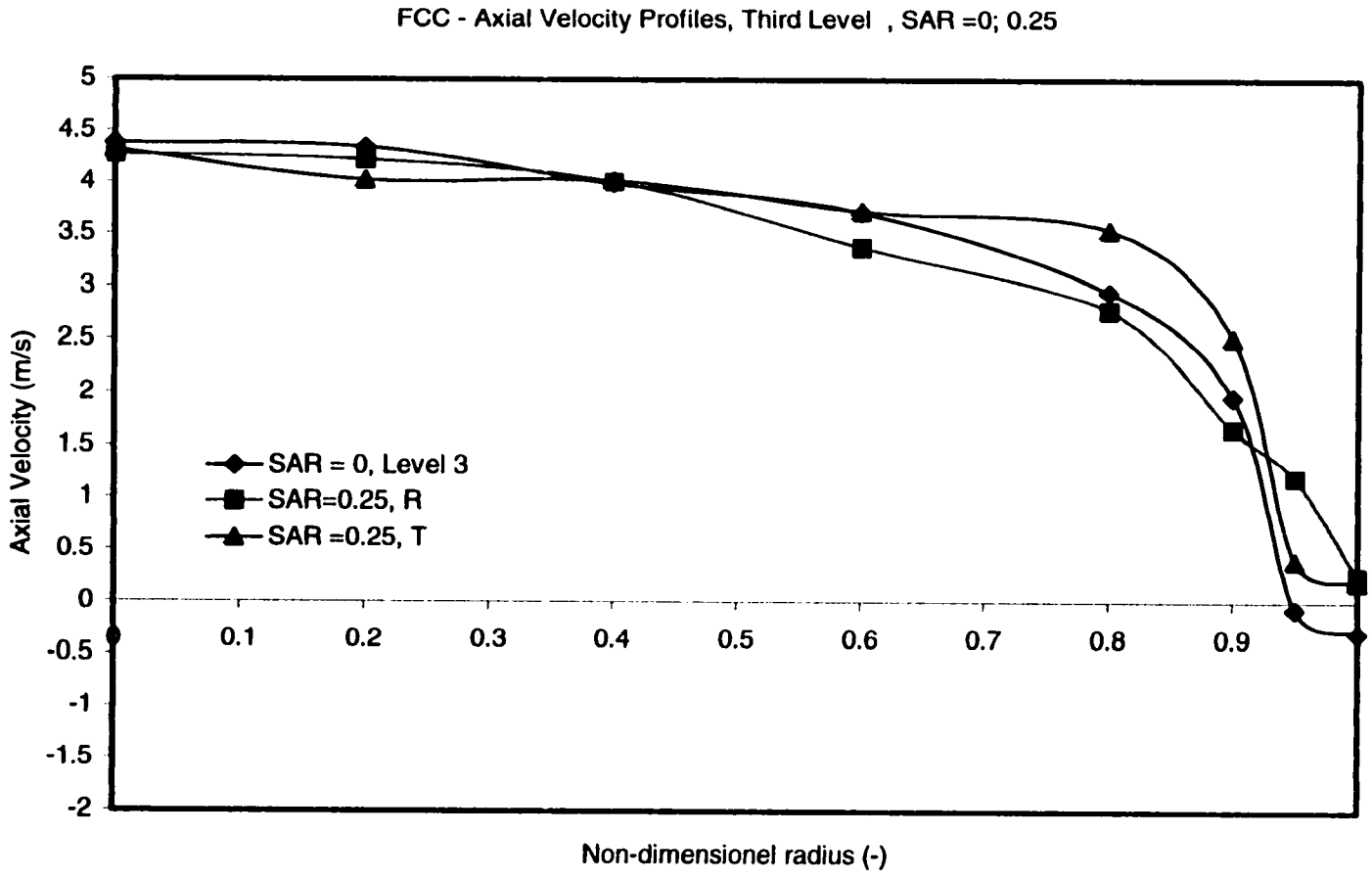

Figure 3.27. Effect of mode of SA injection on radial variation of particle axial velocity. FCC particles. Uo= 3 m/s Velocity test section: 3, at 6 cm above SA injection port. Gs = 18 kg/m²s. SA injection level 2.

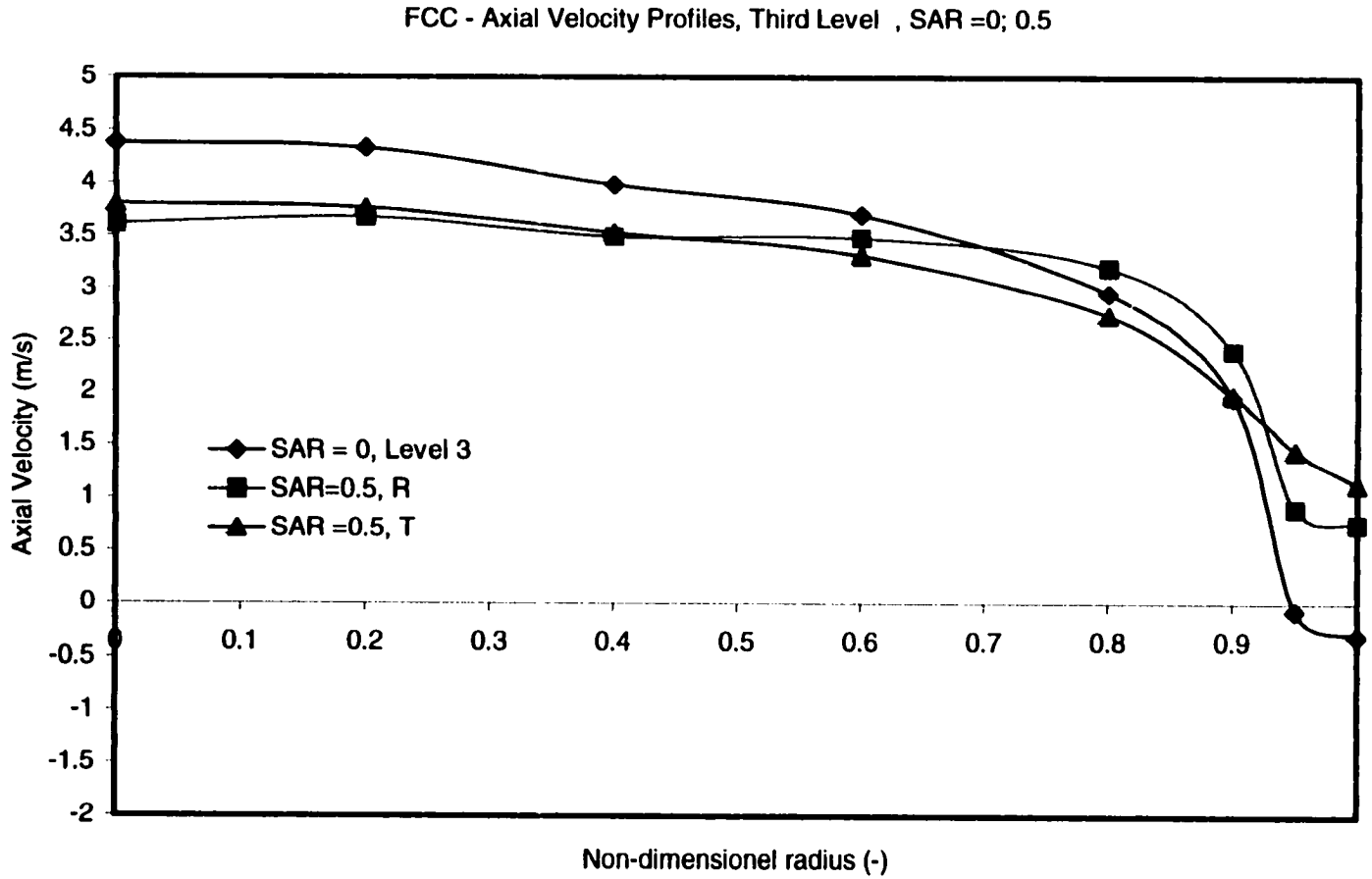

Figure 3.28. Effect of mode of SA injection on radial variation of particle axial velocity. FCC particles Uo= 3 m/s. Velocity test section: 3, at 6 cm above SA injection port. Gs = 18 kg/m²s. SA injection level 2.

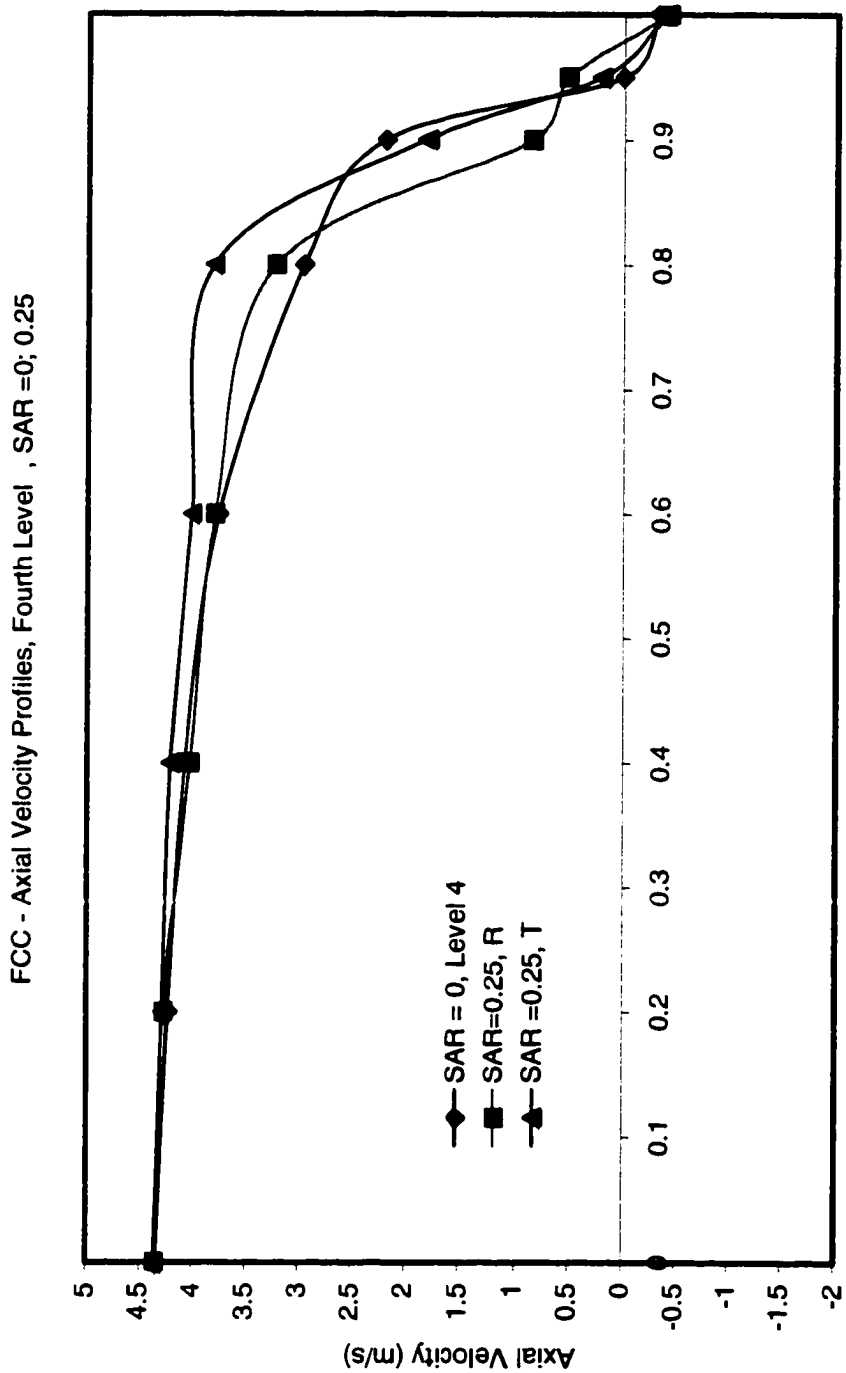

Figure 3.29. Effect of mode of SA injection on radial variation of particle axial velocity. FCC particles, Uo= 3 m/s Velocity test section: 4, at 62 cm above SA injection port. Gs = 18 kg/m²s. SA injection level 2.

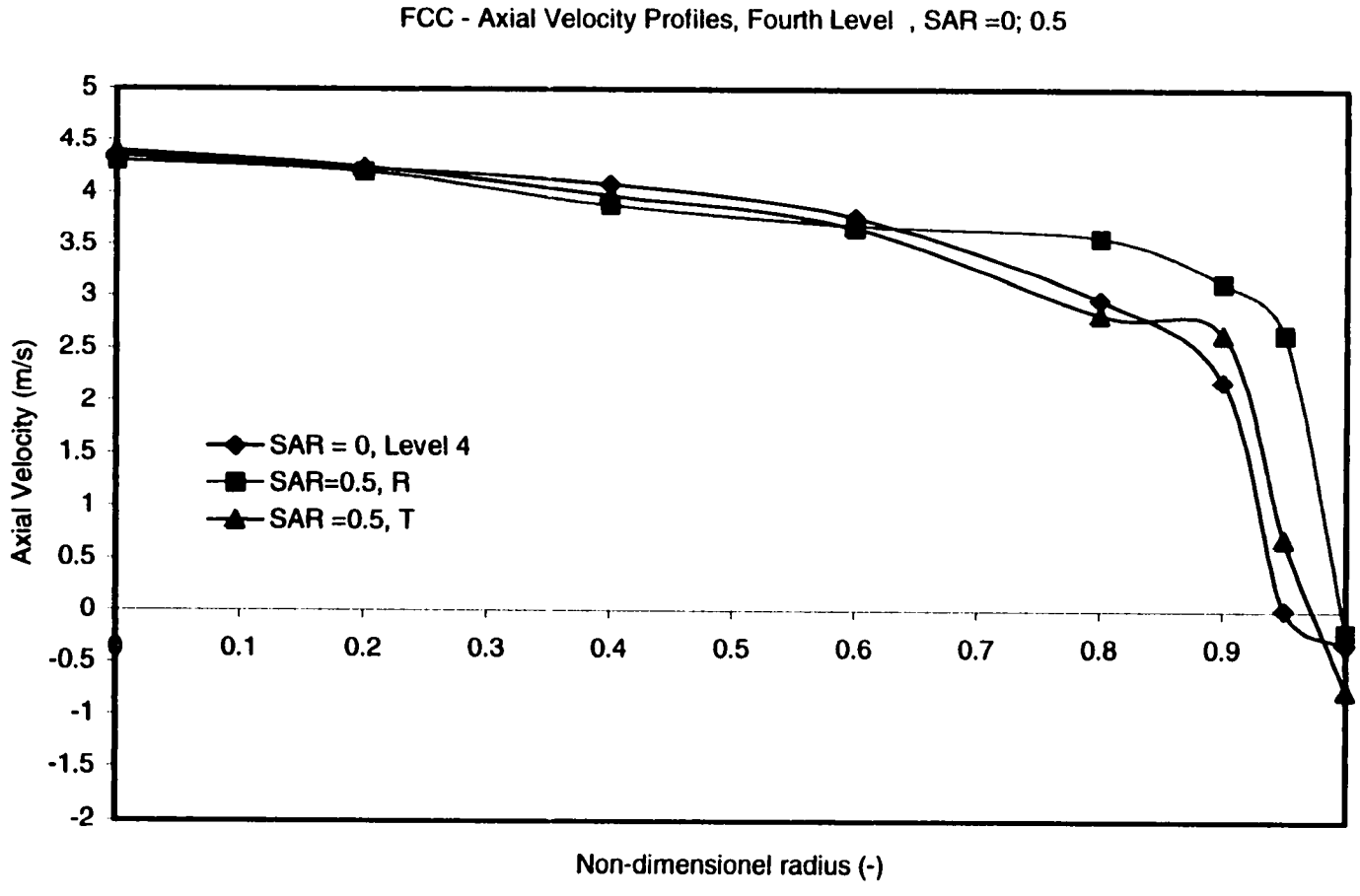

Figure 3.30. Effect of mode of SA injection on radial variation of particle axial velocity. FCC particles Uo= 3 m/s Velocity test section: 4, at 62 cm above the SA injection port. Gs = 18 kg/m²s. SA injection level 2.

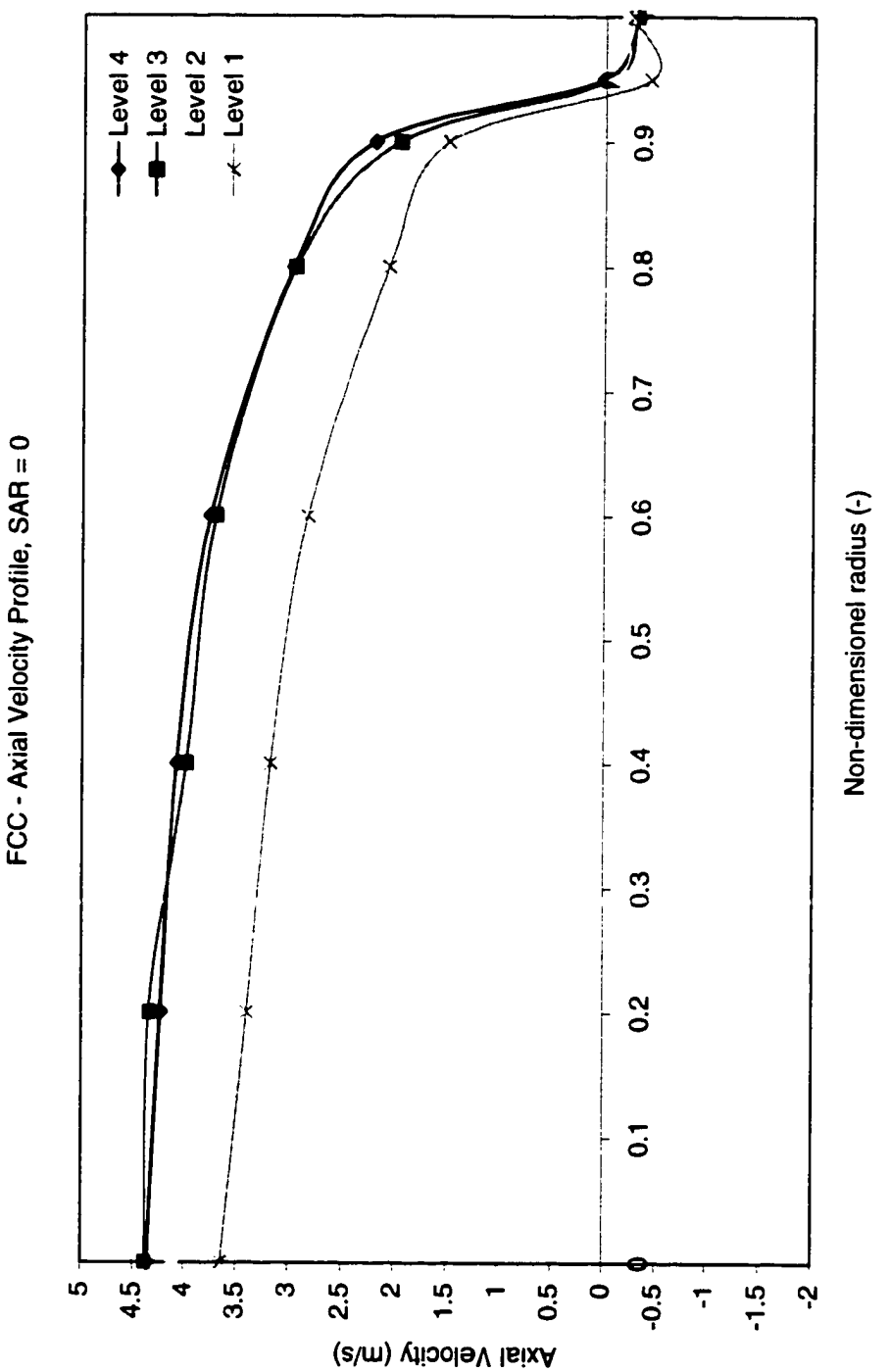

Figure 3.31. Axial development of particle axial velocity profile, SAR = 0, Uo = 3 m/s, Gs = 18 kg/m²s

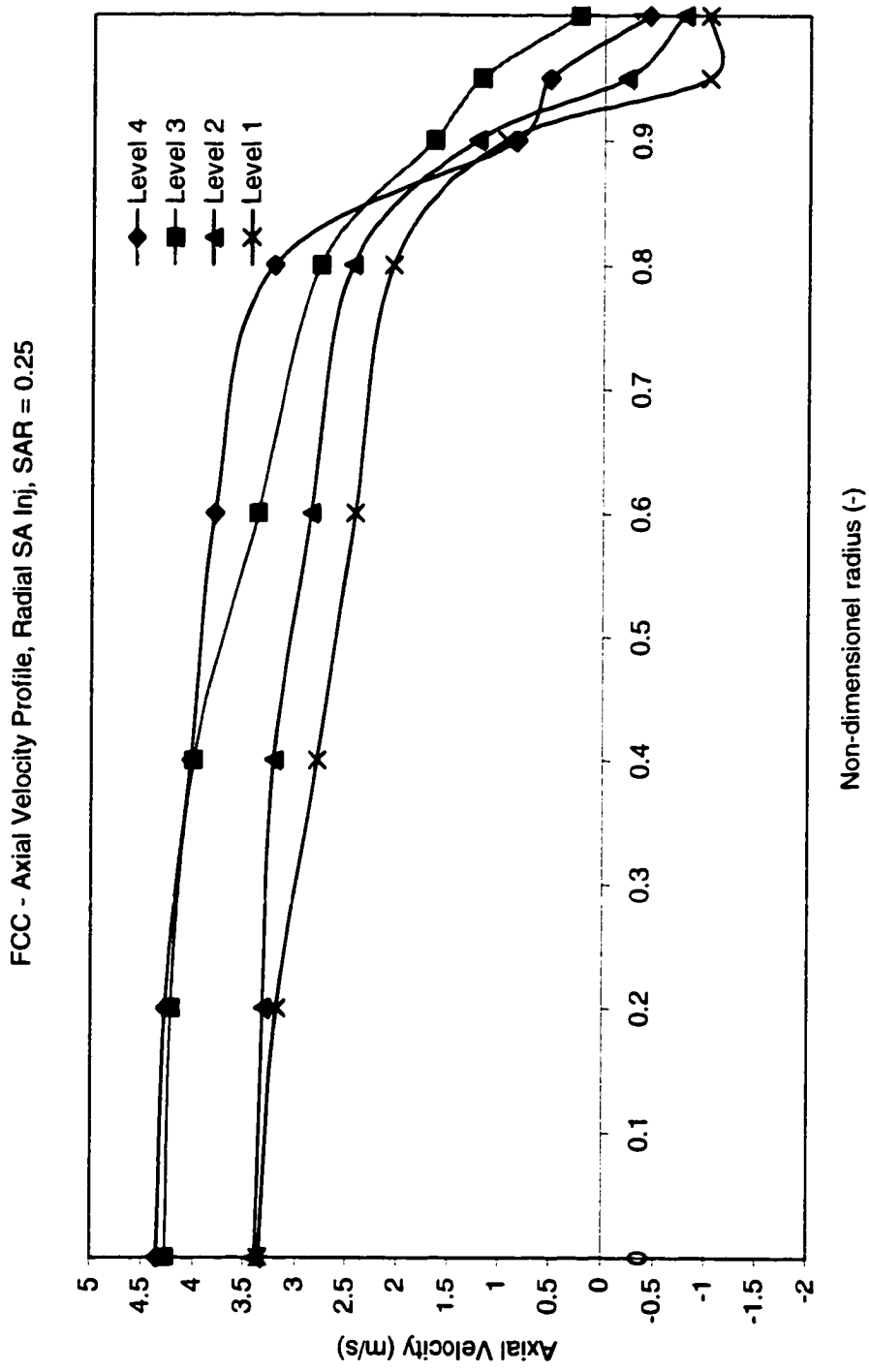

Figure 3.32. Axial development of particle axial velocity profile, SAR = 0.25, Radial SA injection from level 2, Uo = 3 m/s, Gs = 18 kg/m²s

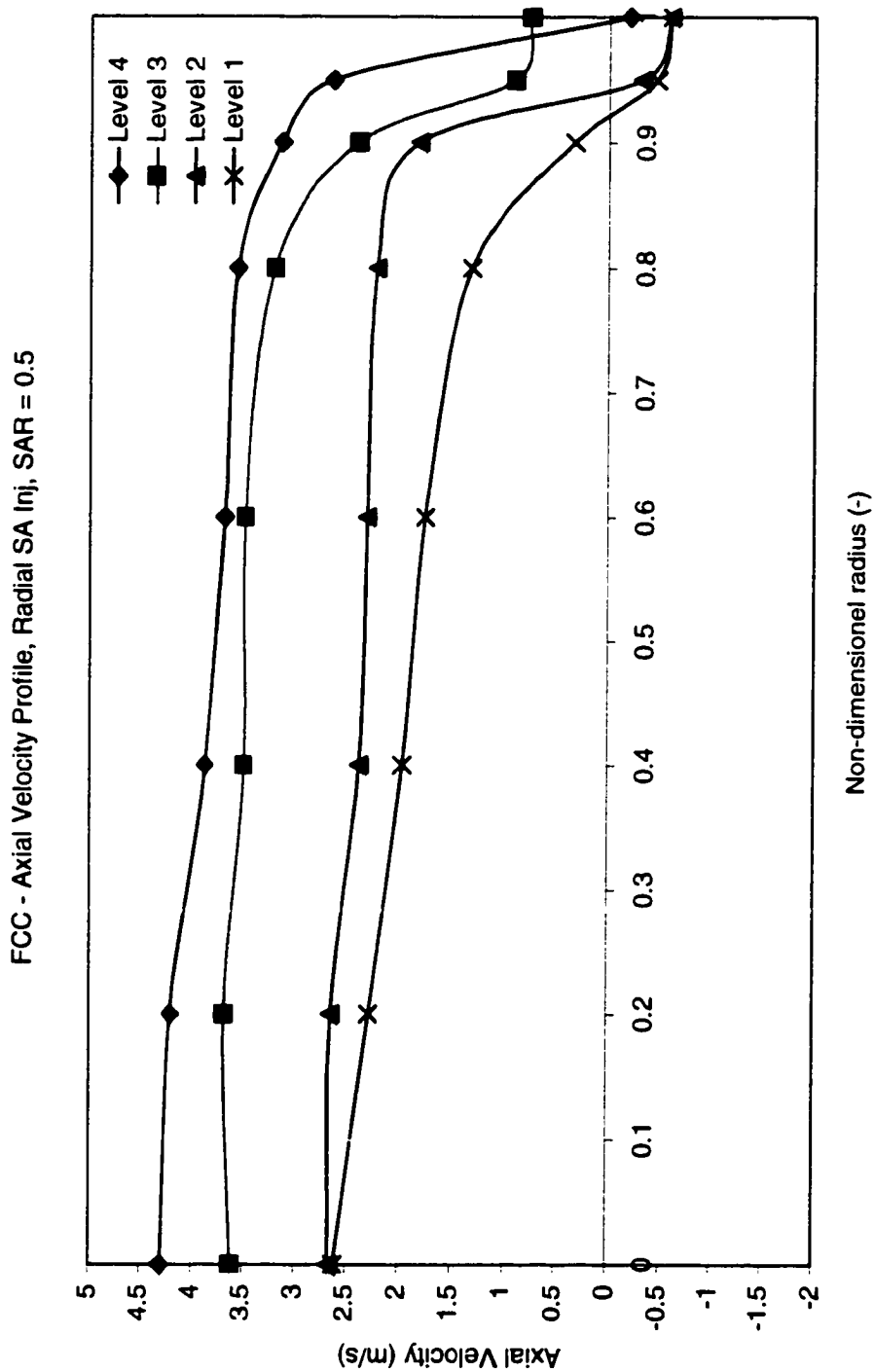

Figure 3.33. Axial development of particle axial velocity profile, SAR = 0. 5, Radial SA injection from level 2, Uo = 3 m/s, Gs = 18 kg/m²s

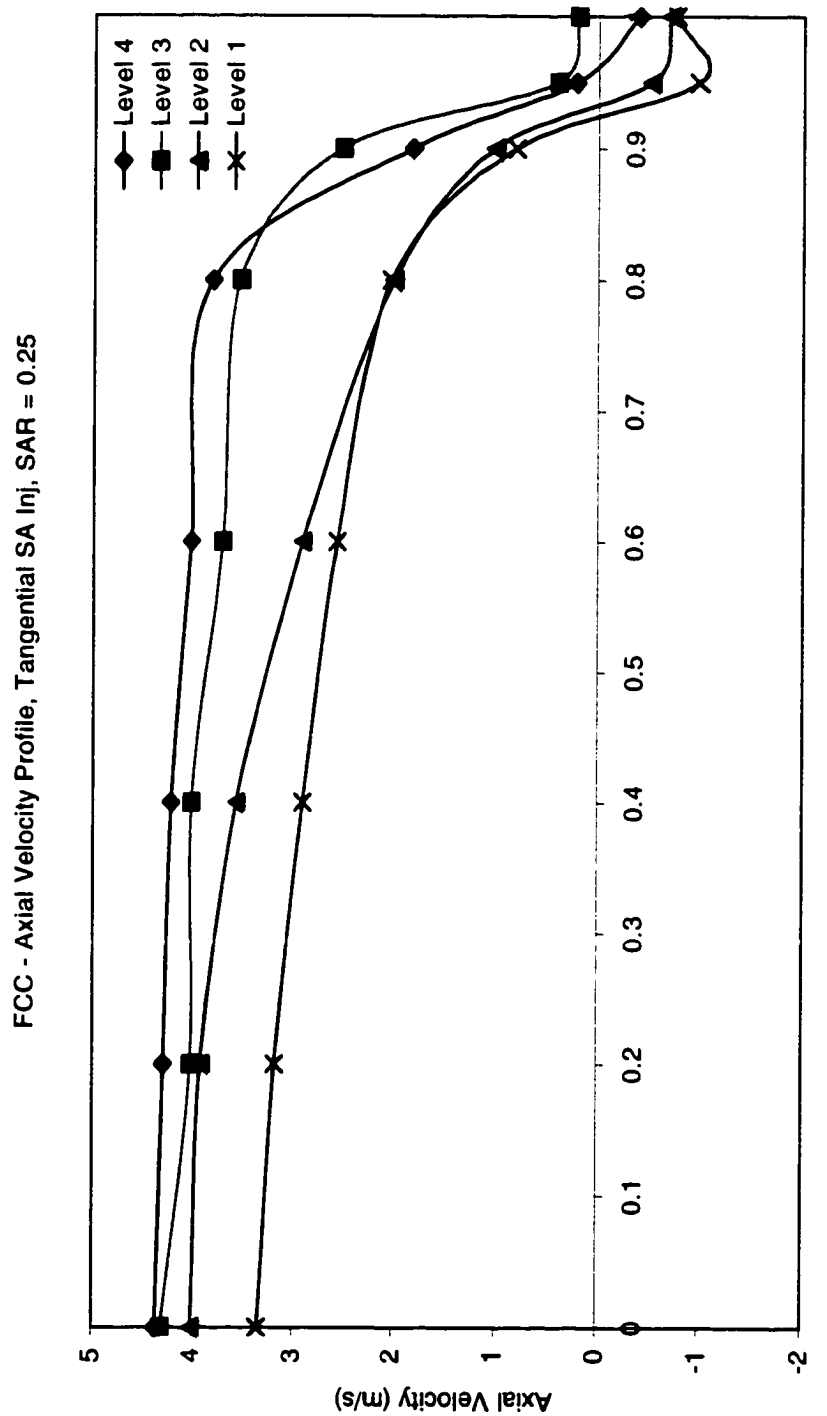

Figure 3.34. Axial development of particle axial velocity profile, SAR = 0. 25, Tangential SA injection from level 2, Uo = 3 m/s, Gs = 18 kg/m²s

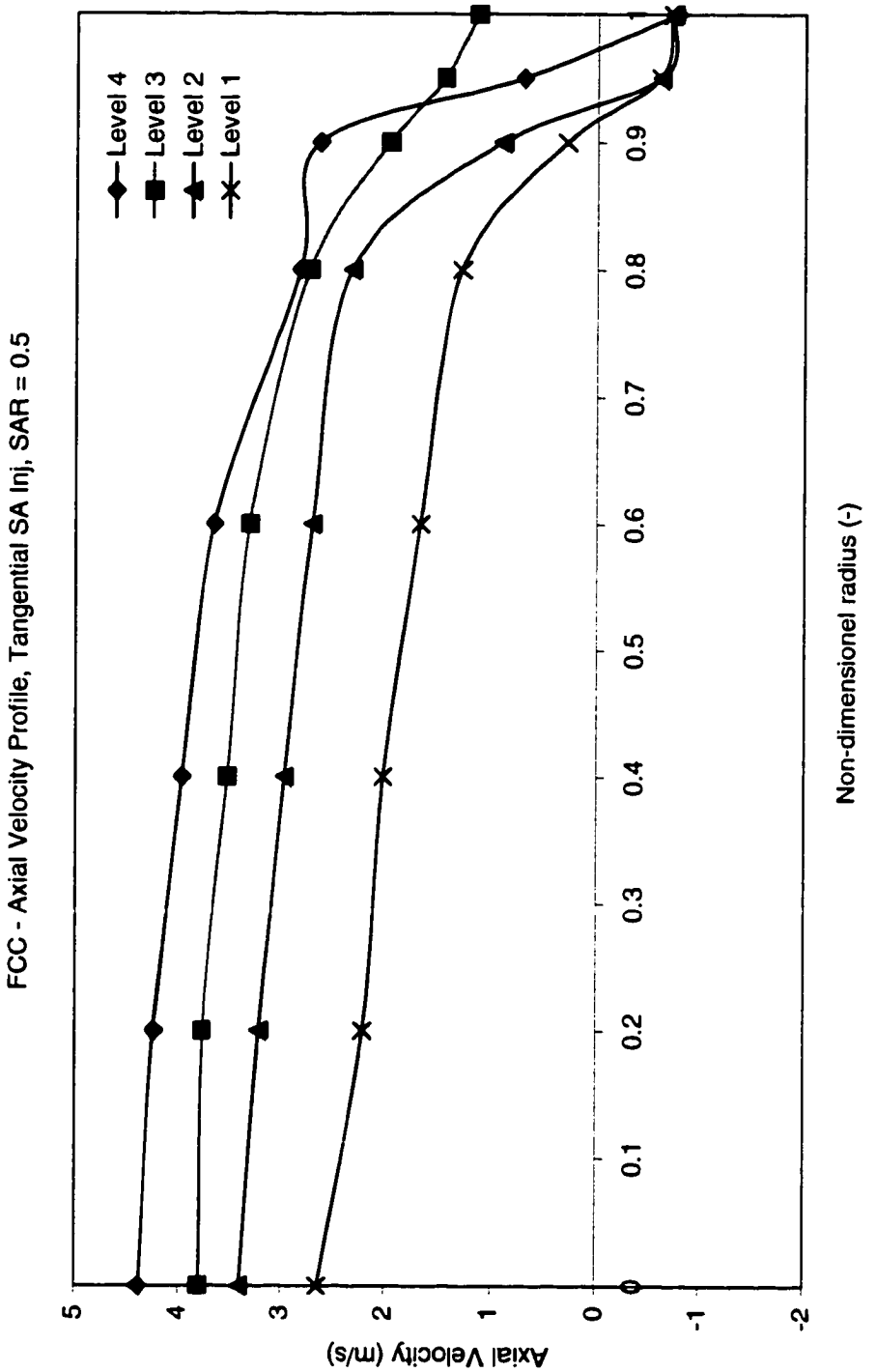

Figure 3.35. Axial development of particle axial velocity profile, SAR = 0. 5, Tangential SA injection from level 2, Uo = 3 m/s, Gs = 18 kg/m²s

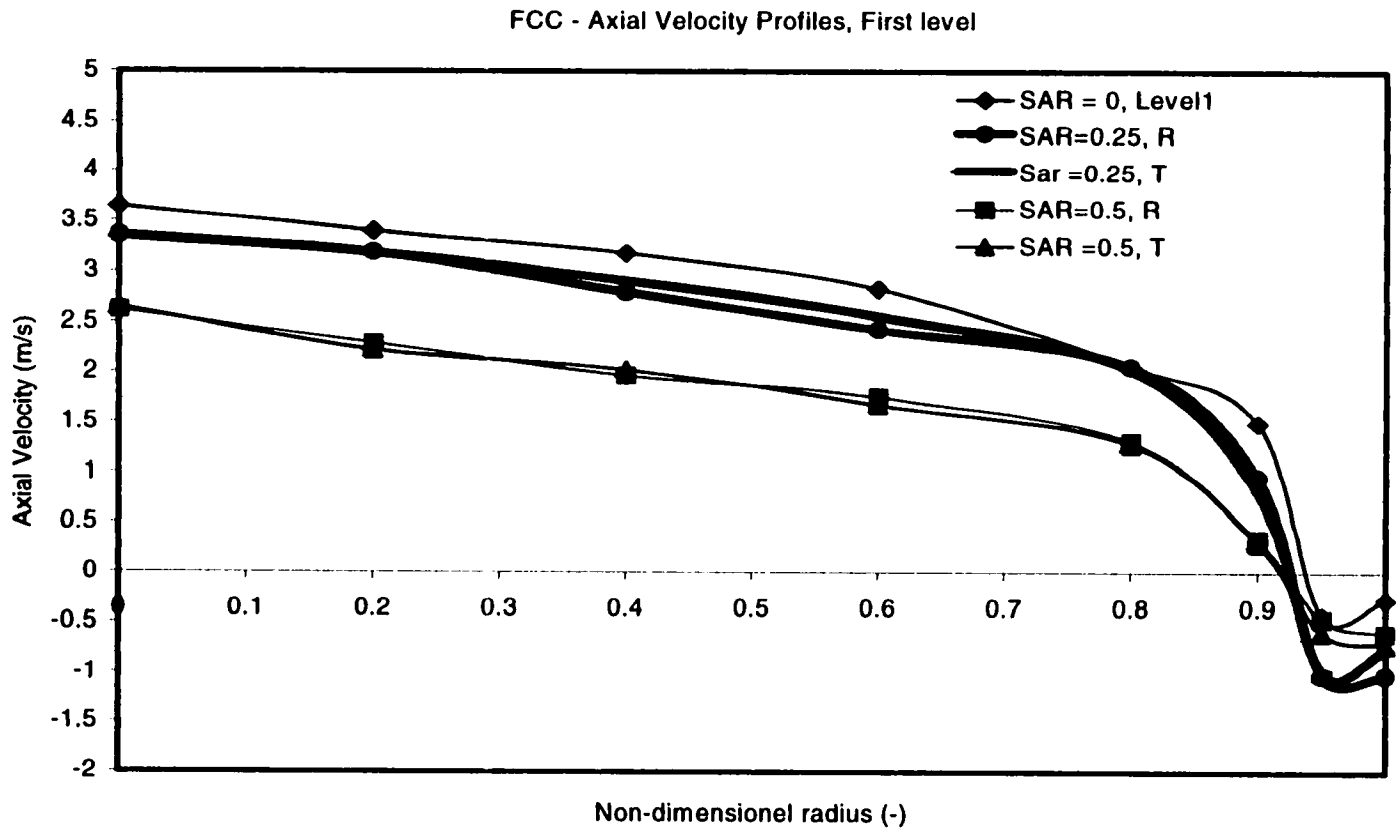

Figure 3.36. Radial profile of particle axial velocity for various SAR and mode of SA injection at the first velocity test section (52 cm above distributor plate, 68 cm below SA port) Uo = 3 m/s, Gs = 18 kg/m²s. SA injection from the second level (120 cm above the distributor plate).

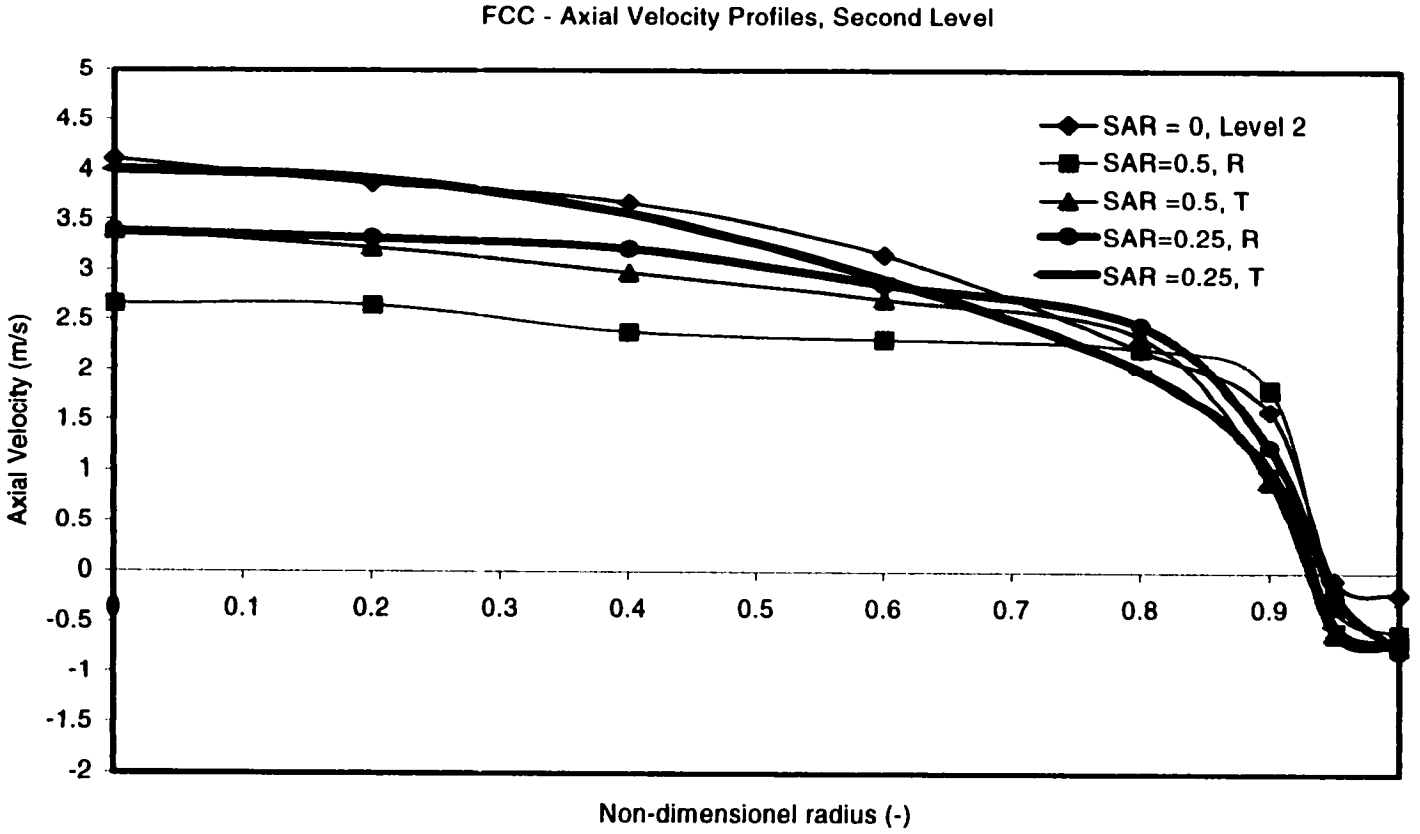

Figure 3.37. Radial profile of particle axial velocity for various SAR and mode of SA injection at the second velocity test section (93 cm above distributor plate) Uo = 3 m/s, Gs = 18 kg/m²s. SA injection from second level (120 cm above the distributor plate).

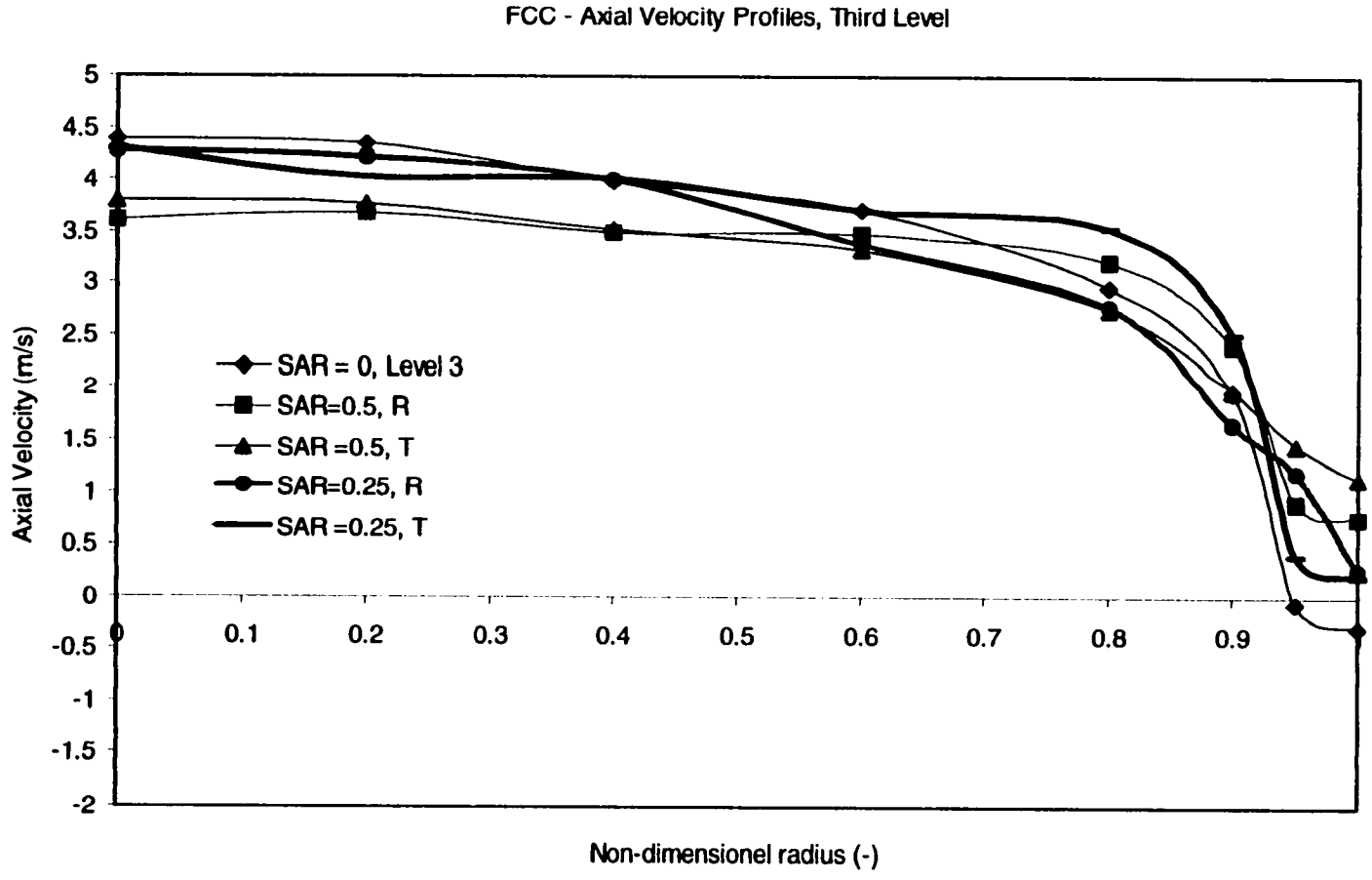

Figure 3.38. Radial profile of particle axial velocity for various SAR and mode of SA injection at the third velocity test section (126 cm above distributor plate) Uo = 3 m/s, Gs = 18 kg/m²s. SA injection from second level (120 cm above the distributor plate).

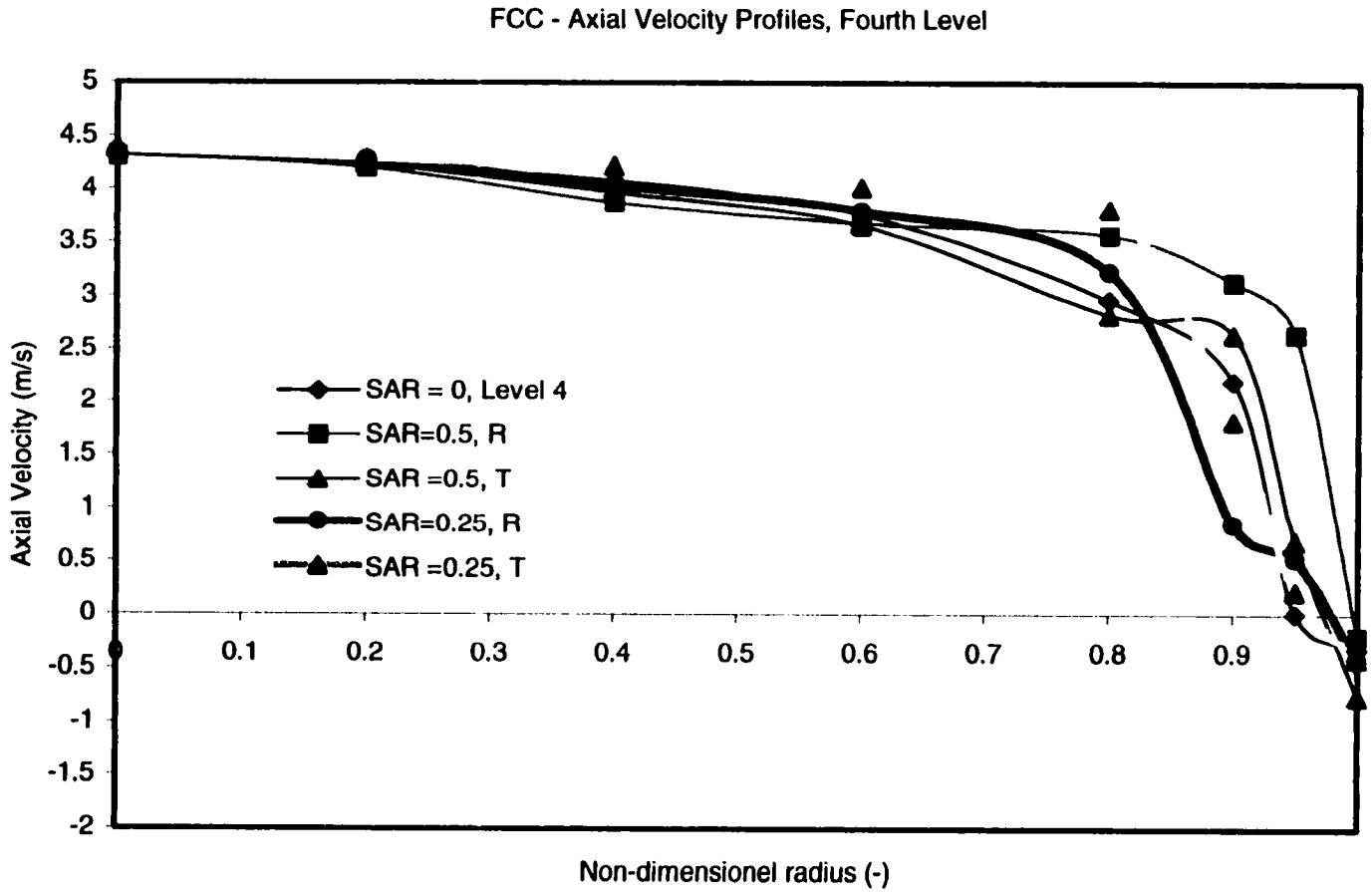

Figure 3.39. Radial profile of particle axial velocity for various SAR and mode of SA injection at the fourth velocity test section (182 cm above distributor plate) Uo = 3 m/s, Gs = 18 kg/m²s. SA injection from second level (120 cm above the distributor plate).

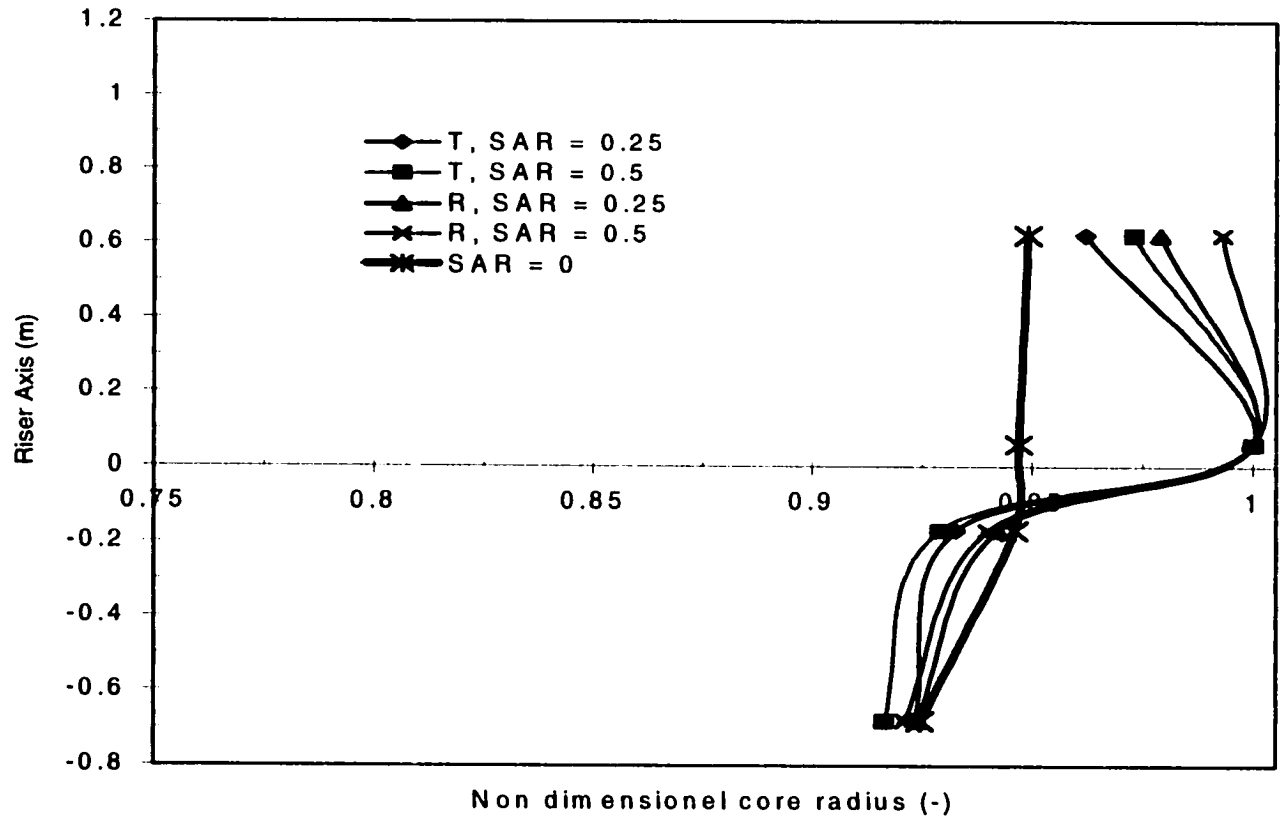

Figure 3.40. Axial development of non-dimensional core radius for various operating conditions FCC particles, SA injection from 1.2 m above the distributor plate. Gs = 18kg/m²s.

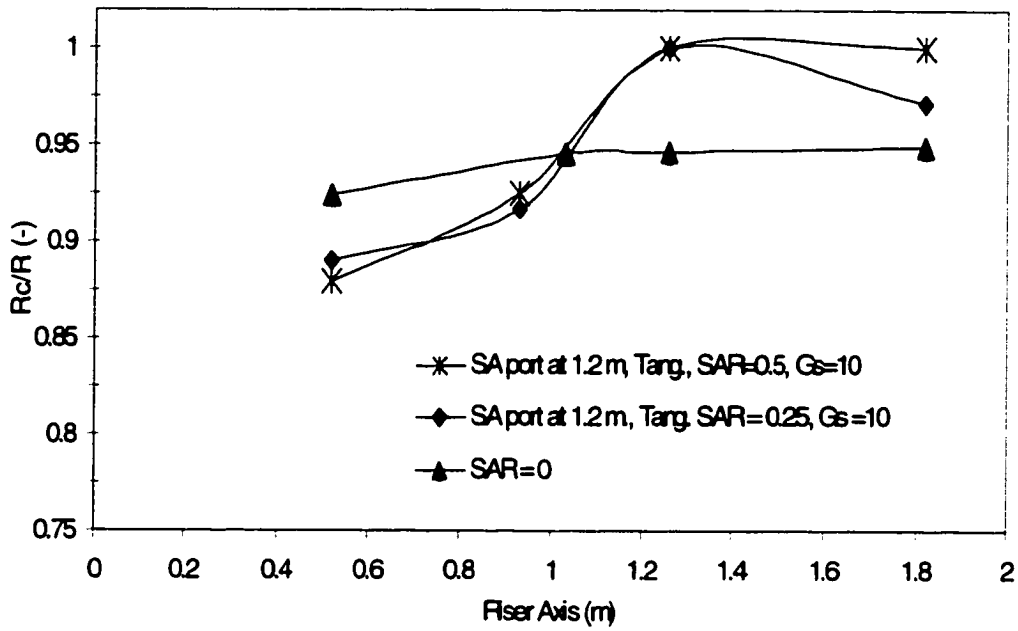

Figure 3.41. Effect of secondary air ratio on the core radius development for sand particles.

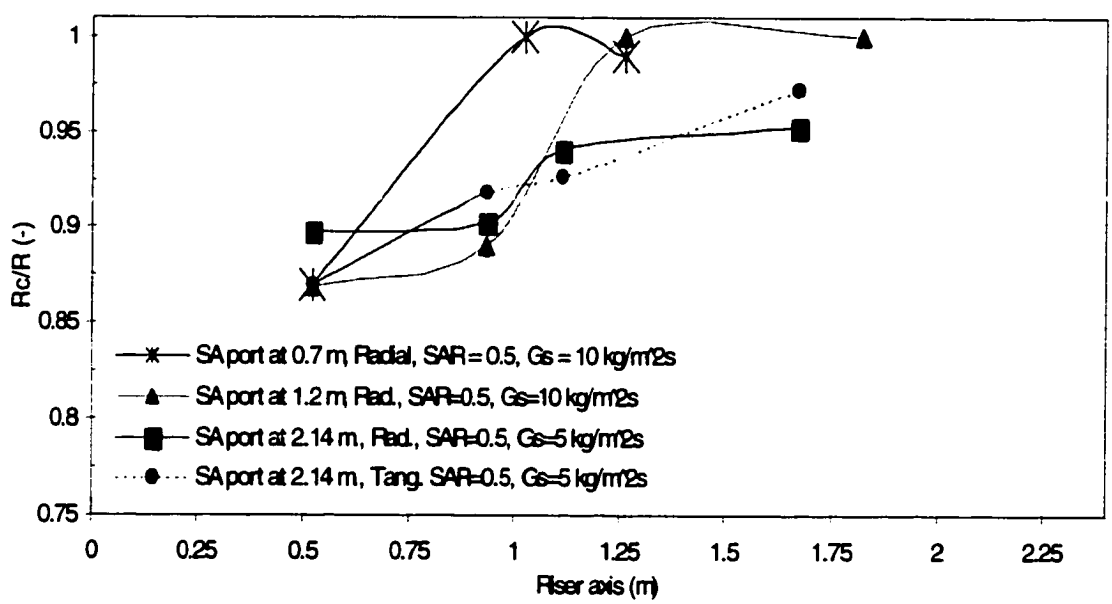

Figure 3.42. Non-dimensional core radius for various operating conditions for sand particles. Effect of secondary air ratio

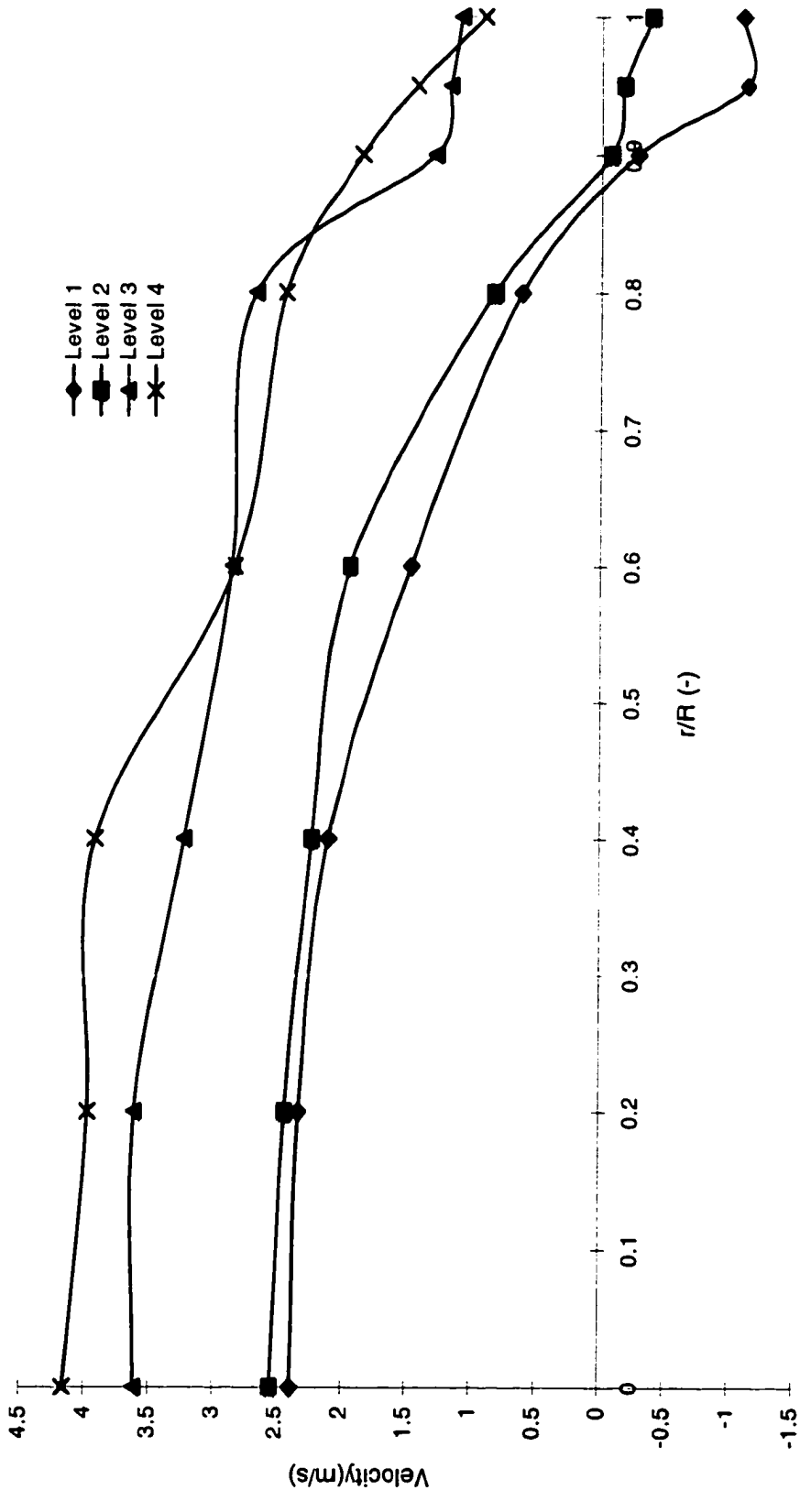

Figure 3.43. Axial development of particle axial velocity profile for sand particles. SAR =0.5. Tangential SA injection from second level (1.2 m above distributor plate). Gs = 5 kg/m²s, Uo = 5 m/s

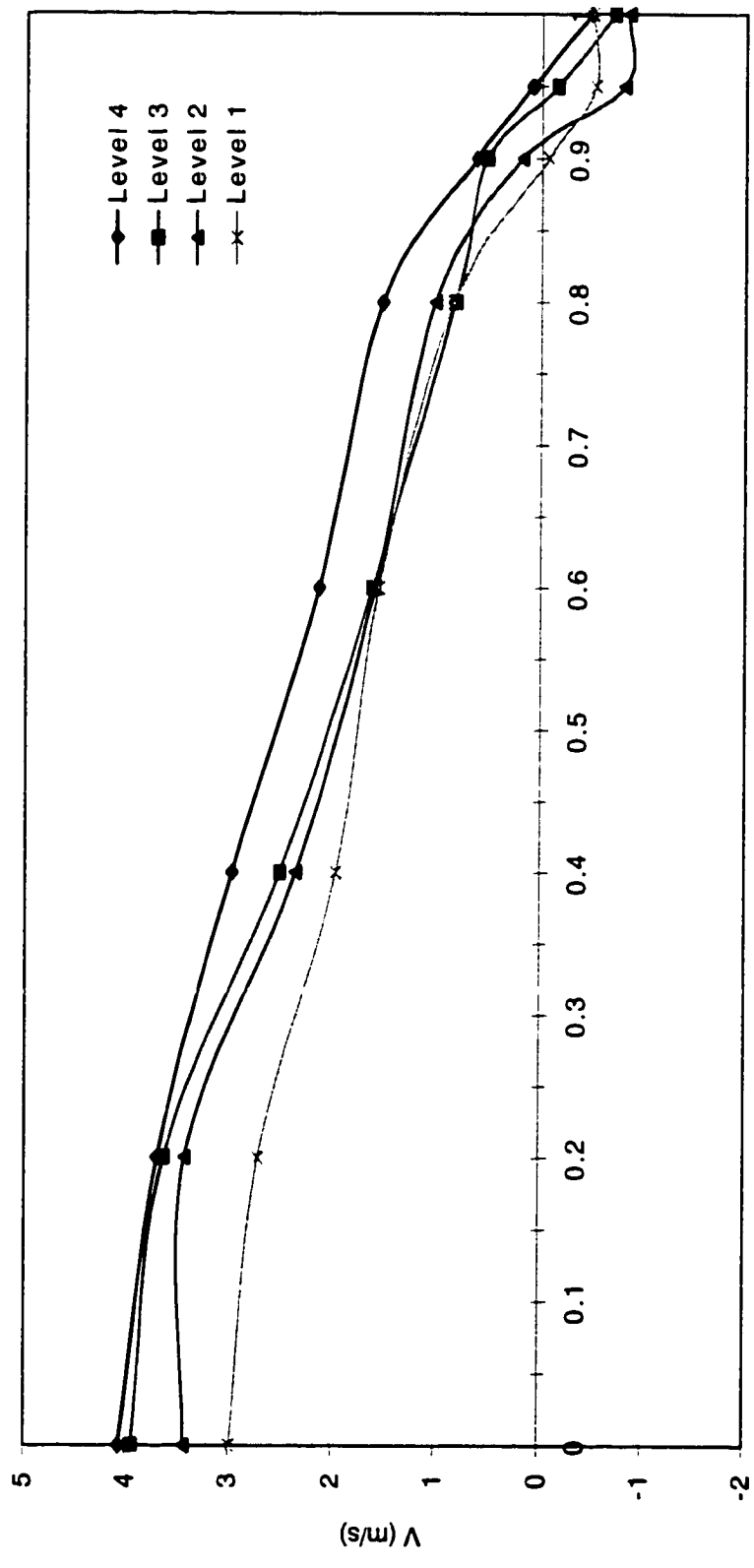

Figure 3.44. Radial profile of particle axial velocity at various axial locations along the riser for sand particles. Radial injection of SA from 2.14-m above the distributor plate. SAR = 0.25, Gs = 5 kg/m²s

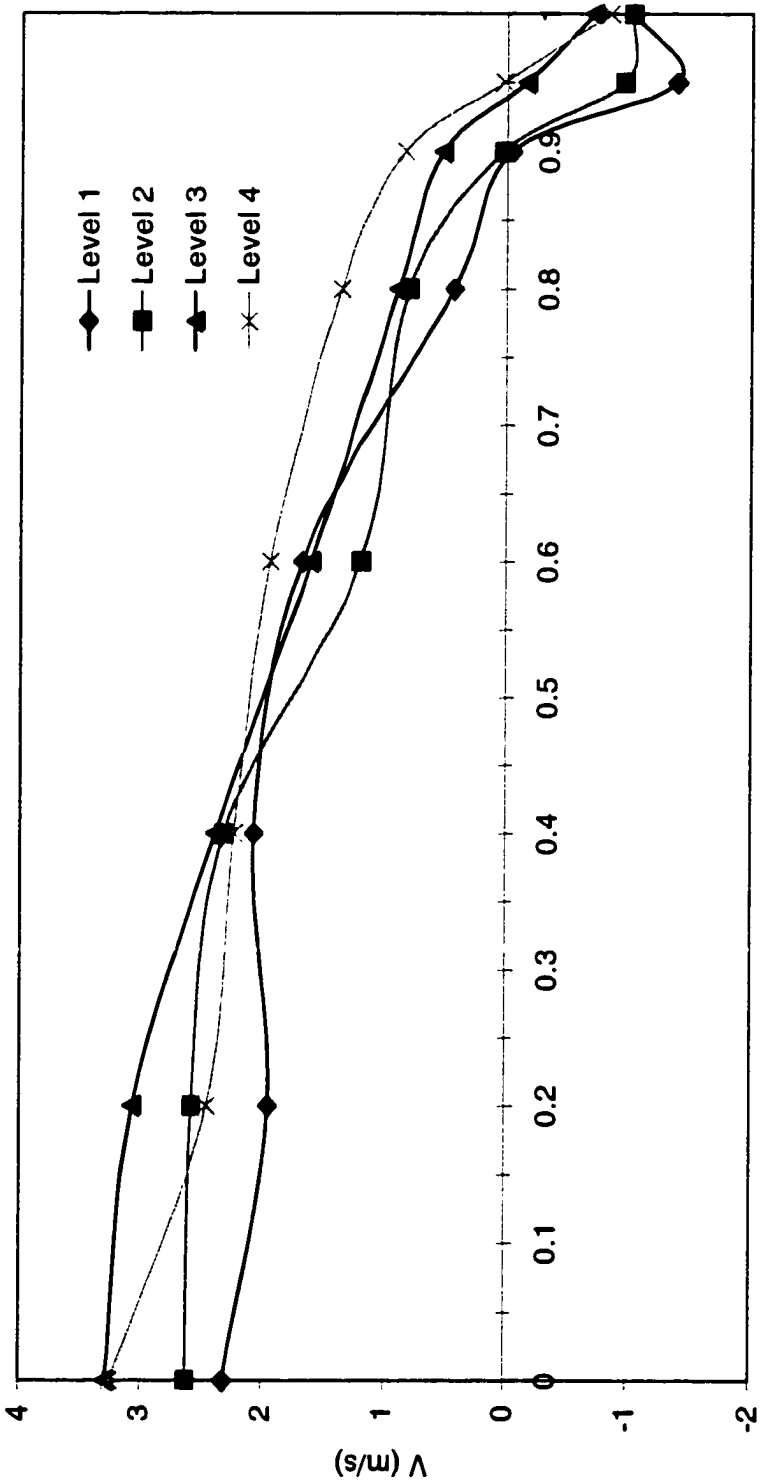

Figure 3.45. Radial profile of particle axial velocity at various axial locations along the riser for sand particles. Radial injection of SA from 2.14-m above the distributor plate. SAR = 0.5, Gs = 5 kg/m2s

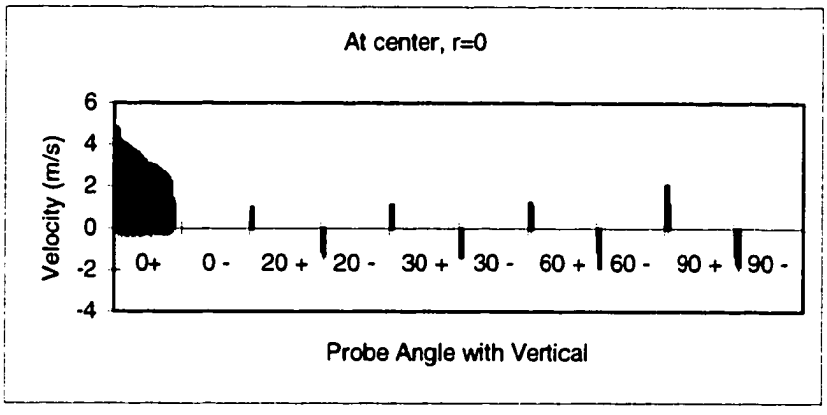

Figure 3.46. Favored particle direction at the center of the riser.

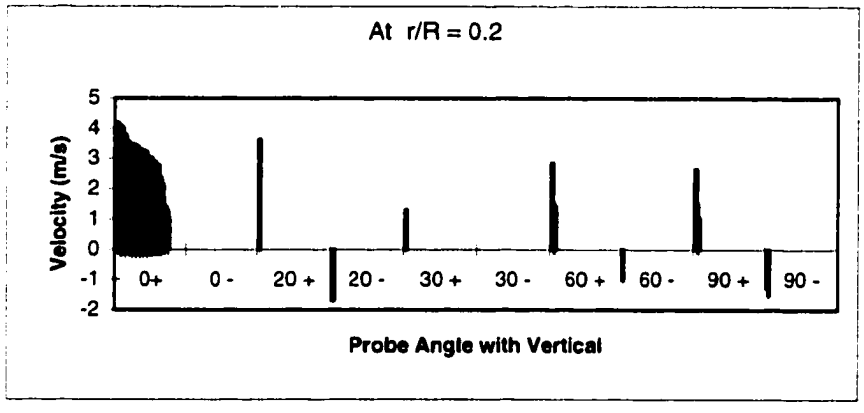

Figure 3.47. Favored particle direction at r/R = 0.2

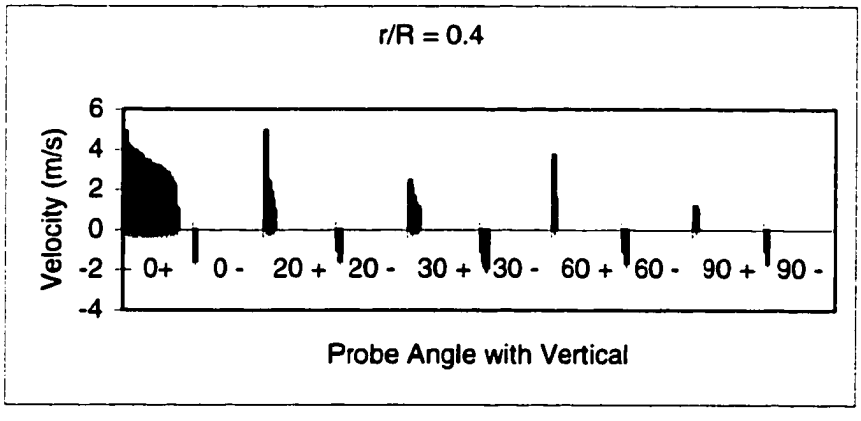

Figure 3.48. Favored particle direction at r/R = 0.4

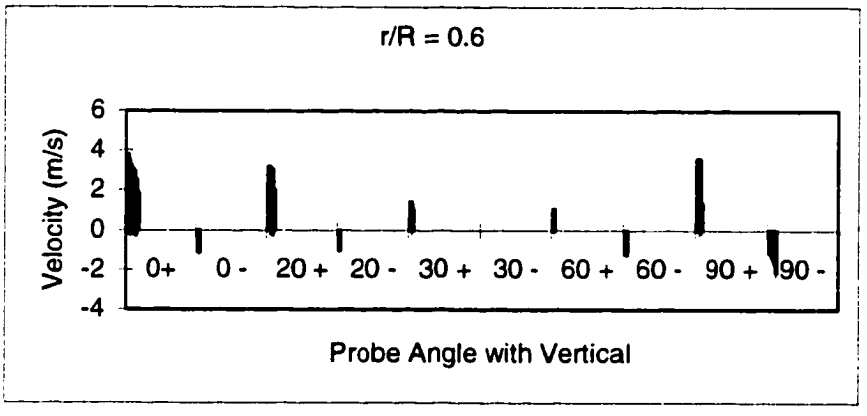

Figure 3.49. Favored particle direction at r/R = 0.6

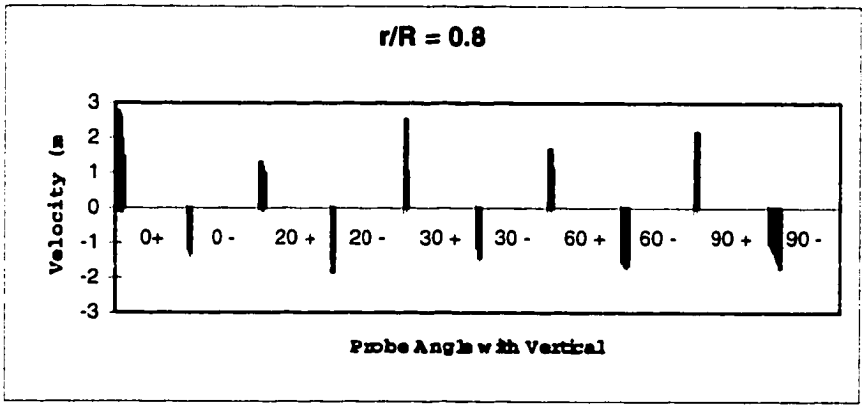

Figure 3.50. Favored particle direction at r/R = 0.8

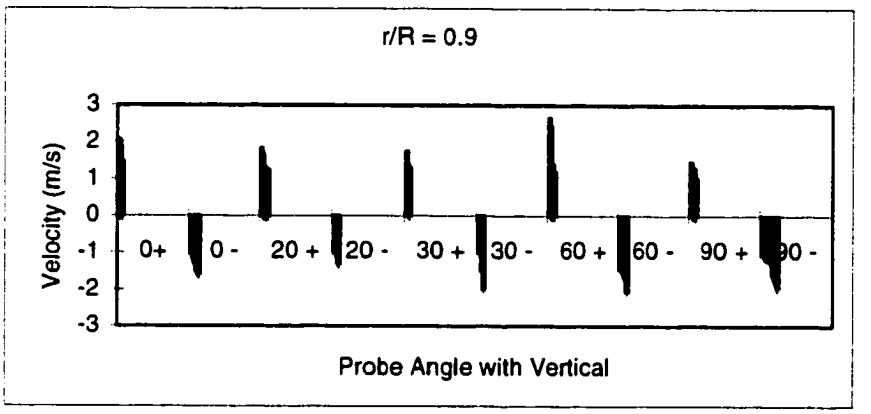

Figure 3.51. Favored particle direction at r/R = 0.9

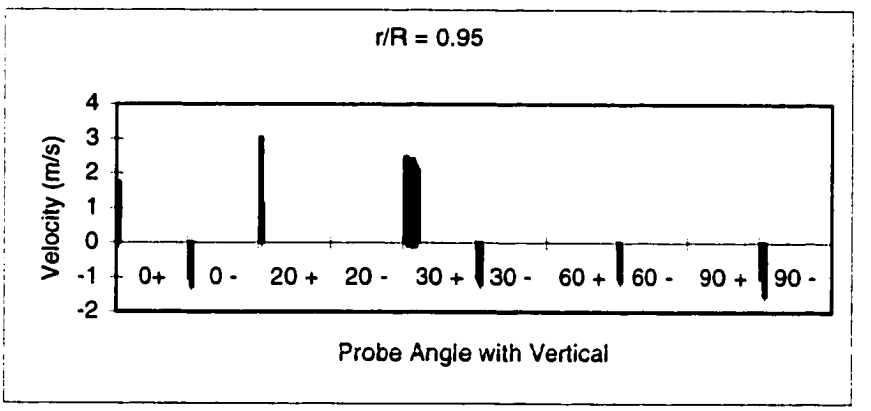

Figure 3.52. Favored particle direction at r/R = 0.95

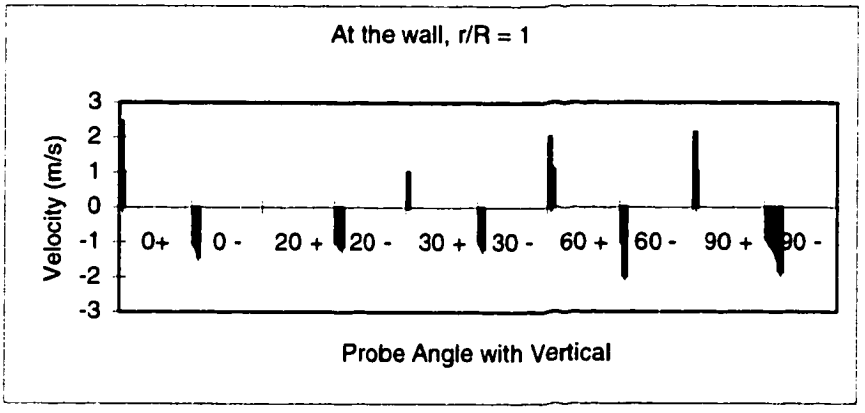

Figure 3.53. Favored particle direction at the riser wall r/R = 1

Figures 3.42-3.48. shows the angular variations in the favored particle path for various radial locations. SA was injected from the first level (70 cm above the distributor plate). Velocity measurements are from 38 cm above SA port. Sand particles, SAR = 0.5, Gs = 5 kg/m^{2}s.

Chapter 4

Gas- Solid Flow Modeling in CFB Risers

This chapter is composed of a brief overview on the present methods used in prediction of two-phase gas-solid flow behavior in CFB risers. Turbulent structure of the gas-solid flow and particle turbulence interactions is discussed briefly prior to the detailed presentation of the proposed mathematical model. Following the model validation section, the chapter concludes with comparisons of the results produced from the proposed model with the experimental data in open literature.

4.1 Overview of Gas-Solid Flow Modeling

The gas and solids flow structure in CFB risers is inherently very complex. The complex nature of the flow, combined with superior benefits obtained from fluidization columns, proposes a challenge towards understanding the flow behavior, and modifying it for specific targets. However, there are some serious difficulties associated with the experimental research on industrial risers. These difficulties usually arise from the high-temperature/highly-turbulent operations inside the columns, which are typically very large in size. Therefore, the experimental work towards understanding hydrodynamics of gas-solid riser flow are usually carried out in small-scale cold beds that are scaled down models of industrial risers. The experimental data gained from smaller scale beds, then, may be used for obtaining approximate correlations to describe the relations between the flow variables and the riser parameters. These approximations, thus, may be used with proper scale ups to describe the flow behavior in large-scale risers.

Over the years, many hydrodynamic models have been proposed to describe the relationship between the riser flow parameters such as solids holdup, particle mass flux, gas-particle velocity fields, etc. Harris and Davidson (1994) classified

them into 3 categories depending on the methodology and extent of the models; *Type I* models are those that predict axial solids suspension density only. *Type II* models (known as core-annular and clustering annular models) characterize both axial and radial variations in solids holdup and velocity profiles, whereas, *Type III* models employ the fundamental equations of fluid dynamics to describe the turbulent gas-solid flow inside risers.

Berruti et al. (1995), in their extensive review paper, mentioned a benchmark testing which targeted to evaluate the performance of some selected hydrodynamic models proposed for riser flows. Ten different research groups were given the physical details of two experimental set-ups and asked to predict the flow properties under a wide range of operating conditions. The experiment set-ups were composed of two risers with dimensions: 14.2 m tall, 0.2 m ID and the other 9 m tall and 0.4 m ID, employing both sand and FCC particles. The results showed that:

- No single model adequately predicted all the conditions and trends in the data,
- Type III models did not show as good agreement with the data as did type II models,
- Some models are good over a limited range of conditions,
- Model of Patience and Chauki (1993) and Puggsley & Berruti (Wong et al., 1995) provided the best overall agreement with the experimental data,
- Best Type III model was found to be created by Gidaspow (Ding and Gidaspow, 1990) which matched some significant trends in the radial mass flux profiles.

The above results alone may state the necessity for further research towards understanding the riser flow. The low level of success obtained from Type III models can be attributed to the complexity of the two-phase riser flow.

The following section covers a brief review of type III models, including turbulent flow modeling in such systems and particle turbulence interactions.

4.2 Turbulent Gas-Solid Flow Modeling

The fundamental difference between type I&II models and type III models is that the latter employs the fundamental equations of fluid dynamics to predict gas-solid riser flow, while the first two type models use empirical relations to predict the flow field. A two-dimensional type III model considers gas and solid phase continuity equations, and momentum balances in both axial and radial directions. The constitutive equations include the drag force and hydrostatic head of both phases in both directions.

The current turbulence models, such as k-ε, k-ω, RSM, etc. are capable in precisely describing the turbulent flow fields in single-phase fluid flows. But the addition of solid phase makes the flow field much more complex. Therefore in the following sections, the emphasis is concentrated on the solid phase modeling efforts.

There are two major approaches in attempting particle phase modeling in turbulent riser flows. Among them, *Lagrangian* approach treats individual particles as separate entities and attempts to track particle paths by using equations of motion of solid mechanics. Whereas, *Eulerian* approach considers both phases as continua, treating the solids phase as a fluid by volume averaging in computational domain. Since the gas phase has a turbulent flow field, both approaches require turbulent modeling for the gas phase. The turbulent flow field in the riser is not only a consequence of the high Reynolds numbers flow of the gas phase, but also due to the remarkable contribution resulting from the interaction of the solids phase (Tsuji, 1984). Therefore the attempts to understand and model the flow field requires with searching the effect of presence of particles on the turbulent flow structure of the suspension.

4.2.1 Particle Turbulence Interactions

In a two-phase riser flow, the existence of solid particles show a major -yet unpredicted- influence on the gas flow field which makes the understanding of

the flow structure more difficult. Recently, remarkable effort is being spent on comprehending the effect of particle phase on the turbulent flow field of the carrier phase. Experiments of Tsuji et al. (1982-84) have shown that presence of particles may either enhance or dampen the turbulent intensity of the carrier fluid depending on the particle properties and solids loading. Yarin and Hestroni (1994) studied the effect of particle size distribution on turbulence intensity of both particle and the carrier phases, and found that the turbulence in a polydisperse system may either be higher or lower than that in a monodisperse one. A decrease in the fluctuation intensity of the carrier fluid and an increase in the velocity fluctuation of the large particles may result in an increase in the fluctuation intensity of smaller particles. Whereas, an increase in the coarse particle size is accompanied by a decrease in spent energy, which leads to an increase in the turbulent intensity of the carrier fluid. These peculiarities of the particle turbulence interactions is seen as one of the important reasons that, type III models were not evaluated as successful compared to the type II models in the previously mentioned benchmark testing.

The loading factor, which is simply defined as the total mass of the particles to the mass of the carrier gas, is seen as another important parameter in the analysis of turbulent two-phase systems. With this definition of loading factor, gas-solid flow systems can be separated into two major groups as *lean* or *dense* flows. In dilute gas-solid suspensions, the particle motion is controlled by the local aerodynamic forces, whereas in dense systems particle-particle collision dominate and control the particle motion (Crowe, 1982). The suspension is referred to as dense or dilute depending on the ratio of aerodynamic response time, τ_a, of the particles, to the time between the collisions, τ_c. The aerodynamic response time is defined as the time required for a particle, released from rest in a flowing stream, to achieve 63% of the free stream velocity, when viscous drag forces are the only forces acting on the particles. This definition also requires that the particle velocity be low enough to assume Stokes flow (Crowe, 1982).

The aerodynamic response time of a rigid sphere is given by Crowe et al. (1982) as:

$$\tau_a = \frac{\rho_p d_p^2}{18\mu} \qquad (4.1)$$

with this formulation, if $(\tau_a/\tau_c)<1$ then the particle has enough time to respond and assume the local gas velocity value before the next collision. Otherwise the particle motion is considered as under the effect of other particles, suggesting a dense phase flow. In CFB risers, however, both dense and dilute flow can exists simultaneously which makes the predictions a bit more complex than already complex uniform gas-solid flows. (According to the above formulation, the Aerodynamic response time of the FCC and sand particles used in the experimental part of this work are: 0.019 and 0.764 respectively.)

Another important indication referred to in turbulence modulation is the Stokes number, defined as the ratio of the particle aerodynamic response time to a time characteristics of the fluid motion (τ_f). If the flow can be scaled with a mean characteristic velocity U, and a characteristic length scale, L, the Stokes number is expressed as:

$$St = \frac{\rho_p d_p^2 U}{18 \mu L} \qquad (4.2)$$

A small Stokes number (St<<1) indicates that the particles follow the fluid motion, whereas a large Stokes number (St>>1) suggests that the particle motion is unaffected by the carrier flow field.

In modeling efforts, the mass, momentum and energy exchange between the phases is referred as *coupling*. If the flow is considered to be controlled by only the carrier gas, neglecting the existence of particles in the carrier fluid, the system is said to be *one way coupled*. But if the particle loading is high enough so that both of the phases effect each other, then the flow is said to be *two way*

coupled. In case of very high particle loading, where particle-particle collisions is an important source of momentum transfer, such as in a bubbling bed, the flow can be considered as *four way coupled* (Elgobashi, 1994).

A decisive parameter in employing the type of coupling is seen as the volume fraction of solids. Figure 4.1 shows the turbulence modulation map presented by Elgobashi (1994). According to the map, for volume fractions less than 10^{-6} the presence of particles would not effect the carrier phase turbulence. For volume fraction of solids between 10^{-6} to 10^{-3} presence of particles may either enhance or dampen the carrier phase turbulence, depending on the ratio of particle response time to the characteristic time of the fluid (turnover time of the largest eddy). For volume fractions higher than 10^{-3}, typical for CFB risers, particle-particle collisions are considered as effective and the turbulence of the carrier phase can be effected by the oscillatory motion of the particles, suggesting a requirement for two or four way coupling in mathematical modeling.

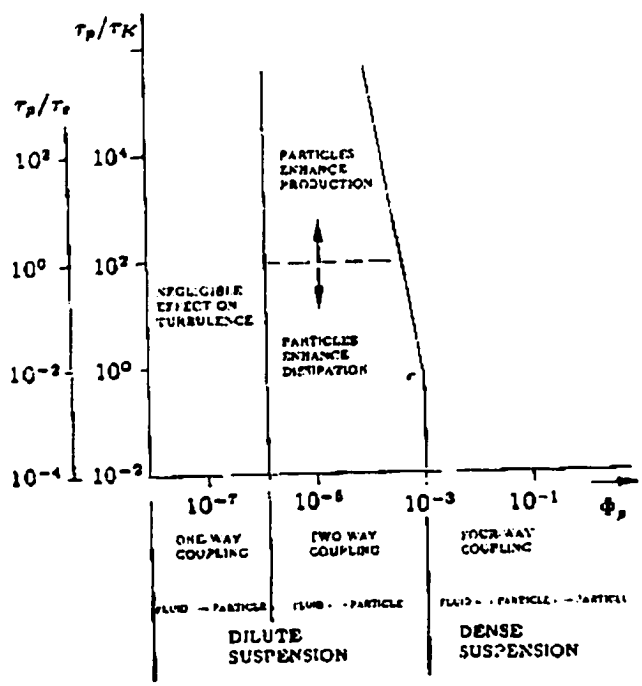

Figure 4.1. Map for turbulence modulation (from Elgobashi, 1994)

The ideal gas-solid numerical model should provide the properties of each particle in the flow field, and the detailed properties of the carrier face at any point in the flow domain. The path, mass and temperature of each particle is obtained by integrating the particle equations using the local velocity, temperature and the density of the carrier gas providing that all the particle-particle and particle-wall collisions are accounted for. In order to be able to gain the above information one must resolve all scales of turbulence, include all particles and influences of all surfaces on fluid, and provide all forces and moments on the particles. Since such an exact model seems well beyond the current computational capability, and the knowledge on two-phase turbulent structure, approximate models are employed for flow prediction purposes.

The type III numerical approaches to gas-solid flows can be categorized in four main groups depending on the modeling of the carrier phase turbulence. These groups are two equation models (Eulerian-Eulerian, Eulerian-Lagrangian), LES (Large Eddy Simulation), Discrete Vortex Simulation and Direct Numerical Simulation (DNS). The difference between the two equation models arises from the difference in modeling of the dispersed phase. The extensive review of LES, Discrete Vortex Simulation and DNS can be found in the literature (Reynolds 1990; Sarpkaya, 1989; and McLaughlin, 1994).

Currently, the two equation models are widely employed due to their 'comparably' lesser computational capacity requirements. Thus, a brief discussion about the two-equation models is presented in the following section.

4.2.2 Eulerian-Lagrangian Models

In this approach, the computational particles are released into the flow field and their instantaneous velocity and position are obtained integrating the particle equation of motion. The particle equation of motion (referred as BBO after Basset-Boussinesq-Oseen) is expressed as Crowe(1982):

$$\frac{dv_i}{dt} = f\left(\rho_f, \rho_p, d, \mu_f, g_i, u_i, \frac{du_i}{dt}, v_i\right) \qquad (4.3)$$

Where, subscripts f and p refer to the fluid and particle phase, u_i and v_i are the local gas and particle velocities, respectively.

In gas-solid flows where the particle diameter is larger than 1μm, the acceleration of the particle is balanced by the viscous drag, added mass, and the Basset history forces. The added mass is the inertial response to the displacement of the surrounding fluid by the particle and the Basset history term represents the diffusion of the vorticity away from the particle as the particle changes its velocity. The BBO equation is only valid for a particle starting at rest relative to the fluid. The complete representation of the equation of motion of a particle should also include the Brownian motion effect, the effect of particle spin (Magnus lift force), and Saffman lift force. But for practical purposes, usually, they are ignored in the analysis of gas solid flows. (Stock, 1996). Tsuji et al. (1985), on the other hand, showed that the Magnus lift force on a particle may be comparable to the drag force when the relative rotational speed between the particle and fluid is high. Collisions between frictional particles with each other and with rough walls could induce high particle spins. The Magnus lift force due to particle rotation may not be neglected in such cases (Liu, 1995)

One of the main advantages of Eulerian-Lagrangian models is the absence of numerical diffusion of the particulate phase (Crowe et al. 1996). Also, this approach preserves the basic nature of the particulate flow and poses no problems with the boundary conditions (rebounds or sticks) provided that the particle rebound information is available. On the other hand, the computational limitations are the basic drawbacks of this method. For instance, in a mixture of 100 μm particles of loading unity, one must track 10^9 particles per cubic meter of the mixture. For this reason grouping concept has been introduced, and instead of tracking the individual particles, a parcel of particles is tracked (Tsuji

et al., 1994). Such models are called Particle Source in Cell models. But, Elgobashi (1994) argues that a significant error can be introduced by using computational particles to represent a packet of real particles.

4.2.3 Eulerian-Eulerian Models

In this approach both phases are treated as continuum with a momentum exchange term between the phases. The transport properties of the particulate phase depend on the local turbulent field of the carrier fluid. This approach uses volume averaging for the phase approximation. The volume average of the property f is defined as:

$$< f >= \frac{1}{V_0} \int_v f dv \qquad (4.4)$$

where V_o is the mixture volume and the integral is over the volume occupied by the phase. Volume averaging requires that the volume dimension be much larger than the particle size, thus the spatial resolution achievable is much larger than the smallest scale of turbulence. Therefore one should not expect that the volume-averaged equations would lead to a very detailed information for the turbulence structure of the carrier phase.

Another disadvantage of two fluid models arises in the wall-dominated flows due to the necessity of an empirical model required to define the boundary conditions at the wall. Also, the incorporation of particle diffusion and viscosity in the two fluid formulations for the particulate phase changes the equations from parabolic to elliptic. This means that the solution to the particle cloud equations becomes a boundary value problem, which is in contrast to the basic nature of the particulate motion. The other main disadvantage of the two fluid models is the need for extra closure equations. Nevertheless, once all the closure schemes are developed and the boundary conditions are set, the solution method is identical to that of single-phase flows other than the coupling interactions between the phases.

For dense flows, most of the two fluid models developed are based on the application of the kinetic theory to the granular flows. Gidaspow (1994) developed an equation for granular temperature, which is the oscillatory velocity of the particulate phase due to particle-particle collisions. This oscillatory velocity is used to predict the effective viscosity of the particle phase. The turbulence of the carrier phase is of no primary concern because particle-particle collisions dominate the flow, not the particle turbulence interaction.

Recent works published in the literature show that the results from the two fluid models are encouraging (Gidaspow, 1994). However, due to the present computational capacity and lack of precise experimental data, type III models still require reliable closure models. Type II models, on the other hand, apparently, have achieved adequate predictions with far less computational time and effort. Next section covers a detailed review of the relations between riser flow parameters, and basics of Type I and Type II models.

4.3 Type I and II Models

4.3.1 Axial Flow Structure: Type I models

The axial variation of cross sectional averaged voidage in the riser was studied by many researchers, Yerushalmi et al. (1976), Kwauk et al. (1980-86), Arena et al. (1988), Bai et al. (1992) are to name a few. Results from type I models often represented in the literature as a plot of radially averaged suspension density (or voidage) versus height graphs. Such profiles are experimentally determined from the pressure distribution along the riser, mostly neglecting the effect of acceleration, weight of the gas phase and friction effects.

Li and Kwauk (1980) observed an "S" shaped profile of axial solids distribution with a dense region at the bottom and a dilute region at the top of the riser, having an inflection point somewhere between the two regions depending on the system parameters. From then on, some other profiles have also been reported. Li et al. (1988) proposed that the axial voidage profile depend on the relative

magnitude of the solids circulation rate to the saturation solids carrying capacity of the carrier gas. Exponential distribution of axial solids suspension density profile can be observed for circulation rates less than the saturation solids carrying capacity; or S shaped or an almost straight line can be observed otherwise.

It appears that the difference between the axial solids holdup profiles may be due to different regimes of fluidization formed in specific risers. Figure 4.2 shows 3 distinct flow regimes in a riser classified by Yang (1988). A dilute phase transport regime (exponential distribution), the fast fluidized regime (S shaped) and dense phase transport regime (straight line) can be observed in the same riser with different operating parameters.

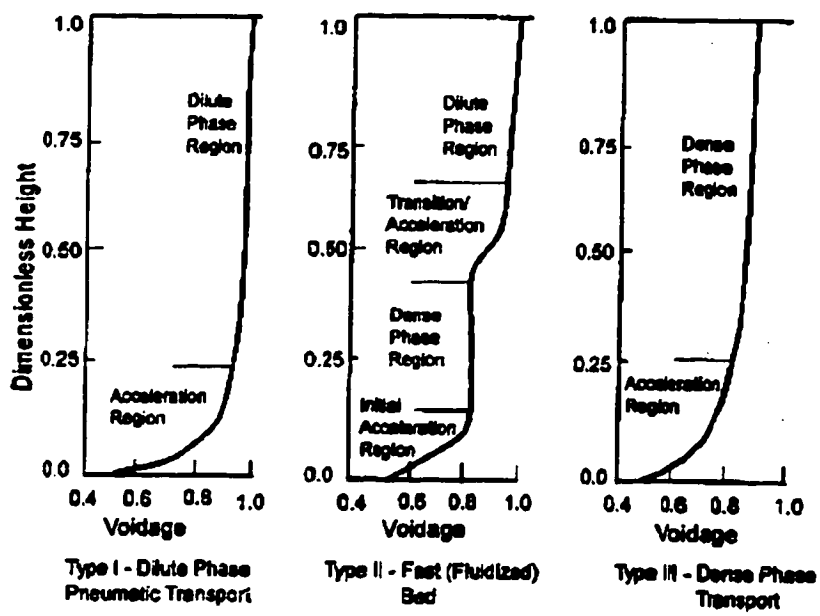

Figure 4.2. Different flow regimes attained in the same riser, from Yang 1988

Bai et al. (1992) observed an increase in solids circulation rate with decreasing superficial gas velocity. Their experiments revealed that increased particle size or density resulted in slightly less dense upper bed but higher solids holdup in

the bottom region. A reduction in bed voidage is also reported in the same work, as the bed diameter is decreased.

Arena et al. (1988) observed a dense phase formation at the bottom of the bed with an increase in the solids circulation rate, while keeping superficial gas velocity constant. The shape of the solids exit port may also influence the axial solids holdup profile, increasing the suspension density in the upper parts in case of an abrupt exit configuration, resulting in a C type solids holdup profile can be expected from such systems (Bai et al., 1992).

Brereton and Grace (1994) noted that the above profiles may also be varied with changes in the axial positions of solids inlet or by injecting secondary air. They showed that feeding the solids from well above the distributor plate could cause an increase in the local suspension density in the vicinity of the solids inlet port. While keeping the total air constant, radial injection of secondary air increased the solids holdup in the bottom portion of the bed where the superficial gas velocity is lower compared to the region above the secondary air injection plane. The extend of the dense phase also increased with increasing height of secondary air injection, suggesting that the height of secondary air injection is an effective parameter for axial solids holdup distribution.

Kwauk et al. (1986) suggested an equation for the calculation of cross sectionally averaged solids holdup for S- shaped profile:

$$\ln\left(\frac{\varepsilon(z)-\varepsilon_a}{\varepsilon^*-\varepsilon(z)}\right)=\left(\frac{-1}{Z_0}\right)(z-z_i) \qquad (4.5)$$

where subscript 'a' and superscript '*' represent the limiting voidage at the dense and lean phases, respectively, 'z_i' is the location of point of inflection in the profile, and 'Z_o', called the characteristic length governs how quickly the top and bottom regions merge into each other and is related to operating conditions and material properties, $\varepsilon(z)$ is the voidage at a distance z from the top of the riser. The above relation predicts that at a fixed solids circulation rate,

increasing superficial gas velocity reduces the cross sectionally averaged solids holdup. One must note here that Equation 4.5 does not consider the secondary air effects. Kwauk et al. (1986), developed another correlation that relates the solids volume fraction to a Reynols number. This new method requires an iterative procedure since their definition of Reynolds number depends on both volume fraction and solids velocity.

Kunii and Levenspiel (1991b) modeled the dilute region of the CFB riser by modifying the freeboard entrainment model originally developed for bubbling fluidized beds. In the modified model, the solids holdup profile is considered as composed of two distinct zones. A lower zone consisting of a constant bulk density and an upper freeboard region where the suspension density decreases exponentially with height. This model seems valid for risers operating on turbulent fluidization regime or for the turbulent bed section of the riser. The equation proposed for the axial solids holdup distribution;

$$\left(\frac{\varepsilon(z) - \varepsilon^*}{\varepsilon_d - \varepsilon^*} \right) = e^{-az} \qquad (4.6)$$

Where ε^* is the limiting voidage at the riser top, which is usually approximated as 0.01 after the experiments of Monceaux et al. (1986), and ε_d is the voidage at the lower dense bed. The model is not predictive since the decay constant 'a' is to be determined experimentally.

Mori et al. (1991) also proposed an empirical correlation to model the average axial properties in a CFB. Their model also based on exponential decay of axial voidage profile. Calculation of the decay constant involves the superficial gas velocity and an experimentally determined constant, which may need to be re-determined for different physical boundaries or operating conditions, thus it can not be considered as predictive.

Yang (1988) developed a pneumatic transport model, and related the particle velocity to the difference between gas velocity and the terminal velocity of a single particle through a friction factor. This model treats the dense and dilute phases separately, dilute phase having a constant voidage throughout. However, Berruti et al. (1995) argues that his correlation underestimates the slip velocities and solids volume fraction.

Matsen (1976), using FCC risers, observed that the ratio of the gas to particle velocity (referred as the slip factor, ψ), was approximately equal to two. The concept of slip factor formulation, became very useful in estimation of cross sectional average values of voidage and particle velocity.

$$\varphi = \frac{U_o / \varepsilon}{v_p} \tag{4.7}$$

Patience et al. (1992) proposed an empirical correlation accounting for the effect of particle characteristics, riser diameter and gas velocity in the slip factor equation (Equation 4.8):

$$\varphi = 1 + \frac{5.6}{Fr} + 0.47 Fr_t^{0.41} \tag{4.8}$$

Where Fr is the Froud number and Fr_t is the Froud number based on the terminal velocity of a single particle. Their experiments have shown that the average slip factor is around 2.6 with a standard deviation of 0.9.

$$Fr = \frac{U_0}{\sqrt{gD}} \tag{4.9}$$

$$Fr_t = \frac{V_t}{\sqrt{gD}} \tag{4.10}$$

Later, Puggsley and Berruti (1996) modified the slip factor equation to fit low solids circulation rates by using a large pool of riser data:

$$\varphi = 1 + \frac{5.6}{Fr^2} + 0.47 Fr_t^{0.41} \qquad (4.11)$$

Using the definition of solids circulation rate and considering that solids density is much larger than that of the gas, they rearranged equation 4.7 to calculate the suspension density as:

$$\rho = \frac{\rho_p}{\left(1 + \frac{\rho_p U_o}{G_s \varphi}\right)} \qquad (4.12)$$

Equation 4.12 predicts that suspension density increases with increasing particle terminal velocity and decreases with increasing superficial gas velocity. It also suggests that higher slip velocities result in high suspension densities which is in conflict with Bai et al. (1992) comments on increased solids circulation rate with decreasing superficial gas velocity.

Berruti et al. (1995) suggested that the slip factor correlation provides a good check on experimental mass flux measurements. If the calculated slip factor, based on the experimental data, approaches unity then either the solids mass flux is overestimated or the system is operating under pneumatic transport regime.

Early experiments investigating the radial profile of flow profiles have shown that radial variation of properties such as suspension density and particle velocity is far beyond being constant. Therefore, it became evident that an excessive amount of information may be neglected by regarding only the cross sectional averages of the flow properties. Thus, more attempts were made to predict the radial distribution of flow properties in risers and one and a half and two-dimensional models were proposed to account for the radial variations in flow properties.

4.3.2 Radial Flow Structure: Type II Models

Results of the experiments (Hartge et al., 1988), for particle velocity and mass flux measurements showed that radial variation in both particle axial velocity and holdup profiles is not only non-uniform but also highly irregular. The averaged values showing a high velocity upward flow in the central region, a comparably slow downward motion around the walls and a transition between the two distinct regions, suggesting a parabolic distribution of properties along the radius.

Lim et al. (1995) published an extensive review covering the particle flow patterns in riser flows. According to their research, Van Breugel et al. (1970) was the first to report a parabolic radial solids flux profile in a riser. Gajdos and Bierl (1978) appears to be the first to present radial voidage profiles showing high voidage in the center region and much lower voidage close to the wall. From then on, many others have confirmed this non-uniformity. Bed voidage is high and relatively uniform in the central region extending out to about 70-85 % of the radius after which the solids concentration increase dramatically towards the wall (Lim et al., 1995). Increasing solids circulation rate and reducing the superficial gas velocity both had the same effect: increased local solids circulation rate, and a steeper solids flux profile along the radius.

Zhang et al. (1991) suggested a universal radial profile for radial distribution of bed voidage for any time averaged solids concentration. This was supported experimentally for various operating conditions such as in experiments with different particles, under varying superficial gas velocities and varying solids circulation rates in two different risers. They proposed an empirical correlation for the radial distribution of voidage, suggesting that the voidage profile depend only on the cross sectional average voidage, ε_{ave}.

$$\varepsilon = \varepsilon_{ave}^{0.19+(r/R)^{2.5}+3(r/R)^{11}} \qquad (4.13)$$

At a first glance, such a universal profile might seem correct since the effect of all other parameters could implicitly be accounted for in the average voidage term. However, findings of Bodelin et al. (1994) reveal that the radial profile may also depend on the particle size distribution. Also, Berruti et al. (1995) mentioned that equation 4.13 underestimates the mass flux in the centerline due to the low value of the exponent assigned. Patience and Chauki (1995) approximated the centerline density to the average void fraction raised to the 0.4^{th} power, i.e.:

$$\frac{\varepsilon_{ave}^{-0.4} - \varepsilon_r}{\varepsilon_{ave}^{-0.4} - \varepsilon_{ave}} = 4(r/R)^6 \qquad (4.14)$$

Using a solid sampling probe, Monceaux et al. (1986) observed 'similar profiles' of solids mass flux in the fully developed region of the riser. The existence of similar profiles is also supported by the experiments of Rhodes et al. (1992) and became one of the reliable approximations used in fully predictive two-dimensional models. They showed that at a given gas velocity, radial profiles of 'reduced' mass flux, the ratio of local mass flux over the cross sectional average, changed very little with changes in mean solids flux in the riser. They also suggested that the thickness of the annular region was independent of the solids mass flux but only a function of the superficial gas velocity, and reported that the following equation with proper constants fits their experimental data very well to predict the radial profile of local solids flux.

$$\frac{G_r}{G} = a\left[1 - \left(\frac{r}{R}\right)^m\right] + b \qquad (4.15)$$

Performing experiments in two different risers, (0.152 and 0.305 m ID), they also noticed that, at higher superficial gas velocities the profile became less parabolic in shape and the thickness of the annulus decreased. Larger diameter riser gave flatter profiles, and the relative thickness of the annulus was smaller than that observed from the smaller diameter riser. Actual thickness of the

annulus region, where the solids descend along the wall region, reported to be 'comparable' in both risers at a given gas velocity. This may suggest that the reverse flow is predominantly a wall effect. Also, they noted that similar solids profile might confidently be assumed for solid fluxes within 10 to 70 kg/m^2s range. Their experiments also showed that the particle flux at the center might show a local minimum for small solids fluxes, even lesser than the upward flux around the wall region. Suggesting that in core-annular approximations of very lean flows, a special care should be given to the annulus region, since the average particle velocity in the annulus might not always be downwards, and the particles tend to concentrate in the wall region even for very lean flows.

Yang et al. (1991) showed that radial profile of particle velocity might show significant variations along the riser axis. Also, using the findings of Yang et al., Berruti et al. (1995) deduced that if a universal radial solids volume profile exists, and the particle velocity profile changes with height, then the mass flux profile must also change with height. The dependence of particle flux profile on the height might be due to the combined effects of both wall factor and particle size distribution.

The effect of particle size distribution on the solids flux profile was studied by Bodelin et al. (1994). They noticed that the suspension descending along the wall contained a higher fraction of coarse particles, and that the radial particle size distribution was independent of the solids loading. Therefore, the suspension in the upper part of the riser might be composed mostly of the smaller size particles, which follow the fluid motion due to their smaller inertia, suggesting a decrease in the thickness of the annulus, or sometimes a diminished down flow in the upper regions of the riser.

Most of the Type II models use the annular approach as the basis of the model, in which the fluctuating nature of the flow is ignored. Brereton et al. (1993) proposed an intermittency index to account for the variations in the solids concentration. The index is defined as the ratio of the standard deviation of the density fluctuations at a given point to the standard deviation of density

fluctuations for fully segregated two phase flow having identical time mean density at the same point. The intermittency index varies between zero, when there is a uniform local suspension, and unity, when regions of gas alone alternate with clusters of voidage equal to the loose packed voidage. A higher value meaning more segregated and time-varying flow structure. Their related experiments have shown that the index varies between 0.1 to 0.6, indicating a neither uniform nor completely segregated flow exists in the riser. The radial variation of intermittency index showed lower values in the core, suggesting more uniform and stable flow in the central region, and higher values around the wall region indicating the time varying and fluctuating suspension density in the wall region. The high intermittency index in the wall region may also be seen as a proof of quickly forming and dispersing clusters, as also observed by Zhou et al. (1995), in a riser with rectangular cross section.

Flow visualization techniques such as high speed video cameras, fiber optical image probes (Li et al.,1991a & b), laser sheet technique (Horio & Kuroki 1994), two dimensional column (Bai et al., 1991) show that there exist at least two distinct solid phases in a riser flow. One phase is the dispersed individual solids and the other phase may be described as the groups or pockets of combined particles that behave like a larger particle of lower density. The latter phase is usually referred as the cluster phase. Li et al. (1991a) showed that the clusters have irregular shapes with varying sizes. They also noticed a strand of clusters in the center transforming into a 'near sphere' shape swarms near the wall, suggesting that the cluster motion may not always be in vertical direction. Most clusters have U-shapes with a round nose facing downwards and particles are shed continuously from the periphery.

Different authors used different terminology, such as particle streamers, strands, ribbons, or dense packets to describe particle grouping. Grace and Tout (1979) suggested that clusters might originate due to instability of gas-solid transport, whereas Li and Kwauk (1980) suggested the trend of energy minimization in natural processes, and Lim et al. (1995) indicated particle-wake

interactions as the reasons for particle grouping. Both stability and energy considerations suggest that particles tend congregated forms rather than remaining dispersed homogeneously. The wake theory, on the other hand, assumes that particles are drawn into the low-pressure wake region behind other particles. Kan (1991) modeled the cluster motion inside riser by using energy minimization principle. He measured velocities of down flowing clusters and revealed that downward clusters motion is much faster than that of dispersed particles.

Nakamura and Capes (1973) proposed that for vertical solids transport, when the gas velocity is decreased or the solids loading is increased, approaching choking condition, the observed internal circulation of solids could be modeled as annular flow. However, Berruti et al. (1995) argues that the proposed model was unable to predict the experimentally determined annulus thickness. Later, Horio et al. (1988) modified Nakamura and Capes model and included cluster voidage and cluster terminal velocity both to be estimated from the experimentally determined annulus thickness. Ishii et al. (1989) refined the clustering annular model by presenting a system of material and momentum balances for both phases, including a wall-solid interfacial shear stress.

A major shortcoming of clustering annular models is that, in riser flows the clusters, instantly forming and dispersing, show a very dynamic behavior. The size, voidage, and the location of the clusters, therefore are irregular parameters that might not be generalized. The cluster voidage, for example, sometimes modeled as equal to that of minimum fluidization voidage (Yarushalmi et al., 1991), or minimum bubbling voidage (Bai et al., 1989). But Wu et al. (1991), have shown that cluster voidage might not be constant and that there might be a range of voidage inside the clusters. On the other hand, the core annular approximation of riser flow has received considerable attention and is constantly being refined.

Many of the early core-annular models including Hartge et al. (1988)'s model required experimentally determined voidage fractions and particle velocities as

input parameters. Later, Rhodes et al. (1990) presented a core annular model, which required average solids flux in the core and the core radius as the input parameters. Major limitations of these early models are that they require experimental data as input parameters therefore they are not predictive. In addition, certain approximations such as average voidage in the annulus being equal to the minimum fluidization voidage and the downward solids flow velocity being equal to the particle terminal velocity do not in general reflect the experimental findings.

There have been several fully predictive core-annular models published in the literature; Wong et al. (1992), Puggsley and Berruti (1995-96), Koenigsdorff and Wherter (1995), Patience and Chauki (1995), and Puchyr et al. (1997), all of which account for the radial variations in solids velocity and holdup profiles. A common assumption for predictive core annular models is that the gas phase motion in the core region is modeled as plug flow. This assumption does not allow any net gas flow between the core and the annulus. Also, calculation of core-annulus interface appears to be an important aspect of predictive core annular approximations.

Patience and Chauki (1993), proposed a semi empirical expression for calculating the core radius based on the gas phase hydrodynamics;

$$\left(\frac{r_c}{R}\right)^2 = \frac{1}{1+1.1Fr(Gs/\rho_s U_0)^{0.083Fr}} \qquad (4.16)$$

The above equation was developed by regressing the value of core radius determined as best-fit parameters for the experimentally generated gas phase residence time distribution curves. In the above formulation, the core radius is assumed to be the location of net zero gas velocity, whereas majority of the core annular models locate the core radius depending on the solid phase hydrodynamics. Also, Puggsley and Berruti (1996) argue that Equation 4.16 underpredicts the core radius when defined as the radial location of zero net particle velocity.

Wherter (1994) presented an empirical correlation for the thickness of the annulus (δ) as a function of the height above the riser inlet (z) and riser hydraulic diameter (D_t);

$$\frac{\delta}{D_t} = 0.55\,\mathrm{Re}_t^{-0.22}\left(\frac{H_t}{D_t}\right)^{0.21}\left(\frac{H_t - z}{H_t}\right)^{0.73} \qquad (4.17)$$

The above correlation gives good agreement with a large pool of experimental data from both industrial scale and laboratory scale rigs. A major shortcoming of the above equation is discussed by Puggsley and Berruti (1996), and seen as its insensibility to the changes in the solids mass flux. Whereas, findings of Rhodes et al. (1992a) on similar profiles of solids flux support the validity of the above approximation. They measured negligible changes in the reduced solids mass flux profile with varying external solids flux. Later, Puchyr et al. (1997) used an average form of the above equation in his fully predictive model. Also, Puggsley et al. (1997) used the above equation to model the exit region of his riser. Both Puggsley (1996) and Puchyr (1997) models, assume that the core radius in the fully developed region is constant, and independent of the height along the riser.

Bai et al. (1995) related the core radius to the cross sectionally averaged voidage and proposed the following empirical formulation to locate the core radius, suggesting that the location of core radius is a function of cross-sectionally averaged voidage, only.

$$r_c = (\varepsilon_{ave})^{-0.62} \qquad (4.18)$$

Most of the previously proposed type II models, except Puggsley & Berruti model, did not consider the existence of primary or acceleration region as can be seen from Table 4.1. And, to the author's knowledge, not a single type II model has been published in the open literature to account for the effects of secondary air. The type I models, on the other hand, either used a constant voidage profile

below the secondary air injection ports (Kunii and Levenspiel) or used a modified form of exponential decay approximation of Kunii and Levenspiel (Choi et al., 1994). The next chapter covers the details of the proposed type II model of this work that accounts for SA injection, also

Parameter	Berruti&Kalegorakis	Bai et al	Rhodes et al (1990)	Puggsley&Berruti (1996)	Dieo et al ( )
Particle Velocity in annulus	Constant, U_t	Calculated	Constant	Model output	Constant
Air flow in the annulus	No	Carrier Phase is not Modeled	No net airflow	No net airflow	Carrier Phase is not Modeled
Cluster modeling	Dispersed particles	Dispersed particles	Dispersed particles	Dispersed particles	Dispersed particles
Voidage in the annulus	Constant (ε_{mf})	Model output	Model output independent of riser height	Model output independent of riser height	Model output, a function of riser height
Upward solids velocity	Slip by Vt	Model output	Slip by Vt	Slip by Vt	Slip by Vt
Acc. Region modeling	No	No	No	Yes	Yes
Model phlosophy	Core-annular	Energy Minimization	Core annular	Core annular	Core annular
SA Modeling?	No	No	No	No	No
Fully predictive ?	No	No	No	Yes	No

Table 4.1. Assumptions used in riser flow modeling from some selected type II models

Chapter 5

Mathematical Model

The present model considers the CFB riser composed of the 3 distinct regions. Namely, *fully developed* region (the fast bed), *primary region* (acceleration region), and *secondary air effective* region. The fully developed region starts from the extent of SA effective zone and occupies the region up to the top of the riser. The primary region is defined as the region that starts from the distributor plate and ends either at the boundary of SA effective region, or diminishing particle acceleration if SA port is located above the acceleration region. The secondary air effective region is located as a transition zone between the primary and fully developed regions where the SA jets are considered as effective on the flow hydrodynamics.

The *base model* includes the fully developed and primary regions while the secondary air modeling modifies the base model depending on the mode of injection. Therefore, in the following sections the details of the base model is presented first, prior to the presentation of secondary air modeling.

5.1 Base Model (SAR = 0)

The proposed base model assumes that the CFB riser to be axially composed of two regions: an acceleration region at the bottom of the riser, where the re-injected solids accelerate to a fully developed velocity, and a fully developed flow region extending from the end of the accelerating zone up to the riser exit. The main reason behind the two-region consideration is that the effect of particle acceleration on the axial pressure profile may be quite significant as shown by Weinstain and Li (1989). They showed that particle acceleration component of the experimentally determined axial pressure drop profile along the acceleration region can be as much as 40%. Also, the difference in the flow patterns of dense

bottom region and fast bed requires that the acceleration region be modeled separately.

The base model assumes a core-annular flow structure throughout the CFB riser. The flow is assumed to be axisymmetric and steady, which reduces the problem to a two dimensional domain.

Following the Plug Flow approximation (PFR) of Contractor et al. (1994), the upward gas flow is restricted with the core region, only. Radial gas flow is allowed from the core to the annulus equal to that from the annulus to the core.

The suspension density is considered to decrease monotonically starting from the riser base. The radial distribution of solids flux profile is modeled to exhibit similar profiles throughout the fully developed region.

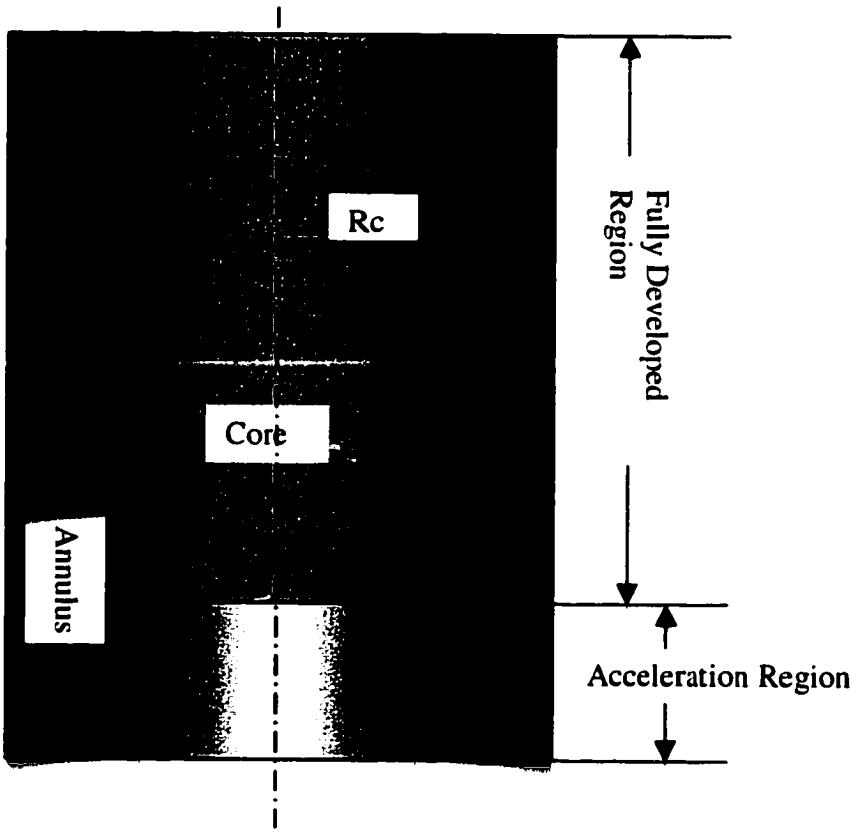

Figure 5.1. Illustration of riser layout as assumed by the base model

It is now well known that the suspension density increases at the exit of the riser due to the exit configurations. But, since the focus of this study is directed toward the secondary air injection region, the proposed model does not consider the exit effects. Figure 5.1 shows a representative sketch of the considered flow domain.

5.1.1 Fully Developed Region

The radial variations in the solids mass flux profile can be approximated using Rhodes et al. (1992)'s expression (Eq. 5.1). The expression envelops a parabolic radial profile for the solids flux distribution at any axial location (G_r). The constants of the parabola are defined after the observation of similar solids flux profiles.

$$\frac{G_r}{G} = a\left[1-\left(\frac{r}{R}\right)^m\right]+1-\frac{ma}{m+2} \qquad (5.1)$$

It was also reported in the same work that varying the parameter m had a negligible effect on the radial solids flux profiles, and that a constant value of 5 best represented their experimental data. From then on, the above equation was used by many others (Puggsley & Berruti, 1996; Puchyr et al., 1997) successfully. A sensitivity study on the parameter m have shown (Figure 5.2) that Gr/G profile seems insensitive to the constant 'm' if m is between 3 and 6, for all r/R values considered. The non dimensional core radius was taken as 0.9 in calculations for Figure 5.2.

At any elevation, when r = r_c, the local particle velocity, and consequently the local solids flux, Gr, must be zero. Therefore the constant 'a' of Equation 5.1 is found from;

$$r_c/R = \left[\frac{1}{a}+\frac{2}{m+2}\right]^{1/m} \qquad (5.2)$$

Equation 5.2 implies that, the constant 'a' in equation 5.1, thus the radial profile of axial solids flux can be determined if the value of the core radius is known.

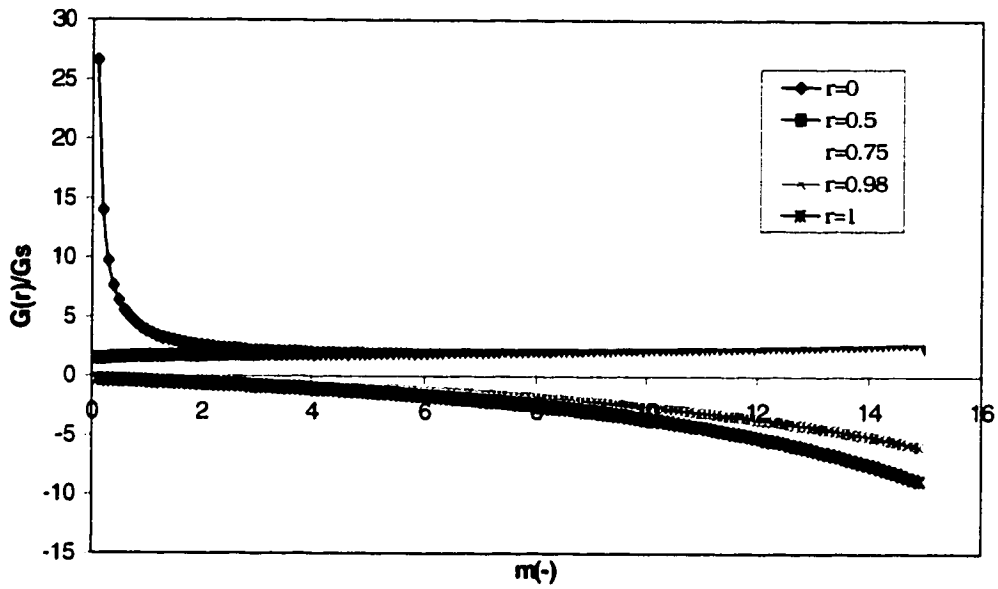

Figure 5.2. Dependence of Gr/Gs profile on the constant m, in equation 5.1. The figure represents the values for a non-dimensional core radius of 0.9.

The thickness of the annulus region and its axial variations can be estimated by using Wherter (1994)'s equation.

$$\frac{\delta}{D_t} = 0.55\,\mathrm{Re}_t^{-0.22}\left(\frac{H_t}{D_t}\right)^{0.21}\left(\frac{H_t - z}{H_t}\right)^{0.73} \qquad (5.3)$$

The core radius predicted with the above equation is compared with the experimental data of this work for FCC and Sand flows (SAR = 0). In the regions considered (covering first 2 meters of the riser, or one third of the riser height), an excellent agreement with the experimental data is obtained if the constants of the above equation are modified. The modification requires that the flow domain be described by two separate equations, instead of one.

If one writes Wherter's equation in its general form:

$$\frac{\delta}{D_t} = a1\,\mathrm{Re}_t^{a2}\left(\frac{H_t}{D_t}\right)^{a3}\left(\frac{H_t - z}{H_t}\right)^{a4}$$

Figure 5.4 compares the core radius profiles obtained from Wherter's equation with modified constants, Werthers equation with its original constants, and the experimental data of this work for FCC particles. Excellent agreement between the core radius estimations and its experimentally found value is reached if Wherter's equation is used with modified constants. Figure 5.5 shows that the predictions of modified equation on the axial development of core radius can confidently be used in lower part of the CFB's operating with sand particles, also.

The modified equations then are:

$$\frac{\delta}{D_t} = 0.45\,\mathrm{Re}_t^{-0.32}\left(\frac{H_t}{D_t}\right)^{0.21}\left(\frac{H_t - z}{H_t}\right)^{0.5} \qquad (5.4)$$

$$\frac{\delta}{D_t} = 0.725\,\mathrm{Re}_t^{-0.32}\left(\frac{H_t}{D_t}\right)^{0.21}\left(\frac{H_t - z}{H_t}\right)^{3} \qquad (5.5)$$

In the modified form, Equation 5.5 is used for the lean-upper part of the bed, and Eq. 5.4 is used for dense-bottom part of the bed. At each axial location, the computer program computes the core radius for both of the equations, then, accepts the one that has a smaller value for a given axial location.

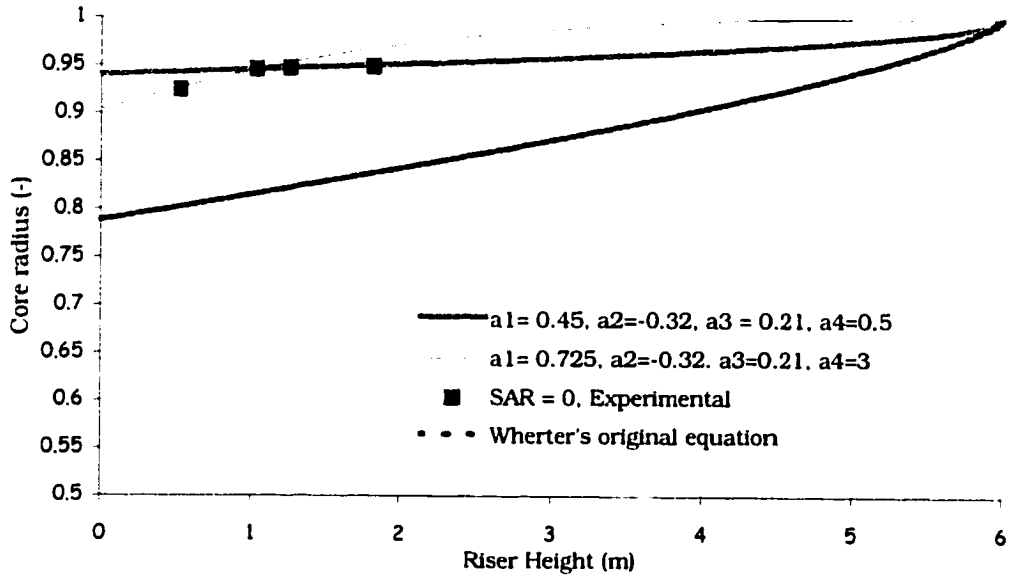

Figure 5.3. Axial development of core radius prediction with Eq. 5.4 and 5.5 for FCC particles, U= 3 m/s. A better agreement is obtained when the coefficients of Wherter's equations are modified.

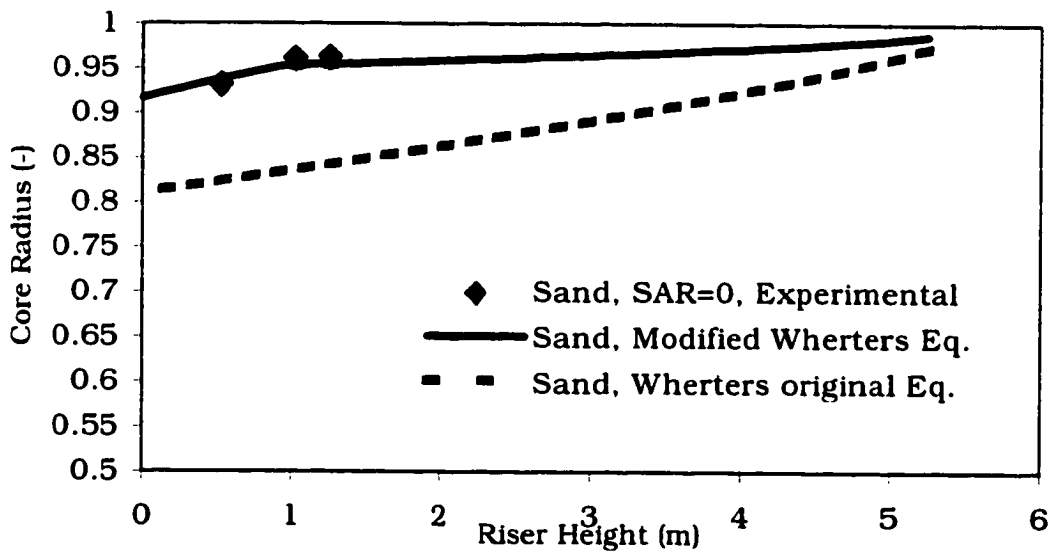

Figure 5.4. Comparison of core radius profiles predicted with Eq. 5.4 and 5.5 (Wherter's original equation) and with its modified version for Sand particles. U= 5 m/s, Gs = 7.5 kg/m2s.

The net solids mass flux, G_s, is defined by;

$$G_s = \rho_s v_p (1-\varepsilon) \tag{5.6}$$

Using localized values instead of averages, one can obtain the voidage profile from a rearranged form of equation 5.6.

$$\varepsilon_r = 1 - \frac{G_r}{\rho_s v_{p,r}} \tag{5.7}$$

Or alternatively, one may use either Zhang et al. (1991, Eq. 4.13) or Patience and Chauki (1995, Eq. 4.14) empirical correlation to predict the radial distribution of voidage, provided that the cross sectional average voidage is known.

Radial distribution of voidage at any axial location, then, can be calculated by using Equation 5.7, if the axial component of particle velocity profile is known. Obviously, the core radius is a singular point in Eq. 5.7, therefore needs special attention in the programming stages.

Particle velocity measurements of Hartge et al. (1988) revealed that the axial component of particle velocity has its highest values at the center, and reduces gradually towards the wall region. Following his findings, with an analogy to the laminar fluid flows, the axial component of particle velocity profile in the fast bed is usually modeled as if it has parabolic distribution over the radius. Later, some others (Pugssley & Berruti, 1996; Puchyr et al., 1997; Rhodes et al., 1992) had used the parabolic distribution assumption for the solids velocity profile. However, our experiments have shown that, in the bottom portions of the riser, the particle velocity profile in the core shows a turbulent velocity distribution rather than a laminar one, which is also observed by Aguillon et al. (1996). Therefore in this work, in the bottom region, the particle velocity profile is modeled with power law, and the fast bed is modeled with a parabolic distribution.

$$Vp = c\left[1-\left(\frac{r}{R}\right)^{n}\right]+d \qquad (5.8)$$

In the above equation, n = 2 gives a parabolic distribution and used for the fast bed, whereas a value between 3 and 5 may be used for the primary bed depending on the particle properties. Although the experimental findings are presented in the previous chapter, it may be helpful to note here that for smaller and lighter particles, due to their shorter response time, a turbulent flow profile is obtained and thus, a value of n=5 represented the experimental results better. Whereas for sand particles used, an exponent of n=4 best represented the experimental findings.

The two boundary conditions to find the constant c & d in equation 5.8 are as follows.

1) At the centerline particle velocity has its maximum value.

$$Vp = Vp,\ max \qquad at \qquad r=0, \qquad (5.9)$$

2) The core-annulus interface is defined as the location of zero net particle velocity. Expressed mathematically,

$$Vp,r=0 \qquad at \qquad r=r_c \qquad (5.10)$$

Applying the above boundary conditions, for the particle velocity profile one can find:

$$V_{p,r} = V_{p,\max}\left[1-\left(\frac{r}{r_c}\right)^{n}\right] \qquad (5.11)$$

where, the maximum particle velocity can be approximated by using the definition of terminal velocity of a particle. In other words, the maximum slip velocity between the gas and the particles are restricted with the terminal velocity of a single particle (V_t) at the center of the riser. However, in the dense

primary region, the above assumption can not be used since the slip velocity in fast beds may be much greater than the terminal velocity of the particles. This is also a feature of CFB's. Therefore, for the dense bed above the acceleration region, a new approach is required to predict the solids velocity. The present model uses an exponential distribution of slip velocity from $U_{0,primary}$ at the bottom to terminal velocity of particles at the fully developed region. Yang et al. (1992) found experimentally that the maximum gas velocity occurs in the center of the riser and its value is 1.5 to 2 times greater than the superficial gas velocity U_0. Later, Puggsley and Berruti, analyzing a large database, have proposed that the maximum gas velocity at the center be best expressed by the following empirical equation.

$$U_{g,max} = 1.5\frac{U_{g,c}}{\varepsilon_c} \tag{5.12}$$

where, $U_{g,c}$ is the average gas velocity, and ε_c is the average voidage in the core. Therefore the maximum particle velocity may be expressed as;

$$V_{p,max} = 1.5\frac{U_{g,c}}{\varepsilon_c} - V_t \tag{5.13}$$

Owing to the plug flow assumption employed by the model, the average gas velocity in the core region can be calculated by;

$$U_{g,c} = \frac{U_o}{\phi} \tag{5.14}$$

where, ϕ is the ratio of core cross sectional area to the riser cross sectional area.

Knowledge of the radial profiles of voidage, particle velocity and solids flux allow calculation of the average values in the core region, by integrating the profiles over the core cross-section. Therefore, the average voidage in the core region can be calculated as:

$$\varepsilon_c = \frac{1}{\pi r_c^2}\int_0^{r_c} 2\pi r \varepsilon_r dr \qquad (5.15)$$

and, the cross sectional average voidage can be estimated with the same method.

$$\varepsilon_{ave} = \frac{1}{\pi R^2}\int_0^{R} 2\pi r \varepsilon_r dr \qquad (5.16)$$

Since the area ratio occupied by the core is known, one can calculate the average cross sectional voidage in the annulus at a given axial position as;

$$\varepsilon_a = \frac{\varepsilon_{ave} - \phi\varepsilon_c}{1-\phi} \qquad (5.17)$$

similarly, the average values of the other flow properties in core and annulus can be calculated. For solids flux for example,

$$G_{s,c} = \frac{1}{\pi r_c^2}\int_0^{r_c} 2\pi r G_r dr \qquad (5.18)$$

If the average upwards solids flux in the core is known, then the average solids flux in the annulus can simply be determined with a material balance at the cross section: $G_{s,a} = G_s - G_{s,c}$

Therefore, the average axial velocity of particles in the core and annulus can be determined from the definition of solids flux.

$$V_{p,a} = \frac{G_a}{\rho_s(1-\varepsilon_a)(1-\phi)} \qquad (5.19)$$

$$V_{p,c} = \frac{G_c}{\rho_s(1-\varepsilon_c)\phi} \qquad (5.20)$$

The above equations close the hydrodynamic model for the fully developed region. The solution procedure for the above equations is as follows:

Axial development of core radius is calculated from equations 5.4 and 5.5. At a given axial position, the radial variations in the solids flux can then be calculated using equations 5.1 and 5.2. Calculation of voidage profile, on the other hand, requires the knowledge of radial distribution of particle axial velocity (Eq. 5.7). Similarly, calculation of particle velocity profile requires the knowledge of average voidage in the core. Therefore a trial and error method is used in calculating the above properties. First, initially assumed values for particle axial velocity is assigned as input values at all nodal points. Then, by using the initial estimate of the voidage profile, a current particle velocity profile is calculated by using Equation 5.11. Then, the same procedure is repeated until the difference between the sum of absolute values of initial and the current particle velocity at all nodes, become less than a limit which is preset as 0.01 m/s. Therefore, the program searches for the combination of particle velocity and voidage profiles, which satisfy the pre-calculated solids flux profile (G_r) at any axial location.

The simulations during the program-testing period have shown that, the magnitude of initial estimation for the particle velocity had no effect on the model output of the above properties.

Having known the voidage and particle velocity profiles, the local and averaged values of the above properties can be calculated easily by using the provided equations. Here, special care has to be given to the numerical integration of voidage and solids flux profiles, since the core radius does not necessarily lie on the grid points.

A very good agreement with experimental data is achieved for the fast bed modeling. Comparisons between model predictions and available experimental data are provided in graphical forms in the section following the presentation of proposed model for the acceleration region.

5.1.2 Acceleration Region

Following Puggsley and Berruti (1996), the proposed model considers flow structure in the acceleration region to be in a core-annular form, similar to that in the fully developed region. However, due to the irregularity of the two-phase flow in the acceleration region, a constant core radius is assumed and a value that is equivalent to the value calculated for the base section of the fully developed zone is assigned. The particles captured by the gas stream at the base of the riser are accelerated to their fully developed velocity value in the core region.

The axial development of average voidage in the annulus region, however, is modeled to increase linearly from a constant voidage at the base, to a value calculated for the base section of the fully developed region. Also, the voidage at the base of the riser is assumed as the same for both core and the annulus regions.

The height of the acceleration region can be estimated by numerically tracking a particle's axial position and velocity with time. The particle, released to the core region at the distributor plate level, followed numerically till it looses its acceleration and assumes the velocity value that was calculated for the base section of the core region of fully developed region. Thus, modeling the acceleration region starts with a force balance on a single particle.

The forces acting on a single particle in a fluid flow field was cited early in the chapter. Neglecting the radial and tangential components of velocity in the flow field, the force balance on a single particle is given by Pugsley and Berruti (1996);

$$\frac{dV'_{p,c}}{dt} = \frac{3}{4} C_d \frac{\rho_g}{d_p \rho_s} V_{sl}^2 + \frac{g(\rho_g - \rho_s)}{\rho_s} \qquad (5.21)$$

From here on, for convenience and clarity, variables of the acceleration region are denoted with a prime exponent. In Equation 5.21, the term on the left hand side represents the acceleration force, the first term in the right hand side is the form drag of the gas on the particle and the last term represents the net vertical force on the particle due to the buoyant and the gravitational forces.

Calculation of the particle acceleration requires the knowledge of the gas and the solid velocities in the core region together with the drag coefficient. The gas velocity at the point of interaction can be estimated with the knowledge of superficial gas velocity, the core radius, and the voidage in the core.

The model considers the particles to be at rest at the distributor plate level. However, it is experimentally observed that the particles, during their horizontal transport from standpipe to riser, settle and form dense clusters at the bottom of the channel due to the gravitational forces. These clusters, then, move downward in the core region of the riser, for a short period, until they are captured back by the upcoming gas, since the axial position of solids injection channel is usually located at a height one to two times the riser diameter up in the riser. The duration of the downward motion of particles is longer when larger and denser particles are fluidized. Therefore, one should note that the height of solids injection channel might be significant, therefore be accounted for, in interpreting the model results for the height of acceleration region especially when particles with smaller Stokes numbers are fluidized. This difference between the experimental observation and the model consideration can be seen from a representative sketch in Figure 5.5.

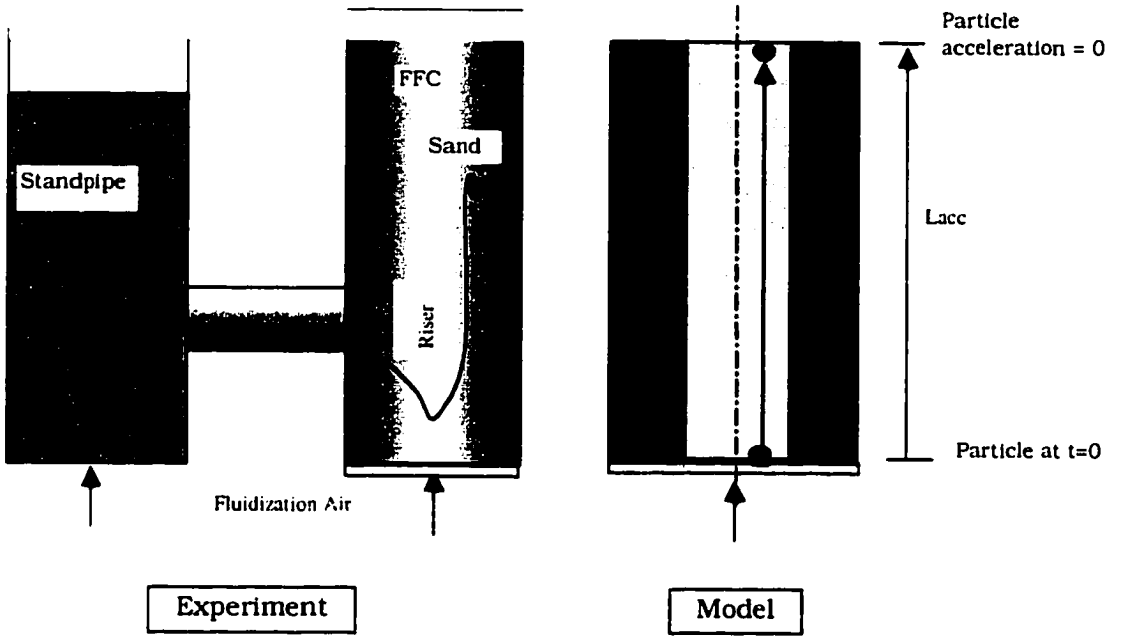

Figure 5.5. A representative sketch of initial solids entrance to the riser. The Figure on the left reflects the experimental observation whereas, the figure on the right shows the model assumption for the particle motion in acceleration region.

Littman et al. (1993) presented a summary of previous efforts to estimate the drag coefficient, and showed that the standard drag curve may severely overestimate its value. Based on his findings Pugssley and Berruti (1996) slightly modified the standard drag coefficient, which is in the form of:

$$C_d = \frac{18.5}{\mathrm{Re}_p^{0.6}} \qquad (0.3 < \mathrm{Re} < 1000) \qquad (5.22)$$

as cited by Flemmer and Banks (1986) (cited from Perry and Chilton, 1973).

Pugssley and Berruti (1996) rewrote the above equation in form of;

$$C_d = \frac{K}{\mathrm{Re}_p^{0.6}} \tag{5.23}$$

and calculated the constant K by using the boundary value of slip velocity which is already known from the calculations of fully developed region. The acceleration term in Eq. 5.21 vanishes at the boundary, thus a new value for K can be calculated. This new value of K insures the transition, in terms of particle velocity, at the boundary of the two regions, the constant K in Eq. 5.24 is then;

$$K = \frac{4g(\rho_s - \rho_g)d_p \mathrm{Re}_p^{0.6}}{3\rho_g\left(\frac{U_c}{\varepsilon_c} - V_{p,c}\right)^2} \tag{5.24}$$

Flemmer and Blanks (1986) also proposed an equation to calculate the drag coefficient of a settling sphere, which is valid for a very wide range of particle Reynolds number.

$$C_d = \frac{24}{\mathrm{Re}_p} 10^E \qquad (\mathrm{Re_p} < 3\mathrm{X}10^5) \tag{5.25}$$

where,

$$E = 0.261\mathrm{Re}_p^{0.369} - 0.105\mathrm{Re}_p^{0.431} - \frac{0.124}{1 + (\log_{10}\mathrm{Re}_p)^2} \tag{5.26}$$

In this work, both of the above relations are tested and results, in terms of the height of acceleration region, were similar.

Following Puggsley and Berruti (1996), the model assumes a constant voidage profile at the base slice, just above the distributor plate. Therefore, the voidage at the base of the annular region is assumed to be equal to the average voidage

in the core region. Also, the model assumes that the average voidage in the annulus varies linearly with axial dimension. Expressed mathematically;

$$\varepsilon_a' = \varepsilon_b + \left(\frac{\varepsilon_a - \varepsilon_b}{L_{acc}} \right) z \qquad (5.27)$$

The assumption of linear variation of the voidage in an annulus of constant thickness may be considered as equivalent to linearly varying annular thickness with constant voidage. The core radius, on the other hand, is considered as constant, and has a value of equivalent to that calculated at the bottom strip of the fully developed region. A varying core radius is not considered in the acceleration region modeling, since the experimentally observed gas-particle motion pattern in the bottom region of the riser showed very irregular and intermittent behavior. The solids entrance configuration seemed effective in the gas motion pattern since a very dense cluster of solid particle is continuously flown into the core region, disturbing the core annular nature of the flow by pushing the upcoming gas towards the walls. Therefore for the above reasons, the core annular approximation for the acceleration region seen as meaningful only in calculating the averaged values of the properties, not for their radial profiles. Therefore the proposed acceleration region model may be classified as a *two-region one-dimensional* model.

In this work, the solution of differential equation (Eq. 5.21) is obtained by using Runge-Kutta method of order four. The solution requires the value of the core voidage at the base of the bed as an initial condition. The value of the base voidage is expected to be a function of operating parameters such as solids velocity, solids flux, superficial gas velocity, riser hydraulic diameter etc. But surprisingly, King's (1989), simple expression which considers the base voidage as a function of superficial gas velocity only, agrees well with the experimental data. Later, Ouyang and Potter (1993) by comparing the results of various researchers reported that the majority of the data presented for the base of a riser operating in turbulent regime falls in the range of 0.8 to 0.9. Therefore

present knowledge about the factors effecting the base voidage limits us to use either King's equation (Eq. 5.28) or an assumed base voidage between 0.8 and 0.9 in order to predict the axial variations in the properties in the acceleration region. Nevertheless, model runs have shown that the output, in terms of height of the acceleration region, seems insensitive to the selected base voidage. Due to comparably lower solids flux values used in the experiments, the base voidage is selected to be equal to 0.9.

$$\varepsilon_b = \frac{U_0 + 1}{U_0 + 2} \tag{5.28}$$

The average downward solids flux in the annulus can be calculated by using the definition of the solids flux, provided that the average particle velocity and the voidage are known. The average downward particle velocity in the bottom of the bed seems to be the smallest of all throughout the riser, due to the intermittent flow behavior in the acceleration region. Thereiore, the average particle velocity in the annulus of acceleration region is considered as constant and equal to that of the smallest value in the fully developed region (i.e. at the top of the riser). Therefore, the solids flux at any axial location in the annulus is given by;

$$G'_a = V_{p,a}\rho_s(1-\varepsilon'_a) \tag{5.29}$$

The average upward solids flux can then be calculated with a material balance at a cross section;

$$G'_c = V'_{p,c}\rho_s(1-\varepsilon'_c) = \frac{G_s + G'_a(1-\phi)}{\phi} \tag{5.30}$$

The average voidage then, can be found by;

$$\varepsilon' = (1-\phi)\varepsilon'_a + \phi\varepsilon'_c \tag{5.31}$$

The calculations start with guessing a value for the height of the acceleration region (L_{acc}). Starting from the riser base, at any given time step, the particle

velocity is calculated from Equation 5.21. At the end of the time step the new core voidage is calculated from Eq. 5.30. The axial location corresponding to the time step is calculated from;

$$Z = V'_{p,c}\,\Delta t + a(\Delta t)^2/2 \qquad (5.32)$$

Where, $V'_{p,c}$ is the current mean velocity of the particle within the time step, and the second term represents the distance traveled due to the acceleration. The calculations are allowed to proceed progressively, by increasing the length of the acceleration region, until the average particle velocity in the core at the end of the acceleration region has reached to that calculated for the boundary value of the fully developed region. The height of the acceleration region is then limited with L_{acc} , the model output which is equal to Z in Equation 5.22 at the end of the last time step that ensures the transition between acceleration and fully developed regions for the core particle velocity. Figure 5.6 shows a flow chart for the iterative procedure in acceleration region modeling.

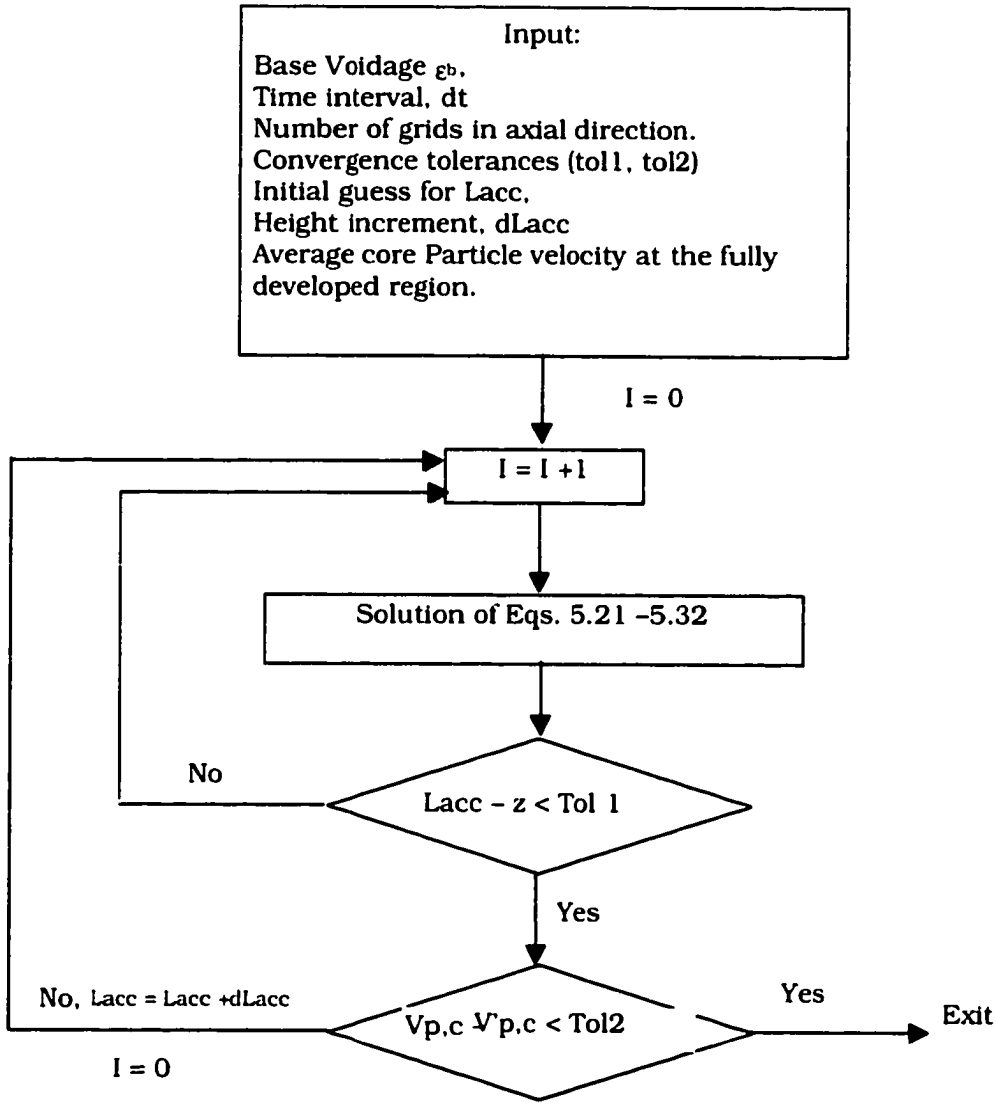

Figure 5.6. Flow chart for iterative procedure to calculate the height of the acceleration region.

The convergence criteria, however, must be re-arranged if the flow is disturbed with the presence of secondary air jets, at some elevation above the distributor plate. The SA jets may penetrate through the upcoming suspension either radially or tangentially depending on the mode of SA injection. The height of injection may also change the axial profiles. The next section covers the

modifications to be built on the base model, in the presence of secondary air injection.

5.2 Validation of the Base Model

The solids flux, solids velocity and voidage profiles predicted by the present model are compared with some experimental data available in the open literature.

Figure 5.7 compares the model predictions for the reduced solids flux profile with experimental data of Rhodes et al. (1992). A good agreement in the annulus and core annulus interface is achieved, but the values at the center seem slightly underestimated. Also Figure 5.8 compares the model predictions on reduced solids flux with the experimental data of Bodelein et al. (1994) for small diameter risers. Similar reduced solids flux profiles assumption seems to agree with the experimental data well.

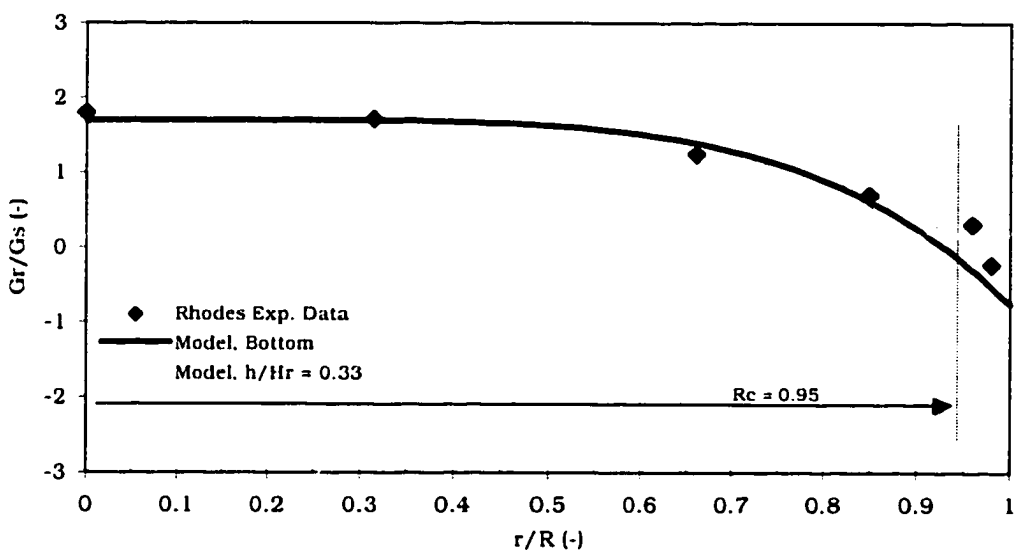

Figure 5.7. Local solids flux data of Rhodes et al is compared with the model predictions. Gs = 60 kg/m²s, U0=4 m/s Dr = 0.305 m, Hr = 6.6 m, d_p = 75 μm, ρs = 2456 kg/m³. "Bottom" refers to the base of the fully developed region.

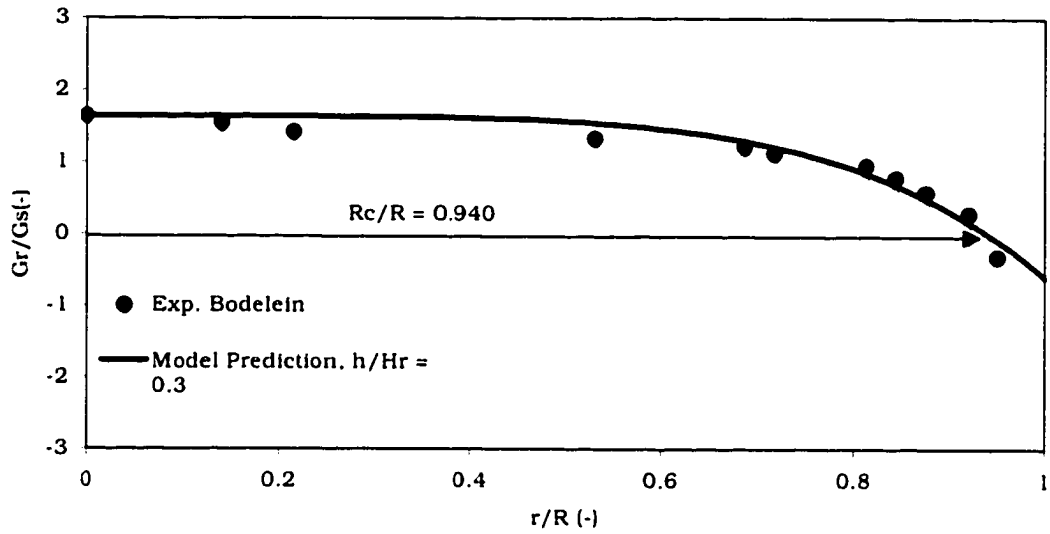

Figure 5.8. Local solids flux data profile of Bodelein et al (1994) is compared with the model predictions in the fully developed region. Gs = 43.3 kg/m^{2}s, U_0=5.4 m/s Dr = 0.144 m, Hr = 10 m, d_p=180 μm, ρs = 2650 kg/m^3.

Model prediction of particle velocity profile is compared with experimental data of Hartge et al. (1988) in Figure 5.9. For sand particles in fully developed region, due to the comparably low superficial gas velocity and moderate solids flux used, the particle velocity profile is parabolic. A good agreement with the experimental data is obtained when the maximum gas velocity at centerline is assumed as twice the average gas velocity in the core.

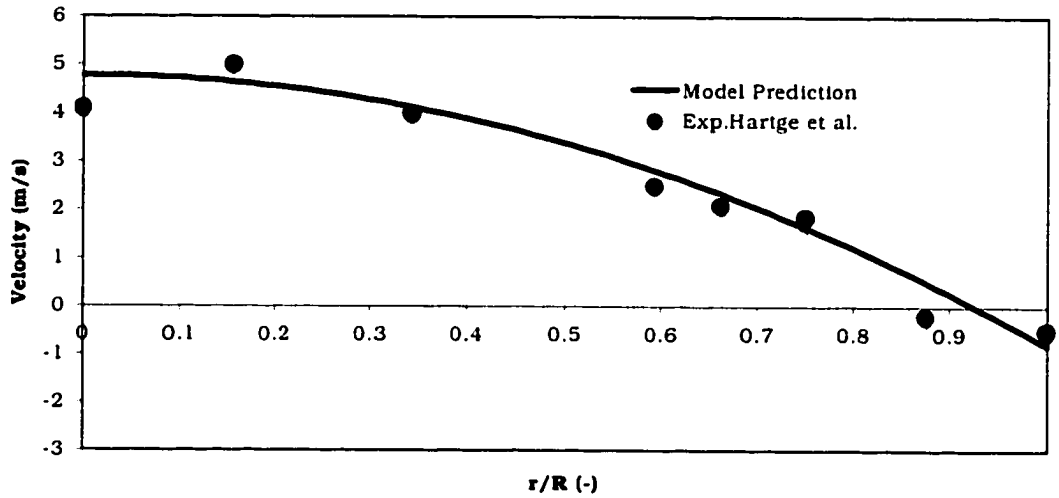

Figure 5.9. Local particle velocity profile data of Hartge et al. (1988) is compared with the model predictions in the fully developed region. Gs = 30 kg/m²s, U_0=3.7 m/s Dr = 0.4 m, Hr = 8.4 m, dp=120 μm, ρs = 2600 kg/m³.

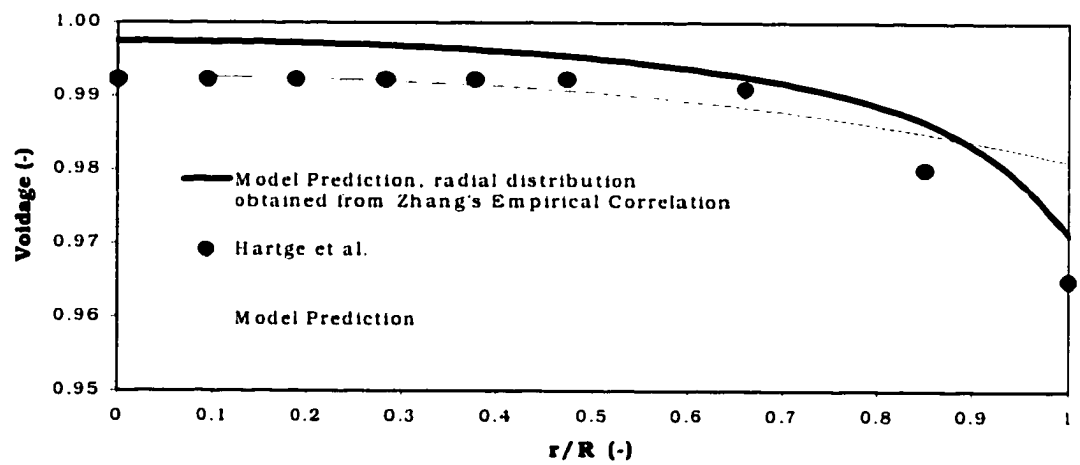

Figure 5.10. Local voidage profile data of Hartge et al. (1986) is compared with the model predictions in the fully developed region. Gs = 75 kg/m²s, U_0=5 m/s Dr = 0.4 m, Hr = 7.8 m, d_p=56 μm, ρs = 2500 kg/m³.

Figure 5.10 compares experimentally obtained voidage profile from Hartge et al. (1986) with the present model predictions. It shows that the model prediction by using Equation 5.7 agrees well with the experimental data in the core region, whereas, Equation 4.13, using the average voidage from Equation 5.7, gives better results in the annulus region. The cross sectional average value of voidage used in Equation 4.13 was estimated integrating the voidage profile obtained using Equation 5.7 over the radius. Thus, a combination of the two correlation would make a better estimate for the voidage profile predictions. The present model uses Equation 4.13 to predict the voidage profile in the annulus.

5.3 Secondary Air Region Modeling

The injection of secondary air, depending on its amount, mode and height, may have a major influence on the hydrodynamics of CFB risers. Although this influence of secondary air have been investigated experimentally (Wang and Gibbs, 1990; Illias et al., 1988; Kim et al., 1994; Arena et al., 1993; Aguillon et al., 1996; Choi et al., 1997), its quantification is yet to be completed. And, thus, the mathematical prediction of the effects of SA injection on the riser hydrodynamics is still in its infancy. To the author's knowledge, there has been only a few models reported in the open literature to model the SA injection. Kunii and Levenspiel (1977) modified their Freeboard Entrainment Model and assumed that there is no axial gradient in suspension density in the region below the secondary air injection plane, as did Rhodes and Geldart (1987). This seems to be valid only if the bed is operating under a very dense flow regime at the bottom, and/or if the injection ports of SA is located very close to the distributor plate that one can assume a constant voidage throughout the lower region. Kim et al. (1994) also modified the exponential decay constant of Freeboard Entrainment Model to account for the presence of secondary air.

All of the above models are classified as type I model since they account for the axial distribution of solids holdup, not the radial variations. Neither did they consider the axial or the radial variations in flow variables such as particle

velocity and/or solids flux. To the author's knowledge no type II model to account for the secondary air injection is published so far.

Although the volume ratio of SA effective region to the riser total may be comparably small, at a given time, considerable fraction of the bed material reside in the primary region, implying the differences between the solids re-flux patterns of primary region and that of fully developed region. The modeling efforts, on the other hand, are mostly limited with the fully developed region modeling in type II models, ignoring the effective back mixing in the dense bottom region. There may be some other reasons for this lack of attention towards mathematical modeling of the SA region, but the main reason seems to be that in the bottom dense region, the flow field is very irregular and it is very difficult to describe the radial variations mathematically. Whereas in the fast bed region, due to low suspension density, the mixture behaves more fluid-like, therefore confident use of fluid-phase-based simplifying approximations such as core annular regions, similar profiles and parabolic distributions of flow variables lead to more realistic model outputs. Whereas, the primary region modeling with secondary air injection is much more complicated due to the complex flow structure, and lack of experimental data.

Nowadays, with the recent advancement in computational fluid dynamics (CFD), it is possible to gather very useful information on the flow structure of fluids in motion. Flow analysis using CFD techniques are very popular, and the simulations reveal very accurate representations of local properties of single-phase flows. However, due to the lack of knowledge on the phenomena, CFD analysis of gas-solid flows is still in its infancy, successful simulations are limited with only very dilute suspensions. However, in order to understand the effects of SA injection on the developing flow, valuable information on the propagation of SA jets and the related effects on the riser flow structure may be gathered from single-phase flow simulations using CFD techniques. Such a simulation may also reflect the flow behavior in a very lean gas-solid flow with particles of very small Stokes numbers. A well-known commercial CFD software,

FLUENT 4.4, was available during the course of this study, and the relevant simulations are performed in order to understand the effects of secondary air jets on the gas flow behavior in the CFB riser. The next section covers the results obtained from the gas phase simulations (radial and tangential SA injection), performed using Fluent 4.4.

5.4 Gas Phase Flow Simulations in a CFB riser with Secondary Air Injection

In order to understand the effects of SA jets on the flow development of two-phase flows, it may be useful to observe its effects in the limiting case of single-phase gas flow within the same envelope of the two-phase flow problem. In the limiting lean flow case, the problem becomes a single-phase fluid dynamics problem, which may be defined as *turbulent gas flow in a circular cylinder with axial and lateral inlets*. In this work, related simulations are performed for a riser with radial and tangential SA inlet geometry using Fluent 4.4.

The fundamental equations that govern the conservation of mass and momentum for steady flow in two-dimensional Cartesian coordinates may be written as:

Continuity equation:

$$\frac{\partial}{\partial x_i}(\rho u_i)=0 \tag{5.33}$$

Momentum Equation:

$$\frac{\partial}{\partial x_i}(\rho u_i u_j)=-\frac{\partial p}{\partial x_i}+\frac{\partial(\tau_{ij,l}+\tau_{ij,t})}{\partial x_i}+\rho g_j + F_j \tag{5.34}$$

In the momentum equation, the LHS represents the convection term, the RHS represents the pressure, the diffusion, the body forces and the external forces, respectively. The above equations describe the time averaged mean flow if

applied to a finite number of discrete control volumes. The effect of turbulence is included by substituting an effective turbulence viscosity in the existing equations.

The laminar stress tensor can be written as below from the Newtonian stress-strain relation,

$$\tau_{ij,l} = \mu_l \left[\left(\frac{\partial u_j}{\partial x_i} + \frac{\partial u_i}{\partial x_j} \right) - \frac{2}{3} \delta_{ij} \frac{\partial u_k}{\partial x_k} \right]$$

and, for the turbulent stress tensor, Boussinesq hypothesis is applied;

$$\tau_{ij,t} = \mu_t \left[\left(\frac{\partial u_j}{\partial x_i} + \frac{\partial u_i}{\partial x_j} \right) - \frac{2}{3} \delta_{ij} \frac{\partial u_k}{\partial x_k} \right] - \rho \frac{2}{3} k \delta_{i,j}$$

The distribution of the turbulent intensity is modeled by k-ε model. The differential equations for k-ε formulations are given by Launder and Spalding (1972);

$$\frac{\partial}{\partial x_i}(\rho u_i k) = \frac{\partial}{\partial x_i} \left(\frac{\mu_t}{\sigma_k} \frac{\partial k}{\partial x_i} \right) - \rho \varepsilon + G_k \qquad (5.35)$$

$$\frac{\partial}{\partial x_i}(\rho u_i \varepsilon) = \frac{\partial}{\partial x_i} \left(\frac{\mu_t}{\sigma_\varepsilon} \frac{\partial \varepsilon}{\partial x_i} \right) + C_1 \frac{\varepsilon}{k} - \rho \varepsilon + C_2 \rho \frac{\varepsilon^2}{k} \qquad (5.36)$$

where G_k is the generation term of k and is given by;

$$G_k = \left(\frac{\partial u_i}{\partial x_i} + \frac{\partial u_j}{\partial x_i} \right) \frac{\partial u_i}{\partial x_i} \qquad 5.37$$

The turbulent viscosity is related to k and ε by the empirical relation:

$$\mu_t = C_\mu \frac{k^2}{\varepsilon} \tag{5.38}$$

The coefficients C_1, C_2, $C\mu$, σ_k, σ_ε are all constants having the values;

C_1= 1.44, C_2 =1.92, $C\mu$= 0.09, σ_k=1 σ_ε=1.3

The governing partial differential equations for the conservation of mass and momentum for the gas phase is written into a general form;

$$\frac{\partial}{\partial x_i}(\rho u_i \phi) = \frac{\partial}{\partial x_i}\left(\Gamma_\phi \frac{\partial \phi}{\partial x_i}\right) + S_\phi \tag{5.39}$$

where, the LHS of the Equation 5.39 represents the convection term and the terms on the right hand side represent diffusion and source terms, respectively.

Fluent uses a control volume based technique to solve the conservation equations for momentum and turbulence quantities. This control volume technique is based on division of the domain into discrete control volumes using a general curvilinear grid, integration of the governing equations on the individual control volumes to construct the algebraic equations for discrete unknowns, and solution of these discretized equations.

Fluent defines the discrete control volumes in a non-staggered grid storage scheme in which all variables including the velocity are stored at the control volume center. Patankar (1980) reduced the equations to their finite difference forms by integrating over computational cells over which the solution domain is divided. The resulting algebraic equations, then are;

$$\phi_p \sum_i (A_i - S_p) = \sum_i A_i \phi_i - S_c \tag{5.40}$$

where, the summation is over the neighboring cells; I=N, S, E, W, F, B. The A_i's are coefficients which contains the contribution from the convective and

diffusion terms and, S_p and S_c are the components of linearized source term, $S_\phi = S_c + S_p \phi_p$. A power law differencing scheme is used for interpolation between the grid points and to calculate the derivatives of flow variables.

The elliptic nature of the conservation equation requires that the boundary conditions must be specified at all boundaries of the flow domain. The inlet conditions are known (either velocity or pressure inlet with known values) beforehand and needs to be assigned at the beginning of the calculations. But although the exit boundary condition is not known beforehand, it needs to be specified prior to the calculations. Therefore, Fluent makes a reasonable assumption that the user must be aware before setting the problem geometry. The assumption is that the flow is considered as fully developed at the exit. Therefore, exit configuration must be smooth and obstructions should not be allowed at just upstream of the exit plane.

The simulations are performed for both tangential and radial SA inlet geometry. The computational grids are constructed for best representation of the experimental set-up used in this work. The 3-D grid constructed for tangential injection simulations is made up of 68 479 cells (47X47X31), covering a 3.5 m portion of the 6 m riser, staring from 0.5 m below the SA injection plane. The cells are concentrated over the SA injection region in order to achieve a better representation of the jet propagation.

The grid for radial SA injection is composed of 38 326 cells (41X26X36) and covers only half of the riser diameter since the radial injection problem is symmetric about a vertical plane in the mid section of SA injection port. Also in radial injection case, only one SA injection port is used due to the difficulties associated with grid formation.

The simulations, which represent the gas phase flow parameters of the experiment with sand, are performed using the k-ε turbulence model for radial injection case, and RNG k-ε turbulence model for the tangential injection case to close the turbulence equations. The gas inlet velocities used in simulation are

exactly the same as that used in the experiments, and the numerical values are presented in Table 5.1. Figures 5.11 and 5.12 show the computational grids used in the simulations for tangential and radial SA injection cases, respectively.

The numerical simulations revealed very useful information on the mixing patterns of SA and primary air streams attained with different SA injection configurations. Figure 5.13 shows the effects of tangential and radial jets on the axial velocity distribution in the riser, at the middle vertical slice which represent the plane expected to be the least effected from tangential SA jets due to its location. The presence of downward velocity in the wall region reveals that the up-coming suspension is forced to accelerate and proceed through the core section whose boundary is determined with the strength of SA jets. On the other hand, the radial SA jets resulted in a major distortion of the upcoming suspension at this plane. The velocity magnitudes at the same horizontal section read as much as twice the superficial gas velocity both upwards and downwards. Although the superficial gas velocity is 5 m/s, it is interesting to see a of velocity difference of 20 m/s at the same section. The lateral momentum imposed by the SA jets force the upcoming suspension to proceed through the wall layer just across the jet inlet, creating local high-pressure regions underneath the strong SA jets. Surprisingly, for SA=0.5, the jet seems to be strong enough to block the whole diameter. In this case the upcoming suspension is separated into two and advance through the sides of the riser as opposed to the tangential injection case where the upcoming suspension is forced towards the center.

Figure 5.14 show the contours of total pressure at the same sections as in Figure 5.13. It can clearly be seen that the high velocity in the core of tangential injection case is due to the contraction in the cross sectional area of flow. The local high pressure regions suggest that the SA jets are most likely to form a pseudo-solid obstruction over the upcoming suspension in the wall region of the riser, which reduces the flow area and forces the upcoming suspension to

accelerate. On the other hand, the radial injection not only result in an area contraction, but also impose cross sectional non-homogeneity to the upcoming suspension even at the bottom of the riser, stressing that the non-uniformity associated with SA injection is not limited only with the region just around the SA injection port.

The local non-uniformity associated with mode of injection is best seen at the cross sectional plane (Figures 5.15 and 5.16) of SA injection. The contours of total pressure show that the SA jets are effective over the whole radius for SAR= 0.5, for radial injection. The local low-pressure regions created away from the SA jets are the regions of high axial velocity which extend axially both up and downstream the SA injection plane. The area contraction must be much more effective in the experimental setup, since there is another SA jet opposing the one used in the computations. In tangential injection case, Figure 5.16 the annulus is thicker in the close vicinity of the SA jet inlets, which reduce the upward flow area, considerably. The figure shows that at the same horizontal section injection of swirling SA imposes a radial gradient in the pressure, which is in the order of 130 Pa, suggesting that similar motion patterns may be expected with the presence of solids, also.

Figure 5.17 shows the total velocity vector at the horizontal cross section of radial SA injection, and compares the effect of SAR on the effective jet propagation. It is interesting to see a swirling flow component over the cross wall for when SAR = 0.5. For SAR = 0.25, however, the upcoming suspension dominate the flow in the cross section, suggesting that there is an optimum value of SAR for each geometry for a desired rate of mixing. In tangential injection case, however, the flow restriction is more uniform (Figure 5.18).

Figure 5.19 and 5.20 show the contours of effective viscosity at various sections along the riser axis for radial and tangential injection cases, respectively. With the addition of secondary air a high kinetic energy region forms along the path of SA jets which is expected due to the high velocity of SA injection (27 m/s).

There is a huge difference between the effective viscosity of turbulent motion of SA jets and that of primary air. It is very interesting to see that this difference in the effective viscosity does not diminish quickly just above the injection plane, but prevail over a long section of the riser. On the other hand, for tangential SA injection the secondary air jets diffuse gradually from the wall region inwards and results in more homogenous upper bed. The mixing is complete in a shorter axial distance if SA is injected tangentially. This axially continuous non-uniformity in the viscosity profile for radial SA injection suggests poor mixing compared to its tangential counterpart. If applied to a CFB boiler, the radial gradient in the effective viscosity can be interpreted as formation of axially continuous local high-oxygen regions, which would lead to a reduction the combustion performance.

Thus, it would be reasonable to deduce that the mode of SA injection has an immense effect on the mixing of SA and PA streams. The radial injection of SA, extending diagonally over the cross section, forms a strong obstruction over the upcoming suspension, which strikingly increase the local non-uniformity in the flow properties. The mixing with PA is poor when compared to the tangential injection case. In tangential injection case, however, the SA streams form an effective, orifice-like obstruction in the plane of injection, creating local low and high-pressure regions above and below itself. This configuration, however, enhances the gas phase mixing above the SA injection plane by imposing more uniform and gradual mixing in a shorter axial distance. The faster mixing achieved over a sorter axial distance attained in tangential injection case is attributed to the helical streamlines of secondary air jets which, increases the residence time of fluid particles.

Table 5.1. Inlet boundary conditions used in the gas-phase simulations.

SAR	$U_{o.\ primary}$	$U_{o.\ total}$	U_{jet}
0.25	4.04 m/s	5 m/s	16.7 m/s
0.5	3.37 m/s	5 m/s	27.85 m/s

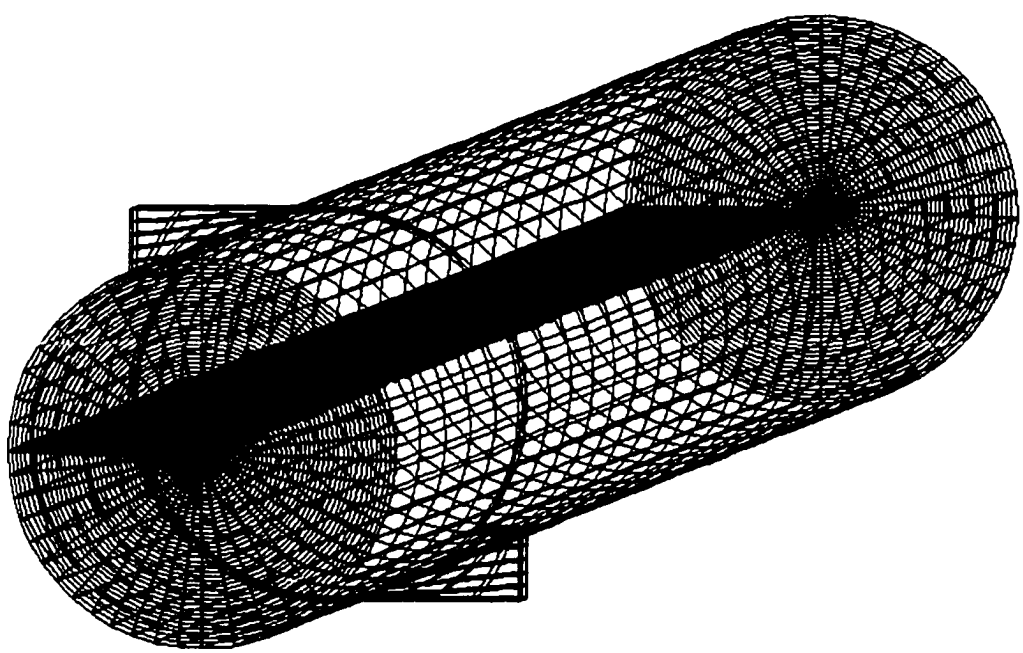

Figure 5.11. Computational grid for tangential SA injection.

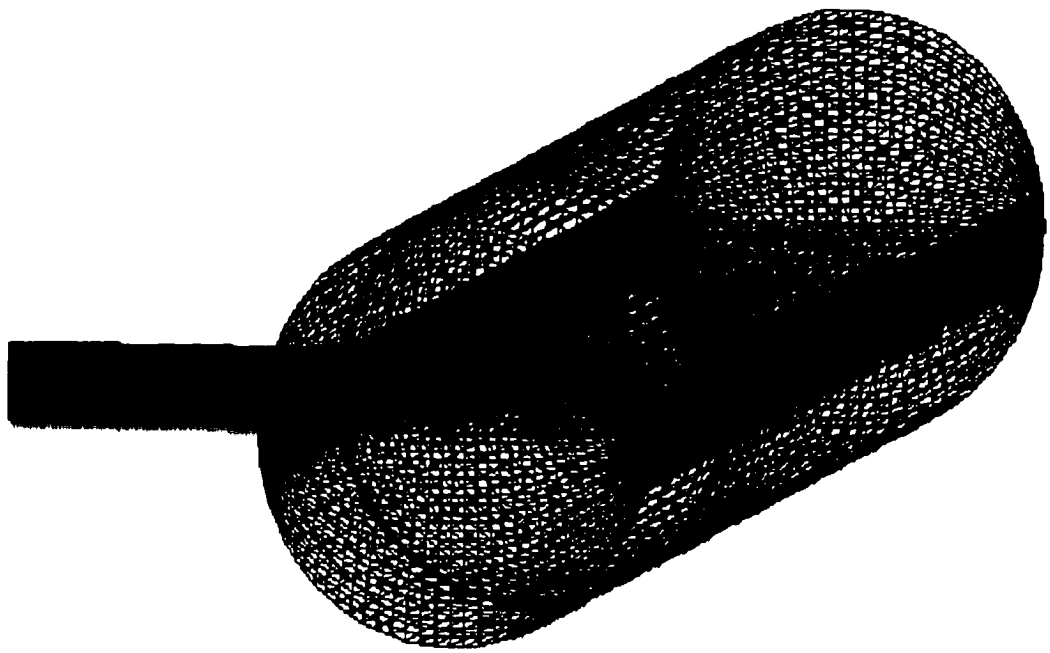

Figure 5.12. Computational grid for radial SA injection

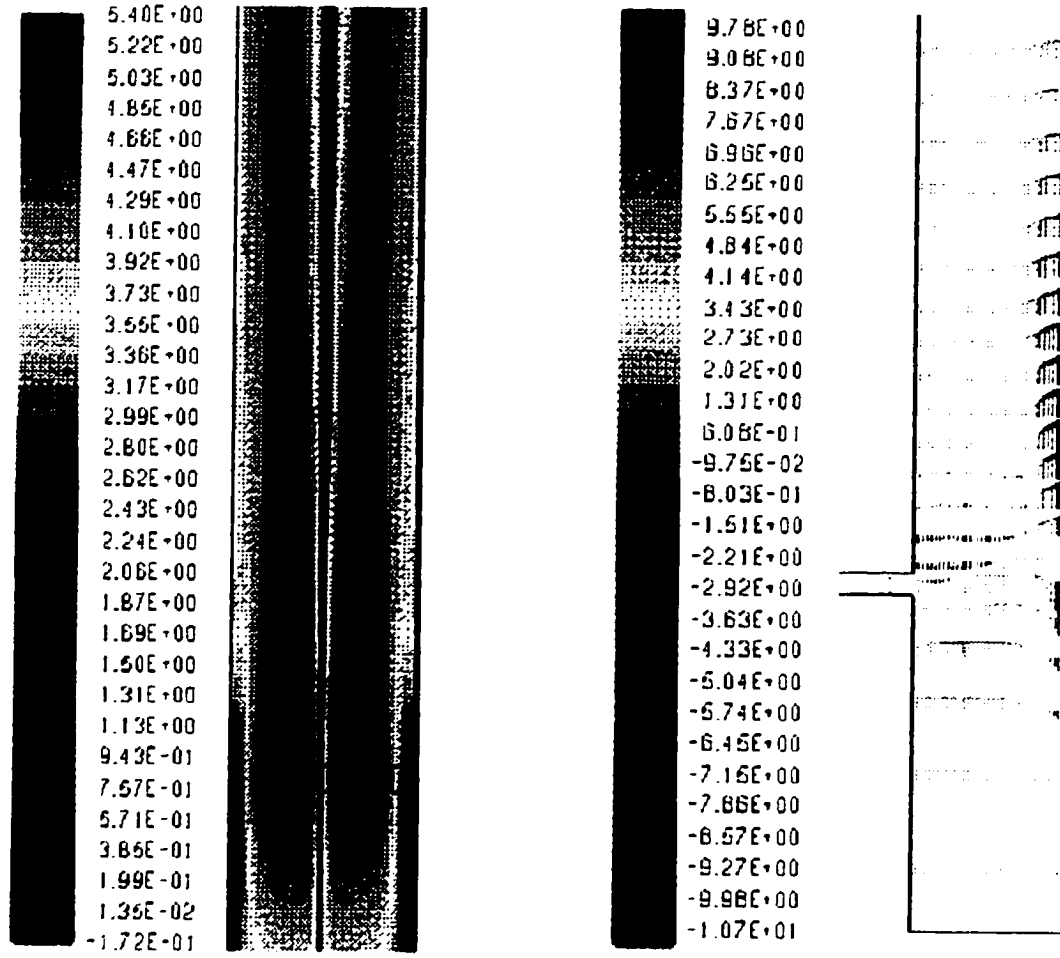

Figure 3.16. The effects of SA jets on the axial profile of axial velocity. Gas phase flow simulations with Fluent 4.4, SAR = 0.5.

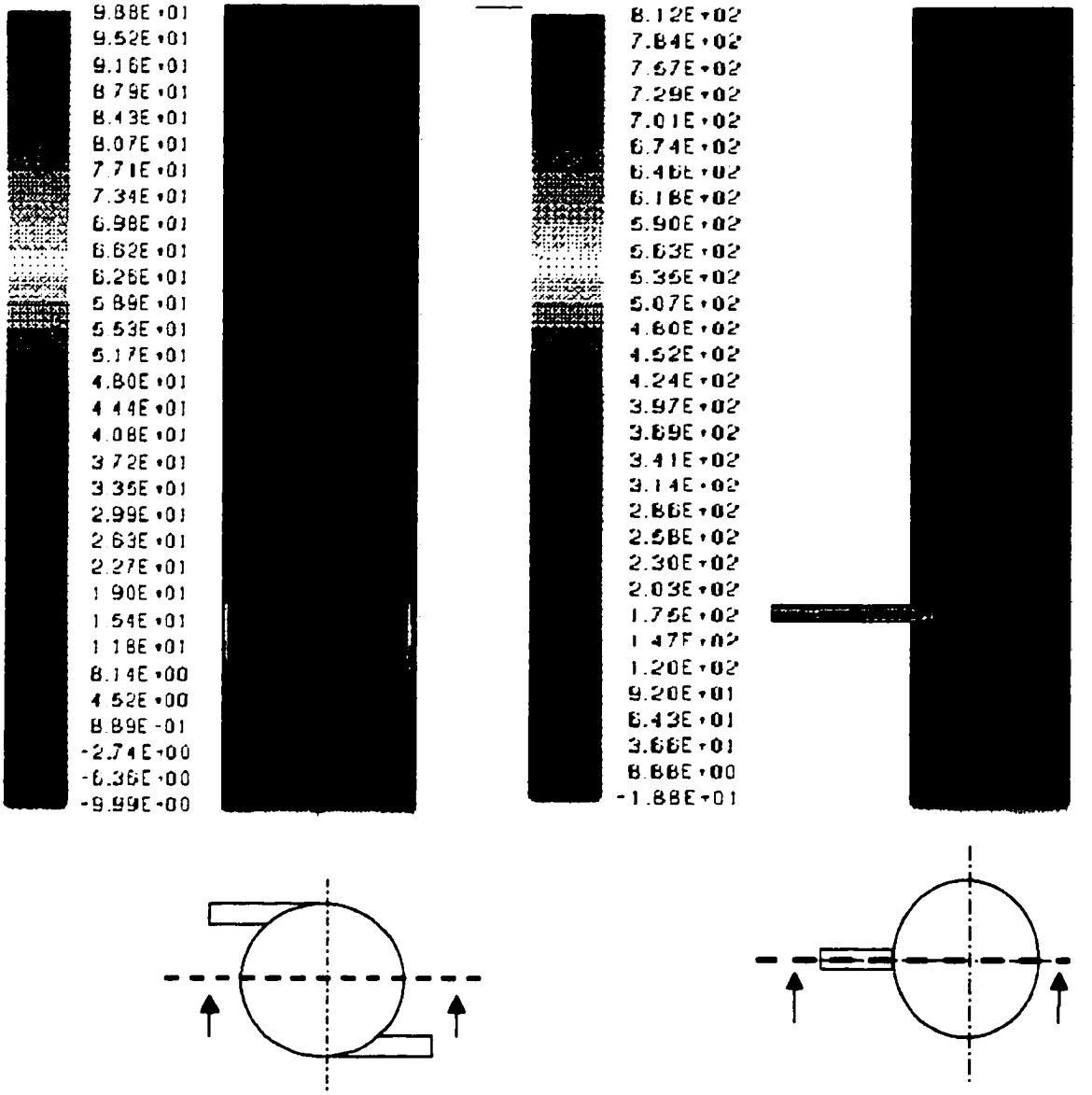

Figure 3.17. The distribution of total pressure (Pa) for tangential and radial SA injections, at the center slice. Fluent simulations, SAR = 0.5,

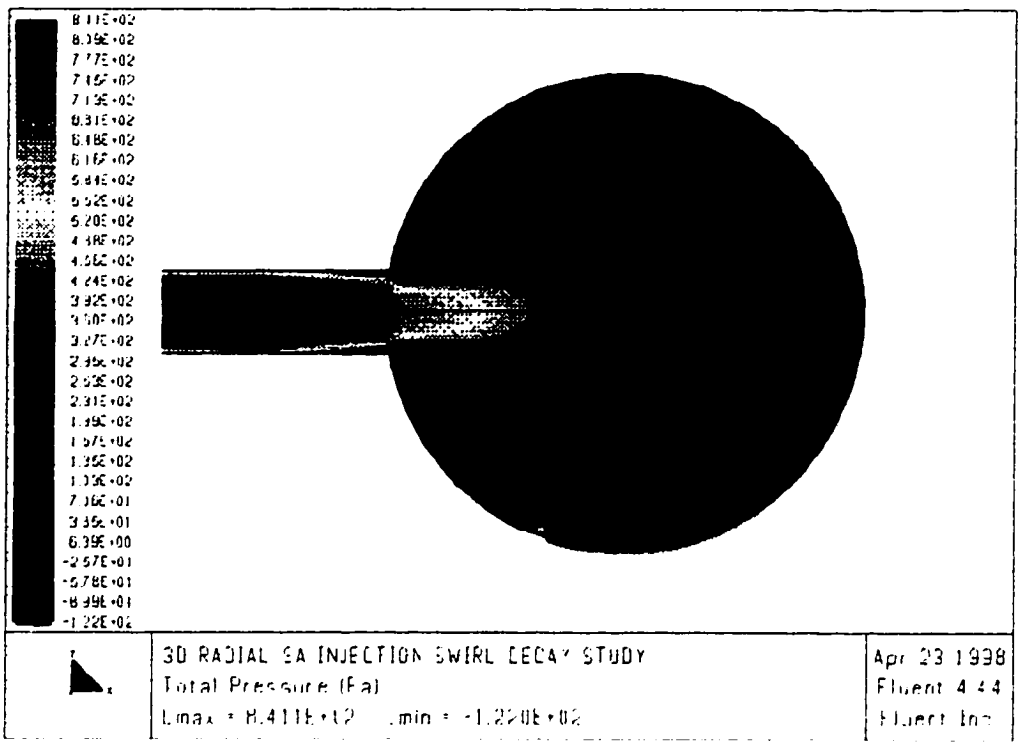

Figure 3.18. Variations in the total pressure at the SA injection plane. Fluent simulations, SAR = 0.5,

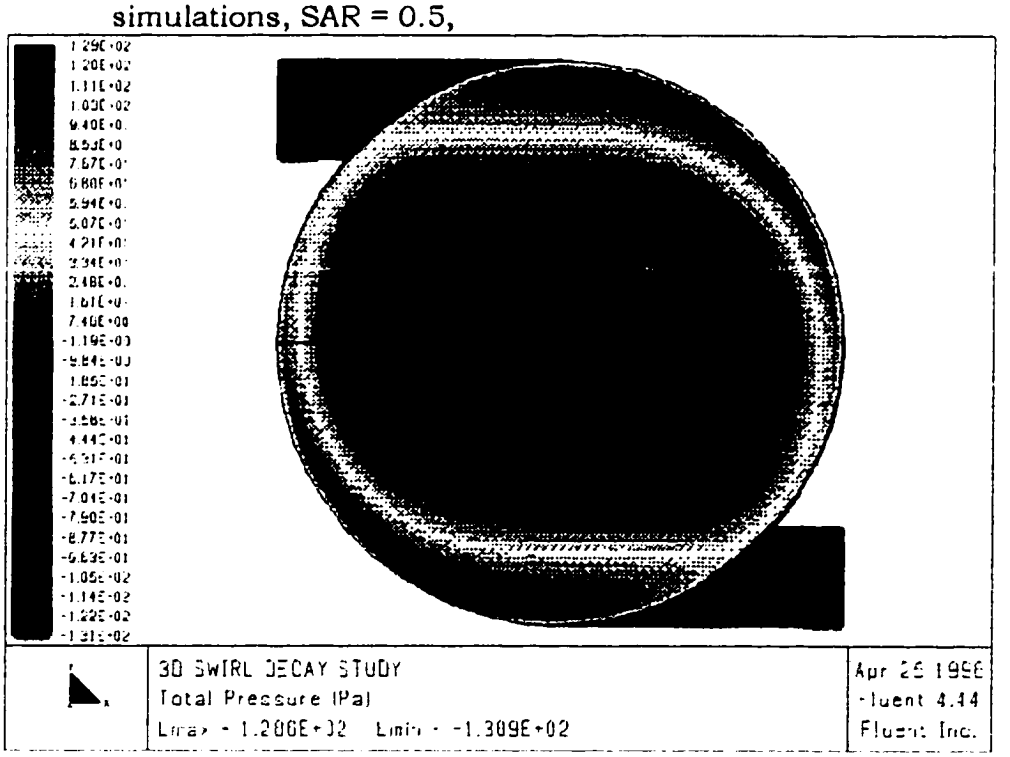

Figure 3.19. Variations in the total pressure at the to slice of SA injection port. Fluent simulations, SAR = 0.5,

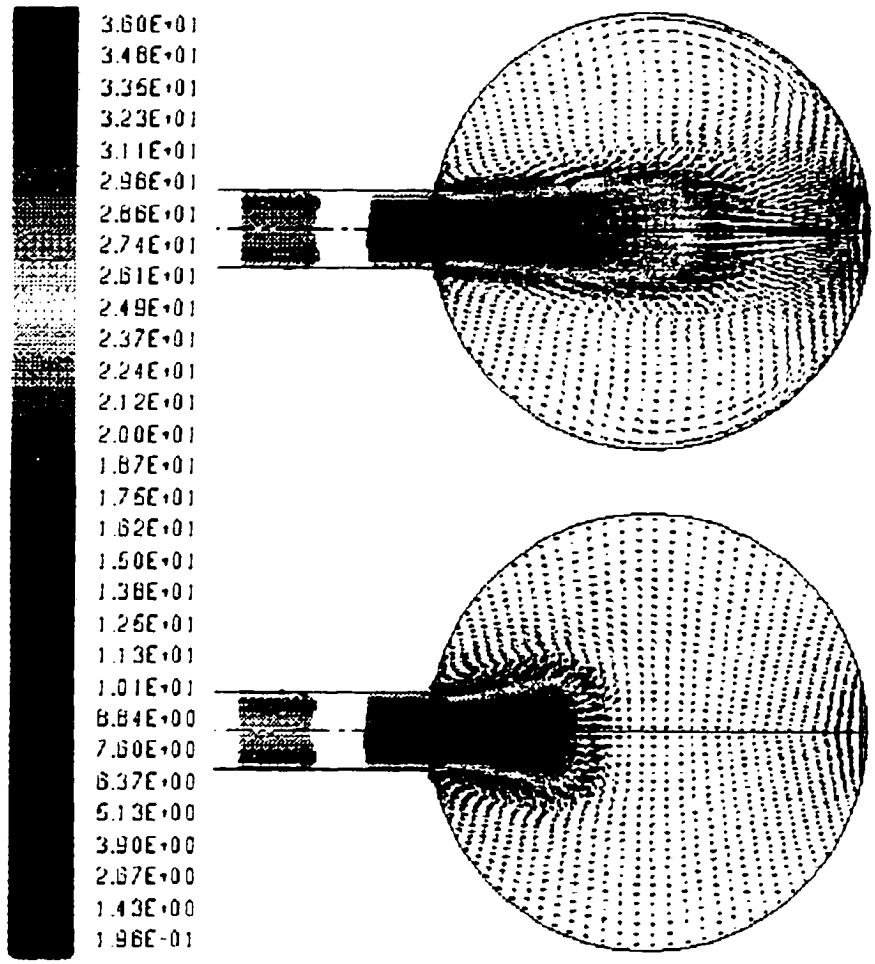

Figure 3.20. The velocity vector for SAR = 0.5 (top), and for SAR = 0.25. Fluent simulations, radial SA injection.

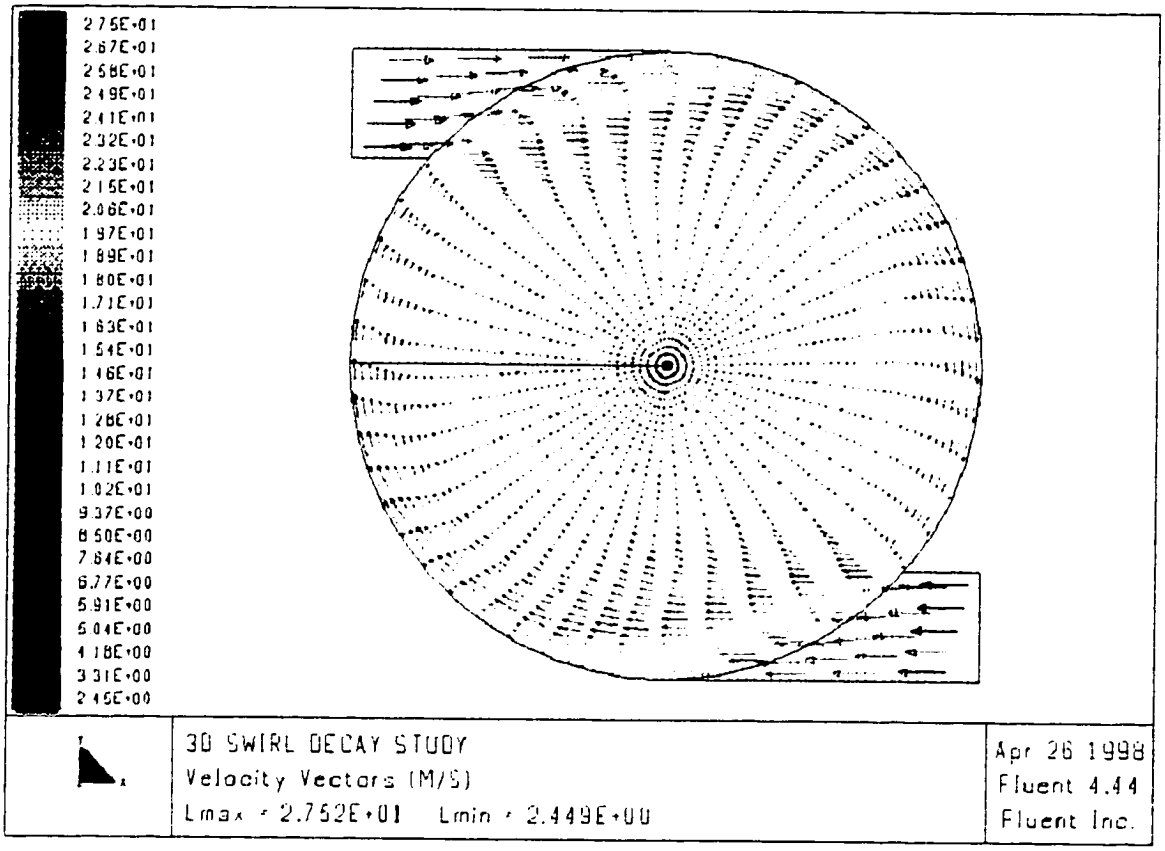

Figure 3.21. Vectors of velocity magnitude at the plane of SA injection. Tangential injection, SAR = 0.25.

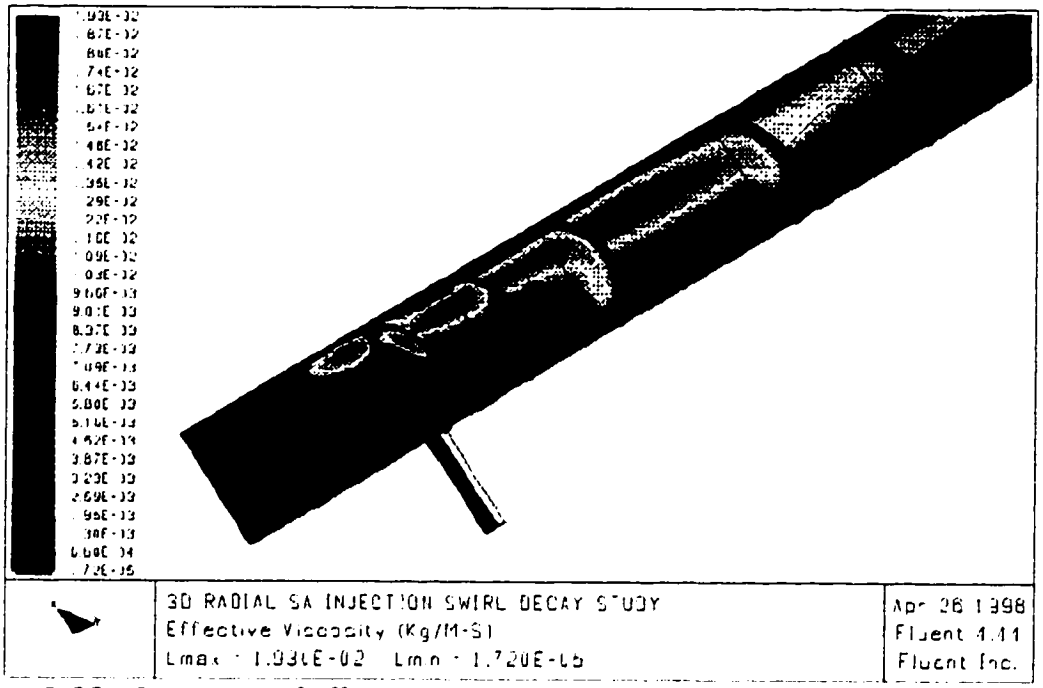

Figure 3.22. Contours of effective viscosity along the riser, radial injection, SAR = 0.5.

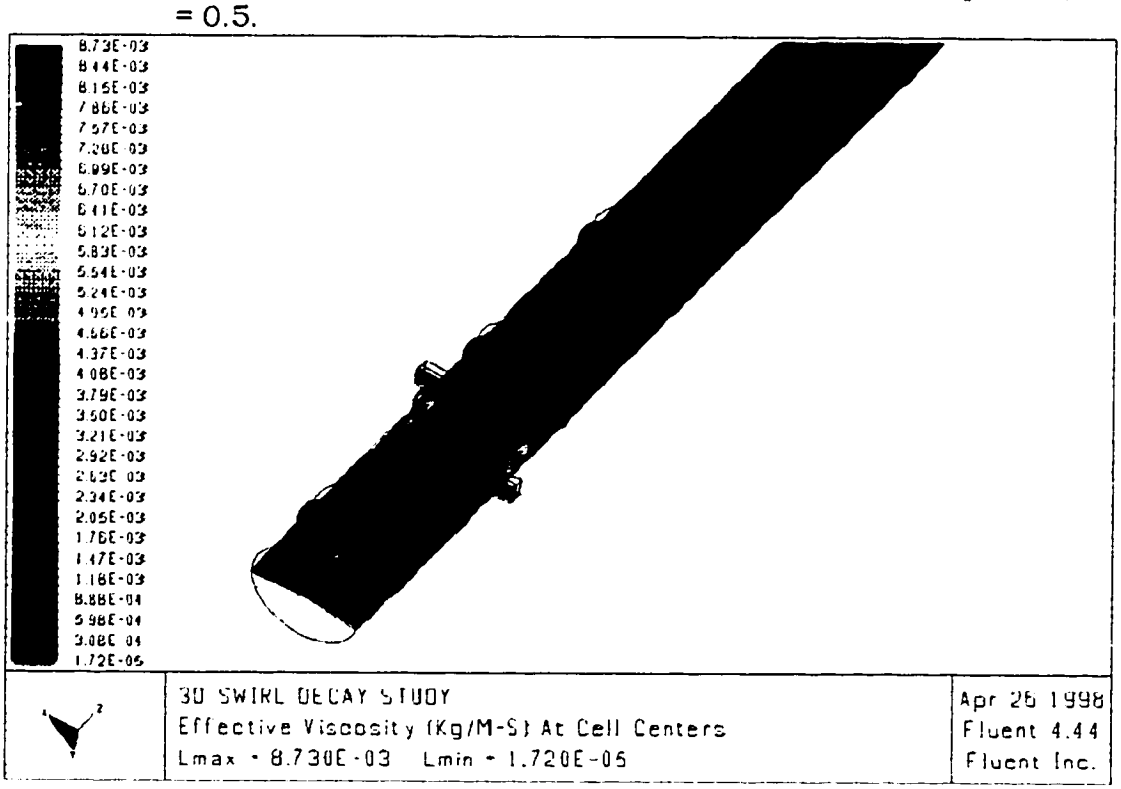

Figure 3.23. Contours of effective viscosity along the riser, tangential injection, SAR = 0.5, Fluent4.4 simulations.

5.5 Present Model for SA injection Region

Before attempting to quantify the effects of secondary air injection on the hydrodynamics of a CFB riser, it may be helpful to itemize the experimentally observed particulars of SA injection. The peculiarities of SA injection drawn from both gas-phase simulations and two-phase flow experiments are, then summarized as follows:

1)Solids Holdup Profiles:

i) Above SA injection region: The cross sectional average solids holdup either remains the same or decreases slightly depending mostly on the SAR.

ii) SA Injection Region: Higher solids holdups are attained when swirling air is injected. The holdup is higher when the SA is injected from lower sections of the riser. Local high-pressure regions are formed just below the SA jets, which pushes the suspension towards the sides like a solid obstruction in radial injection case, and towards the center core region for the swirling injection case. But, one has to consider the effects of centrifugal forces, which may impose a radial velocity component on the particles resulting in a motion towards the wall region. Therefore, a change in the suspension density profile is expected due to the jet mixing patterns. Emerging radial SA jets may result in a denser annulus and leaner core regions since the mixing with PA starts at the center of the riser, increasing the voidage in the core region. In the tangential injection case, however, although the radial diffusion of SA may result in a reverse effect on the local solids holdup profile, the suspension in the annulus region is denser due to the centrifugal and refluxing effects. The expected gas mixing patterns are illustrated in Figure 5.21.

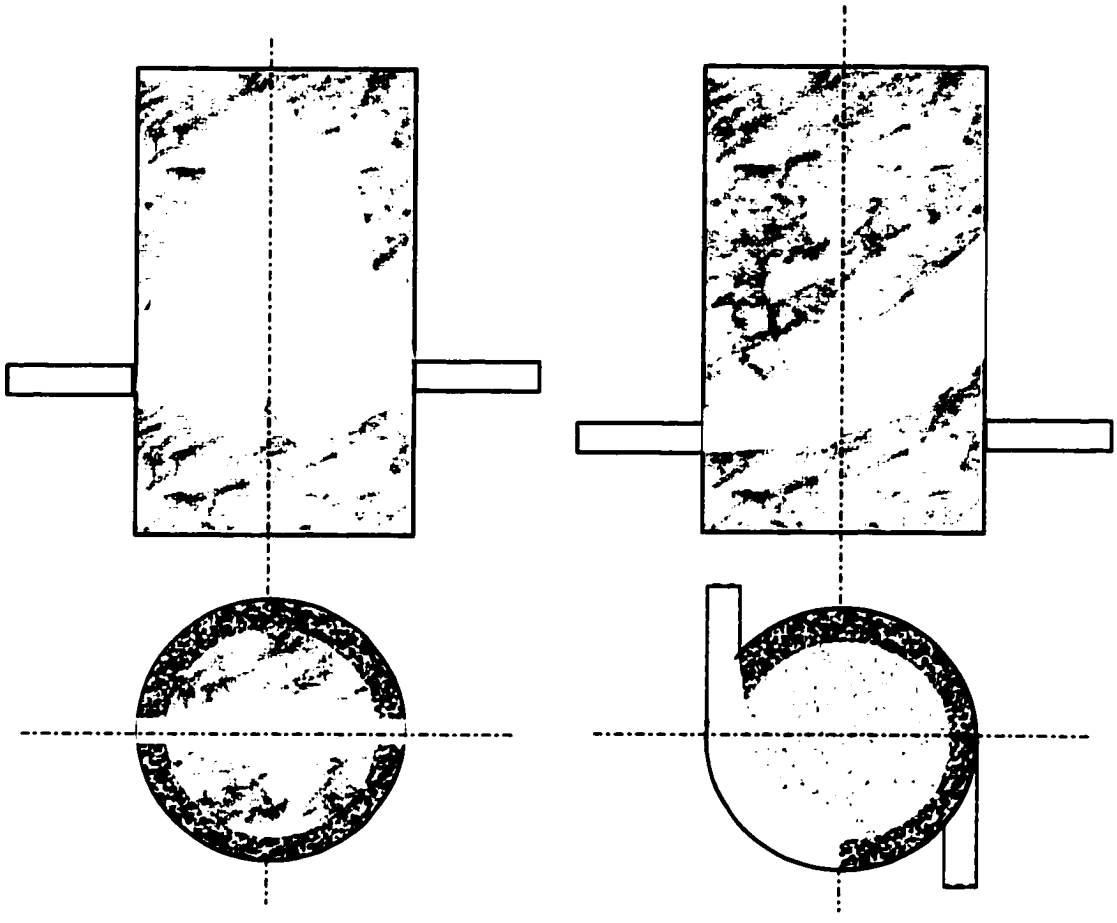

Figure 5.21. An illustration of gas mixing patterns and expected voidage profiles in the SA effective region for radial and tangential secondary air injections.

iii) Below SA injection Region: Addition of SA increases the suspension density in this region considerably. This increase is more pronounced with increasing SAR. Tangential injection of SA results in higher solids holdup in this region if a strong swirl is imposed. The extent of the dense region varies with the height of SA injection port, while an axial gradient in suspension density exists for all cases tested. The axial distribution of average (cross sectional) solids holdup is more uniform, and reduces sharply

above the SA injection level if SA is injected from lower sections. In other words, the axial gradient in the suspension density is more apparent if SA is injected from higher elevations.

2) Particle Velocity and Core Radius Profiles:

i) Above the SA Injection Region: The axial component of particle velocity and its radial profile seems similar for both SA and non-SA operation above a point where the jet emerging is complete. Down-flow in the annulus region exists. A more dispersed bed is observed which may suggest a flatter gas and particle velocity profile in this region.

ii) The SA Injection Region: Particle acceleration in the core region is observed just above the SA ports. Annulus region (in terms of downward particle velocity) seems to diminish in the very close vicinity of the SA jets, for high SAR injection for all modes of injection. Especially, the tangential SA jets seem to break the continuity of the annulus at the plane of injection, partitioning it axially into two separate regions. Gas phase simulations have shown that the radial location of maximum tangential velocity resides around the wall region at the axial location of injection, and shifts towards the centerline as the axial distance. Same pattern is also observed for the axial velocity for strongly swirling flows, which probably is the main reason behind this partitioning.

Acceleration of particles due to the injected additional air is followed by a deceleration due to the increase in the core radius. The thickness of the annulus region increases sharply just above the SA jets and expected to decrease gradually with axial location. Core flow is expected to assume a parabolic profile for all types of SA injection, except for high SAR swirling flows. Due to the reason explained above, higher axial gas velocities in the wall region may

impose a more turbulent particle velocity profile in the swirl effective region. The height of the swirl effective region is observed to vary proportionally with SAR and inversely proportionally with the local (annulus) suspension density.

Just below the SA jets, the lower extent of SA jets may distort the development of upcoming flow towards the sides. The particle upward motion in the core region is faster in the tangential injection case than it is in its radial counterpart, but non-SA operation gives the highest velocity due to the higher primary superficial gas velocity. The particle velocity profile is flat in the core, for both tangential and radial SA injections, while the extent of the flat region stretches more towards the wall if SA is injected radially. The particle velocity reduces to negative values sharply around the core-annulus interface.

iii) Below SA injection Region: Thickness of the annulus region is greater below the SA jets when compared to that of non-SA operation. Although the averaged values of particle velocity profile give a flat distribution, the RMS of velocity fluctuations is comparably higher than that obtained from the test sections above the SA port. This turbulent structure is more pronounced in the core-annulus interface. Particle velocities are greater for non-SA operations, and reduce considerably with increasing SAR.

Therefore a complete Type II model for prediction of the SA effects on the riser hydrodynamics need to account for the effects of emerging SA jets on local non-uniformity formed in the flow variables. These properties if listed are; 1) axial development of the core radius, 2) voidage profile in both primary and secondary air effective regions and, 3) particle motion patterns.

The local values of hydrodynamic properties may have different trends for various modes of SA injection. Therefore the height and mode of SA injection must be considered separately in considering the above items.

5.5.1 Height of SA Effective Region

Modeling of SA effective region starts with the estimation of the axial position of the SA effective region (H_{SAE}) and its extent through the riser (L_{SA}). Both the experiments and the gas phase simulations have shown that the lateral momentum incorporated with the secondary air jets influence the flow structure both upstream and downstream of the SA injection plane. The extent of the SA effective region towards the primary region may be considered as minor compared to that of its downstream counterpart. The local high-pressure regions created underneath the jet influence the upcoming flow by pushing the upcoming suspension towards the local low-pressure regions away from the jets, and create circulation regions beneath the jets. Related experiments have shown that at the first velocity test section the particle velocity profile is very similar for both tangential and radial SA injection cases. At the second test section (17 cm below SA jets), however, although the profiles are similar for SAR= 0.25, the effect of mode of the SA injection was apparent for SAR=0.5, tangential injection resulting in higher particle velocities in the core region. Therefore, the extent of SA effective region towards upstream into suspension is related to the SAR and the diameter of the riser. Although the effect of the riser diameter on the lower extent of the SA effective region is not studied experimentally, the model, as a first approximation, assumes that the extent increases with increasing riser diameter and models as:

$$H_{SAE} = H_{SA} - SAR^{*}D_t \qquad (5.41)$$

H_{SAE} denotes the axial coordinate of the beginning of SA effective region and it is estimated with Equation 5.31 regardless of the mode of injection. Here, one has to note that the above equation is a very rough approximation and should be re-considered for larger rises. The height of the SA effective region, on the other

hand, is governed by the boundary of the emerging jets and should be modeled separately for different modes of SA injection.

Ljungdahl and Zethraeus (1996) investigated the jet propagation through a two-phase gas solid flow experimentally. Based on Beer and Chigier (1983) formulation for jet propagation through a cross flow, they proposed an empirical formula, which relates the axial propagation to its radial counterpart.

$$\frac{r}{d_0} = k\lambda^b \left(\frac{z}{d_0} \right)^n \tag{5.42}$$

where λ is the momentum ratio of cross flow and approximated by;

$$\lambda^2 = \frac{1}{\rho_j u_j^2} \left(\rho_g u_g^2 + \frac{G^2}{\rho_b - \rho_g} \right) \tag{5.43}$$

the subscripts j and g refers to the properties of the jet and of the upcoming gas, respectively. Also, ρ_b denotes the bulk density of the suspension and can be estimated locally by;

$$\rho_b = \varepsilon \rho_g + (1-\varepsilon)\rho_s \tag{5.44}$$

Ljungdahl and Zethraeus, by using data both from industrial and laboratory scale fluidized beds, found that the equation 5.42 represents the experimental data very well if the constants are selected to be;

k= 1.23, b=-0.8, n=0.218

Therefore the model estimates the height of the SA effective region above the SA injection plane by using Equation 5.42. Here, one has to note that in case of comparably small diameter risers, the radial component of the penetration length estimated by the above formula may be even bigger than the radius of the riser. In our riser, for example, since the radial SA jets are opposing each

other at the same horizontal plane, some simplifying assumptions has to be made especially if strong secondary air jets are issued. In such a case, since the location of SA jets in our problem is symmetric with respect to the center of the riser, the radial component of the jet penetration may be limited with the riser radius. The axial location which defines the upper end of secondary air effective region is estimated by considering the difference in the radial distance traveled between the two consecutive iterations. i.e., the computation ends if the radial location of jet center is within 0.001m of that calculated for the previous axial location.

The local radial velocity of the jet can be calculated from an equation given by Ljungdahl and Zethraeus (1996).

$$\frac{du_j}{dz} = -\frac{u_j}{r}\frac{\rho_g}{\rho_j}\frac{\sin(5\alpha)+3\sin(3\alpha)+2\sin(\alpha)}{\cos(5\alpha)+5(\cos(3\alpha)+2\cos(\alpha))} \qquad (5.45)$$

where z is the axial coordinate, r is the jet radius, α is the angle of dispersion and approximated by;

$$\alpha = 11+11^{*}\cos(\phi) \qquad (5.46)$$

ϕ is the angle of deflection and is given by the same reference to be 22°.

Therefore the height of the SA effective region for radial SA injection is given by;

$$L_{SA} = z + SAR^{*}D_t \qquad (5.47)$$

Where z is estimated by using Equation 5.42. In case of a tangential injection, the height of the SA effective region must be estimated differently due to the different jet emerging patterns attained in the riser.

Chang and Dir (1994) experimentally studied the swirl decay problem in a similar geometry. They measured the axial, the radial and the tangential components of the local gas velocity in a single-phase swirling flow by a straight

wire anemometer, in search for the axial decay of tangential component of gas velocity. They also proposed an empirical correlation, which relates the swirl intensity to initial momentum ratio to estimate the axial decay of swirl intensity in single-phase flows. Our model is based on their propositions and modifies their relation for two-phase flows.

The ratio of the momentum flux through the injectors to the total momentum flux through the test section is an important parameter of the swirl decay modeling and defined as;

$$\frac{M_s}{M_t} = \frac{\dot{m}_s^2}{\dot{m}_t^2}\frac{A_t}{A_s} \tag{5.48}$$

where subscripts s and t refer to the SA region and riser total respectively, m and A denote the mass flow rate and the cross sectional area of flow respectively.

It is also important to define the decay rate of swirl intensity along the riser. The local swirl intensity, Ω, is defined as the ratio of rate of tangential to total momentum flux at a cross section, and given as (Chang and Dhir, 1994):

$$\Omega = \frac{2\pi\rho\int_0^R UWrdr}{\rho\pi R^2 U_{ave}^2} \tag{5.49}$$

where U_{ave} is the bulk axial velocity of the gas, and R is the radius of the riser. The numerator in Equation 5.49 is the tangential momentum flux integrated over the cross section, while the denominator is the total momentum flux based on the bulk axial velocity. It may be useful to note that at the injection location, the local swirl intensity defined by Equation 5.49 should be equal to the initial momentum flux ratio defined by Equation 5.48 due to the conservation of momentum.

The experimental findings of Chang and Dhir (1994) showed that the swirl intensity decays approximately exponentially with the axial distance. The ratio of decay rate $-d\Omega/d(x/D)$ to the local swirl intensity as a function of the dimensionless axial distance is correlated as $(x/D_t)^{-0.3}$. As a result of the study, they proposed the following relation to express the decay of swirl intensity;

$$\Omega = 1.48\left(\frac{M_s}{M_t}\right)^{0.93} \exp\left[-K\left(\frac{x}{D_t}\right)^{0.7}\right] \qquad (5.50)$$

where x is the axial distance downstream the swirl generator and the decay constant is modeled as a function of the initial momentum ratio as:

$$K = 0.113\left(\frac{M_s}{M_t}\right) \qquad 5.51$$

Incase of two-phase flow however, the axial decay of swirl intensity is faster due to the presence of particles. Unfortunately, there is not enough information in the open literature to estimate the axial decay of swirl intensity for the case of gas-solid riser flows. In this work, Equations 5.50 is modified to account for the presence of particles. The proposed model uses:

$$\Omega = 1.48\left(\frac{M_s}{M_t}\right)^{0.93} \exp\left[-K\left(\frac{x}{D_t}\right)^{1.55+100\varepsilon_s - SAR}\right] \qquad 5.52$$

and,

$$K = 0.113\left(\frac{M_s}{M_t}\right)^{0.95} /(1-8\varepsilon_s) \qquad 5.53$$

where ε_s is the solid fraction in the annulus. Here, one has to note that the suspension in the wall region of the SA effective zone is observed to be much

denser than it is for SAR = 0. In the computations, the value of ε_s is assumed to be equal to that of the average solids holdup in the annulus.

The modifications of Equations 5.50 and 5.51 are performed considering the visually observed height of swirling wall region, which is explained in Chapter 3. The visual observations covered only the wall region and the data obtained from related measurements are very scattered. Therefore re-modification and verification with other experimental data may be necessary for confident use in predictions. The problem; effect of particle loading in a CFB riser on the swirl intensity, is still open for further investigations. The present study uses equations 5.52 and 5.53 to estimate the upper extent of SA effective region.

5.5.2 Axial Development of the Core Radius

The thickness of the annulus region is an effective parameter for the prediction of flow properties in the core annular models. Therefore its accurate estimation is seen as an asset for reliable model results.

The experimental results related with the development of the core-annulus interface are presented and discussed in Chapter 3. Qualitatively, upon introduction of the SA, core radius in the primary bed shifted towards the riser center, increasing the thickness of the annulus. The axial gradient in the axial profile of the core radius is smaller in the primary region compared to that of the flow with SAR=0. However, the thickness of the annulus becomes very thin or sometimes completely diminishes just above the SA jets, suggesting a discontinuity in the axial profile of the annulus region. But, further up along the riser, re-development of the annulus region is observed. A comparison of the predictions of Equations 5.4 and 5.5 gives that the discrepancy between the experimental results and the prediction may result in up to 5% of the radius at the section of the injection. The velocity measurements (FCC) from the second level SA injection experiments show that the height of this region may be more than 80 cm, and therefore should be taken into consideration.

According to the results of the experimentally found core development profiles for both sand and FCC particles, the model modifies Equation 5.4 and 5.5 to account for staging with secondary air injection. The modified decay constants account for the SAR and the density of particles. The new sets of equations is in better agreement with the experimentally determined core radius in the region of measurements as can be seen from Figures 5.21-5.24. The modified equations are:

$$\frac{\delta}{D_t} = \frac{(SAR + 1.55)\rho_s}{2\rho_{sand}} \mathrm{Re}_t^{-(0.30)} \left(\frac{H_t}{D_t}\right)^{0.21} \left(\frac{H_t - z}{H_t}\right)^{2*(1+SAR)} \tag{5.54}$$

$$\frac{\delta}{D_t} = \frac{\left(0.9 - SAR\dfrac{\rho_s}{\rho_{sand}}\right)}{2} \mathrm{Re}_t^{-(0.31+SAR/10)} \left(\frac{H_t}{D_t}\right)^{0.21} \left(\frac{H_t - z}{H_t}\right)^{0.7-SAR} \tag{5.55}$$

where ρ_{sand} is the density of the silica sand used in the experiments (2600 kg/m^3).

The proposed model predicts the core radius between the acceleration region and the SA effective region with Equation 5.54. It is experimentally observed that within the SA effective region, the core radius increases sharply starting from just below the SA jets. Then, it reduces steeply just above the SA injection plane and increases gradually with the riser height, expected to converge to a thinner annulus than that of non-SA operation at the extent of SA effective region. This sharp increase and decrease in the core radius profile occurs over a short axial distance, thus an average profile may be assumed within the region considered. The model assumes a sudden increase in the core radius profile at the upper extent of the primary region, and determines the core radius with Equation 5.55. Therefore, the model predicts the core radius with Equation 5.54 in the primary region, then with Equation 5.55 in the upper parts of the riser.

Figures 5.22 to 5.25 show the axial profile of the core radius predicted by Equations 5.54 and 5.55. In these figures the model predictions are compared with the experimental data for various operating conditions in the riser. Figure 5.22 shows that the model predicts experimental data in the primary and SA effective region very well, except in the very close vicinity of the SA jets. In that specific region, although a vanishing annulus region is measured, the model assumes that the annulus region is continuous throughout the riser, which probably is the case for larger diameter risers. For larger risers, although the injection velocity of SA jets are in the same order of magnitude, the fraction of the peripheral area that the SA jets occupy is expected to be much smaller than it is in our lab-scale riser. Therefore one may expect a continuous down-flow with a thinner annulus in the SA injection region of larger diameter risers. This argument could not be verified due to lack of experimental data from larger risers.

It may be interesting to note that the model also predicts an increase in the axial gradient of solids suspension density with decreasing height of SA injection plane as it can be seen from Figure 5.23. The same behavior is verified with the pressure drop measurements that, as the SA injected from lower positions, the difference in the suspension density just above and below the SA jets increases considerably.

Figure 5.24 show that the combination of Equations 5.54 and 5.55 successfully predict the effect of SA jets on the thickness of the annulus region not only for various SAR but also for different particle groups. Figure 5.25 shows the model predictions on the effect of SA injection (SAR=0.5) on the axial profile of core radius for sand and FCC particles. It is very interesting to see that the model predicts a more apparent distortion on the core radius profile of sand particles than it is for FCC particles if both operated under the same conditions. Unfortunately due to the different fluidization characteristics of the particle groups, it was not possible to operate both sand and FCC under the same

operating conditions, thus experimental verification of the above prediction is not complete.

A major disadvantage of Equations 5.54 and 5.55 is that they take neither the solids flux nor the mode of the SA injection into consideration. Also, the predictions depend on the aspect ratio of the riser, which may need to be re evaluated for specific risers.

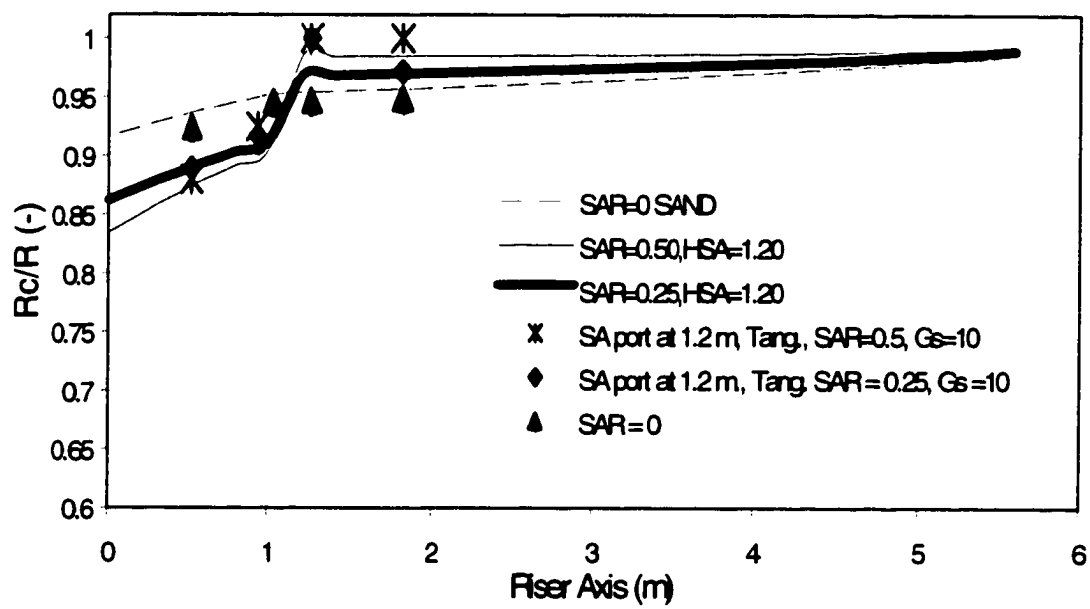

Figure 5.22. Comparison between experimental data and model predictions on the variation of core radius with SAR. SA injection from 1.2 m above distributor plate. Sand particles, U_0=3.37 m/s below and 5m/s above SA port.

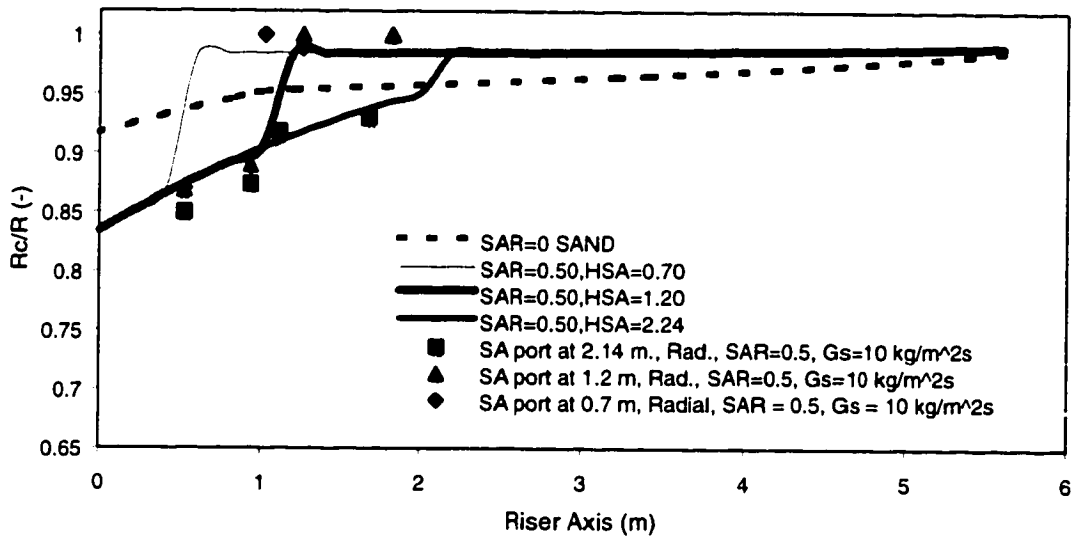

Figure 5.23. Comparison of experimental data with model prediction on the axial development of core radius for varying height of SA injection. Sand particles, SAR = 0.5, Uo=3.37 m/s below and 5 m/s above SA jets.

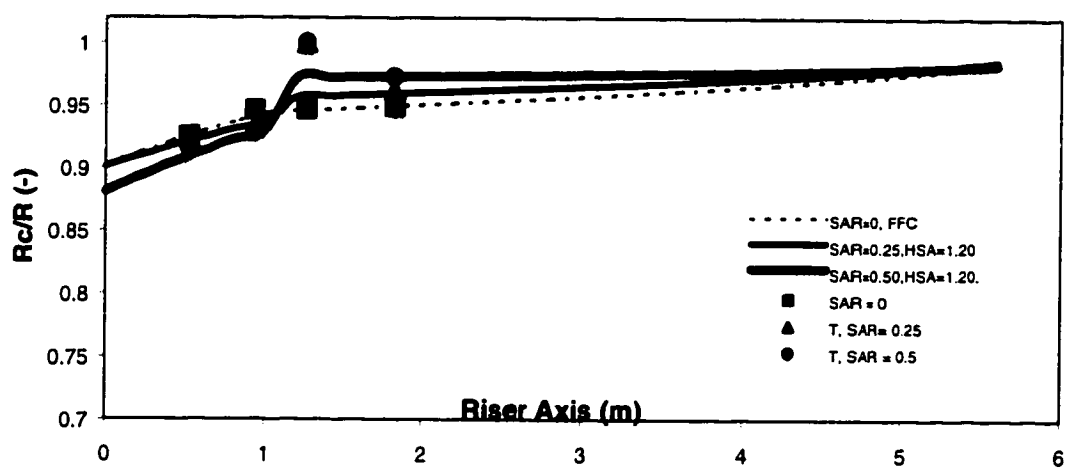

Figure 5.24. Comparison of model predictions with experimental data for the effect of SAR on the axial profile of the core radius. FCC particles, SAR= 0.5, Uo=2 m/s below and 3 m/s above SA port.

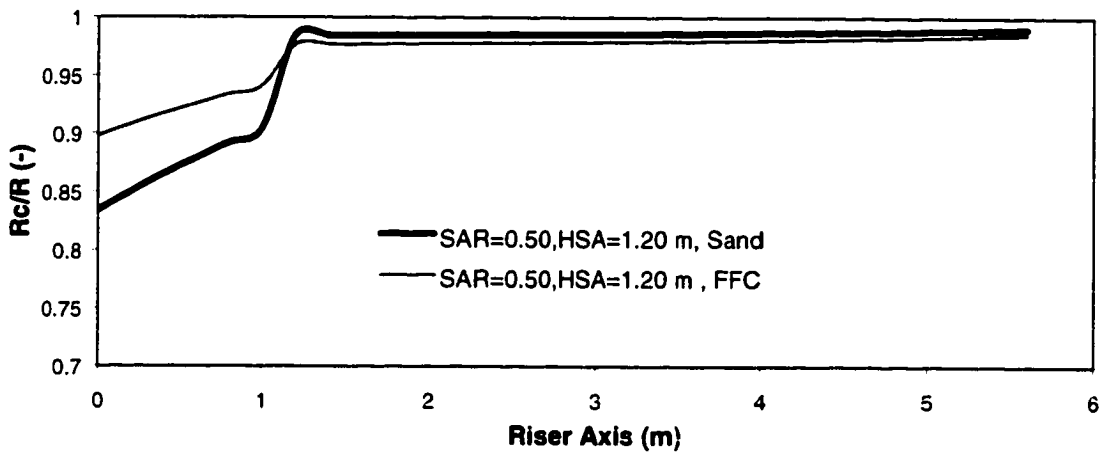

Figure 5.25. The effect of particle properties on the axial development of core radius. Model predictions, SAR = 0.5, Uo=3.37 m/s in the primary region and 5 m/s above SA port.

5.5.3 Voidage and Particle Velocity Profiles in the riser with SA injection

For a steady operation, the mass flow rate of solids through the riser is constant due to the continuity, and axial variations in the cross sectional average properties are calculated by considering the axial continuity in the properties (Equation 5.56). The radial variations, on the other hand, are estimated by incorporating radial profiles for pre-determined cross sectional average values. The base model estimates the particle velocity and voidage profiles in the fully developed region by assuming that the solids flux profile in the riser is governed by Equation 5.1, based on the idea of "similar" solids flux profiles.

$$\dot{m}_s = v_p \rho_p A_r (1-\varepsilon) = \text{Constant} \qquad (5.56)$$

With the introduction of secondary air, however, due to the increase in superficial gas velocity, the cross-sectional average particle velocity in the region above the SA injection plane increases. Since the mass flow rate of the solids is constant throughout the riser, the increase in particle velocity in SA injection

case, must be accompanied by an increase in the cross sectional average voidage in the related region.

Before modeling radial profiles of the flow properties, it may be necessary to discuss the effect of staging to the axial distribution of cross sectionally averaged flow properties. In search for the response of the solids mass flow rate to staging with secondary air, it may be helpful to compare the results of three different operating conditions; operation with primary superficial gas velocity throughout, operation with total superficial gas velocity throughout, and operation with staging.

Let subscript '1' denote the flow properties with primary superficial gas velocity only (SAR = 0), subscript '2' for flow with total air (SAR = 0), subscript '3' for operation with staging. And let subscripts 'b' and 'a' denote the regions below and above the SA injection plane respectively.

Ignoring the cut-off effects of the SA jets, and assuming that the primary superficial gas velocity is adequate enough so that no changes in the regime of fluidization is expected with staging, the mass flow rate of solids for each operation;

$$\begin{aligned} \dot{m}_{s1} &= v_{s1}\rho_s A_r \varepsilon_{s1} \\ \dot{m}_{s2} &= v_{s2}\rho_s A_r \varepsilon_{s2} \\ \dot{m}_{s3,a} &= v_{s3,a}\rho_s A_r \varepsilon_{s3,a} \\ \dot{m}_{s3,b} &= v_{s3,b}\rho_s A_r \varepsilon_{s3,b} \end{aligned} \qquad (5.57)$$

for staged flow, the mass flow rate of solids above the SA injection plane must be equal to that of below the SA injection plane due to the continuity, therefore

$$\dot{m}_{s3,a} = \dot{m}_{s3,b} \qquad (5.58)$$

on the other hand, in staging case, the mass flow rate of solids in the lower section of the riser should be equal to that of flow only with primary superficial

gas velocity if the solids flux (Gs) is kept constant. And since the superficial gas velocity is the same, one may expect that the voidage should be the same, also.

$$\dot{m}_{s3,b} = v_{s1}\rho_s A_r \varepsilon_{s1} = \dot{m}_{s1} \tag{5.59}$$

Although the superficial gas velocity is greater, the solids mass flow rate in the upper region of the staged flow is exactly the same as that of the non-staged flow, provided that the same amount of fluid is introduced through the distributor plate. In such a case, the cross sectional average value of the voidage in the upper region of a staged riser is comparable with that of the non-staged flow operating with the same primary superficial gas velocity. This can be seen from Equation 5.60.

$$\varepsilon_{s3,a} = \frac{\varepsilon_{s1} v_{s1}}{v_{s3,a}} \tag{5.60}$$

Equation 5.57 states that, if the solids flux is kept constant, the cross sectional average voidage attained with various superficial gas velocities are also comparable through the cross-sectional average particle velocity and riser diameter.

Therefore, the cross sectional average voidage in the upper section of a staged riser can be calculated by using Equation 5.60 provided that the average particle velocity is known. The radial distribution of the voidage, however, may be slightly different than that of non-SA operations in the SA effective region.

The local values of voidage and particle velocity for non-SA flow are estimated with numerical iterations (trial and error method), using the similar solids flux profiles of Rhodes et al. (1992) and the definition of solids flux (Gs). The non-dimensional solids flux profile is assumed to be a parabolic profile, maximum in the center, zero at the core annulus interface and negative in the annulus region. Therefore the shape of the parabola is determined by the location of

core-annulus interface at any axial location, smaller core radius implying more 'laminar' profiles.

The visually observed effects of SA injection parameters on the solids holdup profiles are explained early in this chapter. Unfortunately, since direct voidage measurements are not performed, the visual observations could not be quantitatively supported by direct measurements. But, the axial variations in the core radius quantitatively support that the voidage just above the secondary air injection plane increases considerably for a short axial distance with the introduction of secondary air. As a qualitative summary; the air staging with SA injection increases the voidage in the region above the injection plane due to the extra amount of air injected, and reduced it in the region below the injection plane. The effects of SAR and the height of injection on the flow properties are accounted for implicitly in the core radius profile formulation.

The results of particle velocity measurements did reveal clear indications of the effects of the intensity and the height of SA injection over the axial development of particle axial velocity. However, it was not possible to confidently quantify a particular trend on the effect of mode of injection on the core radius development. Therefore, the effects of mode of SA injection need to be identified and accounted for separately.

It is visually observed that the mode of SA injection is a major parameter determining the mixing patterns of primary and secondary air streams. Tangential SA jets diffuse into the upcoming suspension gradually through the walls inward, whereas radial SA jets mix with the primary stream diffusing from the center region, outwards. Also, the effect of mode of SA injection on the solids suspension density in both primary and SA effective regions are clearly seen from the differential pressure drop measurements. Tangential injection of SA, compared to its radial counterpart, resulted in higher solids suspension density in both of the regions (primary and SA effective regions). One of the reasons for this increase in suspension density is seen as the helical motion path imposed

on the particles, which is discussed in detail in the presentation of experimental results. But, although the helical motion pattern is seen as an important source of increased solids holdup just above and below the SA injection plane, it is not applicable in explaining the higher solids holdups attained in the bottom region of the riser if tangential SA is injected. The difference obviously is a consequence of the jet emerging patterns, since it is the only operational difference between the two cases considered.

The different jet propagation patterns attained with different modes of SA injection impose difficulties in two-dimensional approximation of the problem by increasing the non-uniformity in the third dimension. For example, the tangential SA jets, just emerging from the SA port (4 cm in diameter), occupy 35% of the riser radius (11.5 cm), considerably reducing the core radius if the core region is defined as the region where the solids move upwards. The variations in the effective thickness of the tangential SA jets as the jets move away from the injection point is believed to vary with both SAR and the axial momentum, stressing the angular non-uniformity associated with jet emerging. Unfortunately, it was not possible to study the extents of the jet emerging in the angular dimension experimentally. The problem at the axial location of SA jets is three dimensional, and some sacrifices has to be made for the two dimensional approximation of riser hydrodynamics.

In this work, the effect of mode of injection is accepted to be resulting from the jet emerging profiles, and considered separately for above and below the SA injection plane for both radial and tangential injections, and modeled as follows;

Above the SA injection plane:

Radial Injection: The solids holdup distribution is expected to be lower in the core region due to the jet propagation, and higher towards the wall. Zhang et al. (1991)'s empirical correlation (Equation 4.13) over-predicts the core voidage and under-predicts the voidage in the wall region for a given cross sectional average voidage. Therefore the model uses Equation 4.13 for the radial

distribution of suspension density using the cross sectional average value of voidage estimated with the method of the base model.

Tangential injection: The wall region is experimentally observed to be denser than the other injection modes, which is attributed to the centrifugal forces exerted on the particles by the swirling air. Therefore, the radial distribution of solids is expected to be more towards the wall, and due to the helical motion of the particles, the suspension density in a selected volume is expected to be higher that it is for the non-SA operation. Thus, the model uses the core voidage distribution calculated with the base model (SAR = 0), and uses Zhang's equation for the radial distribution in the annulus region to account for the centrifugal forces. Expressed mathematically;

$$\begin{aligned} \varepsilon_r &= 1 - \frac{G_r}{\rho_s v_{p,r}} && \text{in the core} \\ \varepsilon_r &= \varepsilon_{ave}^{0.19+(r/R)^{2.5}+3(r/R)^{11}} && \text{in the annulus} \end{aligned} \qquad (5.61)$$

Below the SA injection Plane:

In this region, the increase in the solids suspension density is seen as the result of the cut-off effects of the SA jets and modeled accordingly for different modes of injection.

The single-phase flow simulations have shown that local high-pressure regions are created underneath the jets. The model assumes that the intensive SA jets form a solids obstruction through a portion of the riser cross section, reflecting the up-coming particles that are axially aligned with the SA jets back to the primary region. Since the effects of reduced superficial gas velocity is accounted for in the core radius formulation, the estimation of jet cut-off effects on the solids holdup in the primary region requires the solution of a special problem which may be defined as the *solid obstruction over an upcoming suspension*, as illustrated below.

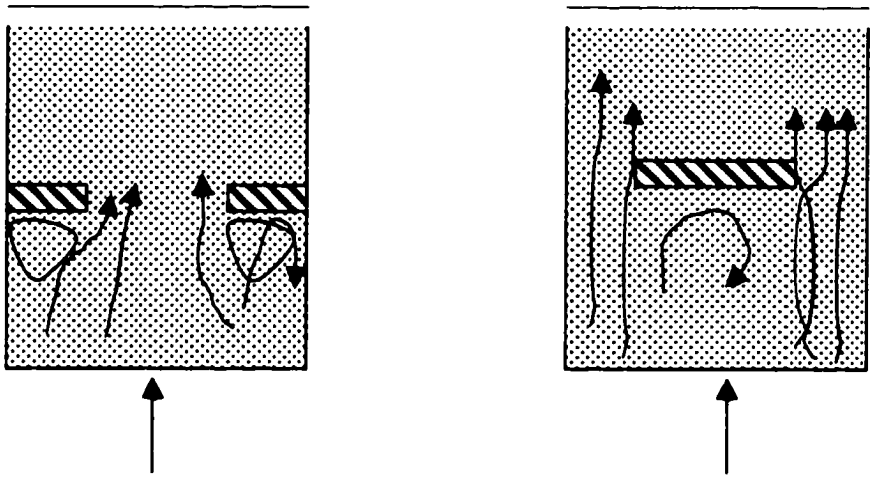

Figure 5.26. Illustration of reduced effective flow area with solid body obstruction.

In such a case, a portion of the solid particles is entrained an re-circulated, but some of them is expected to hit the obstruction and stay in the dense bottom part. In this problem the external solids circulation rate is kept constant. Then, since the superficial gas velocity is constant, a denser suspension at the reduced cross sectional area is expected in order to account for the solids that hit the obstruction and stay in the bottom region. In the extreme case of very large and dense particles, if the obstruction area is very large, it may not be possible to keep the solids circulation rate constant. On the other hand, in the extreme case of single-phase fluid, the obstruction would create some extra load on the blower due to the extra pressure drop, but would not effect the amount of incompressible fluid in the primary region. Further, in case of very light and small particles some solids accumulation in the primary region is expected, but this amount would be comparably small since the aerodynamic response time of the particles is very small. Therefore, in this work the amount of solids accumulation in the primary region due to *jet cut-off effects* is related to the aerodynamic response time of the particles through the Stokes number.

In this work, the amount of solids accumulation in the primary region due to the cut-off effects is estimated with the following equation.

$$\varepsilon_{s,cutoff} = \varepsilon_s \frac{A_c}{A_r}\sqrt{St} \qquad (5.62)$$

where, A_c is the area of contraction and A_r is the total area of flow. Then, the total solids holdup is calculated by superposing $\varepsilon_{s,\ cutoff}$ over ε_s. The exponent of Stokes number is taken as 0.5 as a first approximation. To the author's knowledge, the exact solution or a better approximation of the cut-off effects of solids obstruction is not complete, and requires further investigations.

The methods used in calculation of the effective jet size for tangential and radial injections are as follows.

Radial injection: Following Ljungdahl and Zethraeus (1996), the jet expansion angle is assumed as 22°. The jet propogation calculations have shown that, for both of the secondary air ratio considered, the radial jets expand through the centerline of the riser. Therefore the jets are assumed to form an effective obstruction, in a trapezoidal cross sectional are between the injection point and the centerline with a symmetric 22° expansion which is illustrated in Figure 5.26. The effective obstruction area is then;

$$V_{J,r} = D_r\,(2d_o + D_r \tan 22^o)/2 \qquad (5.63)$$

Where d_o is the diameter of the SA jets at the plane of injection, and $V_{J,r}$ is the cross sectional area occupied by the effective SA jets for radial SA injection.

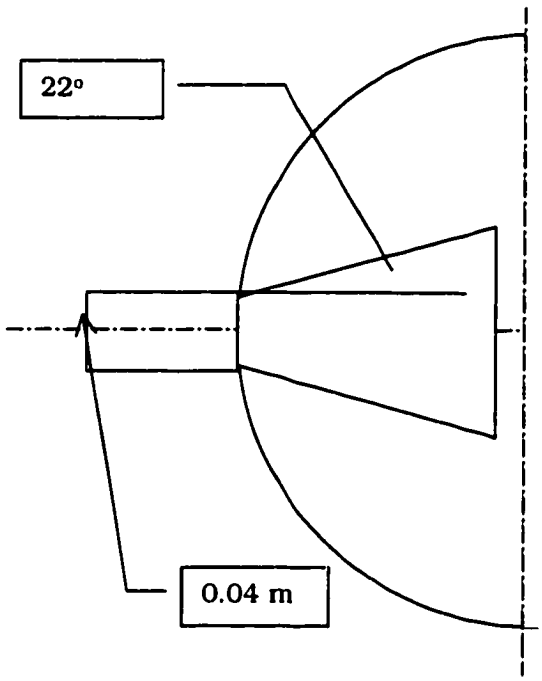

Figure 5.27. Cross sectional view of radial SA jet propagation.

Tangential injection: For this case the jets are assumed to form an obstruction in the form of a hollow cylinder with a thickness of jet diameter over the riser cross section.

$$V_{j,t} = d_o * \pi (2 D_r - d_o)/4 \qquad 5.64$$

Various modeling methods are proposed in the literature for estimation of particle velocity in the annulus. Some of the approaches are presented in Table 4.1. Due to the very intermittent gas-solid flow in the core-annulus interface in the primary region, usually a constant particle velocity is assumed. Generally, the particle velocity in the annulus is approximated as equal to the terminal velocity of particles. However, our experimental results have revealed different trends. For FCC particles, for example, although the terminal velocity of the particles is calculated as 0.3 m/s, a down-flow velocity of up to 1 m/s is measured. Kan (1980) have showed that the terminal velocity of clusters may be much higher than that of the single particles. Therefore this high downward velocity is attributed to the formation of clusters in the annulus region. For sand particles, on the other hand, although the single particle terminal velocity

is calculated as 3 m/s, the measured downward particle velocity was measured as high as 2 m/s, with average in the order of 1 m/s. The explanation for the FCC particles can not be valid for this case, since with the cluster formation, one would expect higher downward particle velocities than that of the single particle terminal velocity. The slower particle downward motion in the case of fluidized sand particles is attributed to the intermittent behavior of the annulus flow.

Although the proposed model calculates the particle velocities in the annulus region, it restricts the downward particle motion in the annulus with a pre-selected 1.5 m/s for sand and 1 m/s for FFC particles, for better representation of the nature of downward flow in the riser.

The results obtained from model simulations are compared with the results from the experiments in Figures 5.28 through 5.37. Figure 5.28 shows the axial profiles of average voidage in the core, average voidage in the annulus and also the cross sectional average voidage along the riser axis for tangential injection of SA from 1.2 m above the distributor plate. Since voidage measurement are not performed, the predictions are not verified with experimental data, but the profiles indicate that the location of SA injection is the upper extent of the dense region.

Figures 5.29 through 5.32 compare the particle axial velocity predictions with that of the experiments for FCC particles. The model predictions are quite satisfactory, except in the third velocity test section, which is located just above the SA injection plane. The measurements show that the particle flow is upward in this section, even in the close vicinity of the wall, whereas the model predicts down-flow in the wall region. The reason for this discrepancy arises from the core radius formulation, which imposes a comparably smooth transition through the SA jet effective region. On the other hand, the vanishing annulus region may be a consequence of the riser diameter used in the experiments, and for larger diameter reactors the annulus region may not vanish but become thinner with the SA injection as the model predicts.

Figure 5.33 show the axial profile of solids flux, which is upwards in the core region, and it converges to the external solids circulation rate at the exit of the riser. Figure 5. 34 and 5.35 show that the model is in good agreement with the experimental data in the case of SAR=0, also.

Figure 5.36 shows the model predictions for the radial distribution of voidage at various axial positions. The voidage just above the SA injection position reads low values in the annulus but even higher in the core region, suggesting a local minimum for the solids holdup just above the SA injection.

Figures 5.37 shows the model prediction on the effect of SA injection height on the particle velocity profile at 1.35 m above the distributor plate. A denser suspension (thicker annulus region) is predicted if SA is injected from higher elevations.

5.6 Conclusion

The gas solid flow behavior in a CFB riser with secondary air injection is mathematically modeled with a type-II core-annular approach. The present model is a two-dimensional model, which predicts axial and radial variations in both suspension density and particle axial velocity. The CFB riser is divided into two regions in the base model; an acceleration region at the riser base and a fully developed above the acceleration region. A third region, which is called the SA effective region, is incorporated in the model to account for the effects of the mode, the height and the intensity of the secondary air jets.

In the present model, the particles are considered as disperse, and move upwards in the core region, downwards in the annulus region. A plug flow assumption is made in modeling the gas phase hydrodynamics, restricting the net upward gas flow with the core region, only. The solids flux profile in the riser is determined from the "similar solids flux profiles" assumption of Rhodes et al. (1992a). Particle velocity profile is assumed to be parabolic. The maximum particle velocity is assumed to be in the riser center with a value determined from the definition of maximum slip velocity. The particle velocity and voidage

profiles are estimated with an iterative numerical technique, to best represent the similar solids flux profiles. Location of the core radius at any axial position of the riser is estimated with a modifying modified form of Wherter (1994)'s empirical equation to predict the thickness of the annulus region. The modified core radius equation account for the effects of both axial location and intensity of secondary air jets, as well as the fluidized particle properties.

The acceleration region is considered as the region where the differential pressure measurements over-estimate the suspension density since the acceleration of particles involves additional pressure drop in the riser. The height of the acceleration (L_{acc}) is calculated by considering the upward motion of a single particle, originally at rest at the distributor plate level. The particle is subjected to the gas flow and its path is followed through equation of motion. The axial location where the particle assume a constant velocity is then located as the upper bound of the acceleration region. In this region, the core radius is assumed as constant and only the cross sectional average values of the properties for both core and annulus regions are calculated. The model requires pre-determination of the voidage at the base of the riser, and following Puggsley et al. (1996) the voidage at the base of the riser is assumed to be equal to 0.85.

The model assumes that the joint effects of the three important parameters of SA injection determine the cross-sectional average suspension density and particle velocity profile in a staged riser. The effects of SAR and the height of injection are accounted for in the core radius formulation. The effects of mode of injection on the other hand, is considered as arising from the jet propagation patterns, and it is incorporated in the model by superposing the cut-off effects of SA jets on the existing solution of the flow field. For the radial injection case, the height of the secondary air effective region is estimated by using and empirical formulae proposed by Ljungdahl and Zethraeus (1996). For the tangential SA injection case, the empirical equation of Chang and Dir (1994) is modified for two phase swirling flows, and the axial location where the momentum ratio decays under 5% of its initial value is accepted as the upper

extent of the SA effective region. The model does not consider the exit effects, therefore it may not reveal good indication of the flow properties at the exit region of the riser.

Comparisons with available experimental data show that the present model not only successfully predicts the particle flow field throughout a CFB riser, but also reflects the effects of secondary air injection parameters on the riser flow field. The model is tested for Geldart's type A and B particles, and the model predictions are in agreement with the experimental data for both cases.

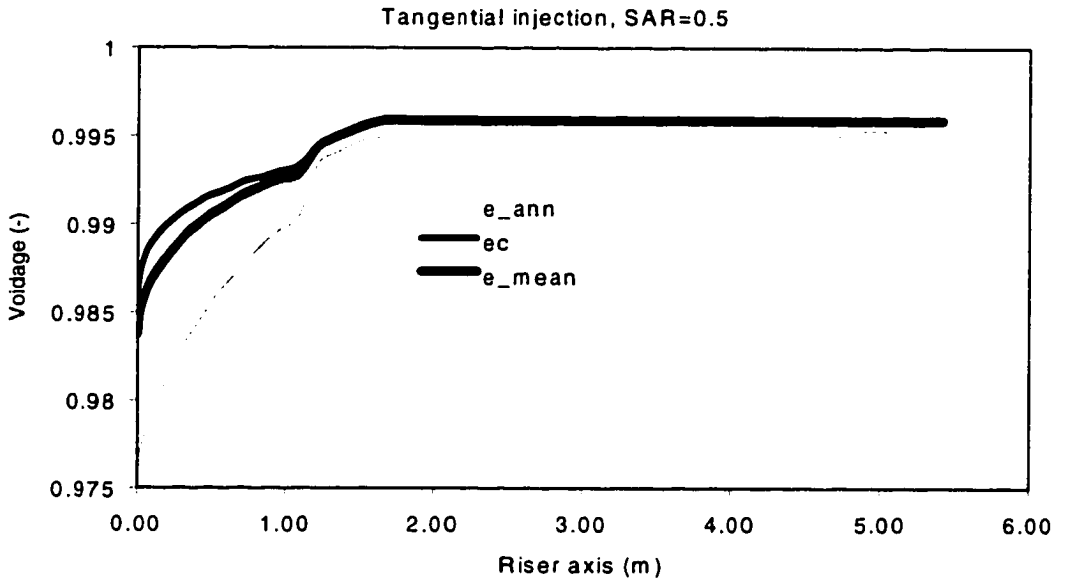

Figure 5.28. Axial profiles of cross sectional average voidage.

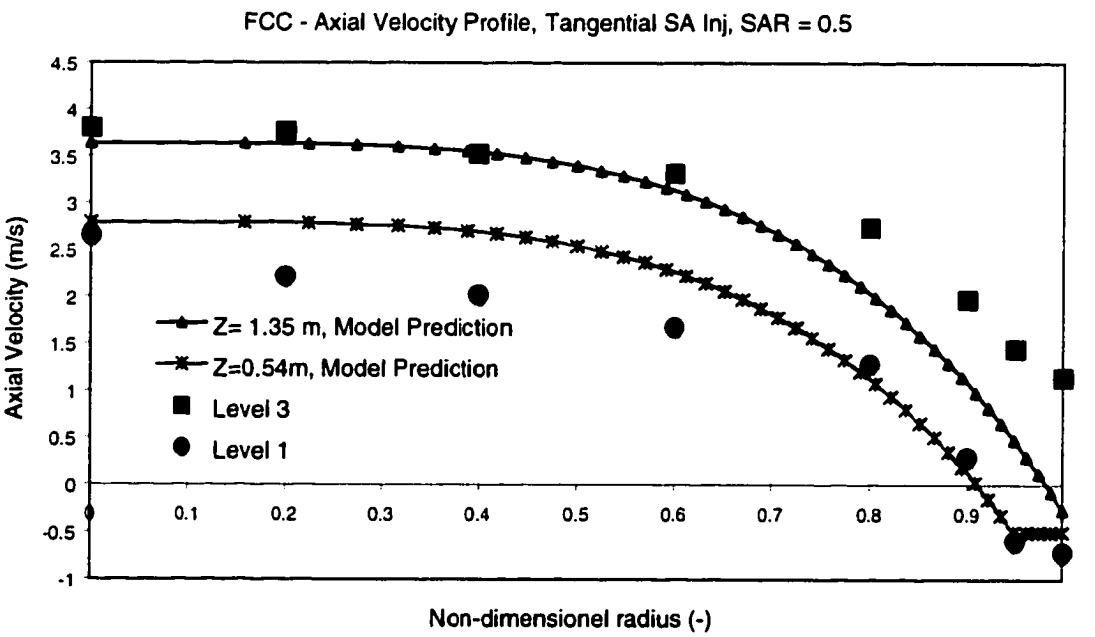

Figure 5.29. Radial variations of particle axial velocity. Model comparison with experiments.

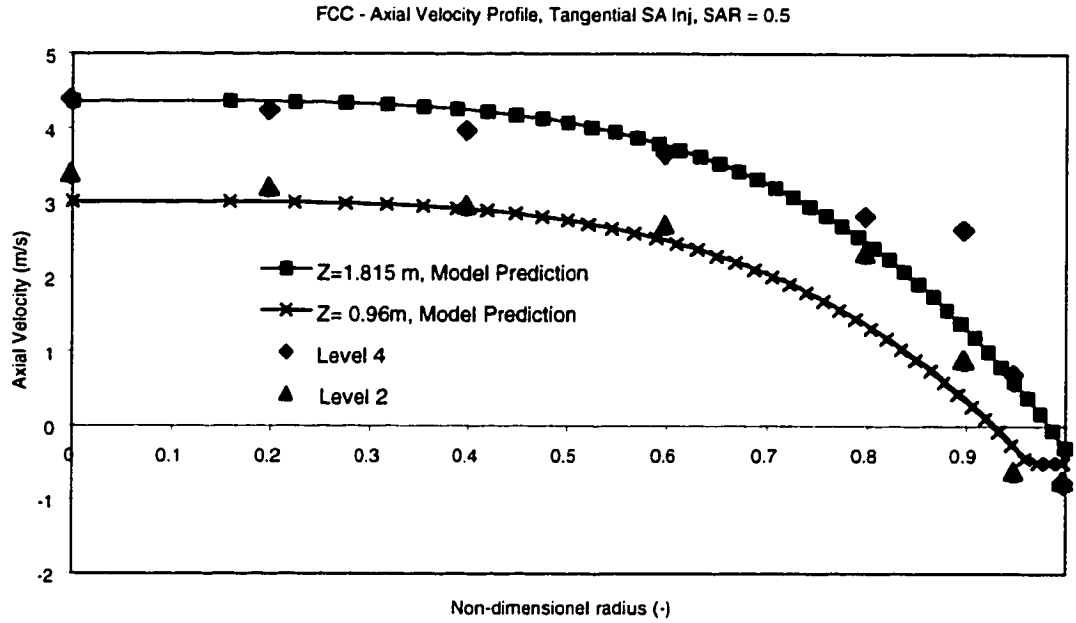

Figure 5.30. Tangential injection, particle axial velocity, SAR 0.5

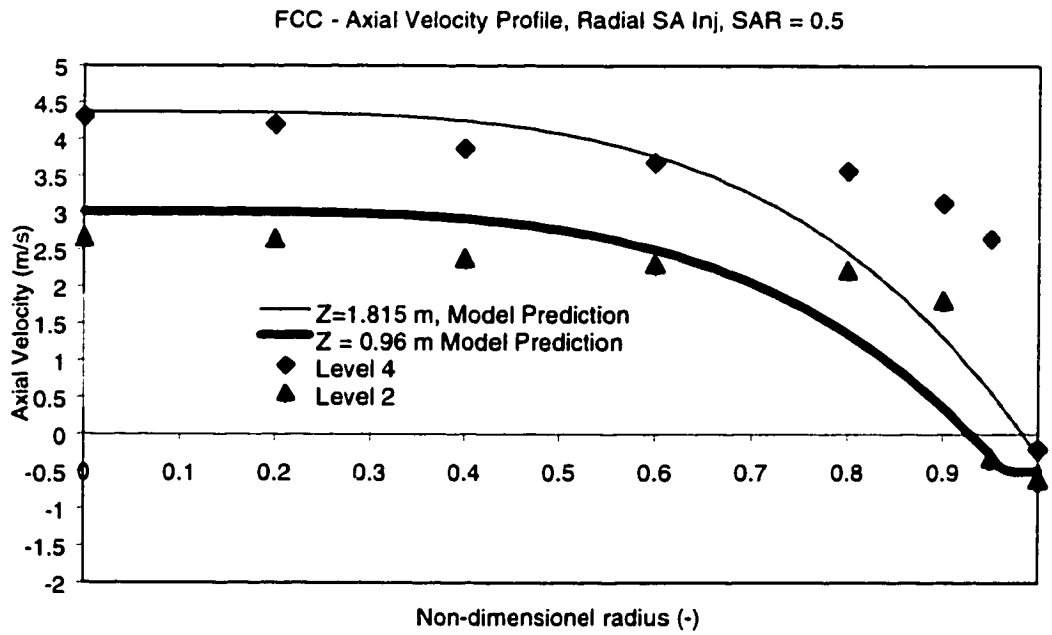

Figure 5.31. Radial profile of particle axial velocity. Gs = 18 kg/m²s, FFC

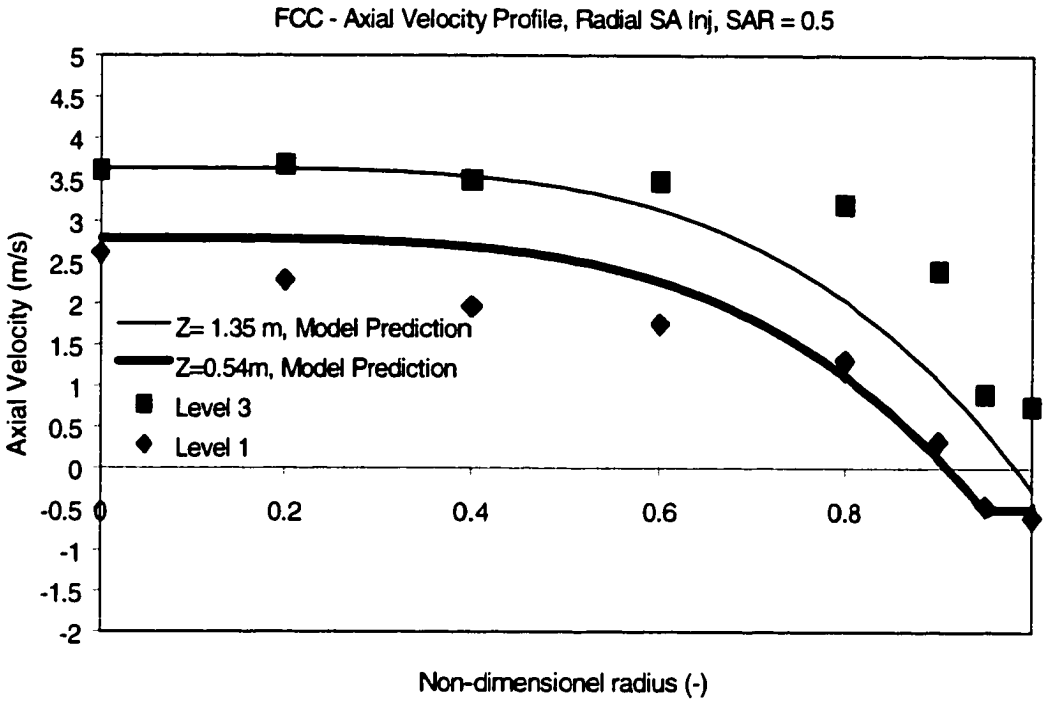

Figure 5.32. Radial profile of particle axial velocity. Model predictions compared with measurements.

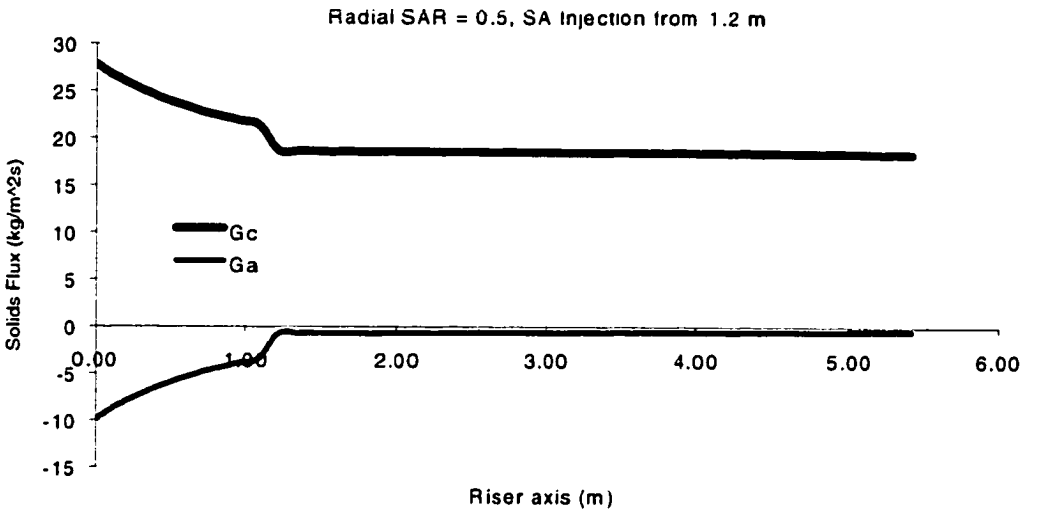

Figure 5.33. Axial profile of cross-sectional average solids circulation rate in core and annulus. Model predictions.

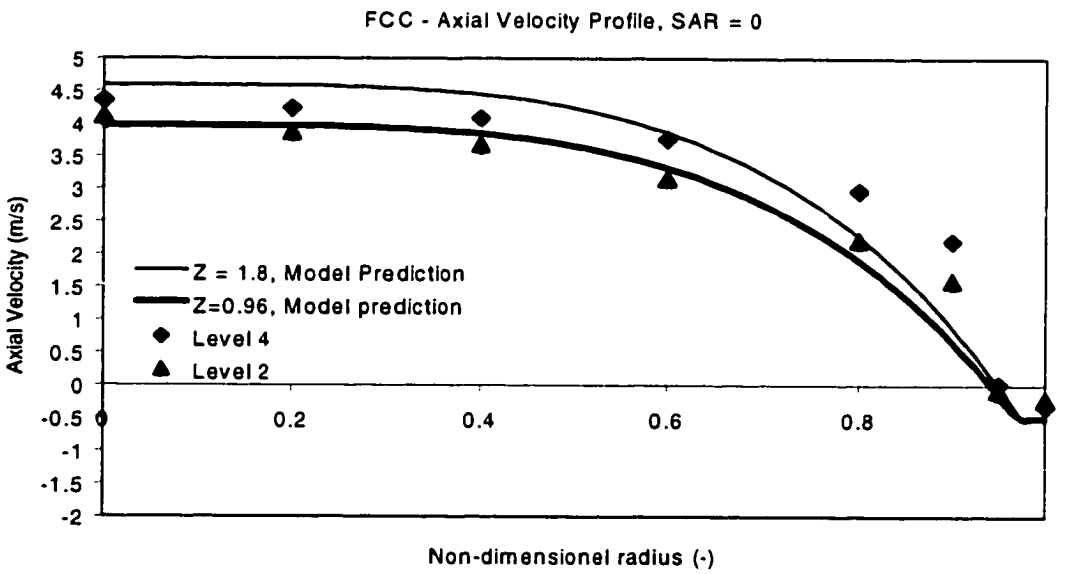

Figure 5.34. Radial profile of particle axial velocity (SAR = 0, FFC)

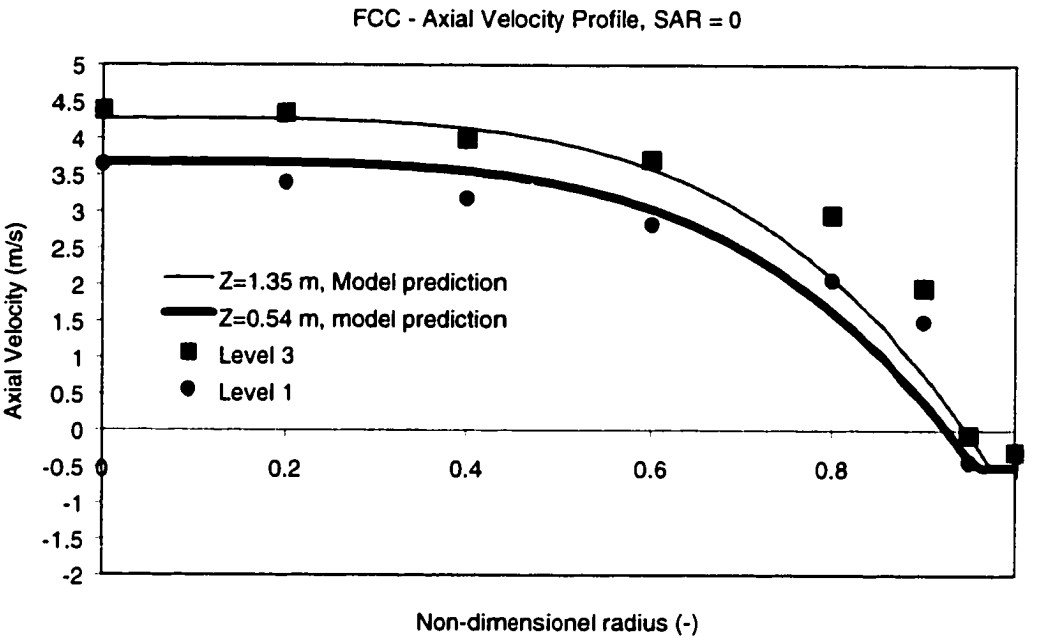

Figure 5.35. Radial profiles of particle axial velocity. SAR = 0, FCC particles.

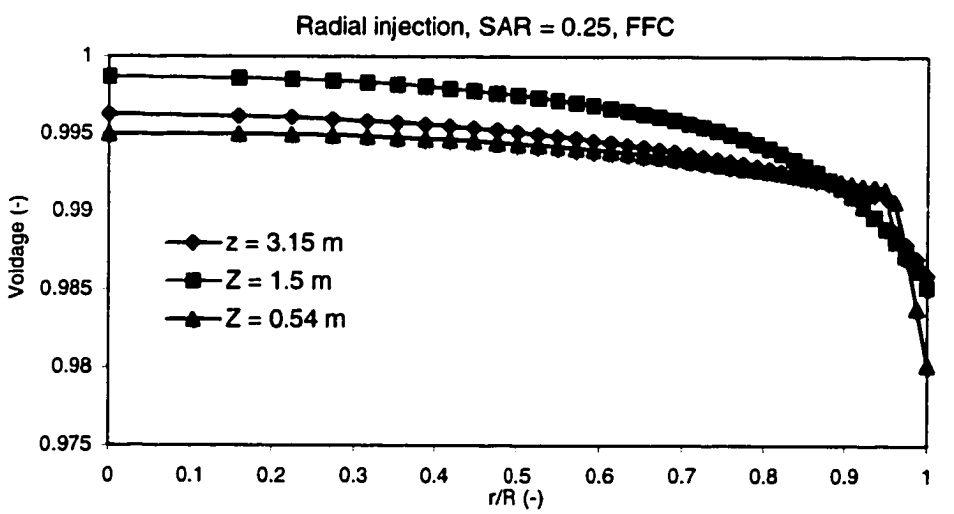

Figure 5.36. Radial variations in voidage at various axial positions, model predictions.

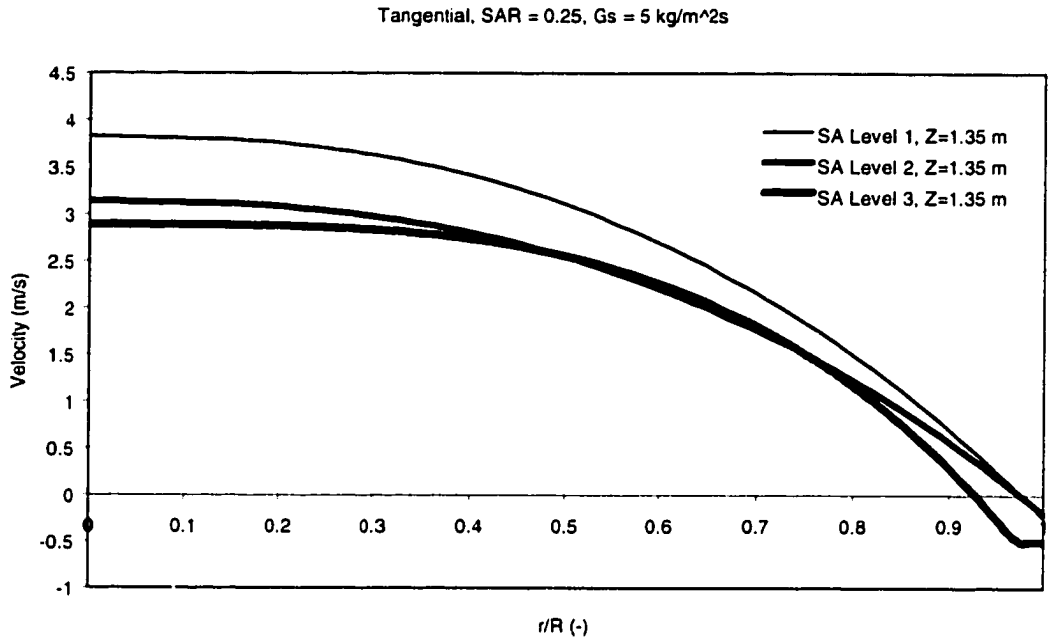

Figure 5.37. Effect of height of SA injection on the radial distribution of particle axial velocity. Model predictions.

Chapter 6

Overall Conclusions and Recommendations

In this study, the individual effects of selected secondary air injection parameters on the hydrodynamic behavior of a cold type CFB riser are studied experimentally. Single-phase CFD simulations are performed in order to understand the jet interactions with upcoming flow. Also, the knowledge gathered on flow behavior is shaped into an approximate, core-annular mathematical model, which accounts for the effects of SA injection parameters on the overall hydrodynamics of the riser flow.

An existing CFB riser is modified in order to incorporate the secondary air injection. A modular secondary air injection device is designed to vary the parameters of SA injection, independently. With the present SA port it is possible to direct the secondary air jets radially, tangentially or with a forty-five degree angle into the riser. The port can be installed at various axial positions along the riser. The volumetric flow ratio of SA jets over the primary air (SAR = SA/PA) can also be varied.

The particle velocity at a local point is measured at four different axial locations to see its axial development and, for eight radial locations along the radius for each of the axial location in order to gather information on the radial profile of particle axial velocity. These experiments are repeated for varying SAR (0.25 and 0.5), height of SA injection (0.7-m, 1.2-m, and 2.14-m above the distributor plate), mode of injection (radial, tangential, and 45 degree) for sand particles. Second level SA injection experiments are also repeated for FCC particles. For the above configurations the pressure drop profile along the riser, and its fluctuations are also measured.

The results, discussed in detail in related chapters, show that the injection of SA effects the riser hydrodynamics by resulting in a denser suspension beneath

the SA jets, while giving rise to a more dispersed bed above the SA injection plane. The suspension density in the region above the SA injection plane either remains the same or slightly reduces with the injection of secondary air. The height of the dense region varies with the height of the SA injection plane while the mode of the SA injection is also found as effective in determination of the suspension density below the SA injection region, tangential injection resulting in the highest solids holdup.

The particle velocity measurement reveals useful data on the flow development of particles. The measurements show that the flow structure in the riser is core annular, and the injection of secondary air increases the thickness of the annulus below the injection plane, while decreasing it above the injection plane. The denser suspension density attained with tangential SA injection is seen as a thicker annulus region in the velocity measurements. It is clearly seen that, due to the reduced superficial gas velocity, the particle velocity under the SA injection plane is lower, suggesting that the two parameters of secondary air injection; height and SAR may be used to achieve a desired solids residence time in the primary region. Also, velocity measurement reveals good indication of variations in the fluidization characteristics of different particle groups. Due to the irregular behavior of sand flow, the velocity data obtained from experiment with sand particles is more scattered and less consistent than that of FCC particles.

CFD simulations using Fluent 4.4. are performed. Results show that different gas mixing patterns are attained with different modes of SA injection, tangential injection of SA results in a gradual mixing from the riser walls towards the center as the flow develops along the riser. Also, the results form gas phase simulations supports the experimental observations on the cut-off effects of SA jets on the presence of local high-pressure and low-pressure regions at the same cross section.

An existing core radius formulation is modified to account for the application of secondary air. The modified equation considers the particle group, height of

secondary air injection and secondary air ratio. The effects of mode of SA injection on the solids suspension density is modeled separately, assuming that the jets form an effective barrier over the upcoming suspension. The results obtained are in good agreement with the experimental data of this work as well as with the data available in the literature.

Recommendations:

1) Same type of experiments must be performed with larger risers to account for the effects of the riser size.

2) Quantification of cut off effects of SA jets may be performed with a simpler experimental set-up by using various obstructions of known cross sectional area over the upcoming suspension. The Equation 3.80 is a very rough estimation, which needs to be modified and verified against experimental data.

3) The effect of particle loading on the axial decay of swirl intensity must be studied extensively.

REFERENCES

Aguillon, J., Shakourzadeh, K., and Guigon, P., A new method for local solid concentration measurement in circulating fluidized bed, *Powder Technology*, vol. 86, pp. 251-255, 1996.

Aouabed, H., Legentilhomme, P., and Legrand, Wall visualization of swirl decaying flow using a dot-paint method, *Experiments in Fluids*, vol. 19, pp. 43-50, 1995.

Arena, U., Camomarota, A., Massimilla, L. and Pistane, L. Hydrodynamics of circulating fluidized beds with secondary air injection. In *Proc. 12th Int. Conf. on Fluidized Bed Combustion* (Edited by L. N. Rubow,), pp. 899-905. ASME, San Diego, CA. 1993.

Arena, U., Camomarota, A., Massimilla, L. and Pistane, L. The hydrodynamic behavior of two circulating bed units of different sizes. In *Circulating Fluidized bed Technology II* (Edited by Basu, P. and Large, J. F.), pp. 223-230. Pergamon Press, Toronto, 1988.

Bai, D. R., Jin, Y., Yu, Z. Q. & Yang, Q. Y. Characterization of clusters and average slip velocity in fast fluidized beds. *Chem. Eng. J.* v. 17, pp 44-49, 1989.

Bai, D. R., Jin, Y., Yu, Z. Q. Cluster observation in a two dimensional fast fluidized bed. *In Fluidization'91-Science and Technology* (Edited by Kwauk, M. and Hasatani, M.), pp. 110-115. Science Press, Beijing, 1991.

Bai, D. R., Jin, Y., Yu, Z. Q., and Zhu, J. X., The axial distribution of the cross-sectionally averaged voidage in fast fluidized beds, *Powder Technology*, vol. 71, pp. 51-58, 1992.

Bai, D., Shibuya, E., Nakagawa, N., Kato, K., Characterizations of gas fluidization regimes using pressure fluctuations. *Powder Technology*, vol. 87, pp. 105-111, 1996.

Bai, D., Zhu, J., Jin, Y., Yu, Z., Internal re-circulation flow structure in vertical up-flow gas-solids suspensions Part i. a core-annulus model, *Powder Technology*, vol. 85, pp. 171-177, 1995.

Basu, P., Fraser, S.A., Circulating Fluidized Bed Boilers, Design and Applications, Butterworth-Heinemann, Stoneham, MA, 1991.

Berruti, F., Chaouiki, J., Godfroy, L., Pugsley, R. S., and Patience, G. S., Hydrodynamics of circulating fluidized bed risers: a review. *Can. Journal of Chem. Eng.* v. 73. pp. 579-602, 1995.

Berruti, Franco, and Kalogerakis, N., Modelling the internal floe structure of circulating fluidized beds, *Canadian Journal of Chemical Engineering*, v. 67, pp. 1010-1014, 1989.

Bodelin, P., Nolodsof, Y., Delebarre, A. Flow structure investigations in a CFB. In *Circulating Fluidized Bed Technology IV*, (Edited by Avidan A. A.) Engineering Foundation, AIChE, New York, pp. 118-122, 1994.

Boemer, A., Braun, A., Renz, U., Emission of N2O from four different large scale circulating fluidized bed combustors. In *Proc. 12th Int. Conf. on Fluidized Bed Combustion* (Edited by Rubow, L. N.), pp. 585-597. ASME, San Diego, CA., 1993.

Brereton, C. M. H., Grace, J. R., Microstructural aspects of the behavior of circulating fluidized beds. *Chem. Eng. Sci.* v. 48. pp. 2565-2572, 1993.

Brereton, C. M. H., Grace, J. R., End effects in circulating fluidized bed hydrodynamics. In *Circulating Fluidized Bed Technology IV*, (Edited by Avidan A. A.) Engineering Foundation, AIChE, New York, pp. 137-144, 1994.

Chang, F. and Dhir, K.V., Turbulent flow field in tangentially injected swirl flows in tubes, *Int. J. Heat and Fluid Flow*, v. 15, No. 5, pp. 346-356, 1994.

Cho, Y. J., Namkung, W., Kim, S. D., and Park, S., Effect of secondary air injection on axial solid holdup distribution in a circulating fluidized bed,

Journal of Chemical Engineering of Japan, vol. 27, no. 2, pp. 158-164, 1994.

Choi, J. H., Kim K. J., and Kim, S. D., Effect of secondary gas injection on the particle entrainment rate in a gas fluidized bed, *Powder Technology*, vol. 90, pp. 227-233, 1997.

Contractor, R. M., Patience, G. S., Garnett, D. I., Horowitz, H. S., Sisler, G. M., and Bergna, H. E., A new process of n-Butane oxidation to maleic anhydride using a circulating fluidized bed reactor. In *Circulating Fluidized Bed Technology IV*, A. A. Avidan Ed. AIChE, New York, pp. 243-248, 1994.

Crowe, C. T., Troutt, T. R., Chung, J. N. Numerical models for two phase turbulent flows. *Annu. Rev. Fluid. Mech.* vol. 28, pp. 11-43, 1996.

Crowe, J. T. Review-Numerical models for dilute gas-particle flows. *Journal of Fluids Engineering*. vol. 104, pp. 297-303, 1982.

Diego, L. F., Gayan P., and Adanez, J., Modeling the flow structure in circulating fluidized beds, *Powder Technology*, vol. 85, pp. 19-27, 1995.

Ding, J., and Gidaspow, D., A bubbling fluidization model using kinetic theory of granular flows. *AIChE J.*, v. 36, pp. 523-538, 1990.

Drahos, J., Chermak, J., Guardani, R., Schugerl, K., Characterization of flow regime transitions in a circulating fluidized bed. *Powder Technology*, vol. 56, pp. 41-48, 1988.

Elghobashi, S. On predicting particle laden turbulent flows. *Applied Scientific Research*, vol. 52, pp. 309-329, 1994.

Ersoy, L. E., Militzer, J., Hamdullahpur, F. Effects of secondary air injection on the hydrodynamics of circulating fluidized beds. *Proceedings of the 14th International Conference on Fluidized Bed Combustion*, (Preto, F.D.S. eds.), p. 1247-1254, Vancouver, 1997

Fan, L. T., Ho, T. C., Hiroaka, S., and Walawender, W. P., Pressure fluctuations in a fluidized bed. *AIChE Journal*, vol. 27, pp. 388-396, 1981.

Fei, W., Fangbin, L., Yong, J., and Zhiqing, Y., Mass flux profiles in a high density circulating fluidized bed, *Powder Technology*, vol. 91, pp. 189-195, 1997.

Flemmer, R. L. C., and Blanks, C. L., On the drag coefficient of a sphere. *Powder Technology*, vol. 48, pp. 217-221, 1986.

Gajdos, L. J., and Bierl, T. W. Studies in support of recirculating fluidized bed reactors for the processing of coal. *Topic report on work performed under DOE/EX-C-76-01-2449*. Carnegie Mellon University, Pittsburg, PA. 1978.

Geldart, D., Gas-Fluidization Technology, Wiley, New York, 1986.

Gidaspow, D., Bezburuah, R., and Ding, J., Hydrodynamics of circulating fluidized beds: Kinetic theory approach, in *Fluidization VII*, O. E. Potter and D. J. Nicklin ed. Engineering Foundation, ?New York, pp. 75-82, 1992.

Gidaspow, D. Multiphase Flow and Fluidization. Academic Press, San Diego, CA, USA. 1994.

Grace, J. R. and Tout, J. A theory for cluster formation in vertically conveyed suspension of intermediate density. *Trans. Institute of Chemical Engineers*. Vol. 4, pp. 49-54, 1979.

Grace, J. R., Riser geometry influence on CFB particle and fluid dynamics, *Proceedings of The Fifth International Conference in Circulating Fluidized Beds, People's Republic of China*, pp. PL2.1-PL2.16, May 28th – June 1st , 1996.

Grace JR, Avidan AA and Knowlton TM (editors), Circulating Fluidized Beds, Chapman & Hall, London, 585 pages, 1997.

Hamdullahpur, F., and MacKay, G. D. M., Two-phase flow behavior in the freeboard of a gas-fluidized bed, *A.I.Ch.E. Journal*, vol. 32, no. 12, pp. 2047-2055, 1986.

Hamdullahpur, F., Zayed, R. S., and Khawaja, E., NO_x reduction in fluidized bed combustors, Presented at the *American Flame Research Comittee's*

1989 International Synposium on Combustion in Industrial Furnaces and Boilers. Short Hills, New Jersey. September 25, 1989.

Harris, B. J. and Davidson, J. F., Modeling options for circulating fluidized beds: A core/annulus deposition model. In *Circulating Fluidized bed Technology IV*, A. A. Avidan ed., AIChE, New York, pp. 32-39, 1994

Harris, B. J. Davidson, J. F., and Xue, Y., Axial and radial variation of flow in circulating fluidized beds. In *Circulating Fluidized bed Technology IV*, A. A. Avidan ed., AIChE, New York, pp. 103-110, 1994

Hartge, E. U., Li, Y., and Werther, J. Analysis of the local structure of the two-phase flow in a fast fluidized bed. In *Circulating Fluidized bed Technology*, P. Basu Ed., Pergamon Press, pp. 153-160, 1986.

Hartge, E. U., Rensner, D., and Werther, J. Solids concentration and velocity in circulating fluidized beds. In *Circulating Fluidized bed Technology II*, P. Basu and J. F. Large Ed., Pergamon Press, pp. 165-180, 1988.

Hartge, E. U., Rensner, D., and Werther, J., Solids concentration and velocity patterns in circulating fluidized beds, *Proceedings of The Second International Conference in Circulating Fluidized Beds*, France, pp. 165-179, Mar 14th -18th, 1988.

Herb, B., Dou, S., Tuzla, K., and Chen J. C., Solid mass fluxes in circulating fluidized beds, *Powder Technology*, vol. 70, pp. 197-205, 1992.

Hippinen, I., Lu, Y., Jahkola, A. The effect of combustion air staging on combustion performance and emissions in PFBC. In *Proc. 12th Int. Conf. on Fluidized Bed Combustion* (Edited by L. N. Rubow), pp. 117-121. ASME, San Diego, CA. 1993.

Hirama, T., Kuramata, K., and Chiba, T., Effects of riser height and downcomer solids inventory on dense-bed height in a riser of CFB, *Proceedings of The International Symposium of The Engineering Foundation- Fluidization VIII, France*, pp. 113-120, May 14-19, 1995.

Hirama, T., Takeuchi, H., and Chiba, T., Regime classification of macroscopic gas-solid flow in a circulating fluidized bed riser, *Powder Technology*, vol. 70, pp. 215-222, 1992.

Hong, J., Shen, Y., and Tomita, Y., Phase diagrams in dense pneumatic transport, *Powder Technology*, vol. 84, pp. 213-219, 1995.

Horio, M. and Kuroki, H. Three dimensional flow visualization of dilutely dispersed solids in bubbling and circulating fluidized beds. *Chem. Eng. Science*, vol. 49, pp. 2413-2421, 1994.

Horio, M., Hydrodynamics of circulating fluidization- present status and research needs. In *Circulating Fluidized bed Technology III*, P. Basu, M. Horio and M. Hasatani eds., Pergamon Press, New York, pp. 3-15, 1991.

Horio, M., Morishita, K., Tachibana, O., and Murata, N., Solid distribution and movement in circulating fluidized beds, *Proceedings of The Second International Conference in Circulating Fluidized Beds*, France, pp. 147-163, Mar 14th -18th , 1988.

Illias, S., Ying, S., Mathur, G. D., and Govind, R., Studies on a swirling circulating fluidized bed. In *Circulating Fluidized bed Technology II*, P. Basu and J. F. Large Ed., Pergamon Press, New York, pp. 537-1546, 1988.

Ishii, H., Nakajima, T., and Horio, M., The clustering annular flow model of circulating fluidized beds, *Journal of Chemical Engineering of Japan*, vol. 22, no. 5, pp. 484-490, 1989.

Issangya, A. S., Bai, D., Bi, H. T., Lim, K. S., Zhu, J., and Grace, J. R., Axial solids holdup profiles in a high-density circulating fluidized bed riser, *Proceedings of The Fifth International Conference in Circulating Fluidized Beds*, People's Republic of China, pp. DB6.1-DB6.7, May 28th – June 1st , 1996.

Kan, J., Hydrodynamics of Circulating Fluidized Beds, Ph. D. Dissertation, Technical University of Nova Scotia, Halifax, NS, Canada, 1990.

Karry, R. S. B., and Knowlton, T. M., A Practical definition of the fast fluidization regime. In *Circulating Fluidized bed Technology III*, P. Basu, M. Horio and M. Hasatani eds., Pergamon Press, New York, pp. 67-72, 1991.

Kato, K., Takarada, T., Tamura, T., and Nishino, K., Particle hold-up distribution in a circulating fluidized bed In *Circulating Fluidized bed Technology III*, P. Basu, M. Horio and M. Hasatani eds., Pergamon Press, New York, pp. 145-150, 1991.

Kim, S. D., Cho, Y. J., Namkung, W. and Park, S. Effect of secondary air injection on axial solids holdup distribution in a circulating fluidized bed. *Journal of Chem. Eng. of Japan*, vol. 27, no 2, pp. 158-164, 1994.

King, D. F., Estimation of dense bed voidage in fast and slow fluidized bed of FCC catalyst. In Fluidization VI, J. R. Grace, L. W. Shemit and M. A. Bergougnou Ed., pp. 1-8, 1989.

King, M K., Rothfus, R. R., and Kermode, R. I., Static pressure and velocity profiles in swirling incompressible tube flow, *A.I.Ch.E. Journal*, vol. 15, no. 6, pp. 837-842, Nov. 1969.

Koeningsdorff, R. and Werther, J. Gas-solid mixing and flow structure modeling of the upper dilute zone of a circulating fluidized bed. *Powder Technology*, vol. 82, pp. 317-329, 1995.

Kramers, H. and Alberda, G., Frequency response analysis of continuos flow systems, *Chemical Engineering Science*, vol. 2, pp. 173-181, 1953.

Kruda, C., and Ogawa, K., Turbulent swirling pipe flow, in Encyclopedia of Fluid Mechanics Vol 1, Flow Phenomena And Measurements, Ed Cheremisinoff, N. P., Gulf Publishing Company, 1986.

Kruse, M. Schoenfelder, H., and Werther, J., A two-dimensional model for gas mixing in the upper dilute zone of a circulating fluidized bed, The *Canadian Journal of Chemical Engineering*, vol. 73, pp. 620-634, 1995.

Kunii, D., and Levenspiel, O., Entrainment of solids from Fluidized Beds: I. Hold-up of solids in the freeboard II. Operation of fast fluidized beds, *Powder Technology*, vol. 62, pp. 193-206, 1990.

Kunii, D., Levenspiel, O., Fluidization Engineering, Butterworth-Heinemann, Stoneham, MA, 1991a.

Kunii, D., Levenspiel, O., Flow modeling of fast fluidized beds. In *Circulating Fluidized bed Technology III*, P. Basu, M. Horio and M. Hasatani eds., Pergamon Press, New York, pp. 91-98, 1991b.

Kunii, D., Levenspiel, O., Fluidization Engineering, Krieger Publishong Co., New York, 1977.

Kwauk, M., N. Wang, Y. Li, B. Chen and Z. Shen, Fast Fluidization at ICM, in *CFB Technology*, P. Basu Ed. Pergamon Press, Toronto, pp. 33-62, 1986.

Launder, B.E. and Spalding, D. B. Mathematical Models of Turbulence. Academic Press, New York, 1972.

Li, H., Xia, Y., Tung, Y., Kwauk, M. Micro visualization of two phase structure in a fast fluidized bed. In *Circulating Fluidized bed Technology III*, P. Basu, M. Horio and M. Hasatani eds., Pergamon Press, New York, pp. 183-188, 1991b

Li, J., Reh, J., Kwauk, M. Application of the principle of energy minimization to the dynamics of circulating fluidized beds. In *Circulating Fluidized bed Technology III*, P. Basu, M. Horio and M. Hasatani eds., Pergamon Press, New York, pp. 105-112, 1991a.

Li, J., Tung, Y., and Kwauk, M. Energy transport and regime transition in particulate fluid two-phase flow. In *Circulating Fluidized bed Technology II*, P. Basu and J. F. Large Ed., Pergamon Press, New York, pp. 75-87, 1988.

Li, Y. and Kwauk, M. The dynamics of fast fluidization. In *Fluidization*, J.R. Grace and J.M. Matsen eds. Plenum Press, New York, pp. 537-544, 1980.

Lilley, D. G., Swirl flows in combustion: a review, *AIAA Journal*, vol. 15, no. 8, pp. 1063-1078, 1977.

Lim, K.S., Zhu, J.X., Grace, J.R., Hydrodynamics of Gas-Solid Fluidization, *Int. J. Multiphase Flow*, vol. 21, suppl., pp. 141-193, 1995.

Littman, H., Morgan, M. H., Paccione, J. D., and Jovanovic, S. Dj. Modeling and measurement of the effective drag coefficient in decelerating and non-accelerating turbulent gas-solid dilute phase flow of large particles in a vertical transport pipe. *Powder Technology*, v. 77, pp. 267-283, 1993.

Liu, H. S. Numerical Simulations of Turbulent Gas-Solid Flows in Horizontal Channels. M.S. Thesis, Technical University of Nova Scotia, Halifax, NS, 1995.

Ljunghahl, B., Zethraeus, B. Air jet penetration into circulating fluidized bed risers, -A simplified model approach. *Proceedings of The Fifth International Conference in Circulating Fluidized Beds*, People's Republic of China, pp. DGS3.1 – DGS3.6, May 28th – June 1st , 1996

Lodes, A., and Mierka, O., Particle velocities in two-phase solid-gas flow. *Powder Technology*, vol. 58, pp. 163-168, 1989.

Marzocchella, A., and Arena, U., Hydrodynamics of a circulating fluidized bed operated with different secondary air injection devices, *Powder Technology*, vol. 87, pp. 185-191, 1996.

Marzocchella, A., and Arena, U., Mixing of a lateral gas stream in a two-dimensional riser of a circulating fluidized bed, *The Canadian Journal of Chemical Engineering*, vol. 74, pp. 195-202, 1996.

Matsen, J. M. Some characteristics of large solids circulating systems. In *Fluidization Technology*, D. L. Keairns eds. Hemisphere, New York, pp. 135-149, 1976.

McLaughlin, J. B. Numerical computation of particle turbulence interactions. *Int. J. of Multiphase Flow*, vol. 20 (Supp.), pp.211-232, 1994.

Militzer, J., Hebb, J. P., Jollimore, G., and Shakourzadeh, K., Solid particle velocity measurements, *Proceedings of Fluidization VII conference on FBC*, Australia, May 3rd –8th ,1992.

Monceaux, L., Azzi, M., Molodtsof, Y. and Large, J. F. Overall and local characterisation of flow regimes in a circulating fluidized bed. In *Circulating Fluidized bed Technology*, P. Basu ed., Pergamon Press, Toronto, pp. 185-191, 1986b.

Monceaux, L., Azzi, M., Molodtsof, Y. and Large, J. F.Particle mass flux profiles and flow regime characteristics in a pilot-scale fast fluidized bed unit. *In Fluidization V*, (Ostergaard, K. and Sorensen, A. eds.), Engineering Foundation, New York, pp. 337-344, 1986a.

Mori, S., Hashimoto, O., Haruta, T., Mochizuti, K., Matsutani, W., Hiraoka, S., Yamada, I., Kojima, T. and Tsuji, K., Flow regime classifications using pressure fluctuations. In *Circulating Fluidized bed Technology II*, P. Basu and J. F. Large Ed., Pergamon Press, New York, pp. 105-112, 1988

Mori, S., Yan, Y., Kato, K., Matsubara, K., and Liu. D. Hydrodynamics of a circulating fluidized bed. In *Circulating Fluidized bed Technology III*, P. Basu, M. Horio and M. Hasatani eds., Pergamon Press, New York, pp. 113-118, 1991.

Motte, J., Molodtsof, Y., and Delebarre, A., Flow development and re-development scales in a CFB, *Proceedings of The Fifth International Conference in Circulating Fluidized Beds*, People's Republic of China, pp. DB16.1-DB16.6, May 28th - June 1st , 1996.

Nakamura, K. and Capes, C. E. Vertical pneumatic conveying: A theoretical study of uniform and annular particle flow models. *Can. Jour. Of Chem. Eng.* vol. 51, pp. 39-46, 1973.

Nieh, S., and Yang, G., Particle flow pattern in the freeboard of a vortexing fluidized bed, *Powder Technology*, vol. 50, pp. 121-131, 1987.

Nieh, S., Yang, G., Zhu, A. Q., and Zhao, C. S., Measurements of gas-particle flows and elutriation of an 18 inch i.d. cold vortexing fluidized-bed combustion model, *Powder Technology*, vol. 69, pp. 139-146, 1992.

Nieuwland, J. J., Delnoij, E., Kuipers, J. A. M., and van Swaaij, W. P. M., An engineering model for dilute riser flow, *Powder Technology*, vol. 90, pp. 115-123, 1997.

Nieuwland, J. J., Meijer, R., Kuipers, J. A. M., and van Swaaij, W. P. M., Measurements of solids concentration and axial solids velocity in gas-solid two-phase flows, *Powder Technology*, vol. 87, pp. 127-139, 1996.

Nissan, A. H., and Bresan, V. P., Swirling flow in cylinders, *A.I.Ch.E.* Journal, vol. 7, no.4, pp. 543-547, 1961.

Novak, W., Mineo, H., Yamazaki, R., and Yoshida, K., Behavior of particles in a circulating fluidized bed of a mixture of two different sized particles, In *Circulating Fluidized bed Technology III*, P. Basu, M. Horio and M. Hasatani eds., Pergamon Press, New York, pp. 219-224, 1991

Ouyang, S. and Potter, O. E. Consistency of circulating fluidized bed experimental data. *Ind. Eng. Chem. Res.* vol. 32, pp. 1041-1045, 1993

Patankar, S. V. Numerical Heat Transfer and Fluid Flow. McGraw-Hill, New York, 1980.

Patience, G. S. Chaouki, J., Berruti, F., Wong, R. Scaling considerations for circulating fluidized bed risers. *Powder Technology*, vol. 72, pp. 31-37, 1992.

Patience, G. S., and Chaouki, J., Gas phase hydrodynamics in the riser of a circulating fluidized bed, *Chemical Engineering Science*, vol. 48, no. 18, pp. 3195-3205, 1993.

Patience, G. S., Chaouki, J., Solids hydrodynamics in the fully developed region of CFB risers, *Proceedings of The International Symposium of The Engineering Foundation- Fluidization VIII*, France, pp. 33-40, May 14-19, 1995.

Perales, J. F., Coll, T., Llop, M. F., Puigjaner, L., Arnaldos, J., and Casal, J., On the transition from bubbling to fast-fluidization regimes. In *Circulating Fluidized bed Technology III*, P. Basu, M. Horio and M. Hasatani eds., Pergamon Press, New York, pp. 73-78, 1991.

Pratte, B. D., and Keffer, J. F., The swirling turbulent jet, *Journal of Basic Engineering*, pp. 739-748, Dec. 1972.

Puchyr, D., M., Behie, A. L., J., Mehrotra, A., K., and Kalogerakis, N., E., Modelling a circulating fluidized bed reactor with gas-solid down-flow at the wall. *Can. J. of Chem. Eng.*, v. 73, pp 317-326, April 1997.

Puggsley, T. S., Lapuinte, D., Hirschberg, B., Werther, J. Exit effects in circulating fluidized bed risers. The *Can. Journal of Chem. Eng.* v. 75, pp 1001-1010, 1997.

Pugsley, T. S., Berruti, F. A predictive hydrodynamic model for circulating fluidized bed risers. *Powder Technology*, vol. 89, pp. 57-69, 1996.

Ramos, J. I., and Somer, H. T., Swirling flow in a research combustor, *AIAA Journal*, vol. 23, no. 2, pp. 241-248, Feb. 1985.

Reh, L., Fluid dynamics of CFB-combustors, *Proceedings of The Fifth International Conference in Circulating Fluidized Beds, People's Republic of China*, pp. PL1.1-PL1.15, May 28th – June 1st , 1996.

Reynolds, W. C. The potential and limitations of direct and large eddy simulations. In Turbulence at the Cross Roads, edited by J.L. Lumley, pp. 313-343, New York: Springer-Verlag, 1990.

Rhode, D. L., Lilley, D. G., and McLaughlin, D. K., Mean flow fields in axisymmetric combustor geometries with swirl, *AIAA Journal*, vol. 21, no. 4, pp. 593-600, Apr. 1983.

Rhodes, M. J., Geldart, D. the hydrodynamics of recirculating fluidized beds. In *Circulating Fluidized bed Technology*, P. Basu Ed., Pergamon Press, New York, pp. 193-200, 1987.

Rhodes, M. J., Laussman, P., Vilain, F., Geldart, D. Measurement of radial and axial solids flux variations in the riser of a circulating fluidized bed. . In *Circulating Fluidized bed Technology II*, P. Basu and J. F. Large Ed., Pergamon Press, New York, pp. 155-164, 1988

Rhodes, M. J., Modelling the flow structure of upward-flowing gas-solids suspensions, *Powder Technology*, vol. 60, pp. 27-38, 1990.

Rhodes, M. J., Wang, X. S., Cheng, H., and Hirama, T., Similar profiles of solids flux in circulating fluidized-bed risers, *Chemical Engineering Science*, Vol. 47, no. 2, pp. 1635-1643, 1992.

Saberi, B., PhD Thesis, Modelisation des Systemes a Ecoulement Gaz-Solide:Application aux Cas des Reacteurs a Lit Fluidise Circulant. Universite de Compiegne, Compiegne, France, 1996.

Sarpkaya, T. Freeman Scholar Lecture: Computational Methods with Vortices. *Journal of Fluids Engineering*, v. 111, pp. 5-52, 1989.

Satija, S. Young, J.B., and Fan, L.S. Pressure fluctuation and choking criterion for vertical pneumatic conveying of fine particles., *Powder Technology*, vol. 43, p. 257, 1985.

Schlingting, H., Boundary Layer Theory, McGraw-Hill, Reissue, 1987.

Schnitzlein, M.G. and Weinstein, H. Flow characterization in high velocity fluidization using pressure fluctuations. *Chem. Eng. Sci.*, v. 43, pp. 2605-2614, 1988.

Senior, R. C., and Brereton. C., Modeling of circulating fluidized bed solids flow and distribution, *Chemical Engineering Science*, vol. 47, no. 2, pp. 281-296, 1992.

Shimizu, T., Inagaki, M., Furusava, T. Effect of sulfur removal and amonnia injection on NO_x emissions from a circulating fluidized bed combustor. In *Circulating Fluidized bed Technology IV*, A. Avidan ed. AIChE, pp. 393-398, 1991.

Shimizu, T., Fujita, D., Ishizu, K., Kobayashi, S., Inagaki, M. Effect of limestone feed on emissions of NO_x and N_2O from a circulating fluidized bed combustor. In *Proc. 12th Int. Conf. on Fluidized Bed Combustion* (Edited by L. N. Rubow), pp. 611-617. ASME, San Diego, CA. 1993.

Snitzlein, M.G and Weistein, H., Flow characterization in high velocity fluidized beds using pressure fluctuations. *Chem. Eng. Science*, Vol. 43, No 10. p. 2605, 1988.

Squire, H. B., Trouncer, J., Round jets in a general stream, *Ministry of Aircraft Production, Aeronautical Research and Memoranda, no. 1974*, Jan, 1944.

Stock, D. E. Particle Dispersion in Flowing Gases -- 1994 Freeman Scholar Lecture, Transactions of the ASME - I - *Journal of Fluids Engineering*, v. 118 N1 pp.4-14, 1996.

Talukdar, J. Coal Combustion in a Circulating Fuidized Bed. Ph.D. Dissertation. Technical University of Nova Scotia, Halifax, NS, 1996.

Thomson, W. T. Theory of Random Vibrations with Applications. Prentice Hall, Englewood Cliffs, New Jersey, 1993.

Tsuji, Y and Morikawa, Y. LDV measurements of an air-solid two-phase flow in a horizontal pipe. *J. Fluid Mech.*, vol. 120, pp. 385-409, 1982.

Tsuji, Y and Morikawa, Y., Mizuno, O. Experimental measurement of the Magnus force on a rotating sphere at low Reynolds numbers. *J. Fluids Eng.*, vol. 107, pp. 484-488, 1985.

Tsuji, Y., Morikawa, Y., Shiomi, H., LDV Measurements of an Air-Solid Two-Phase Flow in a Vertical Pipe, *J. Fluid Mechanics*, vol. 139, pp.417-434, 1984.

Tsuji, Y. Numerical Methods in Multiphase Flows (Edited by Crowe, C., T.,Johnson, R., Prosperetti, A., Sommerfeld M. and Tsuji, Y.) , ASME FED.Vol.185, 1994.

van Breugel, J. W., Stein, J. M. de Vries, R. J. Isokinetic sampling in a dense gas-solid stream. *Proc. Inst. Mech. Eng.* v.184, pp18-23, 1970.

Wang, X. S., and Gibbs, B. M., Hydrodynamics of a circulating fluidized bed with secondary injection. In *Circulating Fluidized bed Technolcgy III*, P. Basu, M. Horio and M. Hasatani eds., Pergamon Press, New York, pp. 225-230, 1991.

Weinstein, H. and Li, J. An evaluation of the actual density in the acceleration section of vertical risers. *Powder Technology*, v.57, pp.77-79, 1989.

Werther, J., Fluid mechanics of large scale CFB units, *Plenary Lecture, Fourth International Conference on Circulating Fluidized Beds*, USA, preprints 1-16, Aug. 1-5 1993.

Werther, J., Fluid mechanics of large-scale CFB units. In *Circulating Fluidized Bed Technology IV*. Edited by A. A. Avidan, AIChE, New York, pp. 1-14, 1994.

Wong, R., Pugsley, T., and Berruti, F., Modeling the axial voidage profile and flow structure in risers of circulating fluidized beds, *Chemical Engineering Science*, vol. 47, no. 9-11, pp. 2301-2306, 1992.

Wu, R. L., Lim, C. G., Grace, J. R., and Brereton, C. Instantenous local heat transfer and hydrodynamics in a circulating fluidized bed. *Int. J. Heat and Mass Transfer*, v. 34, pp. 2019-2027, 1991.

Wu, S., and Alliston, M., Cold model testing of the effects of air proportions and reactor outlet geometry on solids behavior in a CFB, ASME, *Fluidized Bed Combustion*- Volume 2, pp. 1003-1009, 1993.

Xu, Y., Zhao, C., Baosheng, J., Kunlei, L. Combustion characteristics and NOx emission control in vortexing fluidized bed. In *Proc. 12th Int. Conf. on Fluidized Bed Combustion* (Edited by Rubow, L. N.), pp. 123-128. ASME, San Diego, CA. 1993.

Yang, H., and Gautam, M., Experimental study on the variation of core-annulus interface in the riser of a circulating fluidized bed, *Proceedings of The Fifth*

International Conference in Circulating Fluidized Beds, People's Republic of China, pp. DB8.1-DB8.5, May 28th – June 1st , 1996.

Yang, W. C. A model for the dynamics of the circulating fluidized bed loop. In *Circulating Fluidized bed Technology II*, P. Basu and J. F. Large Ed., Pergamon Press, New York, pp. 181-191, 1988.

Yang, W. C. Criteria for choking in vertical pneumatic conveying lines. *Powder Technology*, v.35, pp.143-150, 1983.

Yang, Y. L., Jin, Y., Yu, Z. Q., and Wang, Z. W. Investigation on slip velocity distributions in the riser of a dilute circulating bed. *Powder Technology*, v.73, pp.67-73, 1992.

Yang, Y. L., Jin, Y., Yu, Z. Q., Wang, Z. and Bai, D. R. The radial distribution of local particle velocity in a dilute circulating fluidized bed. In *Circulating Fluidized bed Technology III*, P. Basu, M. Horio and M. Hasatani eds., Pergamon Press, New York, pp. 201-206, 1991.

Yang, Y., Jin, Y., Yu, Z., Wang, Z., and Bai, D., The radial distribution of local particle velocity in a dilute circulating fluidized bed. In *Circulating Fluidized bed Technology III*, P. Basu, M. Horio and M. Hasatani eds., Pergamon Press, New York, pp. 201-206, 1991.

Yarin, L. P., Hestroni, G., Turbulence intensity in dilute two phase flows-1. *Int. J. Multiphase Flow*, v. 20, no. 1, pp. 1-15, 1994.

Yerushalmi, J., and Cankurt N.T. Further studies of the regimes of fluidization. *Powder Technology*, v. 24, pp. 187-205, 1979.

Yerushalmi, J., Turner, D. H., Squires, A. M. The fast fluidized bed. *Ind. Eng. Chem. Process Des. Dev.*, v.15 pp. 47-53, 1976.

Zhang, H., Xie, Y., Mathematical modeling for longitudinal voidage distribution of fast fluidized beds. In *Circulating Fluidized bed Technology III*, P. Basu, M. Horio and M. Hasatani eds., Pergamon Press, New York, pp. 151-156, 1991.

Zhang, W., Tung, Y., and Johnsson. F., Radial voidage profiles in fast fluidized beds of different diameters, *Chemical Engineering Science*, vol. 46, no. 12, pp. 3045-3052, 1991.

Zheng, Z., Zhu, J., Grace, J. R., Lim, C. J., and Brereton C. H., Particle motion in circulating fluidized beds via microcomputer controlled color-stroboscopic photography. *In Fluidization VII* (Edited by O. E. Potter and D. J. Nicklin), pp 781-789, Engineering Foundation, New York, 1992.

Zhou, J, Grace, J. R., Lim, C. J., and Brereton, C. M. H., Particle velocity profiles in a circulating fluidized bed riser of square cross-section, *Chemical Engineering Science*, vol. 50, no. 2, pp. 237-244, 1995.

Appendix A

AIR FLOW RATE MEASUREMENTS

The fluidization gas supplied by the blower is introduced to the riser bottom via a 4" diameter pipe. The secondary air, on the other hand, is diverted from the main air supply through two identical 1.62" ID pipes, and injected into the riser from SA injection port. This appendix explains method used in airflow rate measurements.

The total pressure of an air stream flowing in a duct is the sum of the static or bursting pressure exerted upon the side-walls of the duct and the impact or velocity pressure of the moving air. Through the use of a pitot tube connected differentially to a manometer the velocity pressure alone is indicated and the corresponding air velocity is determined (user manual of Dwyer pitot tubes).

Air velocity at a local point, is estimated with the following equation supplied by the manufacturer: Dwyer Instruments Inc, bulletin no H-11

$$\text{Air velocity} = 1096.2*(Pv/D)^{1/2} \qquad \text{(A-1)}$$

Where, Pv is the velocity pressure in inches of water and D is the air density in lb/cu. ft. The velocity pressure is measured with a pressure transducer (Omega, type PX 160)

An equation to calculate the air density (D) is also provided in the bulletin;

$$\text{Air density} = 1.325\ (Pb/T) \qquad \text{(A-2)}$$

Where, Pb is the barometric pressure in inches of mercury and T is the absolute temperature (indicated temperature in °F plus 460).

It is recommended by the pitot tube manufacturer that for precise measurements (accuracy of plus minus 2%), a traversing method is applied. The traversing method is based on dividing the flow area into 10 equal area sections and performing the measurements in the centers of equal area circles.

The flow rates calculated by this method, then, can be integrated over the whole diameter. The flow rate obtained by this method minimizes the cross sectional non-uniformity in the flow area. However, since this method is very time consuming, another criterion given by the manufacturer is applied for quick measurements. This criterion, given by the manufacturer, is based on the turbulent flow profile and approximates the average velocity of the fluid with 0.9 times the velocity at the centerline of the tube. This method is stated as accurate within plus/minus 5%.

The traversing method is performed once prior to the course of the experiments, and the results obtained showed that averaging with the equation, $U_{ave} = 0.5*U_{center}$, confidently be used in the air flow rate calculations.

The results obtained from pitot tube-pressure transducer pair is tested against the blower output (0.23 m^3/s at 5 PSI) and results obtained by using the turbulent flow profile approximation are found to be satisfactory (within a range of plus/minus 4 %).

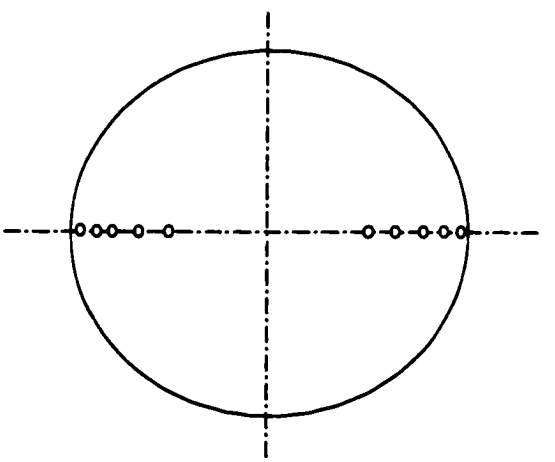

Figure A1. Illustrative figure shows the centers of the equal areas, as advised by the pitot tube manufacturer. This configuration is used in the air velocity measurements with pitot tube in the traversing method.

Appendix B

CALIBRATION OF PRESSURE TRANSDUCERS

The pressure transducers need to be tested against known pressures and calibrated for the accuracy of the measurements.

4 different pressure transducers are used in this study, which are:

MKS 0-1 Torr. (0-1 volt voltage output)

MKS 0-10 Torr(0-1 volt voltage output)

MKS 0-100 Torr Transducers. (0-1 volt voltage output)

OMEGA type PX 160. (0-5" of H_2O, 0-5 volts voltage output).

The pressure fluctuations are measured with the sensitive very MKS 0-1 Torr transducer, which is re-calibrated by the manufacturer prior to the experiments. The other transducer are tested and calibrated as follows.

One opening of a U tube manometer is connected to the plus port of the differential pressure transducers, leaving other port exposed to the atmospheric pressure. A known amount of water is added to the other leg of the manometer, which is exposed to atmospheric pressure, also. Then the resulting pressure increase in the plus port of the transducer is due to the weight of the water which occupies the difference in the water level in the manometers. This is illustrated in Figure A2.1.

The results showed that the MKS pressure transducers gave a linear pressure output (0-1 Volts) within its range (0-10 and 0-100 Torr) with zero offset as shown in Figures A2.2 and A2.3, respectively. The Omega pressure transducer, which is used to measure the air flow rates, on the other hand had an offset with a linear voltage output (Figure A2.4). Therefore a data is fitted to a linear curve to estimate the corresponding pressure from the voltage output from the transducer.

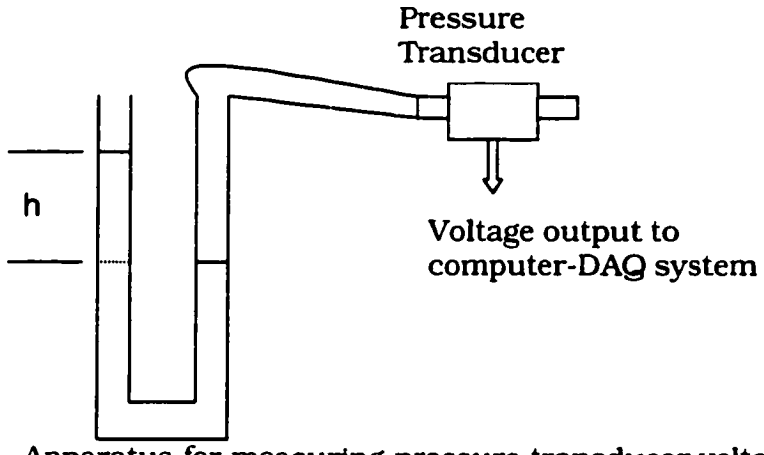

Figure A2. 1. Apparatus for measuring pressure transducer voltage output for a known pressure input.

0-10 Torr. Transducer:

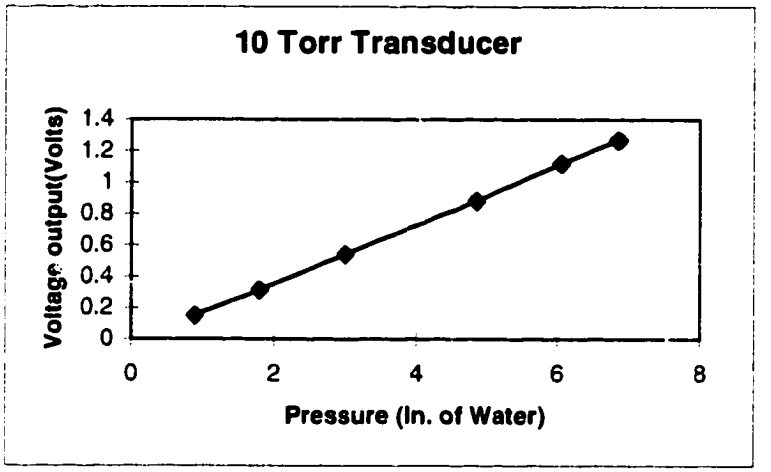

10 Torr Transducer, Input-output data

In. of Water	Voltage Output
0.9	0.154
1.8	0.314
3	0.546
4.85	0.882
6.05	1.119
6.85	1.268

The 10-Torr transducer obeys: Vel Pressure (in. water) = volts*5.362

Figure A2.2. The test data in tabular and graphical form for 0-10 Torr MKS transducer.

0-100 Torr transducer:

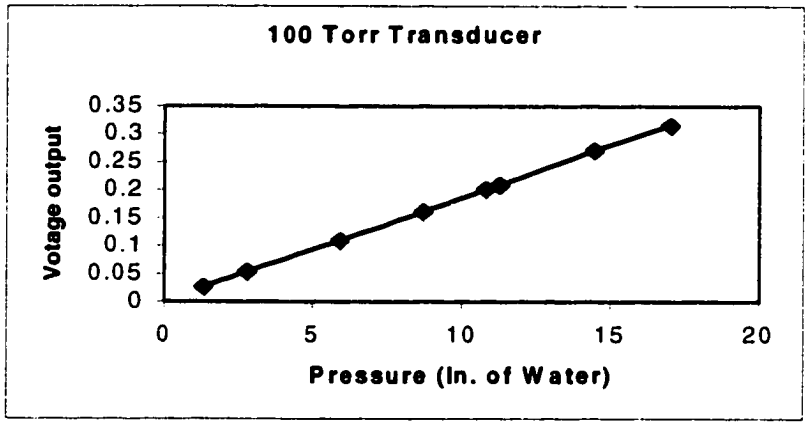

Inches of Water	Voltage output
1.3	0.0266
2.8	0.0536
5.9	0.109
8.7	0.161
10.8	0.201
11.3	0.21
14.45	0.27
17	0.316

0-100 Torr pressure transducer obeys: Pressure = 53.61* (Voltage output)

Figure A2.3. The test data of 0-100 Torr MKS transducer

Omega P-160:

mm water	Inc. of water	Voltage output
0	0	1.288
7	0.285714	1.456
28	1.142857	2.01
40	1.632653	2.27
57	2.326531	2.7
69	2.816327	2.92
87	3.55102	3.39
102	4.163265	3.79
113	4.612245	4.08
123	5.020408	4.31
133	5.428571	4.54
142	5.795918	4.77
152	6.204082	5.03
164	6.693878	5.32
172	7.020408	5.5
182	7.428571	5.72
192	7.836735	5.98
196	8	6.09
205	8.367347	6.32
213	8.693878	6.49
232	9.469388	6.94
240	9.795918	7.15
250	10.20408	7.36

Data fitting gives: Voltage output = Pressure (In water)*0.6 +1.28

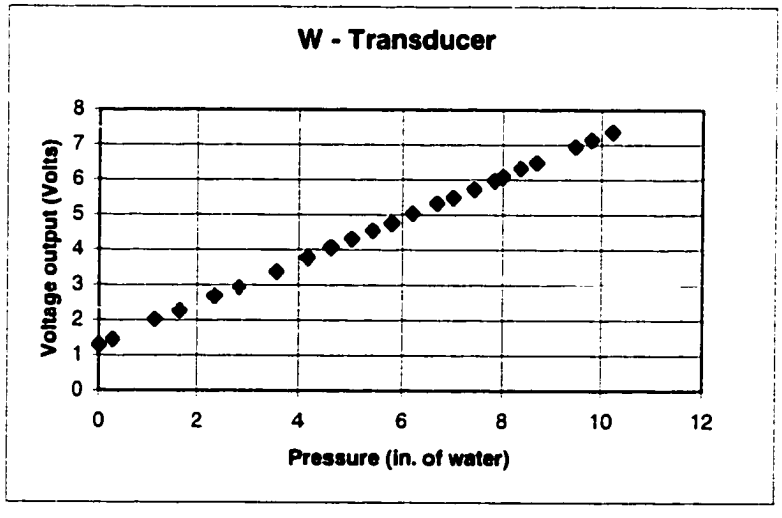

Figure A2.4. The test data of Omega-PX160 transducer

IMAGE EVALUATION TEST TARGET (QA-3)

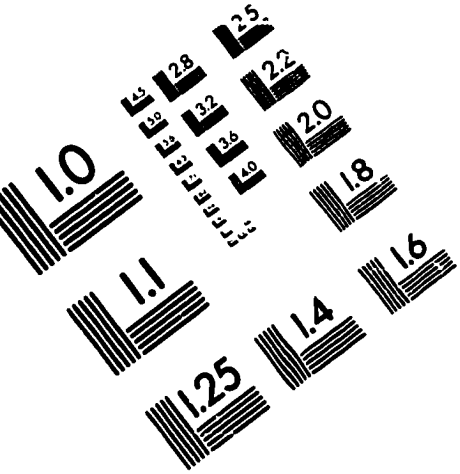

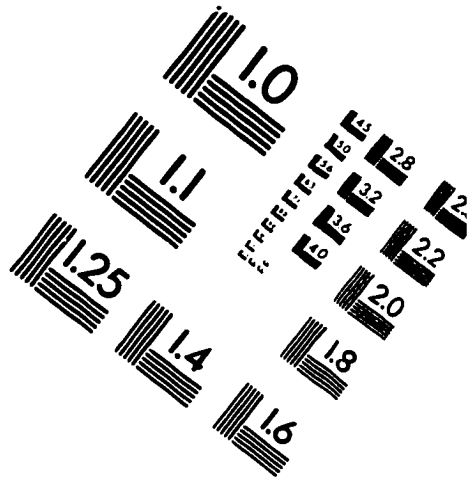

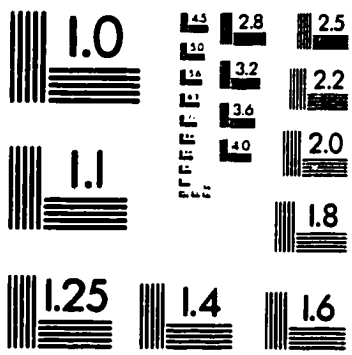

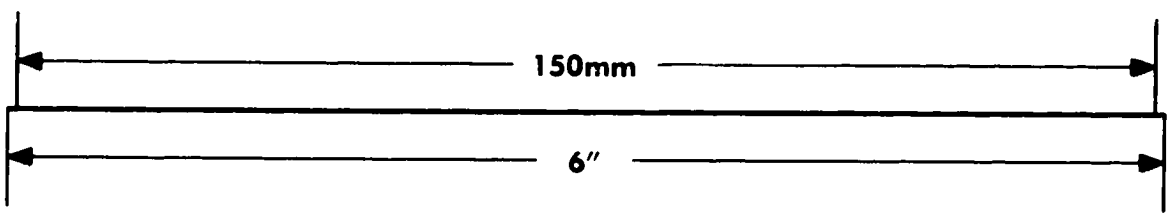

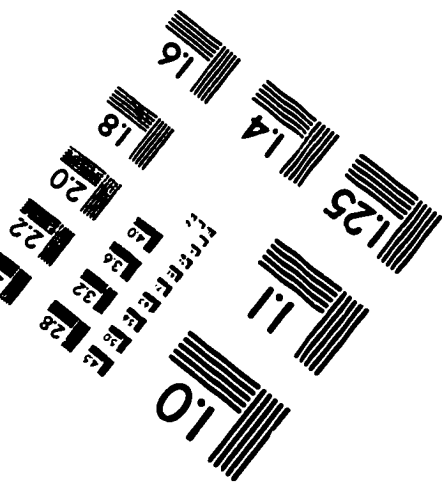

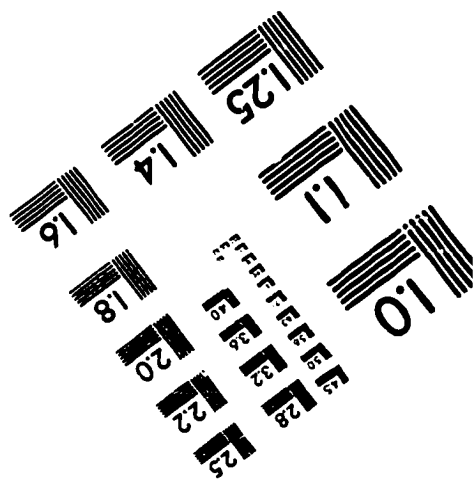

APPLIED IMAGE, Inc
1653 East Main Street
Rochester, NY 14609 USA
Phone: 716/482-0300
Fax: 716/288-5989